# CHARACTERIZATION OF CATHODE MATERIAL FOR LITHIUM-ION BATTERIES

# EXPLORING $LiFeV_2O_7$ AS A POTENTIAL CATHODE FOR LITHIUM-ION BATTERIES: AN INTEGRATED STUDY USING $^7$Li NMR, DFT, AND OPERANDO SYNCHROTRON X-RAY DIFFRACTION

TAIANA LUCIA EMMANUEL PEREIRA, M.Sc.

A Thesis Submitted to the School of Graduate Studies in Partial Fulfilment
of Requirements for the Degree Doctor of Philosophy

McMaster University

McMaster University, Hamilton, Ontario

Doctor of Philosophy (2024) Chemistry and Chemical Biology

Title: Exploring $LiFeV_2O_7$ as a Potential Cathode for LIBs: An Integrated Study Using $^7$Li NMR, DFT, and Operando Synchrotron X-Ray Diffraction

Author: Taiana Lucia E. Pereira, M.Sc.

Supervisor: Professor Gillian R. Goward

Number of Pages: (xxii,192)

# Lay Abstract

This thesis explores the lithium-ion dynamics and structural changes in the new cathode material $LiFeV_2O_7$ using solid-state NMR spectroscopy and density functional theory (DFT). As the demand for high-performance lithium-ion batteries (LIBs) grows, discovering cathode materials with better energy density, stability, and safety becomes crucial. $LiFeV_2O_7$ is particularly interesting due to its structure, which includes two transition metals that undergo redox processes. This study combines advanced DFT calculations with experimental techniques to understand how structural disorder and the oxidation state of transition metals affect NMR results. Solid-state NMR spectroscopy and diffraction methods are used to examine lithium-ion exchange and structural changes during battery cycling. The research identifies how specific crystallographic changes enhance lithium mobility, providing insights that can improve cathode design. This comprehensive study contributes to the development of more efficient and stable LIBs by revealing the complex interplay between structure, dynamics, and electrochemical performance.

# Abstract

This thesis investigates the lithium-ion dynamics and structural changes in the novel cathode material $LiFeV_2O_7$ by solid-state NMR spectroscopy and density functional theory (DFT). With the escalating demand for high-performance lithium-ion batteries (LIBs), exploring cathode materials that can offer superior energy density, cycle stability, and safety is crucial. $LiFeV_2O_7$ presents a fascinating structure because it incorporates two transition metals capable of undergoing redox processes, a feature highly beneficial for lithium-ion batteries. The research employs advanced DFT calculations to predict the electronic structure and $^7$Li NMR shifts. These theoretical insights are essential for understanding how structural disorder influences NMR results and how the oxidation state of transition metal impacts the Fermi contact shift. Experimental techniques, including solid-state NMR spectroscopy and diffraction methods, are applied to study the lithium-ion exchange process and structural evolution during electrochemical cycling. Selective inversion NMR experiments were used to quantify the exchange rates relative to lithiation levels, and in combination with diffraction methods and DFT calculations, enabled the development of a structure model that elucidates the corresponding phase changes in the material. Moreover, the thesis discusses the impact of structural modifications on the lithium-ion dynamics within $Li_{1.71}FeV_2O_7$, revealing a direct link between specific crystallographic changes and enhanced lithium mobility. The integration of DFT calculations with experimental observations provides a comprehensive understanding of the material's behavior, paving the way for improvements in cathode design. Overall, this research contributes significantly to the field of LIBs, offering novel insights into the

complex interplay between structure, dynamics, and electrochemical performance in cathode materials.

# Acknowledgments

First and foremost, I extend my deepest gratitude to God for this achievement. His unwavering support and guidance provided me with the strength to persevere when I felt incapable of continuing. I am profoundly thankful for His blessings and constant presence throughout this journey. I would like to express my sincerest thanks to my supervisor, Dr. Gillian Goward. Thank you for saying yes to me and my family, giving us the opportunity to extend my knowledge in a different field, which finally I found my place, and to build a better life in Canada. Dr. Goward was patient, understanding, and supportive during the most challenging time in my life, for which I am forever grateful. The achievements of this thesis would not have been possible without her tremendous support and inspiration.

Thank you to my committee members: Dr. Giuseppe Melacini and Dr. Yurij Mozharivskyj for your continued guidance and advice throughout my studies. I am grateful to Prof. Dany Carlier for warmly welcoming me in Bordeaux and for providing support throughout the DFT calculations. I am also grateful to Jon Serrano Sevillano for teaching me about VASP and for always being available to answer my questions. My thanks go to all of my colleagues/friends in the current and past Goward lab: Mengyang Cui, Walker Zheng, Kevin Sanders, Aiman Quadiri, Olivia Velanosi, Zoya Sadighi, Annie Cheng, Cameron Gurwell, Emma Magee, Christopher Franko, Blossom Yan, Annica Freytag and David Bazak. Thank you also to the NMR staff, Bob, Hilary, and Megan, for their endless assistance. A big thanks to Jim Britten and Victoria Jarvis for always being there to chat with me, and answer my questions.

I'd like to express my gratitude to McMaster University. Not only did I expand my knowledge across various fields here, but it's also where my son was born. The care he received during those critical first days of his life was exceptional, and I'm truly thankful for that.

Thank you to my family, especially to my parents, my sisters, and my aunt Flavia, for always believing in me and supporting me. Their belief in my abilities has been a constant source of motivation, driving me to push forward and pursue my goals. A special thank you to my youngest sister, Maria Eduarda, for moving her life to Canada to support me during the last year of this thesis. Finally, thank you to my husband for supporting me and giving me the purest and truest love I could have, our son. Over the past 10 years, we have learned a bunch from each other. We have shared both good and challenging moments, sticking together through it all and overcoming every hurdle. Thank you for always being by my side.

This manuscript is dedicated to my son, Anthony.

# Table of Contents

# List of Figures

# List of Tables

# List of Symbols and Abbreviations

| | |
|---|---|
| 2D | Two-dimensional |
| BVEL | Bond Valence Energy Landscape |
| CB | Carbon Black |
| CLS | Canadian Light Source |
| CIFIT | Selective Inversion Fitting Program |
| CSA | Chemical Shift Anisotropy |
| DFT | Density Functional Theory |
| DMC | Dimethyl Carbonate |
| DOS | Density of States |
| EC | Ethylene Carbonate |
| EV | Electric Vehicle |
| eV | Electron Volt |
| EXSY | Exchange Spectroscopy |
| FC | Fermi Contact |
| FID | Free Induction Decay |
| FWHM | Full Width at Half Maximum |
| GGA | Generalized Gradient Approximation |
| $\hat{H}$ | Hamiltonian |
| HEW | Higer Energy Wiggler |
| LAPW | The Linearized Augmented Plane Wave |
| LCO | Lithium Cobalt Oxide, $LiCoO_2$ |
| LDA | Local Density Approximation |
| LEW | Lower Energy Wiggler |
| LFP | Lithium Iron Phosphate, $LiFePO_4$ |
| LIB | Lithium Ion Battery |

| | |
|---|---|
| $LW_{1/2}$ | The line width at half-high of the signal |
| MAS | Magic Angle Spinning |
| NASICON | Na Super Ionic Conductor |
| NCA | Nickel Cobalt Aluminum Oxide |
| NMC | Nickel Manganese Cobalt Oxide |
| NMR | Nuclear Magnetic Resonance |
| NSI | Non-selective Inversion |
| PAW | Projector Augmented Wave |
| PBE | Perdew-Burke-Ernzerhof |
| ppm | Parts per Million |
| PVDF | Polyvinylidene Fluoride |
| PXRD | Powder X-ray Diffraction |
| RF | Radiofrequency |
| SPXRD | Synchrotron Powder X-Ray Diffraction |
| SI | Selective Inversion |
| ssNMR | Solid-state NMR |
| $T_1$ | Longitudinal Nuclear Relaxation (Spin-lattice Relaxation) |
| $T_2$ | Transverse Nuclear Relaxation (Spin-spin Relaxation) |
| TM | Transition Metal |
| $t_{mix}$ | Mixing Time |
| USPP | Ultra Soft Pseudo Potential |
| VASP | Vienna Ab-Initio Simulation Package |
| VESTA | Visualization for Electronic and Structural Analysis |
| $\langle S_z \rangle$ | Time-averaged Electron Spin Density |
| $V_H(r)$ | Hartree Potential |
| $V_{xc}(r)$ | Exchange-Correlation Potential |
| $\delta_{FC,iso}$ | Isotropic Fermi Contact Shift |
| $\rho_i$ | Spin Density at Nucleus |

| | |
|---|---|
| $A_{iso}$ | The hyperfine coupling constant |
| $A_{FC}$ | Fermi Contact Hyperfine Interaction |
| $B_0$ | External Magnetic Field |
| $B_1$ | Magnetic Field Generated by the RF pulse |
| $C_Q$ | Quadrupole Coupling Constant |
| ecut | Cutoff Energy |
| eQ | Quadrupole Moment |
| $g_e$ | The free electron g value of 2.0023 |
| $\hbar$ | Reduced Planck's constant |
| $I$ | Nuclear spin number |
| $k_B$ | Boltzmann's Constant |
| $k_{ij}$ | Rate Constant for *i-j* Exchange |
| $M_i(\infty)$ | Magnetization of site *i* at equilibrium |
| $M_i(t)$ | Magnetization of site *i* at time t |
| $N_\beta$ | The number of spins in up |
| $N_\alpha$ | The number of spins in down state |
| $N_0$ | Avogadro's number |
| $R_i$ | Relaxation Time Constant for site *i* |
| $R_{wp}$ | Weighted profile of the Rietveld refinement |
| V | Volt |
| $\gamma$ | Gyromagnetic Ratio |
| $\Delta E$ | Energy Difference |
| $\eta_Q$ | Asymmetry Parameter |
| $\mu$ | Nuclear magnetic moment |
| $\mu_e$ | Electron Magnetic Moment |
| $\mu_B$ | The Bohr magneton |
| $\nu$ | Frequency |
| $\sigma_{CS}$ | Chemical Shielding |

| | |
|---|---|
| $\chi_M$ | Magnetic Susceptibility |
| $\omega_0$ | Larmor Frequency |
| $\psi(r)$ | State function |

# Declaration of Academic Achievement

The initial pristine samples of $LiFeV_2O_7$ were provided by Yasmine Benabed and Dr. Mickael Dollé (Université de Montréal). Prof. Dany Carlier was instrumental in the design of the Density Functional Theory calculations performed at the Université de Bordeaux under her and Dr. Jon Serrano Sevillano supervision. Dr. James Britten was a great help in collecting the single-crystal XRD data and interpreting it. Dr. Beatriz Moreno and Dr. Joel Reid were a great help in processing the data collected by *operando* and *ex-situ* synchrotron XRD. All other sample preparation, setups, data acquisition, and interpretation were performed by Taiana L.E. Pereira.

# Chapter 1: Introduction

## 1.1 Motivation

The urgent global need for sustainable and clean energy solutions drives interest in lithium batteries. As the world increasingly recognizes the impacts of climate change and the limitations of fossil fuels, the demand for renewable energy sources and efficient storage mechanisms has increased. In Europe, the European Commission aims to significantly decrease greenhouse gas (GHG) emissions by 2030 and achieve carbon neutrality by 2050. A major factor in realizing this goal is the shift from internal combustion engine vehicles to electric vehicles. [1] The annual demand for electric vehicles (EVs) has shown a consistent growth rate of 30% each year until 2020. Looking ahead, forecasts indicate that EV production is projected to exceed 40 million units by 2030.[2,3]

Lithium-ion batteries, known for their high energy density and long cycle life, stand at the forefront of this transition. [4] They enable the storage and mobilization of renewable energy, facilitating a shift towards more sustainable energy systems. Projections indicate a market size reaching 93.1 billion US dollars by 2025.[5] The escalating demand necessitates not only an expansion in production capacities but also a concerted effort towards enhancing battery safety and reducing manufacturing costs. This involves continuous research and development to improve battery chemistry and design, ensuring batteries are not only more affordable but also adhere to high safety standards. Additionally, as the industry strives toward sustainability, it is crucial to consider the environmental impact of battery production and disposal, emphasizing the need for recycling and circular economy practices. This context not only makes the study of lithium-ion batteries relevant but also infuses it with a sense of purpose directed toward environmental care and innovation for a sustainable future.

## 1.2 Lithium-ion Battery (LIB)

The pioneers of this technology were acknowledged with the 2019 Nobel Prize in Chemistry by John Goodenough, Stanley Whittingham, and Akira Yoshino.[6] LIBs were commercialized in the early 1990s by Sony and quickly became ubiquitous in portable consumer electronics, enabling the revolution in communication with cell phones, now indispensable to modern society.[7,8] More importantly, LIBs are emerging as the dominant technology in the pursuit of electrification and decarbonization of transportation including personal electric vehicles (EVs) as well as large-scale transportation on land and sea.[9,10] While we use the term lithium-ion battery as a moniker for the entire class of electrochemical devices, there is a wide range of chemistries that have been considered and characterized as possible constituents of cathode, anode, and electrolytes.

The basic structure of LIB consists of two electrodes, a positive electrode (cathode) and a negative electrode (anode), and an ionically conductive electrolyte. When the battery is discharged, the negative electrode (anode) is oxidized as electrons flow through the external circuit and lithium ions move to the positive electrode which is reduced. [11,12] The same process occurs when charging, but in the opposite direction. The amount of current that an electrochemical cell can deliver depends directly on how many lithium atoms can be moved from the cathode to the anode at the same time. Therefore, the stoichiometry and capacity of the electrode material are key in determining a battery's overall capacity. A schematic of a typical lithium-ion battery is depicted in **Figure 1.1**.

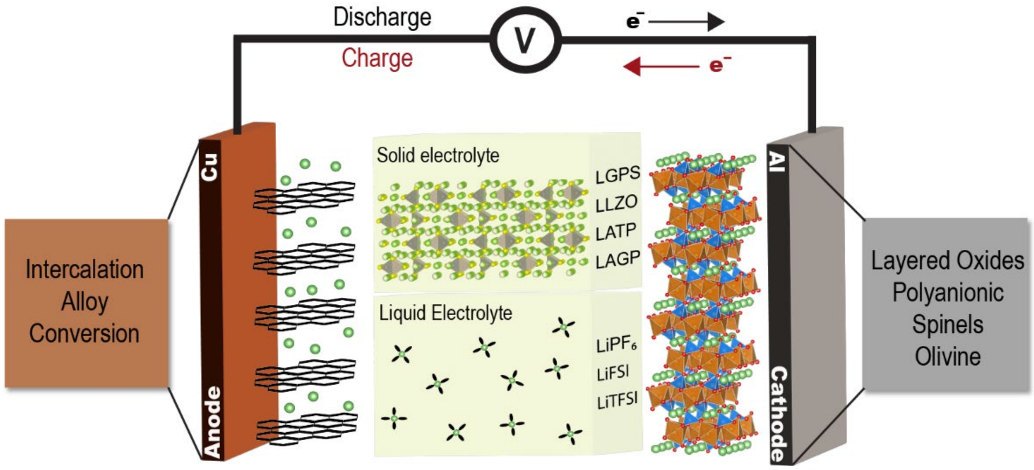

**Figure 1. 1** Schematic illustration of the configuration of a rechargeable lithium-ion battery (LIB) and common components. LIBs are composed of a cathode as the positive electrode, and anode as the negative electrode, and an electrolyte that conducts only ions.

Anode materials are differentiated based on their operational mechanisms. Intercalation anodes are characterized by their ability to incorporate lithium ions within their structural layers, a process that occurs without significant structural alteration. Examples of such materials include graphite and lithium titanium oxide ($Li_4Ti_5O_{12}$).[13] Alloying anodes represent another class, comprising elements like tin and silicon that form an alloy with lithium ions, a reaction known for causing notable changes in volume and structural integrity. The final group, conversion anodes, consists of transition metal oxides and sulfides that undergo a chemical reaction with lithium, resulting in energy storage through conversion mechanisms.[14]

Electrolytes serve as the conduit for lithium-ion movement between the anode and cathode. They are available in two primary forms: solid and liquid state. The primary function of an electrolyte is to act as a medium that allows for the efficient transport of lithium ions across the cell, ensuring the continuous flow of charge during the battery's operation. Solid-state electrolytes, such as LGPS ($Li_{10}GeP_2S_{12}$), LLZO ($Li_7La_3Zr_2O_{12}$), LATP ($Li_{1+x}Al_xTi_{2-x}(PO_4)_3$), and LAGP ($Li_{1+x}Al_xGe_{2-x}(PO_4)_3$), permit the passage of lithium ions without the need for a liquid. They can enhance safety by removing flammable liquids. In addition to these, polymer electrolytes stand as another class within the solid-state category. Comprising a polymer matrix such as polyethylene oxide (PEO), these electrolytes merge the mechanical robustness of a solid with the processability of a plastic, allowing for flexibility and shape versatility in battery design. They hold lithium salts that dissolve within the polymer to facilitate the mobility of lithium ions. On the other hand, liquid electrolytes are generally composed of lithium salts such as $LiPF_6$, $Li(SO_2F)_2N$ (LiFSI), and $LiC_2F_6NO_4S_2$ (LiTFSI), which are dissolved in organic solvents. This combination is well-suited for efficient ionic conduction, but it does present some safety concerns, particularly regarding the flammability and leakage of the solvents.[15–19]

Cathode materials consist of a redox-active structural network within which Li ions can be intercalated/deintercalated. As such the framework of the cathode has a large effect on the reversibility and structural stability of the material. Numerous research efforts have been conducted in order to find a good framework for the positive electrode. Several materials have been developed to supply the lithium-ion battery, each with its distinct chemical profiles, capacities, and applications, balancing benefits, and drawbacks.

## 1.3 Cathode Materials

The cathode material significantly influences the battery's energy density, which determines how much power the battery can store per unit of weight or volume. [20] By finding materials that can hold more lithium ions, researchers can create batteries that last longer on a single charge, making them more suitable for applications requiring high energy output, such as electric vehicles and portable electronic devices. In addition, research into cathode materials seeks to enhance the stability of batteries during charge and discharge cycles, which helps them last longer. This not only makes batteries more reliable but also reduces waste and the environmental impact associated with battery disposal.

There are several common types of frameworks for cathode materials, however, the most common structures are layered oxide and polyanionic compounds (**Table 1.1**). $LiCoO_2$ (LCO) was the first layered oxide material to be commercialized, due to its high capacity, good cycle life, and reliability. [21] This structure wherein Li atoms are housed between layers of metal-oxide octahedra has been modified to create the most successful modern commercial materials, namely $LiNi_xMn_yCo_zO_2$ (NMC) and $LiNi_{0.8}Co_{0.15}Al_{0.05}O_2$ (NCA).[22] However, they suffer from safety and resource limitations due to the high cost of Ni and Co, which encouraged the search for new materials.

Polyanionic structures offer a stable framework during the delithiation/lithiation process due to a network of $XO_4$ (x=P, S) anions that are electro-chemically stable and therefore maintain the integrity of the structure.[23] $LiFePO_4$ (LFP) is the most famous example of a polyanionic framework cathode, which exhibits high capacity and electrochemical reversibility.[24] Iron is a particularly desirable cathode active material due to its low cost and natural abundance, as well as low toxicity. Iron-based polyanionic compounds were initially presented as an alternative to the layered oxides, such as $LiFePO_4F$[25], $LiFeP_2O_7$[26], and $Li_3Fe_2(PO_4)_3$[27]. They tend to exhibit $Fe^{2+}/Fe^{3+}$ redox voltages in a safe range to work in the current electrolyte systems. [28] Polyanionic frameworks opened the field to the use of more cost-effective and low-toxicity metals in cathode material. Beyond iron, vanadium compounds also have received attention due to the ability to move among four oxidation states, thus being able to exhibit a wide range of capacities as a cathode material.[29] Vanadium oxides, such as $V_2O_5$[30,31], $LiV_3O_8$[29,32] and $LiVO_3$[33], have shown interesting cathode properties and favorable stability. Therefore, the combination of these two elements, iron, and vanadium, has been explored based on the ternary phase diagram $Li_2O$, $Fe_2O_3$, and $V_2O_5$ (**Figure 1.2**).

**Table 1.1** Comparison of the theoretical and practical capacity of selected cathode materials for lithium-ion batteries.

| Cathode | Theoretical/Practical Capacity ($mAh.g^{-1}$) | Voltage *vs* $Li^+/Li^0$ |
|---|---|---|
| NMC811[34] | 275/170-200 | 4.20 V |
| NCA[35] | 279 / 180-200 | 4.20 V |
| LCO[36] | 274 / 130-148 | 4.00 V |
| LFP[37] | 170/ 150-165 | 3.45 V |
| $LiMn_2O_4$[37] | 148/ 120-140 | 4.10 V |
| $V_2O_5$[38] | 294/ 104-143 | 3.35 V |
| $LiVPO_4O$[39] | 159 / 135 | 4.20 V |

Several cathode materials have been developed, and a fundamental aspect of these explorations involves the detailed analysis of how a material's structure, composition, properties, and performance are interrelated. The solid structural information is often obtained by characterization techniques that are based on the phenomena of diffraction and resonance. In particular, the non-destructive character of the process and the fact that it does not require any prior preparation of the samples, show advantages for the use of these two techniques for structural characterization. While the long-range order structural characterization of electrode materials typically relies on diffraction methods, solid-state NMR spectroscopy is a powerful tool for characterizing local structures in these materials, even in highly disordered systems.

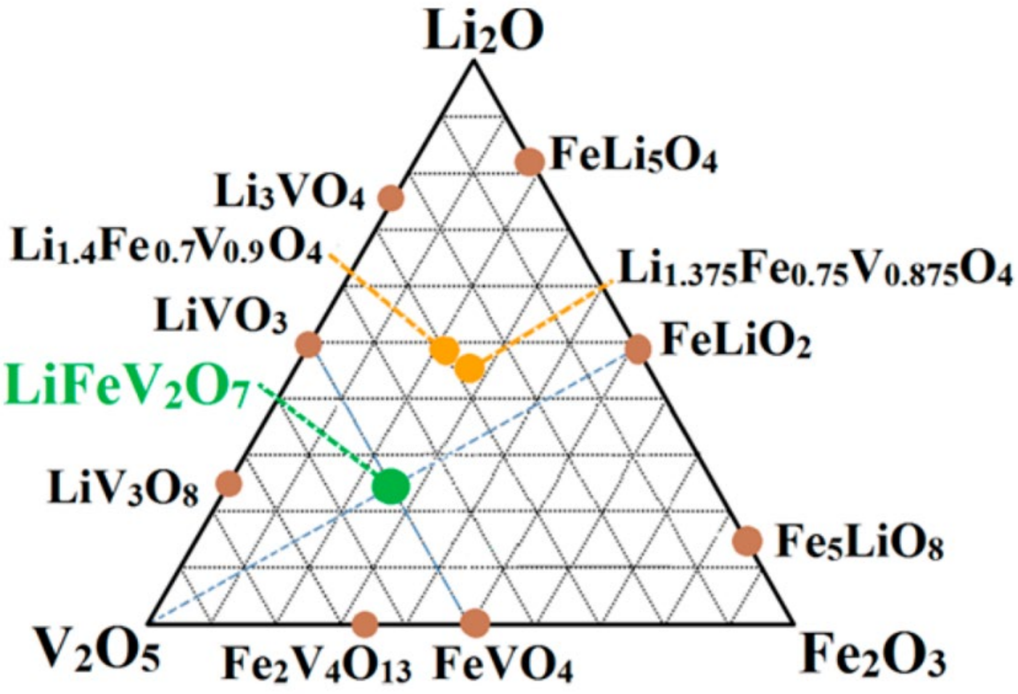

**Figure 1. 2** $Li_2O$ – $Fe_2O_3$ – $V_2O_5$ Ternary phase diagram (atom %). Reprinted with permission from [40].

## 1.4 The Contribution of ssNMR Spectroscopy on Lithium-Ion Battery Development

Solid-state nuclear magnetic resonance (ssNMR) has been employed to characterize LIB components since the 1990's, first to elucidate structural differences among electrode materials both in their pristine state and following electrochemical cycling using *ex situ* (Latin: out of position; measurements made on a disassembled cell) methods, and later to probe ion dynamics using NMR's well-known capability to quantitatively measure mobility and exchange.[41] More recently, *in situ* (Latin: in position; measurements made on an electrochemical cell without opening it) and *operando* (Latin: operating; measurements made during operation of the cell) magnetic resonance methods have been implemented to provide a real-time characterization of the changing lithium distribution and speciation within several bespoke cell geometries.[42]

In general, *ex situ* studies offer the highest resolution, as material samples can be isolated and resolution enhancement techniques like MAS and 2D sideband separation experiments can be leveraged to provide isotropic resolution of sites within a material. However, *ex situ* methods do not offer real-time information and can thus fail to observe non-equilibrium or metastable states[43]**,** although it may be the only option to study materials where large anisotropic contributions to the NMR spectra prevent the use of static NMR methods. *Ex situ* studies are commonly employed in the study of battery cathode materials, where paramagnetic contributions of redox-active metal centers dominate the NMR spectra and thus fast magic angle spinning methods are typically the only way to recover sufficient resolution to make meaningful chemical assignments.

Initial $^6$Li & $^7$Li MAS NMR studies of the spinel cathode material $LiMn_2O_4$ as a function of synthesis temperature by Lee & Grey demonstrated the difference in lithium-ion populations of the tetrahedral and octahedral sites of the metal oxide framework.[44,45] These population differences were not readily evident by powder X-ray diffraction but they were evident at ssNMR. This work demonstrated how NMR is very sensitive to local symmetry. $LiFePO_4$ is a well know cathode that has been extensively investigated by $^7$Li and $^{31}$P ssNMR in order to providing insight into the lithium environment for new structure composition, lithium diffusion mechanisms, and phase transitions between lithiated and delithiated states.[46–49] Shimoda et al used $^{31}$P ssNMR to observe the reversibility of two-phase reaction behavior between $LiFePO_4$ and $FePO_4$.[48] Kim et al. presented the efficacy of $^7$Li MAS NMR in detecting signals from the diamagnetic lithium salts that accumulate on the surface of LFP electrode material. This capability is crucial for assessing capacity loss during battery operation, providing vital insights into the degradation mechanisms. [50]

In the study of cathode materials dynamics, two NMR techniques have been employed to investigate and quantify lithium ion hopping, namely two-dimensional exchange spectroscopy (EXSY) and selective inversion (SI) spectroscopy. The 2D EXSY experiment has been used in studies of lithium transport in various materials, such as $Li_3V_2(PO_4)_3$[51], $Li_3Fe_2(PO_4)_3$[52], and $LiMn_2O_4$[53]. These studies have measured lithium transport rates at different temperatures to derive activation energies, which are subsequently linked to structural characteristics of the materials, such as interatomic Li-Li distances.[9-11] Conversely, the one-dimensional (1D) SI technique offers several advantages. It allows for the individual probing of each exchange pair, unlike the 2D EXSY method, which may not adequately account for the presence of multiple exchange pairs. Additionally, 1D experiments are generally less time-consuming and produce higher signal-to-noise at the same time relative to analogous 2D experiments.[54] Given the advantages described above, several materials have been studied using the SI pulse sequence, such as $Li_2(Mn_{1-y}Fe_y)P_2O_7$[55], $Li_5V(PO_4)_2F_2$[56] and $Li_3Fe_2(PO_3)_3$[57].

While the thesis does not include *In situ* and *operando* techniques, it is important to highlight their significance. *In situ* and *operando* studies offer the most information as they are collected on whole batteries. *In situ* NMR methods have now been used for more than 20 years to gain invaluable and unprecedented insight into the evolution of electrolyte and anode materials for Li-ion batteries. Many *operando* NMR studies have focused on detecting structural changes in anode materials upon metalation by $^7Li$ spectroscopy. The first published study by Gerald *et al.*[58] showed that graphite lithiates in discrete phases (previously reported by Dahn using diffraction methods[59]), with clearly resolved signals at ~12 ppm and ~50 ppm corresponding to two detectable phases; these are now known today as "dilute" and "concentrated" stages of lithiated graphite, respectively. Follow-up studies by Letellier *et al.*[42,60] and many others[61–65] have reproduced these results and shown by $^7Li$ NMR that 5 clearly-identifiable $Li_xC_6$ phases exist and are reversible: stages 4, 3, 2L, 2 and 1, where the number describes the layers of graphene sheets separating a layer of intercalated lithium.

Overall, NMR offers a wide range of tools with which to probe the materials evolution and dynamic processes occurring within LIBs and related energy storage systems. The versatility of NMR is unrivaled by other spectroscopic techniques, and including MRI, the treasure trove of tools continues to deliver new methodologies. The application of magnetic resonance techniques provides powerful insights that continue to advance the field of energy storage, which is of critical importance to our collective efforts to mitigate climate change. Chapter 2 contains a comprehensive explanation of how NMR spectroscopy works, and its uses in studying cathode materials.

## 1.5 Material Studied in This Thesis

The exploration of new materials for energy storage technologies, particularly those involved in lithium-ion batteries, has significantly propelled advancements in this field. Compounds containing iron and vanadium within their structures have attracted considerable interest. These materials stand out for their affordability and promising capacity for lithium storage, marking them as key subjects in ongoing research efforts.

This thesis focuses on $LiFeV_2O_7$ which was first reported by Benabed Y et al.[40] The iron vanadate structure crystallizes in a non-centrosymmetric monoclinic Cc space group with three unique Li sites in a 1:1:1 ratio in the 4, 5 and 6 coordination. It is a complex three-dimensional structure that was considered by the author as a layered compound alternating (Li, Fe) and V sheets, perpendicular to the [101] direction (**Figure 1.3**). With a theoretical capacity of 97 $mAhg^{-1}$ which corresponds to the full conversion of $Fe^{3+}$ to $Fe^{2+}$, surprisingly the experimental capacity achieved around 100 mAh/g on the first cycle from

3.50 V to 2.35 V. Impressively, 85% of this capacity was retained after 60 cycles.[40] The hypothesis suggested by the authors is that both $V^{5+}$ and $Fe^{3+}$ ions may be electrochemically reduced during the lithiation process.[40,66] A similar behavior was observed for the other phases such as $LiFeVO_4$, $Fe_4(V_2O_7)_3$ and $Fe_2V_4O_{13}$.[67,68] Based on $^{57}Fe$ Mössbauer spectroscopy and X-ray diffraction results, Denis S. et al. demonstrating that in $LiFeVO_4$, both $Fe^{3+}$ and $V^{5+}$ undergo reduction during lithiation. Notably, the structure of $LiFeV_2O_7$, was initially thought to be a polyanionic framework due to the presence of $VO_4$, however, vanadium also engages in the redox process. The promising behavior of this new structure type as a positive electrode encourages us to investigate the Li dynamics of the phase. Additionally, it was the unexpected findings that made along the way in our research that inspired this thesis.

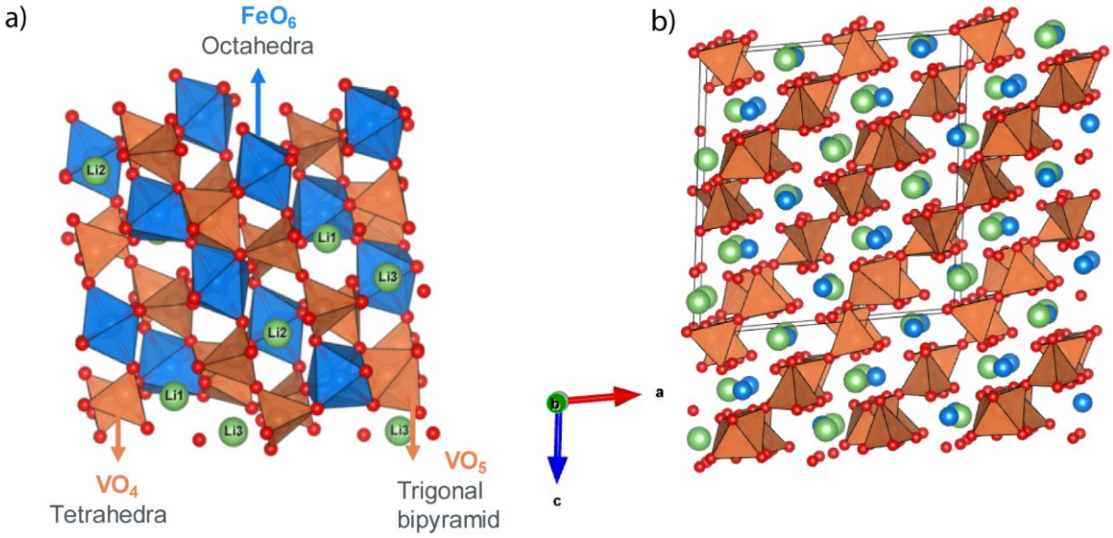

**Figure 1.3** Structure of monoclinic $LiFeV_2O_7$. a) Unit cell and b) Representation of the layered compound alternating (Li, Fe) and V sheets, perpendicular to the [101] direction.

## 1.6 Thesis Outline

This thesis describes a deep structural investigation of $LiFeV_2O_7$ as a potential cathode for LIBs. $^7Li$ ssNMR, X-ray diffraction, and density functional theory (DFT) were used to investigate defects, lithium-ion dynamics, and structural changes in the novel cathode. This thesis highlights the use of ssNMR to elucidate the local structures and dynamics in cathode materials.

The present chapter (**Chapter 1**) summarizes the background and motivation behind the work in this thesis. This chapter also briefly introduced the material of interest and also the application of ssNMR in LIBs. **Chapter 2** discusses solid-state magnetic resonance spectroscopy with a focus on the theoretical basis from which all NMR experiments are derived. **Chapter 3** introduces the characterization methods used in this thesis besides the NMR. The general principles of X-ray diffraction and the concept of density functional theory (DFT) as a complement to NMR spectroscopy. **Chapter 4** presents a detailed examination of defects within the pristine $LiFeV_2O_7$ structure through the integration of ssNMR spectroscopy and DFT calculations. **Chapter 5** focuses on the study of lithium dynamics of $Li_{1.x}FeV_2O_7$ during the discharge cycle using ex situ ssNMR. **Chapter 6** reports an extended exploration using *operando* synchrotron powder x-ray diffraction and DFT calculations to model the lithiated phase $Li_{1.71}FeV_2O_7$. The results are linked back to experimental NMR data presented in Chapter 5. Finally, **Chapter 7** provides a comprehensive summary of the study, highlighting the key findings and offering recommendations for future research in the field.

## 1.7 References

(1) Degen, F.; Winter, M.; Bendig, D.; Tübke, J. Energy Consumption of Current and Future Production of Lithium-Ion and Post Lithium-Ion Battery Cells. *Nat. Energy* **2023**, *8* (11), 1284–1295. https://doi.org/10.1038/s41560-023-01355-z.

(2) International Energy Agency. *Global EV Outlook 2023*; 2023. https://www.iea.org/reports/global-ev-outlook-2023.

(3) McKinsey MineSpan. McKinsey and Global Battery Alliance. *McKinsey Co.* **2023**.

(4) Xu, B.; Qian, D.; Wang, Z.; Meng, Y. S. Recent Progress in Cathode Materials Research for Advanced Lithium Ion Batteries. **2012**, *73*, 51–65.

(5) Mohammadi, F.; Saif, M. A Comprehensive Overview of Electric Vehicle. *e-Prime - Adv. Electr. Eng. Electron. Energy* **2023**, *3* (November 2022), 100127.

(6) Kamat, P. V. Lithium-Ion Batteries and Beyond: Celebrating the 2019 Nobel Prize in Chemistry - A Virtual Issue. *ACS Energy Lett.* **2019**, 2757–2759. https://doi.org/10.1021/acsenergylett.9b02280.

(7) Goodenough, J. B.; Kim, Y. Challenges for Rechargeable Li Batteries. *Chem. Mater.* **2010**, *22* (3), 587–603. https://doi.org/10.1021/CM901452Z.

(8) Tarascon, J.-M. M.; Armand, M. Issues and Challenges Facing Rechargeable Lithium Batteries. *Nature* **2001**, *414* (6861), 359–367. https://doi.org/10.1038/35104644.

(9) Mohammadi, F.; Saif, M. A Comprehensive Overview of Electric Vehicle Batteries Market. *e-Prime - Adv. Electr. Eng. Electron. Energy* **2023**, *3* (November 2022), 100127.

(10) Mayyas, A.; Moawad, K.; Chadly, A.; Alhseinat, E. Can Circular Economy and Cathode Chemistry Evolution Stabilize the Supply Chain of Li-Ion Batteries? *Extr.*

*Ind. Soc.* **2023**, *14* (April). https://doi.org/10.1016/j.exis.2023.101253.

(11) Dunn, B.; Kamath, H.; Tarascon, J. M. Electrical Energy Storage for the Grid: A Battery of Choices. *Science (80-. ).* **2011**, *334* (6058), 928–935. https://doi.org/10.1126/science.1212741.

(12) Liu, C.; Neale, Z. G.; Cao, G. Understanding Electrochemical Potentials of Cathode Materials in Rechargeable Batteries. *Mater. Today* **2016**, *19* (2), 109–123. https://doi.org/10.1016/j.mattod.2015.10.009.

(13) Lu, Y.; Yu, L.; Lou, X. W. (David). Nanostructured Conversion-Type Anode Materials for Advanced Lithium-Ion Batteries. *Chem* **2018**, *4* (5), 972–996. https://doi.org/10.1016/j.chempr.2018.01.003.

(14) Hossain, M. H.; Chowdhury, M. A.; Hossain, N.; Islam, M. A.; Mobarak, M. H. Advances of Lithium-Ion Batteries Anode Materials—A Review. *Chem. Eng. J. Adv.* **2023**, *16* (October), 100569. https://doi.org/10.1016/j.ceja.2023.100569.

(15) Xing, J.; Bliznakov, S.; Bonville, L.; Oljaca, M.; Maric, R. *A Review of Nonaqueous Electrolytes, Binders, and Separators for Lithium-Ion Batteries*; Springer Nature Singapore, 2022; Vol. 5. https://doi.org/10.1007/s41918-022-00131-z.

(16) Xu, K. Electrolytes and Interphases in Li-Ion Batteries and Beyond. *Chem. Rev.* **2014**, *114* (23), 11503–11618. https://doi.org/10.1021/cr500003w.

(17) Zhou, D.; Shanmukaraj, D.; Tkacheva, A.; Armand, M.; Wang, G. Polymer Electrolytes for Lithium-Based Batteries: Advances and Prospects. *Chem* **2019**, *5* (9), 2326–2352. https://doi.org/10.1016/j.chempr.2019.05.009.

(18) Safanama, D.; Sharma, N.; Rao, R. P.; Brand, H. E. A.; Adams, S. Structural Evolution of NASICON-Type Li1+xAlxGe2-x(PO4)3 Using in Situ Synchrotron X-Ray Powder Diffraction. *J. Mater. Chem. A* **2016**, *4* (20), 7718–7726. https://doi.org/10.1039/c6ta00402d.

(19) Yu, S.; Schmidt, R. D.; Garcia-Mendez, R.; Herbert, E.; Dudney, N. J.; Wolfenstine, J. B.; Sakamoto, J.; Siegel, D. J. Elastic Properties of the Solid Electrolyte Li7La3Zr2O12 (LLZO). *Chem. Mater.* **2016**, *28* (1), 197–206. https://doi.org/10.1021/acs.chemmater.5b03854.

(20) Goodenough, J. B.; Park, K. S. The Li-Ion Rechargeable Battery: A Perspective. *J. Am. Chem. Soc.* **2013**, *135* (4), 1167–1176. https://doi.org/10.1021/ja3091438.

(21) Pell, A. J.; Pintacuda, G.; Grey, C. P. Paramagnetic NMR in Solution and the Solid State. *Prog. Nucl. Magn. Reson. Spectrosc.* **2019**, *111*, 1–271. https://doi.org/10.1016/j.pnmrs.2018.05.001.

(22) Julien, C. M.; Mauger, A. NCA, NCM811, and the Route to Ni-Richer Lithium-Ion Batteries. *Energies* **2020**, *13*, 6363. https://doi.org/10.3390/en13236363.

(23) Masquelier, C.; Croguennec, L. Polyanionic (Phosphates, Silicates, Sulfates) Frameworks as Electrode Materials for Rechargeable Li (or Na) Batteries. *Chem. Rev.* **2013**, *113* (8), 6552–6591. https://doi.org/10.1021/cr3001862.

(24) Padhi, A.k.; Nanjundaswamy, K.S.; Goodenough, J. B. Phospho-olivines as Positive-Electrode Materials for Rechargeable Lithium Batteries. *Soc. Electrochem.* **1997**, *144* (4), 1188–1194.

(25) Chen, D.; Shao, G. Q.; Li, B.; Zhao, G. G.; Li, J.; Liu, J. H.; Gao, Z. S.; Zhang, H. F. Synthesis, Crystal Structure and Electrochemical Properties of LiFePO4F Cathode Material for Li-Ion Batteries. *Electrochim. Acta* **2014**, *147*, 663–668. https://doi.org/10.1016/j.electacta.2014.09.131.

(26) Salah, A. A.; Gendron, F.; Mauger, A.; Julien, C. M. Synthesis and Characterization of Lithium Iron Diphosphate as Positive Electrode for Lithium Batteries. *Proc. - Electrochem. Soc.* **2008**, *PV 2005-14* (February 2017), 113–120.

(27) Wurm, C.; Morcrette, M.; Rousse, G.; Masquelier, C. Lithium Insertion / Extraction into / from LiMX 2 O 7 Compositions ( M ) Fe , V ; X ) P , As )

Prepared via a Solution Method. **2002**, No. 10, 2701–2710.

(28) Padhi, A. K.; Nanjundaswamy, K. S.; Masquelier, C.; Okada, S.; Goodenough, J. B. Effect of Structure on the Fe3 + / Fe2 + Redox Couple in Iron Phosphates. *J. Electrochem. Soc.* **1997**, *144* (5), 1609–1613. https://doi.org/10.1149/1.1837649.

(29) Kannan, A. M.; Manthiram, A. Low Temperature Synthesis and Electrochemical Behavior of LiV3O8 Cathode. *J. Power Sources* **2006**, *159* (2), 1405–1408. https://doi.org/10.1016/j.jpowsour.2005.12.026.

(30) Fu, R.; Ma, Z.; Zheng, J. P.; Au, G.; Plichta, E. J.; Ye, C. High-Resolution 7Li Solid-State NMR Study of Li XV2O5 Cathode Electrodes for Li-Rechargeable Batteries. *J. Phys. Chem. B* **2003**, *107* (36), 9730–9735. https://doi.org/10.1021/jp0305077.

(31) Dickens, P. G.; French, S. J.; Hight, A. T.; Pye, M. F. Phase Relationships in the Ambient Temperature LixV2O5 System (0.1<x<1.0). *Mater. Res. Bull.* **1979**, *14* (10), 1295–1299. https://doi.org/10.1016/0025-5408(79)90006-0.

(32) He, P.; Yan, M.; Liao, X.; Luo, Y.; Mai, L.; Nan, C. W. Reversible V3+/V5+ Double Redox in Lithium Vanadium Oxide Cathode for Zinc Storage. *Energy Storage Mater.* **2020**, *29* (February), 113–120. https://doi.org/10.1016/j.ensm.2020.04.005.

(33) X.M. Jian, J.P. Tu*, Y.Q. Qiao, Y. Lu, X.L. Wang, C. D. G. S. Synthesis and Electrochemical Performance OfLiVO3 Cathode Materials for Lithium Ion Batteries X.M. *Ceram. Int.* **2013**, *236*, 33–38. https://doi.org/10.1016/j.jpowsour.2013.02.004.

(34) Märker, K.; Reeves, P. J.; Xu, C.; Griffith, K. J.; Grey, C. P. Evolution of Structure and Lithium Dynamics in LiNi0.8Mn0.1Co0.1O2 (NMC811) Cathodes during Electrochemical Cycling. *Chem. Mater.* **2019**, *31* (7), 2545–2554. https://doi.org/10.1021/acs.chemmater.9b00140.

(35) Singh, P.; Dudeja, V.; Panwar, A. K. Electrochemical Performance of NCA Based Cathodes for Variable Thickness of Electrode through Modelling and Simulation. *Mater. Today Proc.* **2022**, *62*, 3742–3748. https://doi.org/10.1016/j.matpr.2022.04.446.

(36) Märker, K.; Xu, C.; Grey, C. P. Operando NMR of NMC811/Graphite Lithium-Ion Batteries: Structure, Dynamics, and Lithium Metal Deposition. *J. Am. Chem. Soc.* **2020**, *142* (41), 17447–17456. https://doi.org/10.1021/jacs.0c06727.

(37) Marincaş, A. H.; Ilea, P. Enhancing Lithium Manganese Oxide Electrochemical Behavior by Doping and Surface Modifications. *Coatings* **2021**, *11* (4). https://doi.org/10.3390/coatings11040456.

(38) Praneetha, S.; Lee, Y. S.; Aravindan, V. V2O5 vs. LiFePO4: Who Is Performing Better in the 3.4 V Class Category? A Performance Evaluation in “Rocking-Chair” Configuration with Graphite Anode. *J. Ind. Eng. Chem.* **2022**, *112*, 389–397. https://doi.org/10.1016/j.jiec.2022.05.036.

(39) Bianchini, M.; Ateba-Mba, J. M.; Dagault, P.; Bogdan, E.; Carlier, D.; Suard, E.; Masquelier, C.; Croguennec, L. Multiple Phases in the ε-VPO4O-LiVPO4O-Li 2VPO4O System: A Combined Solid State Electrochemistry and Diffraction Structural Study. *J. Mater. Chem. A* **2014**, *2* (26), 10182–10192. https://doi.org/10.1039/c4ta01518e.

(40) Benabed, Y.; Castro, L.; Penin, N.; Darriet, J.; Dollé, M. Synthesis, Structure, and Electrochemical Properties of LiFeV2O7. *Chem. Mater.* **2017**, *29* (21), 9292–9299. https://doi.org/10.1021/acs.chemmater.7b03271.

(41) Grey, C. P.; Dupré, N. NMR Studies of Cathode Materials for Lithium-Ion Rechargeable Batteries. *Chem. Rev.* **2004**, *104* (10), 4493–4512. https://doi.org/10.1021/cr020734p.

(42) Pecher, O.; Carretero-Gonzalez, J.; Griffith, K. J.; Grey, C. P. Materials’ Methods: NMR in Battery Research. *Chem. Mater.* **2017**, *29* (1), 213–242.

https://doi.org/10.1021/acs.chemmater.6b03183.

(43) Key, B.; Bhattacharyya, R.; Morcrette, M.; Seznéc, V.; Tarascon, J. M.; Grey, C. P. Real-Time NMR Investigations of Structural Changes in Silicon Electrodes for Lithium-Ion Batteries. *J. Am. Chem. Soc.* **2009**, *131* (26), 9239–9249. https://doi.org/10.1021/ja8086278.

(44) Lee, Y. J.; Wang, F.; Grey, C. P. 6Li and 7Li MAS NMR Studies of Lithium Manganate Cathode Materials. *J. Am. Chem. Soc.* **1998**, *120* (48), 12601–12613. https://doi.org/10.1021/ja9817794.

(45) Grey, C. P.; Lee, Y. J. Lithium MAS NMR Studies of Cathode Materials for Lithium-Ion Batteries. In *Solid State Sciences*; Elsevier Masson SAS, 2003; Vol. 5, pp 883–894. https://doi.org/10.1016/S1293-2558(03)00113-4.

(46) Cabana, J.; Shirakawa, J.; Chen, G.; Richardson, T. J.; Grey, C. P. MAS NMR Study of the Metastable Solid Solutions Found in the LiFePO 4/FePO4 System. *Chem. Mater.* **2010**, *22* (3), 1249–1262. https://doi.org/10.1021/cm902714v.

(47) Clément, R. J.; Pell, A. J.; Middlemiss, D. S.; Strobridge, F. C.; Miller, J. K.; Whittingham, M. S.; Emsley, L.; Grey, C. P.; Pintacuda, G. Spin-Transfer Pathways in Paramagnetic Lithium Transition-Metal Phosphates from Combined Broadband Isotropic Solid-State MAS NMR Spectroscopy and DFT Calculations. *J. Am. Chem. Soc.* **2012**, *134* (41), 17178–17185. https://doi.org/10.1021/ja306876u.

(48) Shimoda, K.; Sugaya, H.; Murakami, M.; Arai, H.; Uchimoto, Y.; Ogumi, Z. Characterization of Bulk and Surface Chemical States on Electrochemically Cycled LiFePO 4 : A Solid State NMR Study . *J. Electrochem. Soc.* **2014**, *161* (6), A1012–A1018. https://doi.org/10.1149/2.060406jes.

(49) Tucker, M. C.; Doeff, M. M.; Richardson, T. J.; Fiñones, R.; Reimer, J. A.; Cairns, E. J. 7Li and 31P Magic Angle Spinning Nuclear Magnetic Resonance of LiFePO4-Type Materials. *Electrochem. Solid-State Lett.* **2002**, *5* (5), 5–9.

https://doi.org/10.1149/1.1464505.

(50) Kim, D.; Lim, J.; Mathew, V.; Koo, B.; Paik, Y.; Ahn, D.; Paek, S. M.; Kim, J. Low-Cost LiFePO 4 Using Fe Metal Precursor. *J. Mater. Chem.* **2012**, *22* (6), 2624–2631. https://doi.org/10.1039/c2jm14499a.

(51) Cahill, L. S.; Chapman, R. P.; Britten, J. F.; Goward, G. R. 7Li NMR and Two-Dimensional Exchange Study of Lithium Dynamics in Monoclinic Li3v2(PO4)3. *J. Phys. Chem. B* **2006**, *110* (14), 7171–7177. https://doi.org/10.1021/jp057015+.

(52) Davis, L. J. M.; Heinmaa, I.; Goward, G. R. Study of Lithium Dynamics in Monoclinic Li 3 Fe 2 ( PO 4 ) 3 Using 6 Li VT and 2D Exchange MAS NMR Spectroscopy †. **2010**, *2* (10), 2215–2221. https://doi.org/10.1021/cm901402u.

(53) Verhoeven, V. W. J. J.; Schepper, I. M. De; Nachtegaal, G.; Kentgens, A. P. M. M.; Kelder, E. M.; Schoonman, J.; Mulder, F. M.; De Schepper, I. M.; Nachtegaal, G.; Kentgens, A. P. M. M.; Kelder, E. M.; Schoonman, J.; Mulder, F. M. Lithium Dynamics in LiMn2O4 Probed Directly by Two-Dimensional 7Li NMR. *Phys. Rev. Lett.* **2001**, *86* (19), 4314–4317. https://doi.org/10.1103/PhysRevLett.86.4314.

(54) Smiley, D. L.; Goward, G. R. Solid-State NMR Studies of Chemical Exchange in Ion Conductors for Alternative Energy Applications. *Concepts Magn. Reson. Part A.* **2016**, *45A* (6), e21419. https://doi.org/10.1002/cmr.a.21419.

(55) Smiley, D. L.; Tessaro, M. Z.; He, X.; Goward, G. R. Correlation of Electrochemical Performance with Lithium Environments and Cation Dynamics in Li2(Mn1-YFey)P2O7 Using 6Li Solid-State NMR. *J. Phys. Chem. C* **2015**, *119* (29), 16468–16474. https://doi.org/10.1021/acs.jpcc.5b04173.

(56) Davis, L. J. M.; Goward, G. R. Differentiating Lithium Ion Hopping Rates in Vanadium Phosphate versus Vanadium Fluorophosphate Structures Using 1D 6Li Selective Inversion NMR. *J. Phys. Chem. C* **2013**, *117* (16), 7981–7992. https://doi.org/10.1021/jp310790g.

(57) Smiley, D. L.; Davis, L. J. M. M.; Goward, G. R. An Improved Understanding of Li+ Hopping Pathways and Rates in Li3Fe2(PO4)3 Using Selective Inversion 6Li NMR Spectroscopy. *J. Phys. Chem. C* **2013**, *117* (46), 24181–24188. https://doi.org/10.1021/jp407510h.

(58) Gerald, R. E.; Sanchez, J.; Johnson, C. S.; Klingler, R. J.; Rathke, J. W. In Situ Nuclear Magnetic Resonance Investigations of Lithium Ions in Carbon Electrode Materials Using a Novel Detector. *J. Phys. Condens. Matter* **2001**, *13* (36), 8269–8285. https://doi.org/10.1088/0953-8984/13/36/304.

(59) Dahn, J. R. Phase Diagram of $Li_xC_6$. *Phys. Rev. B* **1991**, *44* (17), 9170–9177.

(60) Letellier, M.; Chevallier, F.; Morcrette, M. In Situ 7Li Nuclear Magnetic Resonance Observation of the Electrochemical Intercalation of Lithium in Graphite; 1st Cycle. *Carbon N. Y.* **2007**, *45* (5), 1025–1034. https://doi.org/10.1016/j.carbon.2006.12.018.

(61) Sanders, K. J.; Aguilera, A. R.; Keffer, J. R.; Balcom, B. J.; Halalay, I. C.; Goward, G. R. Transient Lithium Metal Plating on Graphite: Operando 7Li Nuclear Magnetic Resonance Investigation of a Battery Cell Using a Novel RF Probe. *Carbon N. Y.* **2022**, *189*, 377–385. https://doi.org/10.1016/j.carbon.2021.12.082.

(62) Krachkovskiy, S. A.; Reza, M.; Aguilera, A. R.; Halalay, I. C.; Balcom, B. J.; Goward, G. R. Real-Time Quantitative Detection of Lithium Plating by In Situ NMR Using a Parallel-Plate Resonator. *J. Electrochem. Soc.* **2020**, *167* (13), 130514. https://doi.org/10.1149/1945-7111/abb7ea.

(63) Freytag, A. I.; Pauric, A. D.; Krachkovskiy, S. A.; Goward, G. R. In Situ Magic-Angle Spinning 7 Li NMR Analysis of a Full Electrochemical Lithium-Ion Battery Using a Jelly Roll Cell Design. *J. Am. Chem. Soc.* **2019**, *141*, 13758–13761. https://doi.org/10.1021/jacs.9b06885.

(64) Arai, J.; Okada, Y.; Sugiyama, T.; Izuka, M.; Gotoh, K.; Takeda, K. In Situ Solid

State $^{7}$Li NMR Observations of Lithium Metal Deposition during Overcharge in Lithium Ion Batteries. *J. Electrochem. Soc.* **2015**, *162* (6), A952–A958. https://doi.org/10.1149/2.0411506jes.

(65) Lopez, J. L. L.; Grandinetti, P. J.; Co, A. C. Enhancing the Real-Time Detection of Phase Changes in Lithium–Graphite Intercalated Compounds through Derivative Operando (DOp) NMR Cyclic Voltammetry. *J. Mater. Chem. A* **2018**, *6* (1), 231–243. https://doi.org/10.1039/C7TA07521A.

(66) Yasmine Benabed. Approche Théorique et Expérimentale Combinée Dans l’exploration de LiFeV2O7 et Son Application Comme Matériau d’électrode Positive Pour Batterie Aux Ions Lithium. **2017**, 112–123. https://doi.org/10.1038/.

(67) Denis, S.; Dedryvère, R.; Baudrin, E.; Laruelle, S.; Touboul, M.; Olivier-Fourcade, J.; Jumas, J. C.; Tarascon, J. M. 57Fe Mössbauer Study of the Electrochemical Reaction of Lithium with Triclinic Iron Vanadate. *Chem. Mater.* **2000**, *12* (12), 3733–3739. https://doi.org/10.1021/cm001084d.

(68) Patoux, S.; Richardson, T. J. Lithium Insertion Chemistry of Some Iron Vanadates. *Electrochem. commun.* **2007**, *9* (3), 485–491. https://doi.org/10.1016/j.elecom.2006.10.006.

# Chapter 2: Solid-State NMR Spectroscopy

This chapter offers a brief description of solid-state nuclear magnetic resonance (ssNMR) spectroscopy, which provides profound insights into the molecular structure and dynamics of solids, enabling a deeper understanding of material properties at the atomic level. NMR uses the radiation range corresponding to radio waves (MHz), and the interaction of this electromagnetic radiation with the sample causes nuclear spin transitions. It is a technique widely used in different fields of chemistry and materials science for structural characterization and studies of dynamics due to its high environmental sensitivity. Solid-state NMR is the primary method utilized in this thesis to characterize the structural and ion mobility properties of the cathode material ($LiFeV_2O_7$). Before going deeper into the technique, it is essential to define some fundamental concepts. What is nuclear spin? What is NMR detecting?

## 2.1 Interaction with External Magnetic Field

Nuclear spin refers to the intrinsic angular momentum possessed by a nucleus, a fundamental property of atomic particles. This angular momentum is quantized and represented by the nuclear spin quantum number, named *I*. The value of *I* can be an integer, half-integer, or zero and is determined by the composition of the nucleus, specifically the number and arrangement of protons and neutrons (known as nucleons).[1] The nuclear spin generates a magnetic moment, which is crucial in NMR as it allows nuclei to interact with external magnetic fields, leading to the splitting of energy levels and enabling the detailed study of molecular structures and dynamics through NMR spectroscopy. Since NMR depends on the existence of nuclear spin, nuclei with $I = 0$ are not active in this technique.[2] There is a method to know if the nuclei are NMR-active:

- Nuclei with an odd mass number have half-integral spin, such as $^{1}H$ ( $I = ½$), $^{7}Li$ ($I$=3/2), $^{23}Na$ ($I$ =3/2), $^{23}Al$ ($I$ =5/2)
- Nuclei with an even mass number but odd number of protons and neutrons have integral spin, such as $^{2}H$ ($I = 1$) and $^{14}N$ ($I$ =1).

Nuclei with spin $I = ½$ have a spherical charge distribution which makes the NMR analyses less complicated to interpret. Other spin nuclei with $I > ½$ have nonspherical charge distribution, resulting in the creation of an electric quadrupole moment. This quadrupole moment significantly influences the relaxation times, directly impacting the linewidth of the NMR signal and the interaction with adjacent nuclei.[3] The effect of quadrupole moment will be discussed further in this chapter. As mentioned, nuclei possess a magnetic moment which is proportional to its spin angular moment by equation 2.1,

$$\widehat{\mu} = \gamma \hbar \hat{I} \qquad \text{Equation 2.1}$$

where μ is the nuclear magnetic moment, $\hbar$ is the reduced Planck's constant, $I$ is the nuclear spin, and γ is the gyromagnetic ratio of the nucleus in units of Rad. $S^{-1}.T^{-1}$ which is a parameter related to the spin angular moment of a nucleus to the strength of the magnetic dipole moment.

### 2.1.1 Zeeman Splitting

In the absence of a magnetic field, the energy of an isolated nucleus is independent of the quantum number ($m_I$), which means all states are degenerate. Once the magnetic field is applied, there are $2I+1$ non-degenerate energy levels corresponding to the $2I+1$ values of $m_I$, separated according to equation 2.2. [1] The separation between energy levels is known as Zeeman splitting. The magnitude of the Zeeman splitting is proportional to the strength of the applied magnetic field and the nuclear gyromagnetic ratio, as shown in equation 2.2,

$$E_{\mathrm{I,m}} = -\hbar\gamma B_0 m = -\mathrm{m}\mu\mathrm{B}_0 \qquad \text{Equation 2.2}$$

where $E_{I,m}$ is the energy of spin-state $m_I$, $m$ is the magnetic quantum number and $B_0$ is the strength of the external magnetic field.

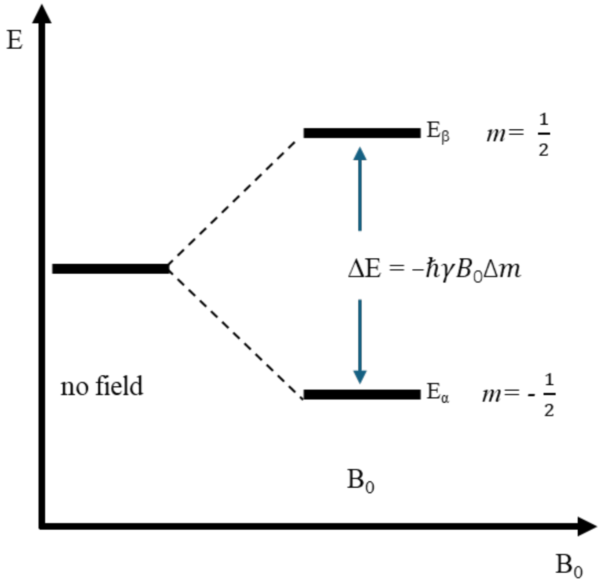

**Figure 2. 1** A schematic representation of Zeeman interaction for a nuclear spin with I = ½

The most common example of energy levels for spin-states after Zeeman splitting is given in **Figure 2.1**. For nuclei with a spin quantum number $I = ½$, there are two energy levels created resulting in only one transition from $m$= ½ and $m$= - ½ spin-states. When a group of spins is placed in a magnetic field, each spin aligns in one of the two possible orientations, parallel to and in the same direction as $B_0$ which is the lower energy level (down state, α), or antiparallel to the external field, which is the higher energy level (up state, β). The spin population distribution between these two states is described based on the Boltzmann distribution and only the difference in population between the two states has physical significance.[2] The difference in energy between these levels corresponds to the resonance frequency observed in NMR spectroscopy. When an NMR active nucleus absorbs radiofrequency energy that matches this difference, a transition between these split energy levels occurs, which is detected as an NMR signal. NMR is a very sensitive spectroscopy, and it is capable to detect these very small population differences. The relative difference in population between those two states is governed by equation 2.3. The only way to increase polarization (sensitivity) in NMR is by either increasing the energy difference $\Delta E$ (i.e., increasing the magnetic field) or decreasing the temperature $T$.

$$\frac{N_\beta}{N_\alpha} = e^{-\frac{\Delta E}{kT}} \qquad \text{Equation 2.3}$$

where $\Delta E$ is the difference between energy levels, $k$ is the Boltzmann constant, $T$ is the temperature in Kelvin, $N_\beta$ is the number of spins in up state and $N_\alpha$ is the number of spins in down state.

### 2.1.2 Precession and Larmor Frequency

When a nucleus with a magnetic moment is placed in a magnetic field, it does not align directly with the field but instead precesses around it. This precession is similar to the wobbling motion of a spinning top in a gravitational field. This precession occurs at a rate defined by the Larmor frequency ($\omega_0$). It is directly proportional to the strength of the magnetic field and is given by the Larmor equation 2.4:

$$\omega_0 = -\gamma B_0 \qquad \text{Equation 2.4}$$

where $\omega_0$ is the Larmor frequency, $\gamma$ is the gyromagnetic ratio (a constant specific to each type of nucleus), and $B_0$ is the strength of the magnetic field. This frequency is related to the transition energy explained above and the relationship is described in Equation 2.5. [4]

$$\Delta E = h\omega = -\hbar\gamma B_0 \Delta m \qquad \text{Equation 2.5}$$

The Larmor frequency is crucial in NMR as it determines the frequency of the radiofrequency (RF) pulse needed to excite the nuclear spins and cause transitions between their energy levels. In real experiments, the precession of nuclear spins depends on the chemical environment of the observed nucleus. The chemical shift is a relative measure, indicating how the resonance frequency of a nucleus deviates from a reference frequency due to the electronic environment around it, generated by its bonding arrangement.

### 2.1.3 Nuclear Spin Relaxation

The NMR spectrum is obtained when the frequency of the applied RF radiation matches the Larmor frequency of the nuclei being observed. When an RF pulse is applied to the coil it generates an oscillating magnetic field ($B_1$), oriented along the x-axis. This field is perpendicular to the z-axis of the external static magnetic field ($B_0$). The introduction of the $B_1$ field causes the bulk magnetization vector to shift from the z-axis to the y-axis. Subsequently, this vector begins to precess around the static $B_0$ field within the x-y plane. This precession induces a current in the same coil, which can be amplified and recorded. The resulting signal, characterized by its decay following the RF pulse, is referred to as Free Induction Decay (FID). The FID represents the observable signal in the spectra and the lifetime of the decay is governed by the phenomena known as spin-lattice ($T_1$) and spin-spin relaxation ($T_2$). An illustration of the described steps of NMR experiment is shown in **Figure 2.2**. To analyze this time-domain signal, a Fourier Transform is applied, converting it into the frequency domain.

Relaxation in NMR spectroscopy primarily arises from the interactions between nuclear magnetic moments and the localized magnetic fields within the sample. These fields have the capability to reorient the nuclear magnetic moments into new positions, similarly to how an RF pulse affects the overall magnetization direction. The impact of these local fields is not consistent across all magnetic moments due to their limited reach at the microscopic level and their dependency on the spatial orientation of the nuclei. The creation of these localized fields, crucial for initiating relaxation processes, is attributed to four main factors: (i) dipolar interactions, which are magnetic interactions between adjacent nuclear spins; (ii) chemical shift anisotropy; (iii) the influence of paramagnetic species, which introduce additional localized magnetic fields; and (iv) quadrupolar interactions, relevant specifically to nuclei with a spin quantum number greater than ½ that exhibit significant quadrupole moments. These elements together account for the variation in relaxation rates observed across different nuclear magnetic moments within the same sample.

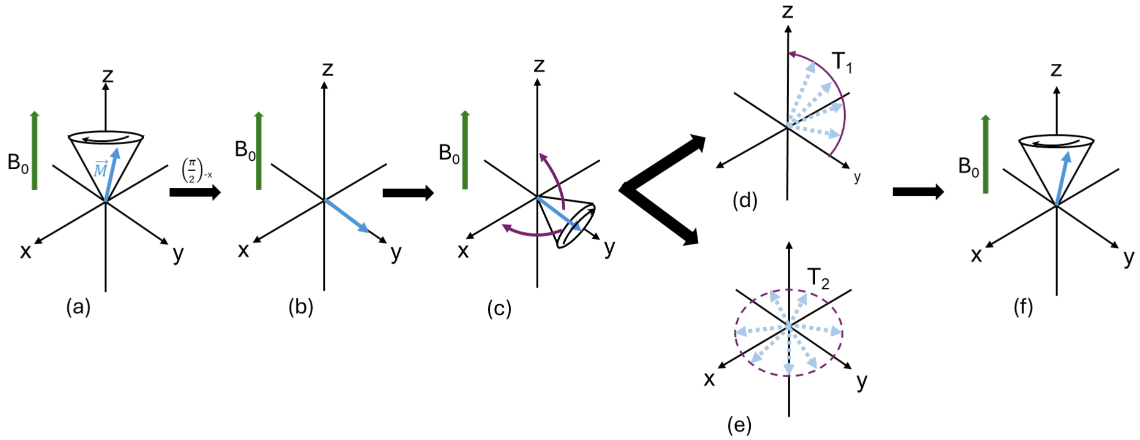

**Figure 2. 2.** Illustration of the NMR experiment. When a $B_0$ field is applied along the z-axis, all the spins precess around the z-axis and (a) an equilibrium magnetization arises, oriented along the same axis. The equilibrium magnetization is shifted towards the transverse xy-plane by the effects of an RF-pulse ($B_1$) applied at resonance frequency (b). When the RF-excitation is released, the magnetization relaxes (d/e) towards its equilibrium value with a precession frequency that depends on the magnetic properties of the environment around the observed nuclei.

Longitudinal or spin-lattice relaxation, also known as $T_1$ relaxation, refers to the process of the net magnetization vector returning to its equilibrium state along the direction of the external magnetic field, following an RF pulse (**Figure 2.2d**). This relaxation mechanism involves the transfer of energy from the nuclear spins to their surrounding lattice or environment. The value of $T_1$ relaxation reflects how quickly the net magnetization recovers usually along the z axis after an RF pulse. In practical terms, $T_1$ affects how long must wait between successive scans in NMR experiment, known as delay time ($D_1$), which is typically set to five times the value of $T_1$.

$T_2$ relaxation describes the process by which the transverse component of the magnetization vector (in the xy-plane, perpendicular to the external magnetic field) dephases following an RF pulse (**Figure 2.2e**). Unlike $T_1$ relaxation, $T_2$ involves the loss of phase coherence among nuclear spins, predominantly due to spin-spin interaction. The $T_2$ relaxation time is the time constant that describes how quickly this coherence is lost in the xy-plane. In practice, $T_2^*$ is the relaxation time that includes both the intrinsic spin-spin interactions captured by $T_2$ and additional dephasing due to inhomogeneities in the external magnetic field. $T_2^*$ is typically shorter than $T_2$ and provides a measure of the overall coherence loss in the NMR signal. $T_2^*$ determines the line width of NMR resonance lines (Equation 2.6); shorter $T_2^*$ times lead to broader lines in the NMR spectrum.

$$\mathrm{LW}_{\frac{1}{2}} = \frac{1}{\pi \mathrm{T}_2^*} \qquad \text{Equation 2.6}$$

where $LW_{1/2}$ is the line width at half-high of the signal.

Through the Bloch equations (Equations 2.7, 2.8, and 2.9), we can quantitatively understand how NMR signals arise from the precession of nuclear magnetic moments and how these signals decay over time due to relaxation mechanisms. These classical equations are mathematical models of how the magnetization vector, represented by $\vec{M}$, evolves in time due to interactions with an external magnetic field and relaxation processes. The Bloch equations consist of three differential equations that describe the time dependence of the magnetization components $M_x$, $M_y$ and $M_z$ in the presence of an external magnetic field:[5]

$$\frac{dM_x}{dt} = -\frac{M_x}{T_2}$$ Equation 2.7

$$\frac{dM_y}{dt} = -\frac{M_y}{T_2}$$ Equation 2.8

$$\frac{dM_z}{dt} = -\frac{M_z - M_0}{T_1}$$ Equation 2.9

The terms $\frac{M_x}{T_2}$ and $\frac{M_y}{T_2}$ depict the exponential decay of the transverse components of magnetization due to dephasing, while the term $\frac{M_z - M_0}{T_1}$ represents the exponential recovery of the longitudinal magnetization towards its equilibrium state. [5]

## 2.2 Internal Interactions

In NMR spectroscopy, internal interactions within the sample significantly influence the characteristics of the final spectra. Unlike in solution NMR, where rapid molecular tumbling averages many spatially-dependent/anistropic interactions to zero, in solid-state NMR, these interactions remain fully active and significantly shape the experimental spectra. Understanding these internal interactions is fundamental for interpreting the experimental data and extracting detailed information about molecular structure, dynamics, and interactions.

These interactions arise from the magnetic and electronic environments surrounding the nuclei and affect the energy splitting of the nuclear spin transitions, thus determining the chemical shifts, line shapes, and relaxation rates observed in NMR spectra.

In the case of solid samples, internal interactions within the sample have pronounced effects on the spectrum, making the technique particularly sensitive to the local structural and dynamic properties of solids. The best way to describe these interactions is using the Hamiltonian operator. The Hamiltonian ($\widehat{H}$) in solid-state NMR incorporates several terms that correspond to these internal interactions, each corresponding to different energy interactions from the magnetic and electronic environments surrounding the nuclei. [6]

$$\widehat{H}_{int} = \widehat{H}_{cs} + \widehat{H}_D + \widehat{H}_J + \widehat{H}_Q + \widehat{H}_k + \widehat{H}_P \qquad \text{Equation 2.10}$$

### 2.2.1 Chemical Shift Anisotropy (CSA)

The chemical shift observed in NMR spectra is a result of chemical shielding experienced by nuclear spins in a molecule. The distribution of electron clouds around a nucleus generates a local magnetic field that shields the nucleus from the external magnetic field. The Hamiltonian $\widehat{H}_{cs}$ is used to describe the perturbation from the electrons. For solid samples or in molecules with restricted mobility, the orientation of the molecule with respect to the external magnetic field remains fixed or limited in motion, leading to an anisotropic shielding effect. [6] The orientation-dependence of the shielding is described as the shielding tensor, σ, which is expressed mathematically by a 3 x 3 matrix:

$$\sigma = \begin{bmatrix} \sigma_{xx} & \sigma_{xy} & \sigma_{xz} \\ \sigma_{yx} & \sigma_{yy} & \sigma_{yz} \\ \sigma_{zx} & \sigma_{zy} & \sigma_{zz} \end{bmatrix}$$

The shielding tensor is defined with respect to the laboratory coordinate system. However, it is useful to reframe this tensor according to the symmetry elements surrounding the nucleus, known as the Principal Axis Frame (PAF). This reference frame is selected by convention to diagonalize the chemical shielding tensor, making the tensor's diagonal elements the principal values (noted as $\sigma_{xx}^{PAF}, \sigma_{yy}^{PAF}\ and\ \sigma_{zz}^{PAF}$) of the chemical shielding tensor.[2,6] For the remainder of this thesis, the Haeberlen[7] convention is used. These principal values of shielding tensor are frequently expressed as the isotropic value $\sigma_{iso}$, the anisotropy Δ, and the asymmetry η, all of which are defined as follows:

$$\sigma_{iso} = \frac{1}{3}(\sigma_{xx}^{PAF} + \sigma_{yy}^{PAF} + \sigma_{zz}^{PAF}) \qquad \text{Equation 2.11}$$

$$\Delta = \sigma_{zz}^{PAF} - \sigma_{iso} \qquad \text{Equation 2.12}$$

$$\eta = \frac{(\sigma_{xx}^{PAF} - \sigma_{yy}^{PAF})}{\sigma_{zz}^{PAF}} \qquad \text{Equation 2.13}$$

To understand how this affects the NMR spectra, the chemical shift frequency can be written in terms of the isotropic and anisotropic interaction in the following expression:

$$\omega_{cs}(\theta, \phi) = -\omega_0\sigma_{iso} - \frac{1}{2}\omega_0 \Delta\{3\cos^2\theta - 1 + \eta\sin^2\theta\cos 2\phi\} \qquad \text{Equation 2.14}$$

where $-\omega_0\sigma_{iso}$ is the isotropic chemical shift frequency, relative to the bare nucleus, and angles $\theta$ and $\phi$ describe the orientation of the molecule with respect to the external field.

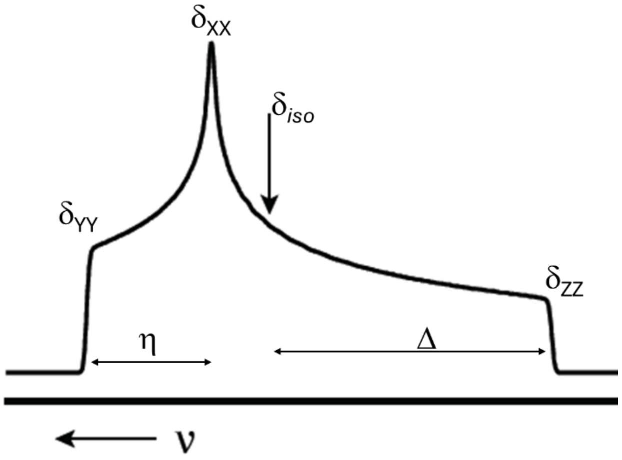

**Figure: 2.3** Simulated static powder pattern with CSA contributions. Each of contributions from the z, x, and y primary axis are labeled.

Every distinct molecular orientation results in a unique alignment of the principal axis frame relative to the external magnetic field, leading to variations in chemical shifts as defined by Equation 2.14. The superposition of many sharp peaks with different frequencies due to the various orientations of crystallites in a powder sample, often results in a very broad spectrum (**Figure 2.3**).[2,6]

### 2.2.2 The Dipolar Interaction

The dipolar (dipole-dipole or dipolar coupling) interaction arises due to the magnetic field produced by one nuclear spin affecting another nearby spin when they are close enough to each other. This happened across space, meaning that it does not rely on chemical bonds to occur. The Hamiltonian for dipolar coupling between two spins *I* and *S* can be expressed as: [6]

$$\hat{H} = -\frac{\mu_0 \gamma_I \gamma_S}{4\pi {r_{IS}}^3}[A + B + C + D + E + F] \qquad \text{Equation 2.15}$$

Where:

$$A = \hat{I}_z \hat{S}_z (3\cos^2\theta - 1)$$

$$B = -\frac{1}{4}\left[\hat{I}_+ \hat{S}_- + \hat{I}_- \hat{S}_+\right](3\cos^2\theta - 1)$$

$$C = -\frac{3}{2}\left[\hat{I}_z \hat{S}_+ + \hat{I}_+ \hat{S}_z\right]\sin\theta\cos\theta\, e^{-i\phi}$$

$$D = -\frac{3}{2}\left[\hat{I}_z \hat{S}_- + \hat{I}_- \hat{S}_z\right]\sin\theta\cos\theta\, e^{-i\phi}$$

$$E = -\frac{3}{4}\left[\hat{I}_+ \hat{S}_+\right]\sin^2\theta\, e^{-i\phi}$$

$$F = -\frac{3}{4}\left[\hat{I}_- \hat{S}_-\right]\sin^2\theta\, e^{-i\phi}$$

$\mu_0$ is the permeability of free space, $\gamma_I$ and $\gamma_S$ are the gyromagnetic ratios of the coupled $I$ and $S$ spins, $r_{IS}$ is the internuclear distance between the I and S spins, with $\theta$ being the angle of the I-S internuclear vector with respect to the external magnetic field. While the dipolar Hamiltonian may initially appear complex, a deeper analysis reveals that the terms, C, $D$, $E$, and $F$ contribute minimally to the energy of the spin system and, therefore, can be disregarded for simplification.[6] The dipolar coupling is separated into homonuclear and heteronuclear interactions, which the Hamiltonian is represented by:

$$\hat{H}_d^{hetero} = -d(3\cos^2\theta - 1)\widehat{I_z}\widehat{S_z} \qquad \text{Equation 2.16}$$

$$\hat{H}_d^{homo} = -d\frac{1}{2}(3\cos^2\theta - 1)[3\widehat{I_z}\widehat{S_z} - \hat{I}\cdot\hat{S}] \qquad \text{Equation 2.17}$$

with

$$d = \hbar\left(\frac{\mu_0}{4\pi}\right)\frac{1}{r^3}\gamma_I\gamma_S \qquad \text{Equation 2.18}$$

$d$ is the dipolar coupling constant. The strength of the dipolar coupling is directly proportional to the product of the gyromagnetic ratios of the two interacting spins. This means that nuclei with higher gyromagnetic ratios will experience stronger dipolar interactions. Stronger dipolar interactions can lead to significant broadening in the spectra.[8] This is particularly relevant in solid-state NMR, where the lack of rapid molecular tumbling allows dipolar couplings to persist, unlike in solution NMR where they are averaged out. Moreover, dipolar coupling serves as a valuable tool for investigating molecular structures, as it is depending only on physical constants and the inverse cube of the distance between nuclei. Knowing the value of this coupling, it is possible to determine nuclear distances and, consequently, molecule structure. [2,9]

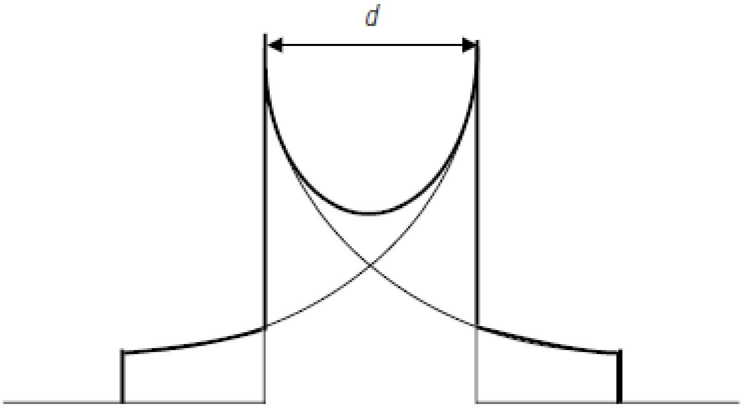

**Figure 2.4** Simulated dipolar coupling powder pattern. The powder lineshape for the spin in a heteronuclear two-spin system. Where d is the dipolar constant. Reprinted with permission from [6].

### 2.2.3 Quadrupole Interaction

Nuclei with a spin quantum number greater than $\frac{1}{2}$ are classified as quadrupolar. The distribution of electric charge around a nucleus is not spherically symmetric, leading to an electric quadrupole moment (eQ) which is an intrinsic property of the nucleus. When this quadrupolar nucleus is in the presence of the electric field gradient (EFG), which is created by the distribution of electrons and nearby charges, the interaction between the quadrupole moment and the EFG occurs, significantly affecting the NMR line broadening. If the EFG is spherically symmetric, the line shape is narrow. However, for a non-spherical EFG, second order quadrupolar broadening is observed. The quadrupolar interaction is most frequently described by two parameters, the quadrupolar coupling constant, $C_Q$, and the asymmetry parameter, $\eta_Q$ as defined by Equations 2.19 and 2.20: [6]

$$C_Q = \frac{e^2 V_{zz} Q}{\hbar} \qquad \text{Equation 2.19}$$

$$\eta_Q = \left(\frac{V_{xx} - V_{yy}}{V_{zz}}\right) \qquad \text{Equation 2.20}$$

Where $V_{xx}$, $V_{yy}$ and $V_{zz}$ are the principal axis frame of the EFG ($V_{zz}$ is the largest one), where $e$ is the proton charge and $Q$ is the nuclear quadrupole moment.

The quadrupole coupling constant ($C_Q$) is the magnitude of quadrupole interaction, expressed in Hz which can vary from many hundreds of kilohertz to tens or even hundreds of megahertz.[10] It describes the spherical symmetry of environment surrounding the nucleus; with an increase in spherical symmetry, the value of $C_Q$ decreases.[11] The asymmetry parameter describes the axial symmetry of the EFG tensor. This parameter can be obtained by fitting the experimental data. However, when there is more than one signal that overlaps it can be difficult to extract that information.

For small quadrupolar couplings, the first-order quadrupolar effect dominates, affecting only the satellite transitions (**Figure 2.5a**). However, for large quadrupolar couplings, second-order effects become significant. The second-order quadrupolar interaction introduces additional complexity and it can be expressed in terms of zeroth-, second- and fourth-order Legendre polynomials: $P_n(\cos\theta)$, where $P_0(\cos\theta) = 1$, and

$$P_2(\cos\theta) = \frac{1}{2}(3\cos^2\theta - 1) \qquad \text{Equation 2.21}$$

$$P_4(\cos\theta) = \frac{1}{8}(35\cos^4\theta - 30\cos^2\theta + 3) \qquad \text{Equation 2.22}$$

Magic Angle Spinning (MAS) is an important technique because it helps to average out the first-order quadrupolar interaction (**Figure 2.5b**). However, when the quadrupolar interactions are very strong, their effects may still need to be considered to second order, which MAS alone cannot completely average out. To improve the spectra resolution, a strong magnetic field narrows the resonance lines and mitigates the effects of quadrupolar interactions, particularly the second-order quadrupolar broadening. The broadening is inversely proportional to the Larmor frequency meaning that higher fields reduce the relative impact of the quadrupolar interaction compared to the Zeeman interaction. In addition, specialized pulse sequences can help to minimize the effect of second-order interaction, which is beyond the scope of this discussion. [10,13,14] In this thesis, we are interested in $^7$Li which has low value of eQ ( Na eQ = 10.4, $^7$Li eQ = -4.01, $^6$Li eQ = -0.08

in units of $10^{-2}$ barns, or $10^{-30}$ $m^2$). The $^6$Li, $^7$Li, and $^{23}$Na nuclei all have spin quantum number of $I=\frac{3}{2}$, making them quadrupolar. However, due to the low eQ value of $^7$Li, it does not significantly affect the final spectra.

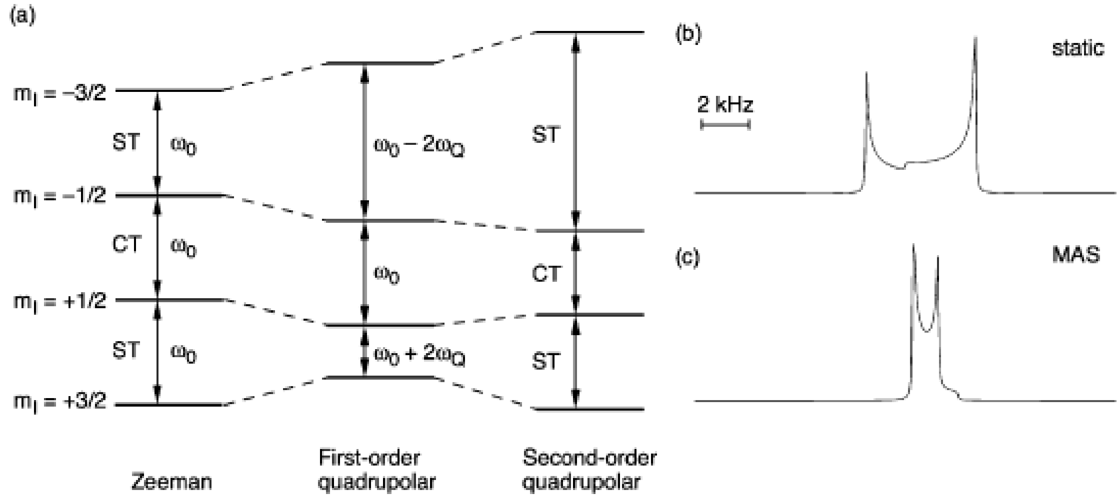

**Figure 2.5** Schematic energy level diagram for a spin I = 3/2 nucleus showing the effect of the Zeeman, first-order and second-order quadrupolar interactions upon the four energy levels. The central transition (CT) is unaffected by the first-order quadrupolar interaction whereas the satellite transitions (ST) show a significant perturbation. All transitions are affected by the second-order quadrupolar interaction. (b, c) spin I=3/2 central transition (b) static and (c) MAS lineshapes simulated with $C_Q$ = 2 MHz, $\omega_0/2\pi$ = 100 MHz and $\eta_Q$ = 0. Reprinted with permission from [12].

## 2.3 Magic Angle Spinning

The chapter begins with the explanation of external and internal interactions that affect solid samples in NMR spectroscopy. Progressing through the text, we could see the orientation-dependence characteristic of solid samples and its significant impact on spectral line broadening. Magic Angle Spinning (MAS) is a sophisticated and well-known technique employed in ssNMR to enhance the resolution of spectra by decreasing the effects of anisotropic internal interactions. Samples are packed into rotors that come in different sizes. The maximum possible MAS rate increases as the rotor diameter decreases. The tiniest rotors on the market, which have a diameter of 0.4 mm, are capable of spinning at speeds 160 kHz.

By rapidly spinning the sample around an axis set at the "magic angle" of approximately 54.74° degrees relative to the external magnetic field, the term $3\cos^2\theta - 1$, present in equations 2.15, 2.16, 2.17, and 2.21 above, becomes zero.[2,15] As such MAS effectively reduces the influence of anisotropic interactions, such as dipolar couplings and chemical shift anisotropy, that typically dominate in solid samples. The idea is to mimic what happens in solution samples, where rapid molecular tumbling naturally averages out these interactions. If the MAS rate is not sufficiently large compared with shift anisotropies, the residual anisotropic interactions are modulated at the spinning frequency, resulting in spinning sidebands. **Figure 2.6** presents a comparison of the material of interest to this thesis, $LiFeV_2O_7$, between static and MAS ssNMR spectra, illustrating the distinct differences in resolution and detail achievable under each condition.

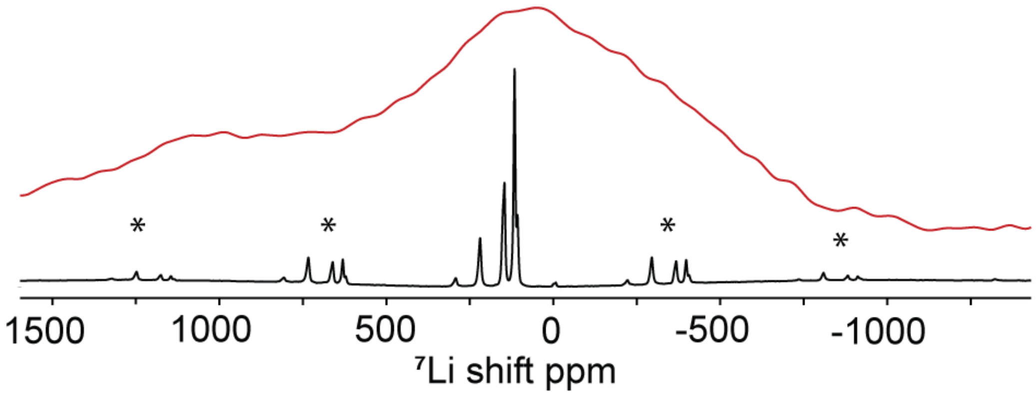

**Figure 2. 6.** (red) Static $^7$Li NMR spectrum and (black) $^7$Li MAS NMR spectrum under 60 kHz of $LiFeV_2O_7$, both spectra were acquired at 7 T. The asterisks are spinning sidebands.

There's no need for concern regarding the potential confusion between isotropic shifts and spinning sidebands in MAS NMR spectra. The isotropic signal corresponds to the central peak, unlike the spinning sidebands that appear at intervals equal to the MAS rotation frequency, the central peak remains at a constant position, independent of the spinning speed as long as the temperature is constant. By conducting experiments at various MAS rates, the isotropic signal can be identified as the peak that does not shift its position with changes in rotation rate.[16]

## 2.4 Hyperfine interaction

In the context of lithium-ion batteries, most cathode materials are paramagnetic in the discharged and/or charged state.[17] The spin of unpaired electrons also has magnetic moments which engage in hyperfine interaction with the surrounding nuclei spin. Due to the fast electron spin relaxation, the nucleus therefore senses an average magnetic moment of the electron, which can be described as:[17]

$$< S_z >= -\frac{B_0}{\mu_0 g_e N_0 \mu_B}\chi_M$$ Equation 2.23

where $\mu_0$ is the permeability of free space, $g_e$ being the free electron g value of 2.0023, $N_0$ is Avogadro's number, $\mu_B$ the Bohr magneton and $\chi_M$ is the molar magnetic susceptibility.

The hyperfine interaction is divided into two main categories: the Fermi contact interaction, which happens through the bond, and the pseudocontact interaction, which is through the space. [18]

### 2.4.1 Hyperfine shift

The chemical shift observed in an NMR spectrum of a paramagnetic sample results from both the diamagnetic component and a hyperfine shift.[19] In most cases, the hyperfine interaction is much larger than any other interaction and can dominate the spectra of these materials. The Fermi contact interaction is a direct measure of the transfer of unpaired electron spin density to the observed nucleus. This interaction contributes to the isotropic shift by:[20]

$$\delta^{contact} = \frac{\mu_0 g_e^2 \mu_B^2 (S+1)}{9kT}\rho_{\alpha\beta}$$ Equation 2.24

where $\rho_{\alpha\beta}$ represents the Fermi contact spin density, k Boltzmann's constant, and S is the electron quantum spin number.

Equation 2.24 can be rewritten in terms of magnetic susceptibility. Where $\chi$ is defined by:

$$\chi_M = \frac{\mu_0 g_e^2 \mu_B^2 (S+1)}{3kT} \qquad \text{Equation 2.25}$$

By combining Equations 2.24 and 2.25 a final solution for the isotropic shift from Fermi contact contribution is:

$$\delta^{contact} = \frac{1}{3} \rho_{\alpha\beta} \chi_M \qquad \text{Equation 2.26}$$

Conversely, the pseudocontact or dipolar interaction is inherently anisotropic, stemming from the dipole-dipole interactions between the unpaired electron and the nucleus. This interaction depends on the spatial configuration of the electron cloud relative to the nucleus and varies with the orientation of the molecule in the external magnetic field. In theory, evaluating the pseudocontact interaction involves integrating the interaction energy across all points in space between the observed nucleus and the electron spin density. However, in practice, the problem can be simplified.[20] In the battery field, this interaction is often ignored to a first approximation due to the small effect in the isotropic shift, while the Fermi contact interaction is dominant.[17] First principles calculations and the Goodenough-Kanamori rules[21–23] have been used to assign a particular value of the hyperfine shift to a specific local environment in a variety of solids in the battery field.[24] Further discussion will delve into the application of first principles calculations and explore the implications of the Goodenough-Kanamori rules in greater detail.

## 2.5 Applying Goodenough-Kanamori Rules for Paramagnetic Shift Assignments in Lithium ssNMR

The application of Goodenough-Kanamori rules in Fermi-contact shift assignments within lithium ssNMR offers a valuable approach to interpreting complex spectral features associated with paramagnetic materials. In the context of ssNMR, these principles can help deduce the nature of electronic environments surrounding lithium ions in paramagnetic compounds, which is crucial for the study of battery materials.

The presence of a paramagnetic center significantly affects the local magnetic field, leading to what is known as paramagnetic shifts. These shifts arise from the transfer of electron spin density from unpaired electrons to the nuclei under observation, in this case, Li nuclei. According to the Goodenough-Kanamori rules, the direction and extent of these shifts can be predicted from the geometrical and electronic configurations of the paramagnetic centers. This rule is presented as a series of general guidelines governing the specific TM-O-Li (Transition Metal -Oxygen-Lithium) interactions in oxides, which vary according to the atomic geometry illustrated in **Figure 2.7**.[17,18,24] Usually, the transition metal center is in the octahedral coordination, resulting in a split of the d-orbital into $t_{2g}$ states ($d_{xy}$, $d_{yz}$, $d_{zx}$) and higher energy $e_g$ state ($d_{x^2-y^2}$ and $d_{z^2}$) that interact with the valence orbitals of oxygen (2p) and lithium (2s). The spin density can be transferred through two mechanisms: delocalization (or hybridization) and polarization and it is maximized when the TM-O-Li orbital geometries are at either 90° or 180°.

The delocalization happens when Li, O, and TM orbitals with the correct symmetry can overlap to form a spin orbital. When the TM-O-Li atoms form a 90° interaction, the $t_{2g}$

orbitals transfer electron density to the Li atom through the oxygen 2p orbitals involved in a π-type bonding (**Figure 2.7a**). Conversely, in a 180° atomic arrangement, the $e_g$ orbitals participate in the bonding interaction. These orbitals are responsible for transferring spin density to the Li nucleus via σ-bonded oxygen 2p orbitals.[24] When the spin transfer occurs via 2p orbital, the polarization is transferred from the O-orbital, involving both 'up' and 'down' electrons. The 'down' electron transfers to the TM-orbital to comply with the Pauli principle, while the 'up' electron transfers to Li, creating both a positive spin density and a positive Fermi-contact shift.[18] On another hand, there is the polarization mechanism, in which the TM-orbital that interacts with O and Li is vacant except for the electron pair present on O. The TM-orbital, which holds the spin-up unpaired electron and is depicted as lower in energy, lacks symmetry compatibility with the O or Li orbitals and therefore does not participate directly in covalent bonding. The unpaired electron density that moves from O to the vacant TM-orbital must align in polarization (spin-up) with the unpaired electron in another TM-orbital to adhere to Hund's first rule (**Figure 2.7b**). As a result, the electronic spin density that is transferred from O to Li is spin-dow and therefore a negative Fermi-contact shift.

These rules facilitate the understanding of how the unpaired electrons affect the observed chemical shift in ssNMR. However, this method depends on the TM-Li interactions being either 90° or 180°. Deviations from these angles can complicate even qualitative shift assignments. To solve this problem, density functional theory (DFT) calculations have been employed to assign Li NMR shifts in complex structures. Further details on DFT calculations can be found in Chapter 3.

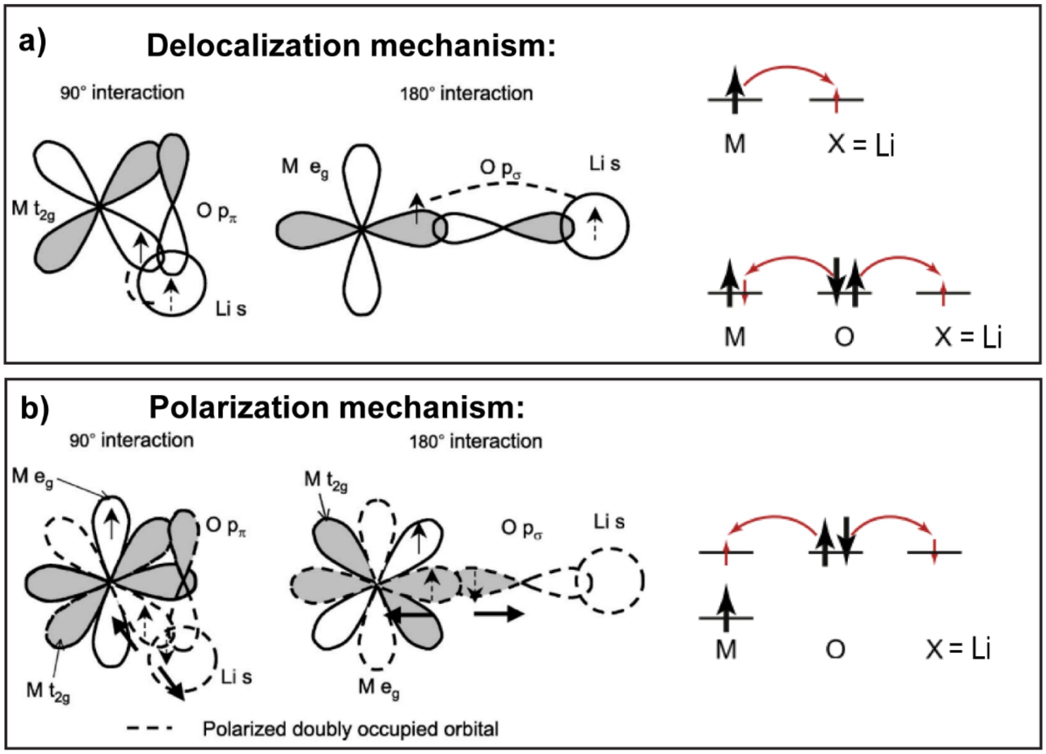

**Figure 2.7** Schematic illustrating the transfer of unpaired-electron spin density between the orbitals of a transition-metal ion M and the vacant s-orbital of the NMR-active nucleus X, possibly via the filled orbital of a bridging atom O. The unpaired electrons formally present in each orbital are illustrated with black arrows. The transfer of polarisation is indicated with a curved red arrow, and the transferred spin is shown with a small red arrow. Adapted from [18] and [24] with permission from American Physical Society.

## 2.6 NMR Spectroscopy Applied in the Development of Cathode Material for LIB

NMR spectroscopy has emerged as an indispensable analytical technique in the development of cathode materials for lithium-ion batteries. The application of NMR provides profound insights into the structural, and dynamic properties of cathode materials, facilitating the design and optimization of high-performance batteries. Due to being very sensitive to the local magnetic environment, it is employed to elucidate the mechanisms of lithium insertion/extraction, identify phase transitions during battery operation, and detect the formation of by-products that contribute to battery failure.

NMR studies of electrode materials for LIBs take advantage of the high natural abundance and high gyromagnetic ratio of $^7$Li to rapidly assess Li$^+$ local environments in different materials. Alternatively, if the resolution is a challenge, it is possible to apply $^6$Li NMR, as its smaller quadrupole moment and lower gyromagnetic ratio reduce the line broadening that arises from quadrupolar coupling and from Li-Li homonuclear dipolar couplings, respectively. However, its lower natural abundance and lower gyromagnetic ratio cause significant losses in sensitivity, leading to long experiment times.[6] In the application of both $^6$Li and $^7$Li NMR many studies take advantage of magic angle spinning to achieve resolution among structurally distinct sites. $^7$Li NMR relaxation studies are frequently done to differentiate species within LIBs, and/or to assess changes in ion dynamics as a function of temperature and evaluate activation energies of ion exchange.

As mentioned in the introduction, initial studies of $^6$Li and $^7$Li MAS NMR on the spinel cathode material $LiMn_2O_4$, conducted by Lee and Grey, demonstrated the sensibility of ssNMR spectroscopy in differentiating the distribution of lithium ions among the tetrahedral and octahedral sites. The ssNMR study of such a paramagnetic system was a first, and assignment of the chemical shifts according to the Goodenough-Kanamori rules laid the groundwork for many further ssNMR studies of paramagnetic cathode materials.[17] Under magic angle spinning, populations of crystallographically unique Li$^+$ sites can be resolved in many structures. However, often the degree of paramagnetic broadening, or the degree of local disorder is sufficient to obscure individual resonances, particularly at low or intermediate spinning speeds. Fast MAS, as well as advanced multi-pulse sequences, have been demonstrated to increase resolution and enhance our ability to understand the performance of these materials.

Cathode materials are typically paramagnetic in their pristine state, or pass through paramagnetic states during cycling, due to the presence of unpaired electrons at the TM centers. These paramagnetic centers can cause significant peak broadening due to the hyperfine interaction between the unpaired electrons and the NMR-active nuclei.[17,18,24] $^{6}$Li MAS NMR at low spinning speeds was successful in resolving the sites in $LiMn_2O_4$ as discussed above, at a modest spinning speed of 9 kHz.[25] However, there are many more cases where MAS at slow spinning speeds is insufficient to provide resolution. Hyperfine coupling between unpaired electrons and nearby nuclei of interest in materials generally causes broadening of the NMR spectrum compared to isostructural diamagnetic analogues.[18] This is due to a number of factors, including paramagnetic relaxation enhancement (which irrecoverably broadens lines by shortening $T_2$), spin-dipolar anisotropy (SA, analogous to CSA), and anisotropic bulk magnetic susceptibility (ABMS) effects. If the local order of the transition metal sites is lost, as in NMC materials, the resulting NMR spectra are heterogeneously broadened by many overlapping sites, causing in extreme cases total loss of resolution. In well-ordered materials with relatively small anisotropic effects, quasi-isotropic spectra can be recovered with fast enough MAS rotation rates. If the SA is large, though, the spectra are still complicated with numerous spinning sidebands.

In the instance where there are multiple similar chemical environments for the $^7$Li nuclei, the small changes in local environment generate multiple unique isotropic chemical shifts, which cannot be separated by MAS. This is the case in the NMC class of cathode materials which arise from the parent LCO and form in the layered rock-salt structure, where $Li^+$ and the transition metal ions occupy alternating layers sandwiched between oxide layers.[26] The objective of this target material was to combine the chemical benefits of environmental friendliness and low cost of manganese with the higher redox potential of nickel and the robustness of the layered LCO structure. Ozukhu was the first to report the layered $LiNi_{0.33}Mn_{0.33}Co_{0.33}O_2$, colloquially called NMC 111, for the 1:1:1 ratio of the transition metals.[26] This material has become a block-buster cathode with wide-spread commercialization. While the original material exhibits spectral resolution sufficient to allow detailed chemical shift assignments, as the ratio increases toward 1:1:1, the resonances overlap and become unresolvable. This is due to the mixing of the TM positions within the TM layer of the rock-salt structure.[27] A subsequent study combined $^7$Li MAS ssNMR and Monte Carlo simulations of the NMC structure as a function of simulated annealing temperature.[28] Comparison of the experimental $^7$Li NMR spectrum to the closest matching simulated spectrum showed the usefulness of the simulation in predicting many features, and illustrates that even under significant paramagnetic broadening, trends in terms of preferred local coordination environments can be well described.[24]

Another commercially important cathode material is $LiFePO_4$, (LFP) which is a polyanionic 1D-tunnel structure that exhibits remarkable stability upon cycling, is low cost and environmentally benign.[26] It has been delayed from wide-spread commercialization due to its lower energy and power density; however, interest in this material is growing again.[29] Both $^{7}$Li and $^{31}$P ssNMR spectroscopy have been successfully applied to the challenging LFP system and its related mixed Mn/Fe phases.[30–33] A $^{7}$Li spectrum of the olivine cathode material $LiFe_{0.5}Mn_{0.5}PO_4$ exhibits large shift and anisotropies due to the hyperfine interactions between the unpaired electron from $Fe^{2+}$ and $Mn^{2+}$ and the Li nuclei. Pell *et al.*[34] showed the effect of three different spinning speed in the $^{7}$Li spectrum. The spectrum obtained at 20 kHz MAS is broad and not very informative. Better resolution is obtained by doubling the MAS frequency to 40 kHz and at 60 kHz MAS there is a very well-defined baseline.[34]

Density Functional Theory (DFT) calculations have proven to be highly effective in facilitating the assignment of NMR spectra and in providing a deeper understanding of local chemical environment in various materials, especially in paramagnetic materials. Clément *et al.*[30] used a combination of aMAT (adiabatic magic angle turning) $^{31}$P NMR and hybrid DFT calculations to study the contribution of different spin-transfer pathways to the observed $^{31}$P spectra in LFP and LFMP ($LiMn_xFe_{(1-x)}PO_4$); details that would not be possible to extract without the combination of the new advanced pulse sequence and DFT calculations.

The application of *ex situ* ssNMR to characterize electrode materials as a function of charge and discharge is a well-established approach.[35] Utilizing different pulse sequences many details of structural evolution during cycling can be elucidated. In the important NMC class of materials, NMC811 ($LiNi_{0.8}Mn_{0.1}Co_{0.1}O_2$) is of current interest due to its high Ni-content and resulting high specific capacity of approximately 200 mAh

$g^{-1}$.[42] However, questions remain as to its stability and reversibility upon extended cycling. Märker *et al.*[36] applied pj-MATPASS to determine changes in the NMC811 cathode during the first charging cycle. It is expected to have three paramagnetic species present: $Ni^{2+}$, $Ni^{3+}$ and $Mn^{4+}$ making the $^{7}Li$ NMR spectrum challenging to interpret. As NMC811 is delithiated, Ni is oxidized from $Ni^{2+}/^{3+}$ to $Ni^{4+}$. The series of spectra reveal a decreasing $^{7}Li$ chemical shift, consistent with the diamagnetic nature of $Ni^{4+}$. In addition, a considerable sharpening of the $^{7}Li$ signal is observed, which is related to the increased rate of lithium ion hopping. This is due to the creation of lithium vacancies and the increasing interlayer spacing, consequently in a reduction in the activation energy for Li hopping. Monitoring the evolution of NMR signals during charging and discharging cycles enables researchers to identify and characterize phase transitions and changes in dynamics within the cathode material. This knowledge is essential for designing new future cathode materials with improved stability and cycle life.

## 2.7 Investigating Lithium Dynamics in Cathode Material

NMR has been used extensively to study chemical exchange in both solution and solid-state fields.[37–39] The observed nuclei are very sensitive to the local magnetic environment which allows detection of chemical exchange. In the case of materials for LIBs, determination of exchange rates and activation energy can reveal details of the movement of lithium ions within the solid-state components which can then be used to inform the process of optimizing battery performance.

In conducting NMR experiments, it is crucial to consider the NMR timescale to effectively extract information regarding the structure and dynamics of molecules. The relevant timescales run from fractions of picosecond (molecular vibrations) to many seconds (macroscopic diffusion, flow, and some chemical exchange processes)[2,40]. The chemical exchange timescales can be categorized into three distinct types: fast, intermediate, and slow exchange, each of which is probed differently by NMR. During fast exchange scenarios, the rate of exchange between nuclei surpasses the separation of their respective resonance frequencies. This results in the coalescence of signals into a single peak. The intermediate timescale is characterized by an ongoing coalescence process where the two signals with different chemical shifts move toward one another relative to their original positions and the occupancies at each site. In the slow-motion limit, the exchange rates are significantly lower than the frequency difference between the NMR shifts of the exchanging sites. In this regime, there is no observable coalescence, and the peaks remain well separated. [37,39,41,42]

The temporal limitations for visualize and quantify the chemical exchange between two sites are determined by the frequency difference between those two species, and thus the nucleus and magnetic field. Two ssNMR methodologies have been accomplished to quantify the site-specific Li ion mobility in slow regime for cathode materials, 2D $^{6,7}$Li Exchange spectroscopy (2D EXSY) and $^{6,7}$Li Selective Inversion experiments.

### 2.7.1. EXSY

The Exchange Spectroscopy (EXSY) experiment in NMR is a powerful two-dimensional (2D) technique used to study chemical exchange processes or molecular dynamics within a sample. EXSY provides detailed insights into the rates and pathways of exchange processes between different chemical species or sites within a molecule. This sequence has been used to study Li ion dynamics in diverse types of materials for energy storage applications, such as the spinel cathode $LiMn_2O_4$ [43], the nitride anode material $Li_7MnN_4$,[44] and polyanionic cathodes, $Li_3M_2(PO_4)_3$ (M= V or Fe)[45–50]. The pulse sequence is illustrated in **Figure 2.8**.

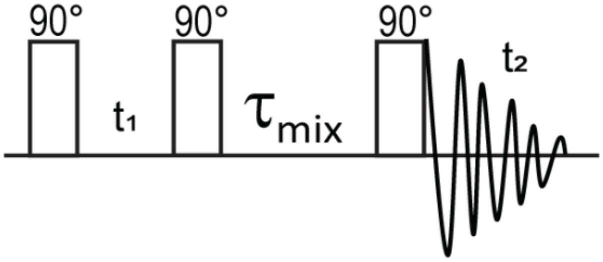

**Figure 2.8** The 2D EXSY pulse sequence used to detect chemical exchange by ssNMR. The initial $t_1$ period stores chemical shift information before exchange, and this information in combination with the exchange allowed to occur during $\tau_{mix}$ is ultimately observed during $t_2$.[37,51]

The first 90° pulse generates transverse magnetization within the *xy*-plane, where the spins start to precess during the evolution time $t_1$ and are labeled according to their frequency. Subsequently, another 90° pulse reorients the magnetization towards the z-axis, where during the mixing time, the chemical exchange processes take place, and the spins acquire the precessional frequency of their new environment. Finally, 90° detection pulse is applied, which brings back to the *xy*-plane the magnetization of the nuclei of the species in chemical equilibrium. [52] One of the advantages of this sequence is to visualize the exchange pairs, as shown in **Figure 2.9.** The diagonal peaks are related to the initial spin label that occurs during the $t_1$, **Figure 2.9a**, and if there is any exchange on the timescale of the mixing time, crosspeaks are observed in the 2D spectrum as shown in **Figure 2.6b.** The exchange rate can be obtained by analyzing the volume ratio between the crosspeak and diagonal peaks within the spectrum. This method provides a quantitative measure of the rate at which species undergo exchange, offering valuable insights into the dynamics of the system under investigation.

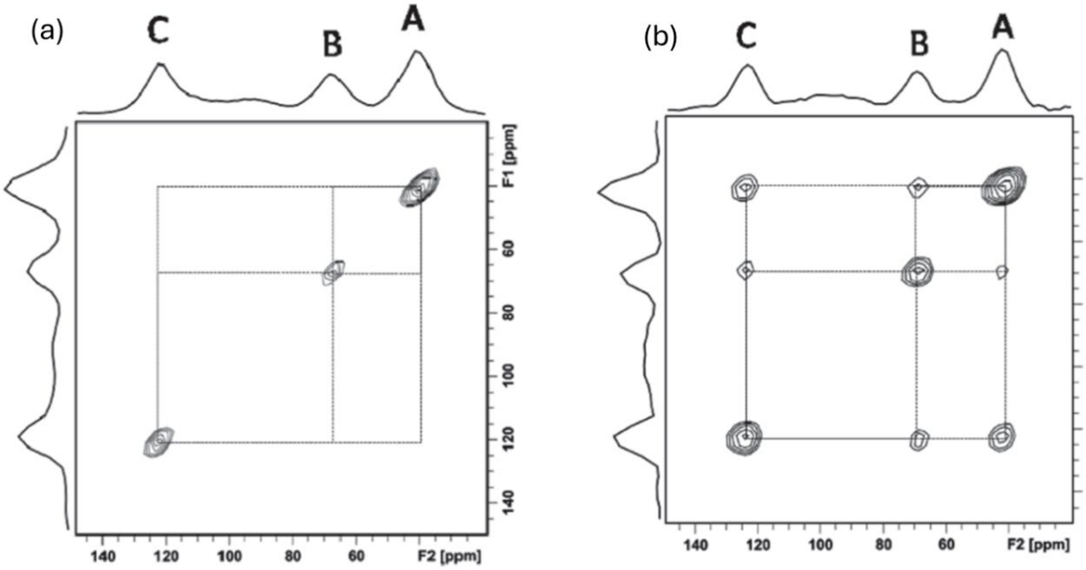

**Figure 2.9.** $^6$Li 2D EXSY spectrum of $Li_3Fe_2(PO_4)_3$ at T = 311K, MAS = 25 kHz, with (a) 0.5 ms mixing time and (b) 3.0 ms mixing time. Reprinted with permission from Davis, L.J.M, Heinmaa, I, Goward, G.R.Study of lithium dynamics in monoclinic $Li_3Fe_2(PO_4)_3$ using $^6$Li VT and 2D exchange MAS NMR spectroscopy. *Chem Mater*. 2010;22(3):769-775. Copyright 2010 American Chemical Society.

One drawback of 2D EXSY experiments appears for materials with slow exchange rates and multi sites in exchange. Longer times may lead to spurious cross-peaks, which means if there is a structure with three lithium sites, A, B and C, at longer mixing times exchange between A and B could arise from a site hop from A to B to C making the value of exchange rates imprecise. To solve this problem, a selective inversion experiment ca be performed.

### 2.7.2 Selective Inversion

EXSY provides excellent visual confirmation of chemical exchange and its practical use as a first method for qualitative identification of exchange pairs. However, the data analysis can be a challenge in some cases to obtain quantitative kinetic information for each pair of sites. The one-dimensional (1D) selective inversion (SI) experiment is a more effective method for quantitative determination of exchange rates and requires less experimental time. As EXSY, this sequence has been used to study Li ion dynamics in diverse types of materials for energy storage applications, such as $Li_3Fe_2(PO_4)_3$[47], and $Li_5V(PO_4)_2F_2$[45].

SI experiments are performed using a 180° $-\tau_{mix}-$90° sequence (**Figure 2.10**) over a series of experiments wherein a single signal is selectively inverted, typically using a selective Gaussian 180° pulse,[53] and the response of the other resonances are measured as a function of time during relaxation back to equilibrium, as shown in **Figure 2.11**. Gaussian pulses are classified as soft pulses because they have a long duration and low power, allowing for selective excitation of a narrow frequency range. This selectivity is crucial for SI experiments where only a specific site needs to be inverted without affecting nearby resonances. The effectiveness of the Gaussian pulse is influenced by the relaxation times of the nuclei. In systems with short $T_1$ relaxation, such as paramagnetic samples, the length of the Gaussian pulse is limited due to the relaxation effects.

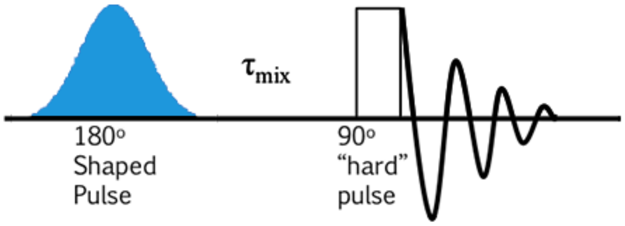

**Figure 2.10** Selective inversion pulse sequence used to quantify the chemical exchange in ssNMR. The initial Gaussian pulse shape inverted the selective frequency range followed by $\tau_{mix}$ where the spins are allowed to exchange.[53,54]

Rate constants are obtained by measuring the intensity of each site as a function of mixing time and fitting the data to a coupled relaxation model describing the build up of magnetization. The inverted peak will behave as an exponential curve until the magnetization reaches a maximum after relaxation by $T_1$. The rate of this build-up process depends on both $T_1$ and the rate constant for chemical exchange with the unperturbed peak. Conversely, the non-inverted peak presents a transient decrease in intensity, followed by relaxation back to equilibrium due to $T_1$ at longer mixing times. A fit of both the inverted and unperturbed resonances as a function of mixing time reveals both the time constant associated with spin-lattice relaxation and the rate constant for chemical exchange between the involved sites. The data is processed using the CIFIT mathematical program developed by A.D. Bain at McMaster University.

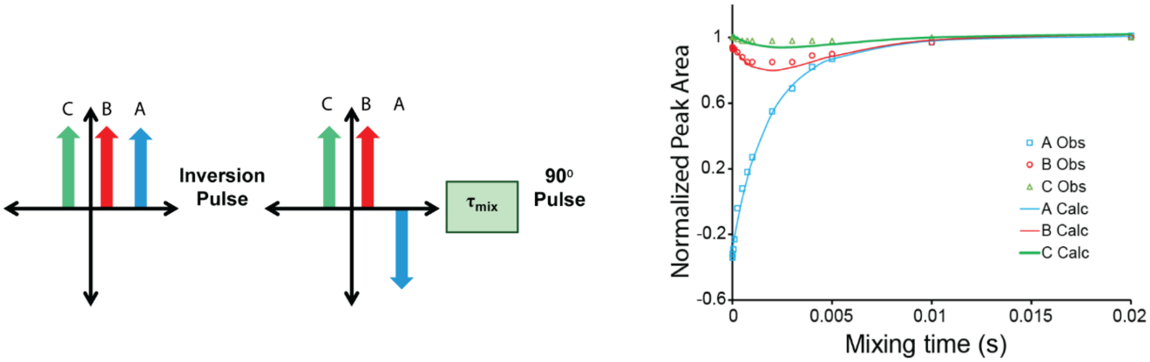

**Figure 2.11** Schematic and results of selective inversion (SI) Experiments. The left panel illustrates the selective inversion pulse sequence, where spins A, B, and C are subjected to an inversion pulse, followed by a period of mixing time ($\tau_{mix}$). The right panel depicts a graph of normalized peak area against mixing time (s). Data points represent measured values, and the lines are the best fit to the data from the CIFIT program.[55]

CIFIT is a mathematical program for fitting data from selective inversion relaxation experiment on a system undergoing slow chemical exchange, where it is possible to visualize the exchange peaks no collapsed. The input file has a table of observed intensities for all signals as a function of mixing time. CIFIT will try to find the set of parameters, such as, exchange rates (k), $T_1$ relaxation and the magnetization intensities from initial to equilibrium conditions, that best match the experimental data.[55]

The fundamental mathematical framework in CIFIT is a rate matrix that models the spin relaxation coupled with exchange. If Mi(t) denotes the magnetization at site i at a given time t, and $M_i(\infty)$ represents the magnetization of the same site at equilibrium, then the mathematical representation of the magnetization vector $M_i(t)$ across 'n' sites as a function of time is given by: [55]

$$\frac{\partial}{\partial t}\begin{pmatrix} M_1(\infty) - M_1(t) \\ \vdots \\ M_n(\infty) - M_n(t) \end{pmatrix} = -A\begin{pmatrix} M_1(\infty) - M_1(t) \\ \vdots \\ M_n(\infty) - M_n(t) \end{pmatrix}$$

Where

$$A = \begin{pmatrix} R_1 & -k_{21} & -k_{31} & \dots & -k_{n1} \\ -k_{12} & R_2 & -k_{32} & \dots & -k_{n2} \\ -k_{13} & -k_{23} & R_3 & \dots & -k_{n3} \\ \vdots & \vdots & \vdots & \ddots & \vdots \\ -k_{1n} & -k_{2n} & -k_{3n} & \dots & R_n \end{pmatrix} \text{ and}$$

$$R_i = \frac{1}{T_{1i}} + \sum_{j \neq i} K_{ij} \qquad \text{Equation 2.27}$$

$T_{1i}$ is the spin-lattice relaxation time of site *i* and $k_{ij}$ is the exchange rate from site *i* to *j*.

The role of the CIFIT program is to adjust the parameters in this model until the sum of the squares of the differences between the modeled and observed data is minimized.

## 2.8 Summary

This chapter provides a comprehensive overview of solid-state NMR spectroscopy, focusing on its application in characterizing the structural and ion mobility properties of cathode materials. It begins by explaining the basics of nuclear spin and NMR detection, delving into the external and internal nuclear interactions. Techniques like Magic Angle Spinning are discussed for their roles in enhancing spectral resolution, especially for paramagnetic samples. The chapter concludes with a detailed exploration of lithium dynamics in cathode materials, using 2D EXSY and SI experiments to investigate lithium-ion mobility, crucial for optimizing battery performance.

This thesis focuses on $LiFeV_2O_7$ pristine cathode material and the evolution of this structure along the first discharge cycle. It employs $^7Li$ MAS NMR to both characterize these structural modifications as lithium ions are inserted and to measure the chemical exchange rates between lithium sites. EXSY experiments are used to identify the existence of lithium dynamics, while SI experiments are used to quantify the exchange rates. This approach allows for a detailed understanding of $LiFeV_2O_7$ behavior under operational conditions.

## 2.9 References

(1) Harris, R. K. *Nuclear Magnetic Resonance Spectroscopy*; 1993.

(2) Levitt, M. H. *Malcolm H. Levitt*; 2000.

(3) Silverstein - Spectrometric Identification of Organic Compounds 7th Ed.Pdf.

(4) Keeler, J. Understanding NMR Spectroscopy. *Choice Rev. Online* **2006**, *43* (10), 43-5896-43–5896. https://doi.org/10.5860/choice.43-5896.

(5) Bakhmutov, V. I. *Solid-State NMR in Materials Science: Principles and Applications*; 2016.

(6) Duer, M. J. *Solid-State NMR Spectroscopy*.

(7) Haeberlen, U. In Advances in Magnetic Resonance. *Suppl. 1; J. S. Waugh, Ed.; Academic Press: New York,*. 1976.

(8) Karunakaran, C.; Rajkumar, R.; Balamurugan, M. *Principles of Nuclear Magnetic Resonance and Pulsed Nuclear Magnetic Resonance*; Elsevier Inc., 2018. https://doi.org/10.1016/B978-0-12-813608-9.00001-0.

(9) Knitsch, R.; Brinkkötter, M.; Wiegand, T.; Kehr, G.; Erker, G.; Hansen, M. R.; Eckert, H. Solid-State NMR Techniques for the Structural Characterization of Cyclic Aggregates Based on Borane–Phosphane Frustrated Lewis Pairs. *Molecules* **2020**, *25* (6), 1–39. https://doi.org/10.3390/molecules25061400.

(10) Ashbrook, S. E.; Sneddon, S. New Methods and Applications in Solid-State NMR Spectroscopy of Quadrupolar Nuclei. *J. Am. Chem. Soc.* **2014**, *136* (44), 15440–15456. https://doi.org/10.1021/ja504734p.

(11) Bräuniger, T.; Jansen, M. Solid-State NMR Spectroscopy of Quadrupolar Nuclei in Inorganic Chemistry. *Zeitschrift fur Anorg. und Allg. Chemie* **2013**, *639* (6), 857–879. https://doi.org/10.1002/zaac.201300102.

(12) Ashbrook, S. E. Recent Advances in Solid-State NMR Spectroscopy of Quadrupolar Nuclei. *Phys. Chem. Chem. Phys.* **2009**, *11* (32), 6892–6905. https://doi.org/10.1039/b914008p.

(13) Reif, B.; Ashbrook, S. E.; Emsley, L.; Hong, M. Solid-State NMR Spectroscopy. *Nat. Rev. Methods Prim.* **2021**, *1* (1). https://doi.org/10.1038/s43586-020-00002-1.

(14) Medek, A.; Marinelli, L.; Frydman, L. Multiple-Quantum Magic-Angle Spinning NMR of Half-Integer Quadrupolar Nuclei. *ACS Symp. Ser.* **1999**, *717*, 136–155. https://doi.org/10.1021/bk-1999-0717.ch002.

(15) Polenova, T.; Gupta, R.; Goldbourt, A. Magic Angle Spinning NMR Spectroscopy: A Versatile Technique for Structural and Dynamic Analysis of Solid-Phase Systems. *Anal. Chem.* **2015**, *87* (11), 5458–5469. https://doi.org/10.1021/ac504288u.

(16) Carlier, D.; Ménétrier, M.; Delmas, C. Transferred d Interaction between a Tetrahedral Transition Metal and Tetrahedral Lithium: Li6CoO4. *J. Phys. Chem. C* **2010**, *114* (10), 4749–4755. https://doi.org/10.1021/jp911364w.

(17) Grey, C. P.; Dupré, N. NMR Studies of Cathode Materials for Lithium-Ion Rechargeable Batteries. *Chem. Rev.* **2004**, *104* (10), 4493–4512. https://doi.org/10.1021/cr020734p.

(18) Pell, A. J.; Pintacuda, G.; Grey, C. P. Paramagnetic NMR in Solution and the Solid State. *Prog. Nucl. Magn. Reson. Spectrosc.* **2019**, *111*, 1–271. https://doi.org/10.1016/j.pnmrs.2018.05.001.

(19) Bertmer, M. Paramagnetic Solid-State NMR of Materials. *Solid State Nucl. Magn. Reson.* **2017**, *81* (November 2016), 1–7. https://doi.org/10.1016/j.ssnmr.2016.10.006.

(20) Bertini, I.; Luchinat, C.; Parigi, G.; Ravera, E. *NMR of Paramagnetic Molecules: Applications to Metallobiomolecules and Models*; 2016. https://doi.org/10.1016/C2013-0-18690-4.

(21) Goodenough, J. B. Theory of the Role of Covalence in the Perovskite-Type Manganites [La,M(II)]MnO3. *Phys. Rev.* **1955**, *100* (2), 564–573. https://doi.org/10.1103/PhysRev.100.564.

(22) Goodenough, J. B. An Interpretation of the Magnetic Properties of the Perovskite-Type Mixed Crystals La1-XSrxCoO3-λ. *J. Phys. Chem. Solids* **1958**, *6* (2–3), 287–297. https://doi.org/10.1016/0022-3697(58)90107-0.

(23) Kanamori, J. Superexchange Interaction and Symmetry Properties of Electron Orbitals. *J. Phys. Chem. Solids* **1959**, *10* (2–3), 87–98. https://doi.org/10.1016/0022-3697(59)90061-7.

(24) Carlier, D.; Ménétrier, M.; Delmas, C.; Grey, C. P.; Ceder, G. Understanding the NMR Shifts in Paramagnetic Transition Metal Oxides Using Density Functional Theory Calculations. *Phys. Rev. B - Condens. Matter Mater. Phys.* **2003**, *67* (17), 174103. https://doi.org/10.1103/PhysRevB.67.174103.

(25) Lee, Y. J.; Wang, F.; Grey, C. P. 6Li and 7Li MAS NMR Studies of Lithium Manganate Cathode Materials. *J. Am. Chem. Soc.* **1998**, *120* (48), 12601–12613. https://doi.org/10.1021/ja9817794.

(26) Ohzuku, T.; Makimura, Y. Layered Lithium Insertion Material of LiCo1/3Ni1/3Mn1/3O2 for Lithium-Ion Batteries. *Chem. Lett.* **2001**, *30* (7), 642–643. https://doi.org/10.1246/CL.2001.642.

(27) Cahill, L. S.; Yin, S. C.; Samoson, A.; Heinmaa, I.; Nazar, L. F.; Goward, G. R. Li NMR Studies of Cation Disorder and Transition Metal Ordering in Li[Ni1/3Mn1/3Co1/3]O2 Using Ultrafast Magic Angle Spinning. *Chem. Mater.* **2005**, *17* (26), 6560–6566. https://doi.org/10.1021/cm0508773.

(28) Harris, K. J.; Foster, J. M.; Tessaro, M. Z.; Jiang, M.; Yang, X.; Wu, Y.; Protas, B.; Goward, G. R. Structure Solution of Metal-Oxide Li Battery Cathodes from Simulated Annealing and Lithium NMR Spectroscopy. *Chem. Mater.* **2017**, *29* (13), 5550–5557. https://doi.org/10.1021/acs.chemmater.7b00836.

(29) Ahsan, Z.; Ding, B.; Cai, Z.; Wen, C.; Yang, W.; Ma, Y.; Zhang, S.; Song, G.; Javed, M. S. Recent Progress in Capacity Enhancement of LiFePO4 Cathode for Li-Ion Batteries. *J. Electrochem. Energy Convers.* **2021**, *18*, 10801–10802. https://doi.org/10.1115/1.4047222.

(30) Clément, R. J.; Pell, A. J.; Middlemiss, D. S.; Strobridge, F. C.; Miller, J. K.; Whittingham, M. S.; Emsley, L.; Grey, C. P.; Pintacuda, G. Spin-Transfer Pathways in Paramagnetic Lithium Transition-Metal Phosphates from Combined Broadband Isotropic Solid-State MAS NMR Spectroscopy and DFT Calculations. *J. Am. Chem. Soc.* **2012**, *134* (41), 17178–17185. https://doi.org/10.1021/ja306876u.

(31) Davis, L. J. M.; Heinmaa, I.; Ellis, B. L.; Nazar, L. F.; Goward, G. R. Influence of Particle Size on Solid Solution Formation and Phase Interfaces in Li0.5FePO4 Revealed by 31P and 7Li Solid State NMR Spectroscopy. *Phys. Chem. Chem. Phys.* **2011**, *13* (11), 5171–5177. https://doi.org/10.1039/c0cp01922d.

(32) Chevallier, F.; Poli, F.; Montigny, B.; Letellier, M. In Situ7Li Nuclear Magnetic Resonance Observation of the Electrochemical Intercalation of Lithium in Graphite: Second Cycle Analysis. *Carbon N. Y.* **2013**, *61*, 140–153. https://doi.org/10.1016/j.carbon.2013.04.078.

(33) Strobridge, F. C.; Middlemiss, D. S.; Pell, A. J.; Leskes, M.; Clément, R. J.; Pourpoint, F.; Lu, Z.; Hanna, J. V; Pintacuda, G.; Emsley, L.; Samoson, A.; Grey, C. P. Characterising Local Environments in High Energy Density Li-Ion Battery Cathodes: A Combined NMR and First Principles Study of LiFexCo1−xPO4. *J. Mater. Chem. A* **2014**, *2* (30), 11948–11957. https://doi.org/10.1039/C4TA00934G.

(34) Pell, A. J.; Pintacuda, G. Broadband Solid-State MAS NMR of Paramagnetic Systems. *Prog. Nucl. Magn. Reson. Spectrosc.* **2015**, *84–85*, 33–72. https://doi.org/10.1016/j.pnmrs.2014.12.002.

(35) Gan, Z. High-Resolution Chemical Shift and Chemical Shift Anisotropy Correlation in Solids Using Slow Magic Angle Spinning. *J. Am. Chem. Soc.* **1992**, *114* (21),

8307–8309.

(36) Märker, K.; Reeves, P. J.; Xu, C.; Griffith, K. J.; Grey, C. P. Evolution of Structure and Lithium Dynamics in LiNi0.8Mn0.1Co0.1O2 (NMC811) Cathodes during Electrochemical Cycling. *Chem. Mater.* **2019**, *31* (7), 2545–2554. https://doi.org/10.1021/acs.chemmater.9b00140.

(37) Bain, A. D. Chemical Exchange in NMR. *Prog. Nucl. Magn. Reson. Spectrosc.* **2003**, *43* (3–4), 63–103. https://doi.org/10.1016/j.pnmrs.2003.08.001.

(38) Bain, A. D.; Cramer, J. A. Slow Chemical Exchange in an Eight-Coordinated Bicentered Ruthenium Complex Studied by One-Dimensional Methods. Data Fitting and Error Analysis. *J. Magn. Reson. Ser. A* **1996**, *118* (1), 21–27. https://doi.org/10.1006/jmra.1996.0004.

(39) Smiley, D. L.; Goward, G. R. Solid-State NMR Studies of Chemical Exchange in Ion Conductors for Alternative Energy Applications. *Concepts Magn. Reson. Part A*. **2016**, *45A* (6), e21419. https://doi.org/10.1002/cmr.a.21419.

(40) Hu, J. Z.; Jaegers, N. R.; Hu, M. Y.; Mueller, K. T. In Situ and Ex Situ NMR for Battery Research. *J. Phys. Condens. Matter* **2018**, *30* (46). https://doi.org/10.1088/1361-648X/aae5b8.

(41) Bain, A. D.; Fletcher, D. A.; Hazendonk, P. What Is a Transition? *Concepts Magn. Reson.* **1998**, *10* (2), 85–98. https://doi.org/10.1002/(SICI)1099-0534(1998)10:2<85::AID-CMR2>3.0.CO;2-R.

(42) Bain, A. D. Blurring the Distinction between Slow and Intermediate Chemical Exchange. *Biochem. Cell Biol.* **1998**, *76* (2–3), 171–176. https://doi.org/10.1139/o98-020.

(43) Verhoeven, V. W. J. J.; Schepper, I. M. De; Nachtegaal, G.; Kentgens, A. P. M. M.; Kelder, E. M.; Schoonman, J.; Mulder, F. M.; De Schepper, I. M.; Nachtegaal, G.; Kentgens, A. P. M. M.; Kelder, E. M.; Schoonman, J.; Mulder, F. M. Lithium

Dynamics in LiMn2O4 Probed Directly by Two-Dimensional 7Li NMR. *Phys. Rev. Lett.* **2001**, *86* (19), 4314–4317. https://doi.org/10.1103/PhysRevLett.86.4314.

(44) Cabana, J.; Dupré, N.; Rousse, G.; Grey, C. P.; Palacín, M. R. Ex Situ NMR and Neutron Diffraction Study of Structure and Lithium Motion in Li7MnN4. *Solid State Ionics* **2005**, *176* (29–30), 2205–2218. https://doi.org/10.1016/j.ssi.2005.07.001.

(45) Davis, L. J. M.; Goward, G. R. Differentiating Lithium Ion Hopping Rates in Vanadium Phosphate versus Vanadium Fluorophosphate Structures Using 1D 6Li Selective Inversion NMR. *J. Phys. Chem. C* **2013**, *117* (16), 7981–7992. https://doi.org/10.1021/jp310790g.

(46) Davis, L. J. M. M.; Heinmaa, I.; Goward, G. R. Study of Lithium Dynamics in Monoclinic Li3Fe 2(PO4)3 Using 6Li VT and 2D Exchange MAS NMR Spectroscopy. *Chem. Mater.* **2010**, *22* (3), 769–775. https://doi.org/10.1021/cm901402u.

(47) Smiley, D. L.; Davis, L. J. M. M.; Goward, G. R. An Improved Understanding of Li+ Hopping Pathways and Rates in Li3Fe2(PO4)3 Using Selective Inversion 6Li NMR Spectroscopy. *J. Phys. Chem. C* **2013**, *117* (46), 24181–24188. https://doi.org/10.1021/jp407510h.

(48) Davis, L. J. M. M.; Ellis, B. L.; Ramesh, T. N.; Nazar, L. F.; Bain, A. D.; Goward, G. R. 6Li 1D EXSY NMR Spectroscopy: A New Tool for Studying Lithium Dynamics in Paramagnetic Materials Applied to Monoclinic Li2VPO 4F. *J. Phys. Chem. C* **2011**, *115* (45), 22603–22608. https://doi.org/10.1021/jp2059408.

(49) Cahill, L. S.; Kirby, C. W.; Goward, G. R. 6Li\{31P\} Rotational-Echo, Double-Resonance Studies of Lithium Ion Site Dynamics in Li3v2(PO4) 3. *J. Phys. Chem. C* **2008**, *112* (6), 2215–2221. https://doi.org/10.1021/jp077254s.

(50) Cahill, L. S.; Chapman, R. P.; Britten, J. F.; Goward, G. R. 7Li NMR and Two-Dimensional Exchange Study of Lithium Dynamics in Monoclinic Li3v2(PO4)3. *J. Phys. Chem. B* **2006**, *110* (14), 7171–7177. https://doi.org/10.1021/jp057015+.

(51) Jeener, J.; Meier, B. H.; Bachmann, P.; Ernst, R. R. Investigation of Exchange Processes by Two-Dimensional NMR Spectroscopy J. *J. Chem. Phys.* **1979**, *71*, 4546–4553. https://doi.org/10.1063/1.438208.

(52) Forsén, S.; Huffman, R. A. Study of Moderately Rapid Chemical Exchange Reactions by Means of Nuclear Magnetic Double Resonance. *J. Chem. Phys.* **1963**, *39* (11), 2892–2901. https://doi.org/10.1063/1.1734121.

(53) Bauer, C.; Freeman, R.; Freniuel, T.; Reeler, J.; Shaka, A. J. Gaussian Pulses. 1984.

(54) Robinson, G.; Kuchel, P. W.; Chapman, B. E.; Doddrell, D. M.; Irving, M. G. A Simple Procedure for Selective Inversion of NMR Resonances for Spin Transfer Enzyme Kinetic Measurements. *J. Magn. Reson.* **1985**, *63* (2), 314–319. https://doi.org/10.1016/0022-2364(85)90321-X.

(55) Bain, A. D. The Cifit Program - Manual. **2000**, No. 1, 1–16.

# Chapter 3: Methods

The development of high and efficient performance batteries requires exploring new materials and a comprehensive understanding of their physical and chemical properties. In addition to nuclear magnetic resonance (NMR) spectroscopy, diffraction methods such as X-ray powder diffraction (XRD) and single crystal X-ray diffraction (SCXRD) are employed as characterization techniques for these synthesized materials. These techniques were utilized in this thesis to analyze the structural properties of the material under investigation. Furthermore, when those techniques are combined with Density Functional Theory (DFT) calculations, a more comprehensive interpretation of the experimental results is possible, enhancing our understanding of the material properties at the atomic level. This chapter will provide an overview of diffraction techniques and DFT calculations and discuss how both methodologies have been applied in the development of lithium-ion batteries (LIBs) and utilized throughout this thesis.

## 3.1 X-Ray Diffraction Techniques

### 3.1.1 X-Ray Sources

X-rays are electromagnetic radiation of short wavelengths, and the most commonly used range in crystallography is between 0.5 and 2.5 Å, since they are of the same order magnitude as the interatomic distance in both organic and inorganic materials. [1,2] X-rays are generated through two primary methods, X-ray tubes and synchrotrons. The first one is a common laboratory device where X-rays are produced when high-energy electrons strike a metal target, usually made of copper (Cu) or molybdenum (Mo). In contrast, synchrotrons, which are large-scale facilities, create X-ray radiation by accelerating electrons to nearly the speed of light. As these electrons are deflected by magnetic fields within the storage ring, they emit high-energy electromagnetic radiation.[3] The brilliance of the X-ray beam produced by synchrotrons can be four to twelve orders of magnitude greater than that from conventional X-ray sources.[1] Using a synchrotron instead of conventional X-ray tubes offers several advantages, including:

- Higher brightness: This means that synchrotron sources pack more photons into a smaller beam of light offering more details about the sample.[4]
- High resolution: The ability of synchrotron radiation to be tightly collimated and focused reduces background noise significantly. Unlike conventional X-ray sources, which can emit radiation in broader beams, synchrotron beams can be directed more precisely. This focused beam minimizes the interaction with non-target areas of the sample or the surrounding environment, thereby reducing unwanted scatter and improving the overall signal-to-noise ratio. [5]
- Reduced exposure times: The intensity of synchrotron radiation enables much faster data collection compared to X-ray tubes. This rapid acquisition is invaluable in reducing experiment times and is particularly beneficial for studying fast chemical reactions or processes that occur over short timescales.

In this thesis, both types of X-ray sources were employed. Molybdenum Kα radiation was utilized for single-crystal X-ray diffraction to achieve high-resolution structural data. Conversely, a synchrotron source investigated phase transitions and structure determination. All synchrotron data were obtained in the beamline of the Brockhouse X-Ray Diffraction and Scattering (BXDS) sector at the Canadian Light Source (CLS).

### 3.1.2 X-Ray Powder Diffraction

X-ray powder diffraction (XRD) is a versatile and widely used technique in material science for identifying the crystalline phases of a material, which includes information such as atom positions, their arrangement in the unit cell, and spacing between the atomic planes. Solid-state compounds can be categorized into three distinct types based on the arrangement of their atoms: amorphous, single-crystalline, and polycrystalline. Amorphous materials, also known as non-crystalline materials, lack a long-range order in their atomic arrangements. This means that atoms do not follow a repetitive pattern extending beyond a few nearest neighbors. Common examples include glasses and many plastics. Single crystalline materials consist of a continuous crystal lattice with a uniform arrangement of atoms throughout the entire structure. Various crystals of different sizes and shapes combine to form polycrystalline materials.[6]

This method involves irradiating a powdered sample with X-rays and analyzing the diffraction pattern that results from the interaction of the X-rays with the sample. As the X-rays interact with the crystal lattice of the material, they are scattered in various directions. According to Bragg's Law, diffraction occurs when the path length difference between rays scattered from consecutive planes of atoms in the crystal lattice equals an integer multiple of the wavelength ($\lambda$). This condition ensures constructive interference, leading to measurable peaks in the diffraction pattern:[6]

$$n\lambda = 2d \sin\theta \qquad \text{Equation 3.1}$$

where d represents the spacing between the planes (hkl) also known as interplanar distance (d-spacing) in the crystal lattice, $\theta$ is the angle of incidence, and $n$ is an integer.

An X-ray powder diffraction pattern is a set of peaks with different intensities and positions. The position of each peak corresponds to the spacing between planes in the crystal, providing valuable insights into the unit cell dimensions. Meanwhile, the intensity of each peak offers information about the crystal structure and the concentration of these planes. Each crystalline solid has a unique diffraction pattern, which can be considered its "fingerprint". By comparing the experimental diffraction pattern to a database of known patterns, it is possible to identify the crystalline phases present in the material.[7] One of the most common methods used for this analysis is the Rietveld refinement technique, which can adjust a hypothesized model of a crystal structure to best fit the experimental data. Several software tools have been developed to facilitate this complex analysis, including GSAS[8], FullProf[9], and DIFFRAC.EVA[10]. Once the refinement converges, the refined model provides detailed information about the crystal structure. The final report from the software includes refined lattice parameters, atomic positions, and factors indicating the quality of the fit, such as the R-factor.

In this thesis, we used ex-situ and operando SPXRD to determine the purity of the synthesized compound and the structural behavior of $Li_{1-x}FeV_2O_7$ cathode during the charge/discharger process.

### 3.1.3 Single Crystal X-Ray Diffraction

Single crystal X-ray diffraction (SCXRD) is a specialized form of XRD that requires a single crystal of the material as a sample. It is used primarily to determine the detailed atomic structure of a material. This technique involves directing X-ray beams at a single crystal which diffracts the X-rays into many specific directions. By measuring the angles and intensities of these diffracted beams, it is possible to produce a three-dimensional map of electron density within the crystal. This map then allows us to determine the positions of the atoms in the crystal, their chemical bonds, any structural disorder, and other structural information.[7] The collected data is then analyzed to solve the crystal structure, in our case, we used the OLEX2 software[11]. In contrast, powder XRD employs samples consisting of many randomly oriented grains, which is effective for identifying different crystal phases and provides averaged structural data. However, it does not yield the detailed atomic structure that single crystal diffraction can deliver.

### 3.1.4 X-Ray Diffraction Applied in the Development of Batteries

X-ray diffraction has been essential in the development and optimization of various materials for lithium-ion batteries, enabling researchers to improve battery performance by understanding the crystal structure and phase behaviors of these materials. Ex-situ XRD is essential for initial characterization, helping to establish baseline structural properties and identify any immediate changes resulting from synthesis processes. It is also used to analyze the material outside of their operating environment, typically before and after a reaction or modification.

In general, material characterization is shifting toward in-situ and operando setups, and XRD would not be different. This trend is particularly pronounced in fields where it is crucial to understand dynamic processes during operation, such as in battery technology. Operando XRD provides continuous collection data that reflects the immediate structural changes occurring within the material. Orikasa et al. explored the phase transformation between $LiFePO_4$ and $FePO_4$ during nonequilibrium battery operation by employing time-resolved in-situ synchrotron XRD (**Figure 3.1a**). Their study revealed a metastable crystal phase with an intermediate composition of $Li_{0.6-0.75}FePO_4$ under high-rate conditions (10C). This marked the first observation of a metastable phase during the electrochemical delithiation of $LiFePO_4$, supporting the hypothesis that a nonequilibrium solid solution forms under high-rate cycling conditions, as opposed to the distinct $LiFePO_4$/$FePO_4$ interface typically observed at lower rates.[12] Another study published by Xu et al.[13], used operando XRD to provide insights into the structural evolution of NMC811 cathodes during electrochemical aging. It revealed the presence of multiple phases and the increase in the fraction of the fatigued phase with cycle number. These observations suggest that this fatigue is not primarily due to kinetic limitations or intergranular cracking, as previously suspected. Instead, the degradation is linked to high interfacial lattice strain between the reconstructed surface and the bulk layered structure, particularly when the bulk is at higher states of charge.

Operando XRD also has been used to monitor changes within the unit cell of materials during real-time operation. For example, Park et al.[14] used this approach to evaluate the structure behavior of NASICON-$Na_4FeV(PO_4)_3$ cathode during the charge/discharger process. During the electrochemical operation, the study identified three distinct voltage domains during the charging process, which are associated with sodium extraction from the structure. This leads to observable changes in the unit cell parameters, such as a decrease in the unit cell volume and modifications to the lattice parameters (**Figure 3.1b**). The analysis reveals a complex interplay of phase transitions, including the formation of a monoclinic distortion and a subsequent reduction in unit cell volume, which directly corresponds to the electrochemical activity observed. Those are examples showing how XRD can be useful for the development of energy storage.

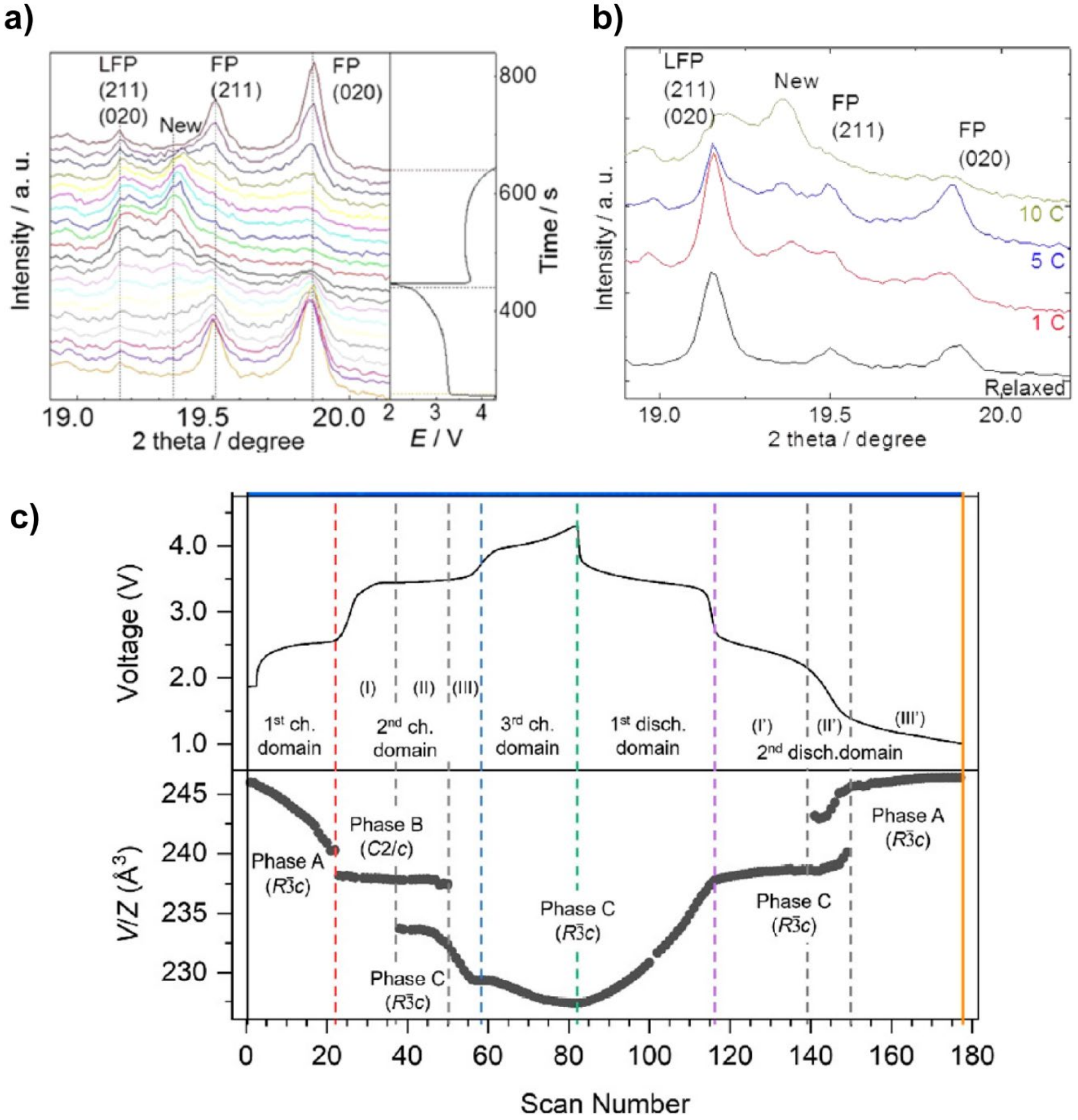

**Figure 3.1** (a) In situ XRD patterns of a Li/LiFePO4 cell at a rate of 10 C. Selected individual diffraction patterns during the first two cycles are stacked. (b) Time-resolved XRD patterns at the end of the first discharge reaction at various charge−discharge rates. Adapted from [15]. (c) Evolution of the unit cell volume per formula unit (V/Z) (bottom), obtained from the full pattern matching refinement of the synchrotron XRPD patterns collected operando during the cycling of the in situ cell and is associated with the electrochemical curve (top). Adapted from [14].

## 3.2 Ab Initio Calculations in VASP

Simulations based on quantum mechanics that describe interactions among electrons, and between electrons and atomic nuclei, have become essential in the fields of solid-state physics, chemistry, and materials science. These computational methods have offered a deeper understanding of the subject studied when coupled with experimental methods and enabled the development of future technologies. [16] In this thesis, we employed Density Functional Theory (DFT) calculations to predict the Fermi Contact shift observed in $^7$Li NMR spectra of $Li_{1.x}FeV_2O_7$ samples.

### 3.2.1 Basic of Density Functional Theory (DFT)

DFT is based on the principle that the energy of the system can be described in terms of electron density, which needs only three spatial coordinates and is independent of the number of electrons involved. While the wave functions depend on all spatial coordinates of all electrons present in the system. This principle is grounded in two foundational theorems proposed by Kohn and Hohenberg and the derivation of a set of equations by Kohn and Sham.

The first theorem proposed that *the ground-state energy from Schrodinger's equation is a unique functional of the electron density,* [17,18] establishing that all observable properties can be derived from the electron density itself. The second theorem provides a variational principle for the electron density, stating that *the true electron density minimizes the total energy of the system*. [17,18] This simplifies the complex many-body problem of interacting electrons into a more manageable form without needing to solve the many-body wave function directly. However, these theorems do not provide a method for solving the full Schrödinger equation. The solution came from Kohn and Sham, who showed that the ground state electron density can be expressed by a set of equations (Equation 3.2) that only involves a system of non-interacting electrons. This non-interacting system has the same electron density as the original system, [17]

$$\left[\frac{h^2}{2m}\nabla^2 + V(r) + V_H(r) + V_{XC}(r)\right]\psi_i(r) = \varepsilon_i\psi_i(r) \qquad \text{Equation 3.2}$$

where the terms on the right are, in order, the electron kinetic energy, the electron-nuclear interaction potential, the Hartree potential that describes the Coulomb interaction between a single electron and the total electron density, and the exchange-correlation functional, which describes all the quantum mechanical effects.

A significant challenge in solving the Kohn-Sham equations arises from the fact that the exact form of the exchange-correlation functional remains unknown. To address this, two principal approximation methods have been developed to estimate the exchange-correlation functional effectively. Local Density Approximation (LDA) is the simplest form where the exchange-correlation energy at each point in space is approximated using the exchange-correlation energy of a uniform electron gas at the same density. Conversely, the Generalized Gradient approximation (GGA) includes not only the density but also the gradient of the density to account more accurately for spatial variations, which was chosen to use in this thesis. [19]

### 3.2.1.1 Plane waves

Thus far, we have discussed all the approximations required to solve the Schrödinger equation. To proceed with solving the Kohn-Sham equations, it is essential to define the basis sets. The choice of a basis set defines how wave functions are represented in the computational model. Basis sets can vary from plane waves, which are suitable for periodic systems, to localized orbitals like Gaussian, which are preferred for molecular systems. Here we have chosen plane waves that are favored for their ability to handle periodic boundary conditions naturally. They allow systematic convergence, where accuracy improves as more waves are included.[20] The plane wave cutoff energy determines the maximum kinetic energy allowed for the plane waves that expand the wave function. Essentially, the basis set of plane waves is limited to include only those plane waves whose kinetic energy is less than or equal to this specified cutoff energy, denoted as $e_{cut}$.[21] This parameter directly influences the precision and computational efficiency of the model.

### 3.2.1.2 Pseudopotential

Based on the plane-wave method, a large number of plane waves is necessary to fully describe the rapid oscillation of the wave functions at and near atomic nuclei. In order to reduce the computational cost, pseudopotentials are used to simplify the treatment of the electron-nuclear interactions, particularly for core electrons by replacing the electron density from a chosen set of core electrons with a smoothed density chosen to match various important physical and mathematical properties of the true ion core.[17] Two advanced types of pseudopotentials commonly used in these calculations are Ultrasoft Pseudopotentials (USPPs) and Projector Augmented-Wave (PAW) methods. Each has its specific advantages and applications depending on the complexity of the material being studied. One disadvantage of using USPPs is that the construction of the pseudopotential for each atom requires a number of empirical parameters to be specified. [17] Conversely, PAW method was developed by combining the USPPs method and the LAPW (Linear Augmented Plane Wave) method.[22] This method aims to reconstruct the orbitals of all electrons from the pseudo-orbitals provided by the pseudopotentials, through a linear transformation. In materials with strong magnetic moments or with atoms that have large differences in electronegativity, the PAW approach gives more reliable results than USPPs.[17] Vienna Ab initio Simulation Package (VASP) is a widely utilized code that employs plane waves and the PAW method. It was selected as the computational tool to perform the calculations in this thesis.

### 3.2.2 Utilizing DFT to predict Fermi Contact shift in cathode materials

The application of DFT in predicting chemical shifts within cathode materials for lithium-ion batteries, especially those that are paramagnetic, has proven to be a useful tool. As discussed in 2.5 section, $^{7}$Li NMR shifts for paramagnetic samples are dominated by the Fermi contact term due to the interaction between the nuclear spin and the surrounding unpaired electron spins. This interaction can be analyzed through the local geometries and their propensity for electron spin transfers, which can be based either on delocalization or polarization mechanism. However, when the M-O-Li angle deviates from the ideal 90° or 180°, identifying the contributions to the shifts can become challenging.[23] DFT proves to be very useful in these situations, offering a deeper understanding of the electronic environments surrounding lithium ions, thereby enabling the identification and assignment of lithium sites in these materials.

The study published by Bitto et al.[24] used DFT calculations to explore the complex phase behavior of β-$LiVOPO_4$ during lithiation processes. The formation of the metastable β-$Li_{1.5}VOPO_4$ phase, which is energetically close to the intermediate between $LiVOPO_4$ and $Li_2VOPO_4$, does not result in a distinct voltage plateau. However, together solid-state NMR experiments and DFT calculations supported the existence and structure of this metastable phase. This was evidenced by specific signatures that appear in the $^7$Li and $^{31}$P NMR spectra.

As discussed in Chapter 2, NMR spectroscopy is sensitive to the local electronic environment of nuclei, making it a powerful tool for studying the structure of disordered materials. DFT plays a role in this context by modeling these systems to predict the most stable or probable structures and computing the expected chemical shifts based on these electronic structures. Serrano-Sevillano et al.[25] used DFT in combination with NMR and XRD to investigate the disorder in $Li_2MnO_3$. Samples synthesized at 900 °C predominantly exhibited stacking faults, which led to additional peaks in their NMR spectra. DFT calculations successfully replicated the peak assignments for both the ideal structure and those with stacking faults. While ideal $Li_2MnO_3$ exhibits three $^6$Li NMR signals, stacking faults generate a high number of overlapped signals (**Figure 3.2a)**. As a consequence, a displacement to higher shifts of the signals of Li2b and Li2c is observed, while the average position for the signal of Li4h is maintained constant (**Figure 3.2b**). These examples illustrate the significant contributions of DFT to enhancing NMR analysis.

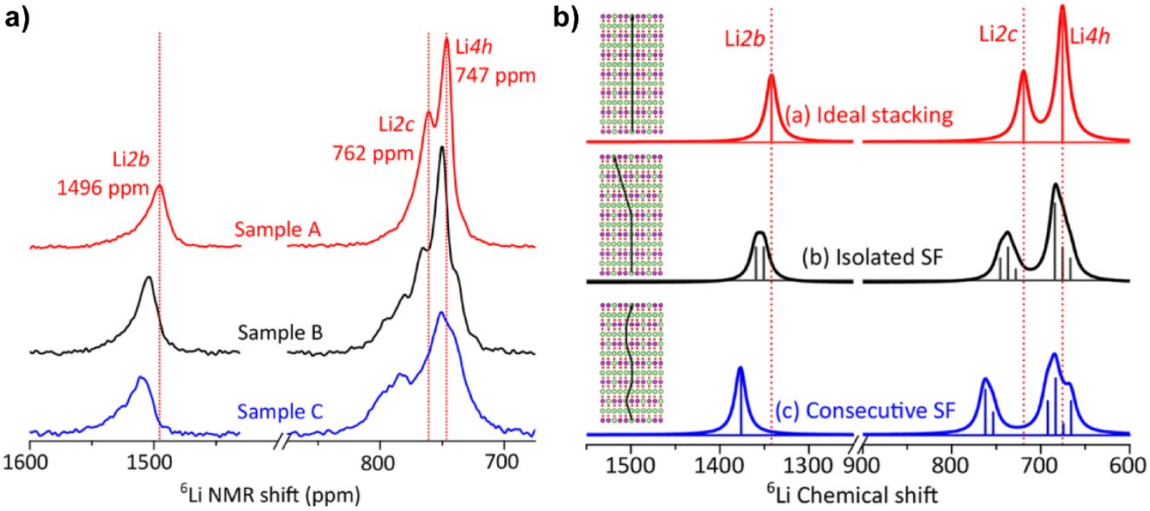

**Figure 3.2** (a) $^6$Li solid-state MAS NMR spectra of samples A−C recorded at 50 kHz.(b) $^6$Li NMR spectra simulation of (red) an ideal, (black) a structure with isolated stacking fault, and (blue) a structure with consecutive stacking faults. The dashed red lines show the position of the simulated ideal peaks for Li2b, Li2c, and Li4h. Reprinted from [25].

## 3.3 Summary

This chapter provides an overview of diffraction and theoretical methods used in this thesis together with ssNMR to analyze the structural proprieties of $Li_{1.x}FeV_2O_7$ samples. Combining experimental techniques with Density Functional Theory (DFT) calculations offers a robust approach to understanding the structural properties of materials. This integrated method provides a comprehensive view of what happens within a sample, allowing for a deeper insight into its behavior at the atomic level. DFT was particularly useful in interpreting NMR data, as it helped correlate observed chemical shifts with electronic structures and molecular environments. By correlating experimental data with theoretical predictions from DFT, we could validate models and hypotheses with more accuracy. This combination is evident in Chapters 4 and 6.

## 3.4 References

(1) Pecharsky, V. K.; Zavalij, P. Y. *Fundamentals of Powder Diffraction and Structural Characterization of Materials*; 2005. https://doi.org/10.1524/9783110364316.121.

(2) Ladd, M. F. C.; Palmer, R. A. *Structure Determination by X-Ray Crystallography*; 2013. https://doi.org/10.1007/978-1-4615-7930-4.

(3) Mobilio, S.; Boscherini, F.; Meneghini, C. Synchrotron Radiation: Basics, Methods and Applications. *Synchrotron Radiat. Basics, Methods Appl.* **2015**, 1–799. https://doi.org/10.1007/978-3-642-55315-8.

(4) CLS - Canadian Light Source. https://www.lightsource.ca/public/what-is-a-synchrotron.php#AboutSynchrotronLight.

(5) Llewellyn, A. V.; Matruglio, A.; Brett, D. J. L.; Jervis, R.; Shearing, P. R. Using In-Situ Laboratory and Synchrotron-Based x-Ray Diffraction for Lithium-Ion Batteries Characterization: A Review on Recent Developments. *Condens. Matter* **2020**, *5* (4), 1–28. https://doi.org/10.3390/condmat5040075.

(6) Ali, A.; Chiang, Y. W.; Santos, R. M. X-Ray Diffraction Techniques for Mineral Characterization: A Review for Engineers of the Fundamentals, Applications, and Research Directions. *Minerals* **2022**, *12* (2). https://doi.org/10.3390/min12020205.

(7) West, A. R. *Solid State Chemistry and Its Applications*; 2003.

(8) Toby, B. H.; Von Dreele, R. B. GSAS-II: The Genesis of a Modern Open-Source All Purpose Crystallography Software Package. *J. Appl. Crystallogr.* **2013**, *46* (2), 544–549. https://doi.org/10.1107/S0021889813003531.

(9) Rodrı´guez-Carvajal, J. FullProfSuite.

(10) Bruker. DIFFRAC.EVA: software to evaluate X-ray diffraction data.

(11) Dolomanov, O. V.; Bourhis, L. J.; Gildea, R. J.; Howard, J. A. K.; Puschmann, H.

OLEX2: A Complete Structure Solution, Refinement and Analysis Program. *J. Appl. Crystallogr.* **2009**, *42* (2), 339–341. https://doi.org/10.1107/S0021889808042726.

(12) Orikasa, Y.; Maeda, T.; Koyama, Y.; Murayama, H.; Fukuda, K.; Tanida, H.; Arai, H.; Matsubara, E.; Uchimoto, Y.; Ogumi, Z. Direct Observation of a Metastable Crystal Phase of LixFePO 4 under Electrochemical Phase Transition. *J. Am. Chem. Soc.* **2013**, *135* (15), 5497–5500. https://doi.org/10.1021/ja312527x.

(13) Xu, C.; Märker, K.; Lee, J.; Mahadevegowda, A.; Reeves, P. J.; Day, S. J.; Groh, M. F.; Emge, S. P.; Ducati, C.; Layla Mehdi, B.; Tang, C. C.; Grey, C. P.; Mehdi, B. L.; Tang, C. C.; Grey, C. P. Bulk Fatigue Induced by Surface Reconstruction in Layered Ni-Rich Cathodes for Li-Ion Batteries. *Nat. Mater.* **2021**, *20* (1), 84–92. https://doi.org/10.1038/s41563-020-0767-8.

(14) Park, S.; Chotard, J. N.; Carlier, D.; Moog, I.; Duttine, M.; Fauth, F.; Iadecola, A.; Croguennec, L.; Masquelier, C. An Asymmetric Sodium Extraction/Insertion Mechanism for the Fe/V-Mixed NASICON Na4FeV(PO4)3. *Chem. Mater.* **2022**. https://doi.org/10.1021/acs.chemmater.2c00501.

(15) Lin, F.; Liu, Y.; Yu, X.; Cheng, L.; Singer, A.; Shpyrko, O. G.; Xin, H. L.; Tamura, N.; Tian, C.; Weng, T. C.; Yang, X. Q.; Meng, Y. S.; Nordlund, D.; Yang, W.; Doeff, M. M. Synchrotron X-Ray Analytical Techniques for Studying Materials Electrochemistry in Rechargeable Batteries. *Chem. Rev.* **2017**, *117* (21), 13123–13186. https://doi.org/10.1021/acs.chemrev.7b00007.

(16) Hafner, R. Ab-Initio Simulations of Materials Using VASP : Density-Functional Theory and Beyond. **2008**. https://doi.org/10.1002/jcc.21057.

(17) Sholl, D. S. .; Steckel, J. A. *Density Functional Theory - A Practical Introduction*; 2009. https://doi.org/10.1201/9781420045451.

(18) Hohenberg, P.; Kohn, W. Inhomogeneous Electron Gas. *Phys. Rev.* **1964**, *136* (3b), B 864-871.

(19) Perdew, J. P.; Burke, K.; Ernzerhof, M. Generalized Gradient Approximation Made Simple. *Phys. Rev. Lett.* **1996**, *77* (18), 3865–3868. https://doi.org/10.1103/PhysRevLett.77.3865.

(20) Nagy, B.; Jensen, F. *Basis Sets in Quantum Chemistry*; 2017; Vol. 30. https://doi.org/10.1002/9781119356059.ch3.

(21) Giustino, F. *Materials Mondelling Ysing Density Functional Therory*; 2014.

(22) Blöchl, P. E. Projector Augmented-Wave Method. *Phys. Rev. B* **1994**, *50* (24), 17953–17979. https://doi.org/10.1103/PhysRevB.50.17953.

(23) Carlier, D.; Ménétrier, M.; Delmas, C.; Grey, C. P.; Ceder, G. Understanding the NMR Shifts in Paramagnetic Transition Metal Oxides Using Density Functional Theory Calculations. *Phys. Rev. B - Condens. Matter Mater. Phys.* **2003**, *67* (17), 174103. https://doi.org/10.1103/PhysRevB.67.174103.

(24) Britto, S.; Seymour, I. D.; Halat, D. M.; Hidalgo, M. F. V.; Siu, C.; Reeves, P. J.; Zhou, H.; Chernova, N. A.; Whittingham, M. S.; Grey, C. P. Evolution of Lithium Ordering with (de)-Lithiation in β-LiVOPO4: Insights through Solid-State NMR and First Principles DFT Calculations. *J. Mater. Chem. A* **2020**, *8* (11), 5546–5557. https://doi.org/10.1039/d0ta00121j.

(25) Serrano-Sevillano, J.; Carlier, D.; Saracibar, A.; Lopez Del Amo, J. M.; Casas-Cabanas, M. DFT-Assisted Solid-State NMR Characterization of Defects in Li2MnO3. *Inorg. Chem.* **2019**, *58* (13), 8347–8356. https://doi.org/10.1021/acs.inorgchem.9b00394.

# Chapter 4: Exploring the Characterization of $LiFeV_2O_7$: Insight from Experimental and VASP Calculations.

## 4.1 Introduction

The development and optimization of cathode materials for lithium-ion batteries represent a critical field of research in the search for advanced energy storage solutions. Their performance is intricately related to their chemical structure which may contain crystallographic defects, such as vacancies, antisites, and dislocations, consequently producing disordered systems.[1,2] In various functional materials, structural and compositional defects are unavoidable, especially when considering large-scale production. With advances in characterization techniques, these irregularities have been identified and their effect on physical and chemical properties have been understood. An example of this is the olivine $LiFePO_4$ (LFP) cathode (theoretical capacity of 170 mAh/g), which is known for its stability, safety, and long cycle life in lithium-ion batteries. Antisite defects in $LiFePO_4$ result in a reduced $Li^+$ diffusion rate, causing a negative effect on the electrochemical performance. [1,3] However, in some cases, the defects contribute positively to the electrochemical performance of batteries. Wang et al [4] showed that introducing a considerable number of twin boundary defects into the lattice of spinel lithium manganate oxide ($LiMn_2O_4$) lowers the barrier of the lithium diffusion process, consequently improving the lithium-ion diffusion rate.

Different types of defects impact the electrochemical performance of electrode materials to greater or lesser extents, depending on their impact on the framework structure including its stability and the exchangeability of lithium ions in the vicinity of the defects. Detecting and understanding these defects in potential cathode structures is crucial for optimizing the performance.

This chapter presents a detailed study of $LiFeV_2O_7$ structure. The material was first synthesized by Benabed et al.[5] and three crystallographically unique $Li^+$ sites were described. The first technique employed to examine the structural dynamics of lithium was $^7$Li NMR. Unexpectedly, the $^7$Li MAS spectrum reveals a multiplicity of peaks beyond the three expected. This prompted a further investigation which involved multiple syntheses, powder and single-crystal XRD analyses, and DFT calculations. The findings of these studies are detailed throughout this chapter.

The work presented in this chapter was published as a part of two separate manuscripts. The Structural Complexity and Evolving Lithium-Ion Dynamics within the Cathode Material $LiFeV_2O_7$ Revealed by Diffraction and Solid-State NMR was published in the Chemistry of Materials (2022, 34, 8551-8560) with authors T.L.E. Pereira, K.J. Sanders, D.L. Smiley, J.F. Britten, and G.R. Goward. The second manuscript was published in Faraday Discissions with the title A Combined $^7$Li NMR, Density Functional Theory and Operando Synchrotron X-Ray Powder Diffraction to Investigate a Structural Evolution of $LiFeV_2O_7$ as a Potential Lithium Cathode Material with authors T.L.E. Pereira, J. Serano-Sevillano, B.D. Moreno, J.W. Reid, D. Carlier and G.R. Goward (2024, DOI: 10.1039/D4FD00077C). The NMR spectroscopy and data analysis was completed at McMaster University under the supervision of Prof. Gillian Goward. The powder XRD and the single-crystal refinement were also completed at the MAX facility at McMaster University under the supervision of Dr. Jim

Britten. The DFT calculations were performed at The Mésocentre de Calcul Intensif Aquitain (MCIA) under the supervision of Prof. Dany Calier.

## 4.2 Methods

### 4.2.1 Solid-State Synthesis of $LiFeV_2O_7$

The $LiFeV_2O_7$ material was prepared by solid-state reaction in air. Stoichiometric amounts of $Li_2CO_3$ (99% pure Sigma-Aldrich), $Fe_2O_3$ (99% pure Sigma-Aldrich), and $V_2O_5$ (99% pure Sigma-Aldrich) were dried at 70 °C for 24h and then manually ground together in an agate mortar. The mixture was placed into a platinum boat and heated to 580 °C with a 5 °C/min rate which was held at this temperature for 150h and then cooled at the same heating rate to room temperature. During the reaction, no visible loss was observed on the inner surface of the quartz tubes used in the furnace. The reaction is as follows:

$$\frac{1}{2}Li_2CO_3 + \frac{1}{2}\,Fe_2O_3 + V_2O_5 \rightleftharpoons LiFeV_2O_7 + \frac{1}{2}CO_2$$

### 4.2.2 Single-Crystal X-Ray Diffraction

A single crystal of $LiFeV_2O_7$ was obtained from the powder sample and analyzed using Bruker Mo Smart APEX2 (λ= 0.71069 Å). The crystal temperature was 296 K while data were collected. The structure was determined by XT[6] and refined using XL[7] package within OLEX2[8] software.

### 4.2.3 X-Ray Powder Diffraction

The powder XRD measurements were collected using the Bruker D8 Discover with Davinci.design diffractometer, equipped with Cobalt Sealed Tube Source ($\lambda_{avg}$= 1.79026 Å) and power settings at 35kV, 45mA. Samples were analyzed at room temperature from 10° to 70° (2θ).

### 4.2.4 $^7$Li MAS NMR

$^7$Li MAS NMR experiments were acquired using a Bruker Avance III HD spectrometer operating at a Larmor frequency of 116.64 MHz (7.05 T) using a Bruker 1.3 mm HX probe at a spinning frequency of 60 kHz. The spectra are referenced to 1M $LiCl_{(aq)}$ at 0 ppm. One-dimensional $^7$Li MAS spectra were obtained using a double spin echo pulse sequence utilizing short, high-power adiabatic pulses (SHAPs)[9] following a 1.25 µs $\frac{\pi}{2}$ excitation pulse. The SHAPs utilized a tanh/tan shape, a 5 MHz frequency sweep, and were 50 microseconds in length with a maximum RF field strength of 200 kHz. Under these conditions, the SHAPs are expected to be >99% efficient.[10] $T_1$ relaxation times were determined using a standard inversion-recovery sequence.

### 4.2.5 VASP Calculations

First principles calculations were performed within the density functional theory (DFT). Vienna Ab-initio simulation package (VASP) was chosen to run the calculation utilizing projector augmented wave (PAW) with pseudopotentials.[11,12] It used the standard PAW− Perdew-Burke-Ernzerhof (PBE) potentials for Fe, V, and O and the "sv" PAW−PBE potential for Li that treats the 1s shell as valence states. For Li Fermi contact shift the sv PAW-PBE potential has been shown to yield more accurate results.[13]

A plane wave energy cut-off of 750 eV and a K-point grid of 2x4x2 were used for all $LiFeV_2O_7$ structures. The experimental crystal structure was used as the input model[5,14], and the calculations were spin-polarized type with imposed ferromagnetic ordering which is considered appropriate for the Fermi contact interaction.[15] The energy minimization and electron density for each atom were calculated using two different approaches: the generalized gradient approximation (GGA) and GGA+U method. The GGA+U method incorporates a Hubbard-type interaction to localize d electrons. In this work, U values of 3.5, 4.3 and 5.3 eV for Fe and 3.25 eV for V (lithiated structure only) were examined as part of the testing process.

The isotropic shifts were calculated using Equation 4.1 and a temperature of 320 K to account for the typical heating of the rotor during spinning at 60 KHz.

$$\delta_{iso}(T) = \frac{\chi_M(\mathrm{T})}{3SN_A} \cdot \frac{A_{iso} \cdot S_{tot}}{\gamma_N} \qquad \text{Equation 4.1}$$

Where $S_{tot}$ is twice the spin quantum number of the paramagnetic ions in the considered unit cell (i.e., the number of unpaired electrons), S is theoretical spin per $LiFeP_2O_7$ mole, $\chi_M$ is the molar magnetic susceptibility for $LiFeP_2O_7$ formula unit, $N_A$ is Avogadro's number, and $\gamma_N$ is the gyromagnetic ratio for the measured nucleus. $A_{iso}$ is the hyperfine coupling constant, which is calculated using VASP program.

As the magnetic measurements for this material are not available, it was considered for $^7Li$ Fermi contact shifts calculations, the molar magnetic susceptibility $LiFeP_2O_7$[16], which also contains $Fe^{3+}$ ions in a rather similar lattice. 3D calculated spin density maps were plotted using VESTA software (visualization for electronic and structural analysis).[17]

## 4.3 Results and Discussion

### 4.3.1 $^7$Li Solid-State NMR of Pristine $LiFeV_2O_7$

Since the structural properties of $LiFeV_2O_7$ had been previously reported[5], it was expected that the $^7$Li NMR spectrum would include three signals, which could be assigned to the three crystallographically unique $Li^+$ positions. However, as **Figure 4.1** shows the $^7$Li MAS spectrum reveals a multiplicity of peaks beyond the three expected. This prompted further investigation, beginning with deconvolution that showed each peak split into two in relatively comparable intensity ratios. In total, the spectrum presents at least seven signals with shifts of 291, 223, 218, 151, 146, 116, and 107 ppm, revealing more subtle details than available from the original single crystal.[5] Deconvolution of the signals enables the determination of relative site occupancies revealing the relationship among sites. The relative intensities of the $^7$Li NMR signals at 107 and 116 ppm are in the ratio of 24%:76% as seen in **Table 1.** The same analysis can be observed for the pair signals 146 and 151, and 218 and 223. It was hypothesized that these extra signals could be related to the presence of a new phase or a disorder in the system.

To confirm the persistence of this behavior, several syntheses were conducted, and their corresponding $^7$Li NMR analyses were evaluated. **Figure 4.2** shows the $^7$Li MAS spectrum of five syntheses. The synthesis of $LiFeV_2O_7$ was initially carried out without controlling the cool-down temperature, resulting in a failure to obtain the desired product (1SLFVO spectrum). Signals observed around 0 ppm were attributed to diamagnetic species which is assigned as $Li_2CO_3$, the started material. Subsequent attempts, where the cool-down temperature was controlled, consistently resulted in a successful product. In **Figure 4.2**, the spectra exhibit a similar behavior, characterized by the presence of the same number of main peaks across the different samples. Additionally, the chemical shift values show consistency. This consistent behavior indicates a reproducible local environment for the lithium ions within the $LiFeV_2O_7$ structure, thereby demonstrating that this characteristic is part of the material's framework.

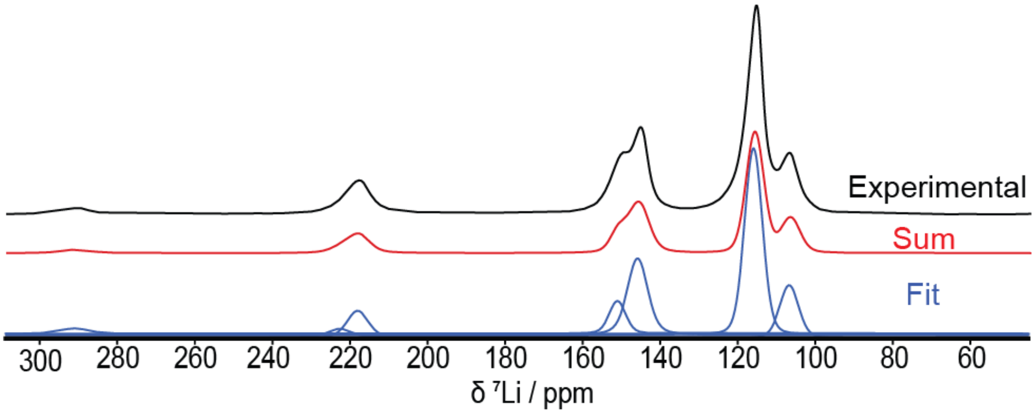

**Figure 4.1:** $^7$Li MAS ssNMR spectrum of pristine $LiFeV_2O_7$. The spectrum was deconvoluted into 7 unique resonances.

**Table 4.1.** Details of the deconvolution of $^7$Li NMR spectrum for pristine $LiFeV_2O_7$ carried out in the ssNake software using Gaussian/Lorentzian line shapes with a ratio of 3.4.

| Signal | Integral | Relative proportion | FWHM (Hz) |
|---|---|---|---|
| 107 | 1.0E+11 | 24% | 170 |
| 116 | 3.1E+11 | 76% | 100 |
| 146 | 1.6E+11 | 76% | 250 |
| 151 | 5.2E+10 | 24% | 130 |
| 218 | 6.3E+10 | 76% | 320 |

| | | | |
|---|---|---|---|
| 223 | 2.0E+10 | 24% | 350 |
| 291 | 1.9E+10 | - | 700 |

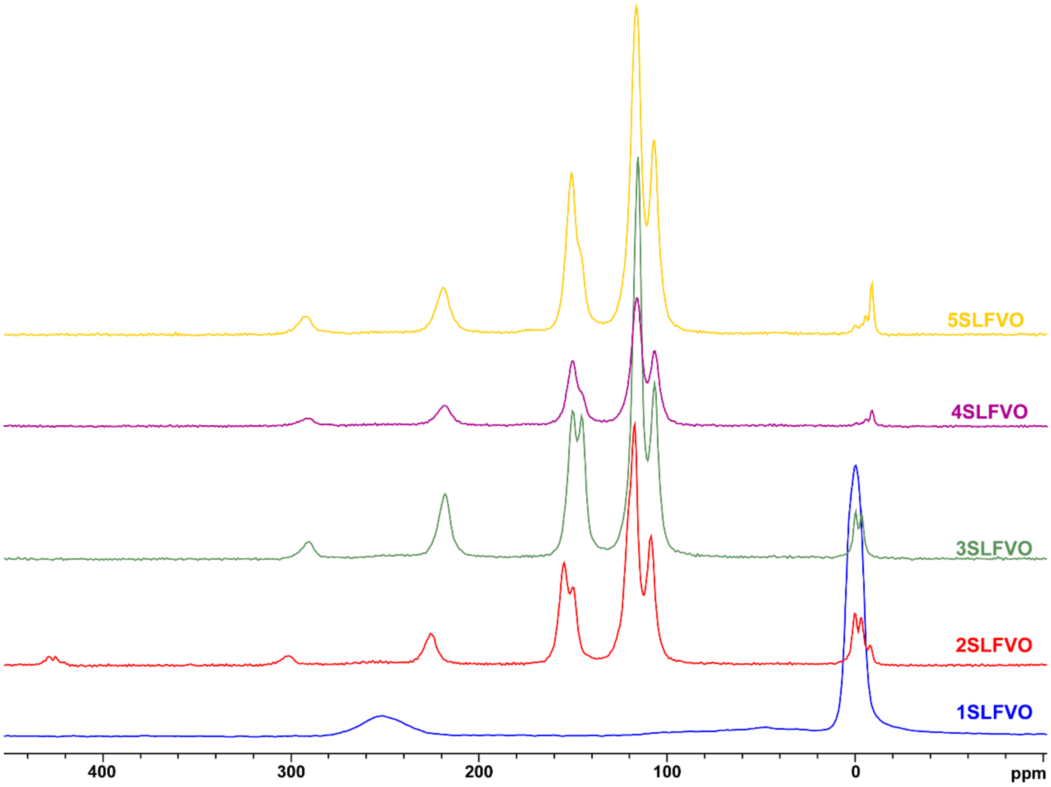

**Figure 4.2:** A series of $^7$Li MAS ssNMR spectrum of various samples of $LiFeV_2O_7$, indicated by the different colored lines.

It is important to note that the $^7$Li NMR spectrum was acquired on a bulk sample, synthesized by powder solid-state chemistry methods, rather than from a flux, as was the case for the original crystal structure. Considering the possible assignment of the signals in the $^7$Li NMR spectrum, initially, it was proposed that the crystallographic sites Li1 and Li3 were expected to appear at similar chemical shifts and are therefore encompassed by the highest intensity peak at 116 ppm. The Li2 site was predicted to give rise to the peak at 146 ppm based on the relative peak area ratio (2:1). However, more information is needed to give a better conclusion about lithium environment, and why it results in more signals that are expected in the $^{7}Li$ spectrum. The pristine structure was explored based on new single-crystal X-ray diffraction data and DFT calculations.

### 4.3.2 Single-Crystal X-ray Diffraction

The previous diffraction dataset of $LiFeV_2O_7$ was determined by X-ray diffraction from a single crystal that was grown using the $LiVO_3$ flux technique.[5,18] The iron vanadate structure crystallizes in the monoclinic Cc space group (non-centrosymmetric) and consists of extended V-O chains that create layers between which Li and Fe-O units alternate. The lattice parameters are a = 13.4630(2) Å, b = 8.18820(10) Å, c = 14.3860(2) Å, and β = 95.5469(10) Å. The structure contains six V sites, 21 O sites, and three different Li and Fe sites, taking a total of 33 independent positions. Fe is displayed as an octahedral $FeO_6$ surrounded by five $VO_4$ tetrahedra. Fe2 shares the last corner with a $VO_5$ trigonal bipyramid while corner-sharing Fe1 and Fe3 share two adjacent edges with the $VO_5$ trigonal bipyramid.

Based on the $^{7}Li$ NMR results, it was determined that there must be structural differences between the sample obtained from melt synthesis and that obtained from solid-state powder synthesis. Therefore, a single crystal was selected from the solid-state reaction (through a microscope) and carried out a new single-crystal data acquisition and subsequent structural refinement. The aim was to identify whether different synthesis processes could produce different crystal structures. The structure crystallizes in the monoclinic Cc space group with the following lattice parameters: a = 13.469(6) Å, b = 8.192(4) Å, c = 14.390(7) Å, β = 96.600(9) Å and volume =

1577.2(13). Details of the data collection procedure and structural refinement results are listed in **Table 4.2**.

The single crystal refinement was found to be very close to the original. However, it was possible to detect a local structural disordering in which V2, V6 and O8 sites split into two positions with occupancy around 85% (called ORG position, which is the one reported previously) and 15% (the new position, V2A, V6A and O8A). The vanadate columns as shown in **Figure 4.3b** remain continuous, with a local reassignment of vanadium coordination environment. For the disordered structure, hereafter referred to as LFVOD, O8A moves closer to V6A resulting in a new arrangement that turns V6A to trigonal bipyramidal and V2A to tetrahedral. An illustration of this structural change is depicted in **Figure 4.3c**, with the bond length for V6 and V2 polyhedrons in both configurations outlined in **Table 4.3**. This result is in agreement with the deconvolution data shown above. The ratio occupancy is not exactly the same value, but it supports the idea that the duplicity of the $^{7}$Li NMR signal arises from the presence of structural disorder at the particular vanadium/oxygen coordination environments revealed by this new single-crystal diffraction study. The powder x-ray diffraction data acquired on bulk sample, was not sensitive to this change in the unit cell (as shown in **Figure 4.4**). The small percentage of atomic rearrangement should have a small effect on the intensities of the lines, but likely not noticeable relative to the normal intensity errors in the powder diffraction experiment. Single crystal analysis is much more sensitive to minor variations in electron density.

**Table 4.2.** Crystal data and structure refinement for $LiFeV_2O_7$

| | |
|---|---|
| Identification code | $LiFeV_2O_7$ |
| Empirical Formula | $LiFeV_2O_7$ |
| Formula weight | 276.67 |
| Temperature/K | 296.15 |
| Crystal system | Monoclinic |
| Space Group | Cc |
| a/Å | 13.469(6) |
| b/Å | 8.192(4) |
| c/Å | 14.390(7) |
| α/° | 90 |
| β/° | 96.600(9) |
| γ/° | 90 |
| Volume/ $Å^3$ | 1577.2(13) |
| Z | 12 |
| $\rho_{calc}$g/$cm^3$ | 3.495 |
| μ/$mm^{-1}$ | 6.178 |
| F(000) | 1572.0 |
| Crystal size/$mm^3$ | 0.3 x 0.2 x 0.2 |
| Radiation | MoKα (λ = 0.71073) |
| 2θ range for data collections/° | 5.7 to 61.258 |
| Index ranges | $-19 \leq h \leq 19$, $-11 \leq k \leq 11$, $-20 \leq l \leq 20$ |
| Reflections collected | 24292 |
| Independent reflections | 4827 [$R_{int} = 0.0724$, $R_{sigma} = 0.0720$] |
| Data/restraints/parameters | 4827/410/309 |
| Goodness-of-fit on $F^2$ | 1.046 |
| Final R indexes [$I>2\sigma(I)$] | $R_1 = 0.0387$, $wR_2 = 0.0839$ |
| Final R indexes [all data] | $R_1 = 0.0551$, $wR_2 = 0.0896$ |

| | |
|---|---|
| Largest diff. peak/hole (e Å$^{-3}$) | 0.69/-061 |
| Flack parameter | 0.43(5) |

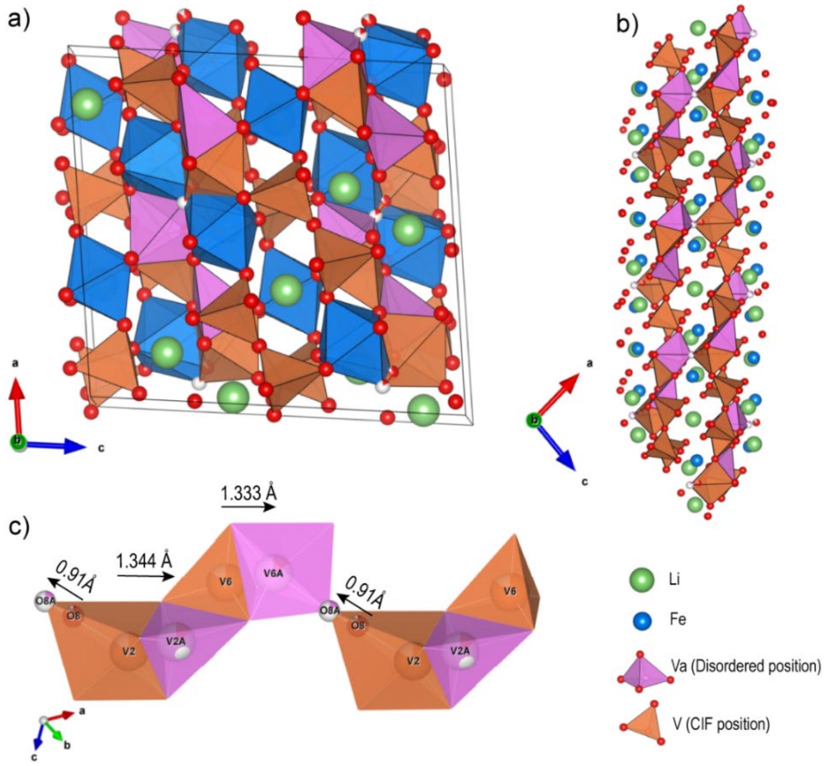

**Figure 4.3:** (a) Representation of unit cell for the new single-crystal refinement from the [010] direction. (b) vanadium polyhedral arrangements from the [010] direction with two options of vanadium position and (c) the vanadium polyhedral disordered model.

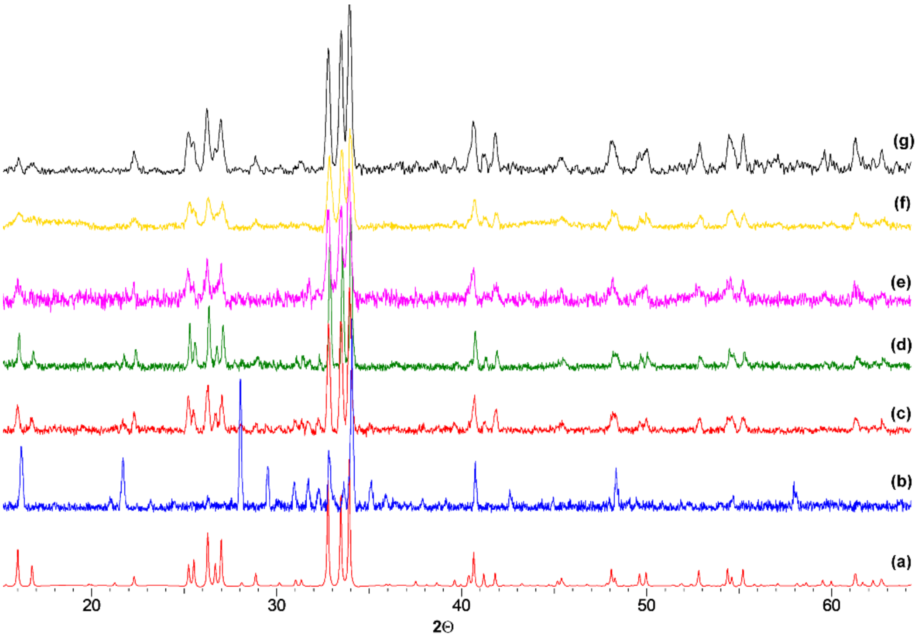

**Figure 4.4.** X-ray powder diffraction patterns of $LiFeV_2O_7$ across different syntheses. (a) CIF; (b) 1SLFVO; (c) 2SLFVO; (d) 3SLFVO; (e) 4SLFVO; (f) 5SLFVO; (g) $LiFeV_2O_7$ used in this thesis.

**Table 4.3.** Summary of V2 and V6 bond length data in two structural configurations.

| ORG position | | Disordered position (LFVOD) | |
|---|---|---|---|
| Bond | Distance (Å) | Bond | Distance (Å) |
| V6-O13 | 1.827(3) | V6A-O8A | 1.990(5) |
| V6-O4 | 1.733(3) | V6A-O4 | 1.844(1) |
| V6-O5 | 1.668(0) | V6A-O5 | 1.705(1) |
| V6-O14 | 1.646(0) | V6A-O14 | 1.772(1) |
| V2-O8 | 1.921(0) | V6A-O19 | 2.221(1) |
| V2-O9 | 2.055(3) | V2A-O5 | 2.125(1) |
| V2-O13 | 1.899(3) | V2A-O13 | 1.649(1) |
| V2-O18 | 1.708(3) | V2A-O18 | 1.720(1) |
| V2-O10 | 1.615(0) | V2A-O10 | 1.662(1) |

### 4.3.3 VASP Calculations

The presence of two possible local environments for a fraction of 85 and 15% of the vanadium centers can be the reason for the set of signals in the $^7$Li NMR spectrum of the pristine phase. However, more information was needed to give an assignment of the distinct chemical shifts observed in the experimental data, and how they correspond to the local lithium environments. DFT calculations are shown here to be a good approach to providing $^{7}$Li NMR chemical shift assignments.

The first step of the calculations, in order to obtain the value of the hyperfine coupling constant, is to optimize the structure of interest. The initial atomic positions were imported from experimental single-crystal diffraction data, then the structures were optimized using VASP code to yield the most stable atomic arrangement. The models were created using three distinct initial positions (**Figure 4.5**): (i) ORG position [5]; (ii) LFVOD position that is related to the disorder position obtained from the new single-crystal analyses reported, and (iii) ORG-D position that combines both positions. For the last one, the position of one asymmetric unit in the ORG structure was changed to a disordered position (LFVOD). This means that the positions of V2, V6, and O8 were changed to V2A, V6A, and O8A, respectively. The structural models consist of supercells comprising four asymmetric unit cells and a total of 132 atoms each. In the ORG-D structure, only three atoms among the 132 were modified to the disorder position, representing localized disordering.

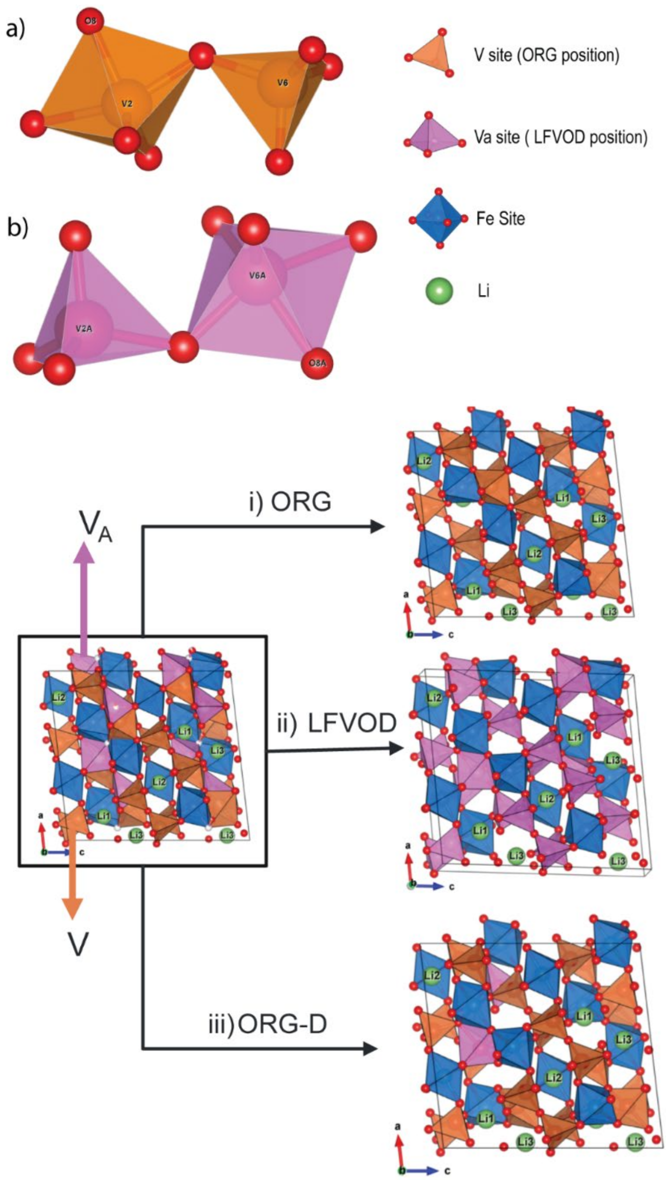

**Figure 4.5.** (a) Vanadium polyhedral original and (b) disordered position. Representation of the unit cell for the single-crystal refinement from the [010] direction: (i) ORG position, (ii) LFVOD position, and (iii)ORG-D position, one asymmetric unit in the ORG structure is changed to a disordered position (LFVOD).

Atomic coordinates and cell parameters were fully relaxed, followed by a calculation of the final energy of the optimized geometry. It is well known that there is a self-interaction error associated with GGA strategy, which is related to insufficient localization of electrons on the d-orbital of transition metal compound. To solve this problem, the generalized gradient approximation with the Hubbard parameter correction (GGA+U) of Dudarev et al[19] was employed. The method applied a unique parameter $U_{eff}$ which is the difference between the traditional U (electro-electron repulsion) and J (exchange interaction). Some values of $U_{eff}$ can be found on the materials project website[20], where they have calibrated $U_{eff}$ values for transition metal oxide systems, for high spin $Fe^{3+}$ is 5.3 eV. However, no $U_{eff}$ values have been optimized for $LiFeV_2O_7$, I therefore considered three values for $U_{eff}$ here and compared structure parameters and the calculated shifts to the experimental ones. **Table 4.4** shows the results of structural optimization by GGA and GGA+U with $U_{eff}$ values of 3.5, 4.3, and 5.3 eV for Fe for all frame models.

All optimized structures showed good agreement with the original reported[5] unit cell. The calculated unit cell parameters exhibited errors of less than 4%. It is worth mentioning that the calculation optimizations were running at 0 K while the experimental results were at room temperature, which can be a source of differences. To a first approximation, the GGA+U approach does not significantly impact the quality of the geometry optimization. However, the difference between the two approaches is evident in the density of states (DOS) plots **(Figure 4.6**). The plotted total DOS illustrates the orbital occupancies, spin state of the metal and estimates the band gap based on the chosen value of $U_{eff}$. The DOS of Fe 3d orbitals is consistent with the expected high-spin $Fe^{3+}$ octahedral configuration, where up spins $e_g$ and $t_{2g}$ states are occupied while the down spins are available. As expected, **Figure 4.6** shows an increase of the band gap with the addition of $U_{eff}$. As mentioned above, with the addition of Hubbard parameter correction ($U_{eff}$) the electron density is more localized at the TM site, Fe, and the difference between the valence and conduction band is increased. These changes directly affect the Fermi contact shift which is sensitive to how much the unpaired electron spin density is transferred from Fe to Li.[13,21,22]

**Table 4.4**: Relaxed cell parameters for the GGA and GGA +U optimized $LiFeV_2O_7$ from ORG, LFVOD, and ORG-D structure unit cell compared to experimental values.

| **Unit cell Parameters** | **a (Å)** | **b (Å)** | **c (Å)** | **Volume (Å $^3$)** |
|---|---|---|---|---|
| **Exp**[5] | 13.463 | 8.1882 | 14.386 | 1575.5 |
| **LFVOD exp**[14] | 13.469 | 8.1924 | 14.390 | 1577.2 |
| **ORG-GGA** | 13.654 | 8.3003 | 14.148 | 1631.4 |
| **ORG- GGA+U**<br>$U_{eff}$= 5.3 eV | 13.697 | 8.2647 | 14.517 | 1632.4 |
| **ORG-GGA+U**<br>$U_{eff}$= 4.3 eV | 13.675 | 8.2529 | 14.497 | 1625.0 |
| **ORG-GGA+U**<br>$U_{eff}$= 3.5 eV | 13.679 | 8.2531 | 14.501 | 1626.2 |
| **LFVOD- GGA** | 13.663 | 8.2393 | 14.454 | 1615.8 |
| **LFVOD – GGA+U**<br>$U_{eff}$= 5.3 eV | 13.656 | 8.2261 | 14.530 | 1620.8 |
| **ORG-D – GGA+U**<br>$U_{eff}$= 5.3 eV | 13.661 | 8.2018 | 14.562 | 1618.9 |

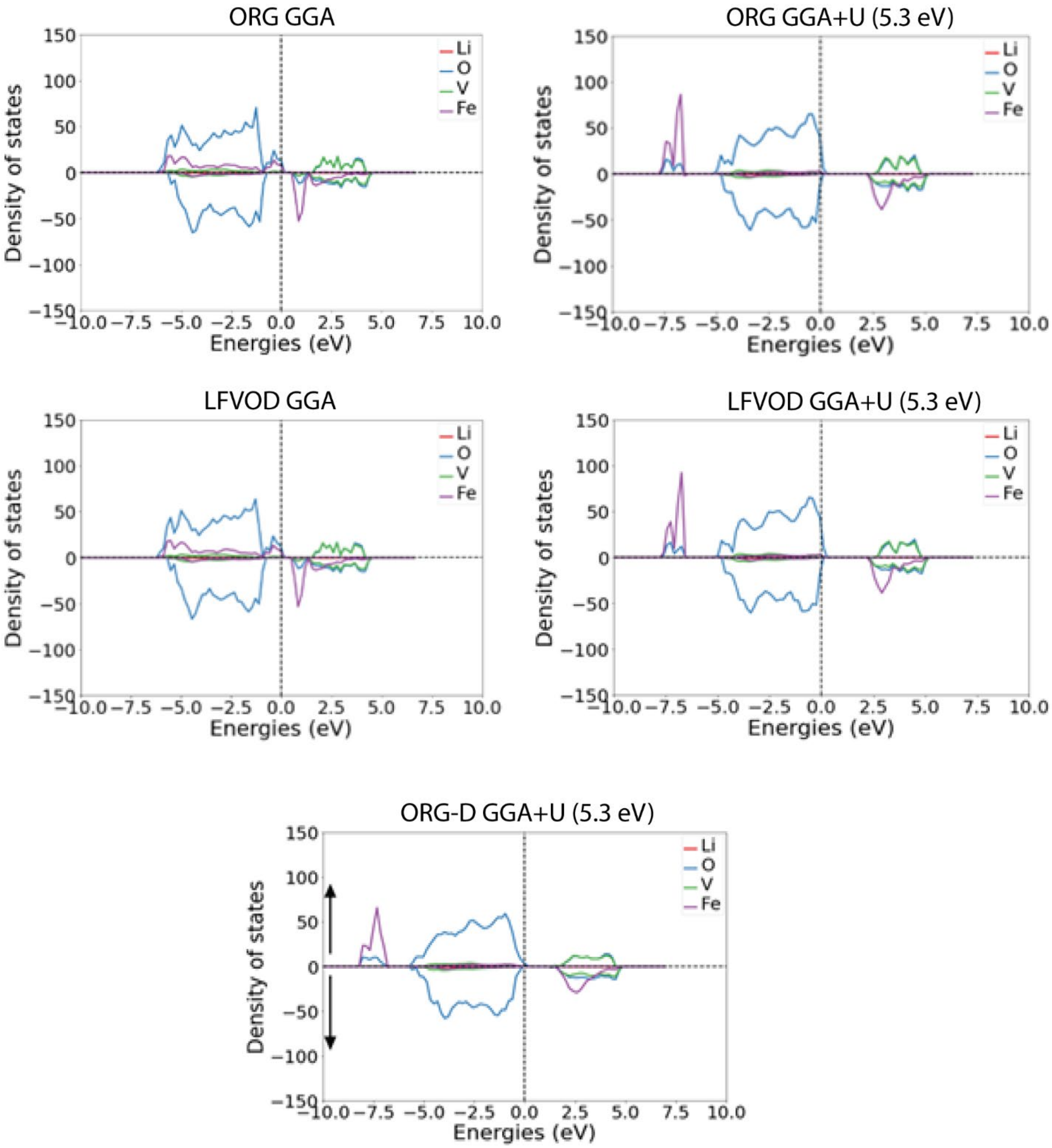

**Figure 4.6.** Calculated total spin DOS for the three models of $LiFeV_2O_7$ (ORG, LFVOD, and ORG-D) with GGA and GGAU where the color coding of lines are elements.

### 4.3.3.1 Fermi contact shift

For paramagnetic samples, the dominant interaction that affects the isotropic shift is the Fermi contact interactions generated by the unpaired electron spin density transferred from the paramagnetic atoms into the observed nucleus. For simple structures, this interaction can be analyzed via local geometries and their capability of electron spin transfer based on two mechanisms, spin delocalization and spin polarization. [15,23,24] However, for complicated structures where there are no ideal 90- and 180-degree interactions, the chemical shift assignments cannot be qualitatively assessed. DFT calculations are employed here as a primary method to explain the origin of extra $^{7}$Li signals in the experimental spectra and assign them to $LiFeV_2O_7$.

According to the experimental data, there is a positive electron spin density transferred to the lithium environments due to the large positive chemical shift observed in the $^{7}$Li NMR spectrum (**Figure 4.1**). The results of calculated $^{7}$Li Fermi contact shifts for ORG and LFVOD structures are compared to the experimental shift values in **Table 4.5**. It is shown that the new position generated by the local disorder generates different values of $^{7}$Li shifts relative to the original structure. This demonstrates that despite being a small variation at the V2, V6, and O8 positions, the Li environments are affected.

In contrast to our observations during structure optimization, there is a notable difference in the calculated Fermi shift when comparing the results from GGA and GGA+U methods. This variation arises due to the influence of electron localization in the GGA+U method, which significantly impacts the predicted magnitude of electron spin density transfer at the Li sites. For ORG structure, the GGA+U approach provides a more accurate Li shift upon addition and increase of the $U_{eff}$ correction term. The increased localization of electron density at Fe minimized the electron spin density transfer to the Li nucleus, which directly affects the Li shift in ssNMR. All values of $U_{eff}$ cause a similar effect to the calculated Li shifts (**Table 4.5**). As the value of $U_{eff}$ is increased, electrons are more localized in the d orbital which decreases the overlap with orbital from oxygen. Consequently, the amount of electron spin density transfer from $Fe^{3+}$ to $Li^+$ sites decreases which results in a smaller paramagnetic shift. Based on the calculations results generated for the ORG structure, the most appropriate Hubbard parameter correction value is 5.3 eV for $Fe^{3+}$. This is applied also to the LFVOD structure. Note however, that will still slightly overestimate the shifts and this may be due to either further need of Ueff optimization or to the fact that I did not consider the magnetic susceptibility of $LiFeV_2O_7$ but approximated it using the value of $LiFeP_2O_7$.

**Table 4.5**: Calculated Fermi contact shifts for Li sites in ORG and LFVOD structures calculated using GGA and GGA+U methods.

| **Atom** | **EXP** | | **Calculated $^7$Li shifts (ppm)** | | | | | |
|---|---|---|---|---|---|---|---|---|
| | | | ORG GGA | ORG GGA+U (5.3 eV) | ORG GGA+U (4.3 eV) | ORG GGA+U (3.5 eV) | LFVOD GGA | LFVOD GGA+U (5.3 eV) |
| **Li1** | 146 | 150.2 | 339.2 | 184.5 | 192.4 | 207.9 | 323.4 | 176.9 |
| **Li2** | 219 | | 454.9 | 276.8 | 300.2 | 323.4 | 338.9 | 284.5 |
| **Li3** | 107.2 | 115.6 | 262.1 | 169.2 | 215.5 | 238.7 | 238.8 | 176.9 |
| **Extra Signal** | 292 | | | | | | | |

Comparing the results obtained for the two modeled structures, there are still fewer resonances calculated than observed in the experimental spectra. The lack of structural disorder in the two distinct ORG and LFVOD structures is consistent with the observed result, namely each structure produces a set of three unique lithium sites in the asymmetric unit which are equivalent throughout the whole unit cell, thus only three different lithium shifts were provided for each set of calculations. However, those separate structures do not represent the real material, but rather what I interpret as two possible structures that co-exist in the experimentally synthesized phase. When the disorder is accounted for, as in the case of ORG-D structure, the lithium sites are no longer equivalent resulting in 12 Li shifts being calculated, shown in **Table 4.6**. The reason for this change may be related to bond length, the angles, and the volume of the polyhedron at the lithium site, which can lead to the shortening or stretching of the distance to the transition metal. The best correlation with experimental $^7$Li NMR spectra was thus obtained with the defect structure, ORG-D. Given the DFT calculations results obtained for ORG-D, the most shifted experimental 292 ppm, may be correlated with the calculated shift $Li2_a$ at 338.7 ppm, explaining the presence of a high shift in the experimental $^7$Li NMR. To improve visualization, all calculated Fermi contact shifts are plotted below with the experimental data in **Figure 4.7**. A detailed explanation of the relevant electron spin transfer pathway will be provided in the following section.

**Table 4.6**: Calculated shifts for Li sites by GGA+U method for the ORG-D structure.

**ORG-D GGA+U** (U= 5.3 eV)

| **CIF site** | Site | Fermi Shift $^7$Li (ppm) |
|---|---|---|
| **Li1** | $Li1_a$ | 192.4 |
| **Li1** | $Li1_b$ | 153.9 |
| **Li1** | $Li1_c$ | 215.5 |
| **Li1** | $Li1_d$ | 177.1 |
| **Li2** | $Li2_a$ | 338.7 |
| **Li2** | $Li2_b$ | 254.0 |
| **Li2** | $Li2_c$ | 292.5 |
| **Li2** | $Li2_d$ | 261.7 |
| **Li3** | $Li3_a$ | 207.8 |
| **Li3** | $Li3_b$ | 184.7 |
| **Li3** | $Li3_c$ | 177.0 |
| **Li3** | Li3d | 192.4 |

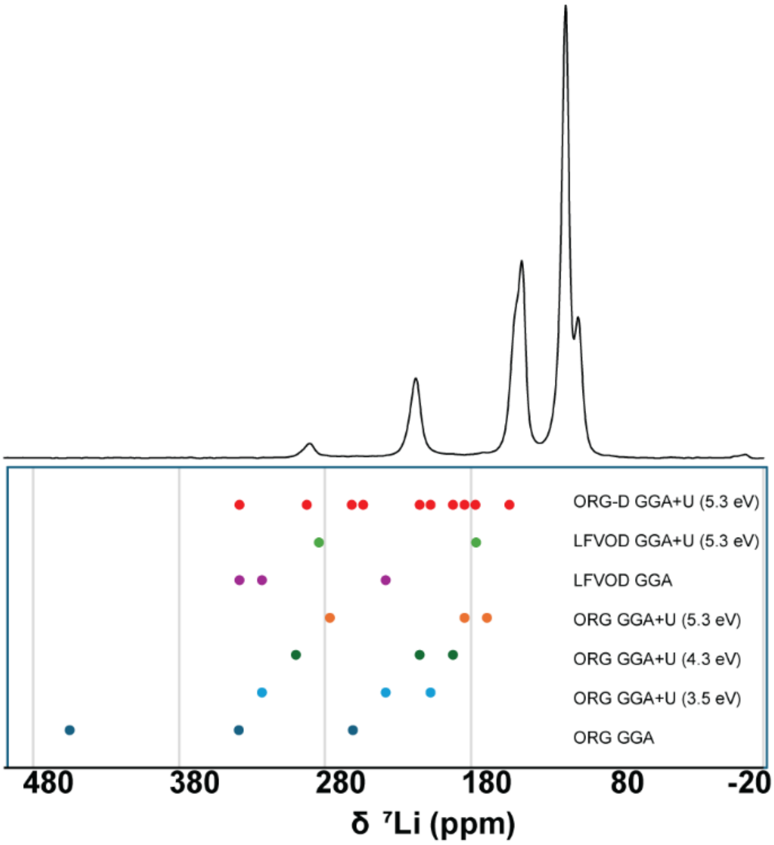

**Figure 4.7.** $^{7}$Li NMR experimental spectra (top) and DFT calculated $^{7}$Li Fermi contact NMR shifts (bottom). The data points are color-coded according to the computational method used.

### 4.3.3.2 Spin Transfer Mechanism

In order to understand the assigned Li signals, spin density maps resulting from the difference between up spin and down spin states, were plotted in three dimensions using the VESTA software (**Figure 4.8**). In these maps, only positive spin density is observed as indicated by the presence of yellow surfaces. Based on the electron spin density transfer mechanism, it proposes an explanation for shift magnitudes of a positive sign of $^{7}$Li observed for $LiFeV_2O_7$ structures. Li2 sites are located in a four-coordinated site surrounded by three $FeO_6$ octahedra where two are sharing a corner and one sharing an edge with $LiO_4$ (**Figure 4.9b**). The unpaired electrons from the three $Fe^{3+}$ are the source of electron spin density transfer to Li sites and the cause of the high paramagnetic shift. In the case of Li1 and Li3, they are located in a six-coordinated site surrounded by two $FeO_6$ octahedra (**Figure 4.9a and Figure 4.9c**). They are expected to appear at a lower paramagnetic shift than Li2 because they only receive contributions from two $Fe^{3+}$.

Two different spin-transfer mechanisms from Fe to Li are present. (i) For the case that $FeO_6$ and $LiO_4$/$LiO_5$ share a corner, a delocalization mechanism occurs through hybridization between Fe $e_g$*, O p, and Li s. The electrons in the Fe $e_g$*orbitals are expected to interact with O p orbitals along the Fe-O-Li pathway through the interaction angle of 180°. In our case, the angles are in the range from 111.69 to 141.72° which differs from 180°, but the transfer is still possible. This mechanism can also be observed for $LiFePO_4$ and $LiNi_2O_4$.[22,25] (ii) In the case of $FeO_6$ and $LiO_4$/$LiO_5$ sharing an edge, the delocalization mechanism occurs through hybridization between Fe $t_{2g}$*, O p, and Li s. The Fe-O-Li angles are in the range from 93.45 to 102.71° which only slightly differs from 90°. As mentioned at the beginning of this section, the polarization mechanism is not present for this intial pristine structure. Based on the results of the ORG-D GGA+U approach, it was possible to assign the experimental $^7$Li NMR spectra as listed in **Table 4.6**.

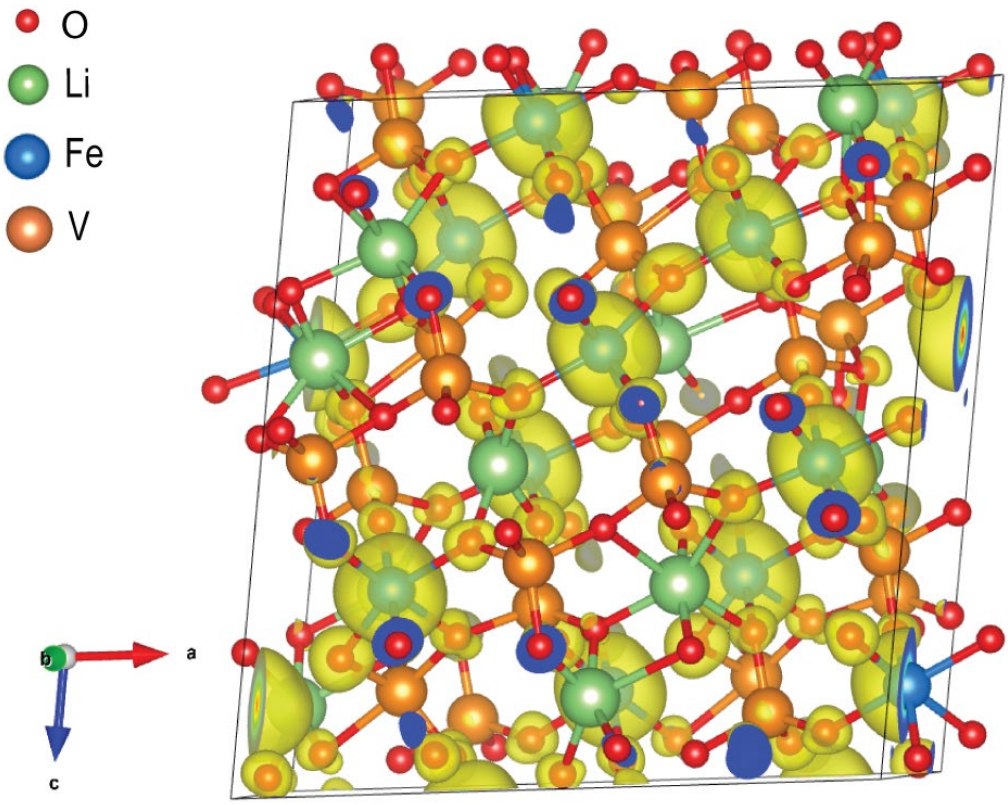

**Figure 4.8.** 3D spin density map calculated for ORG-D with GGA+U and isosurfaces value equal to 0.005 spin/Å$^2$. The positive electron spin densities map is represented in yellow.

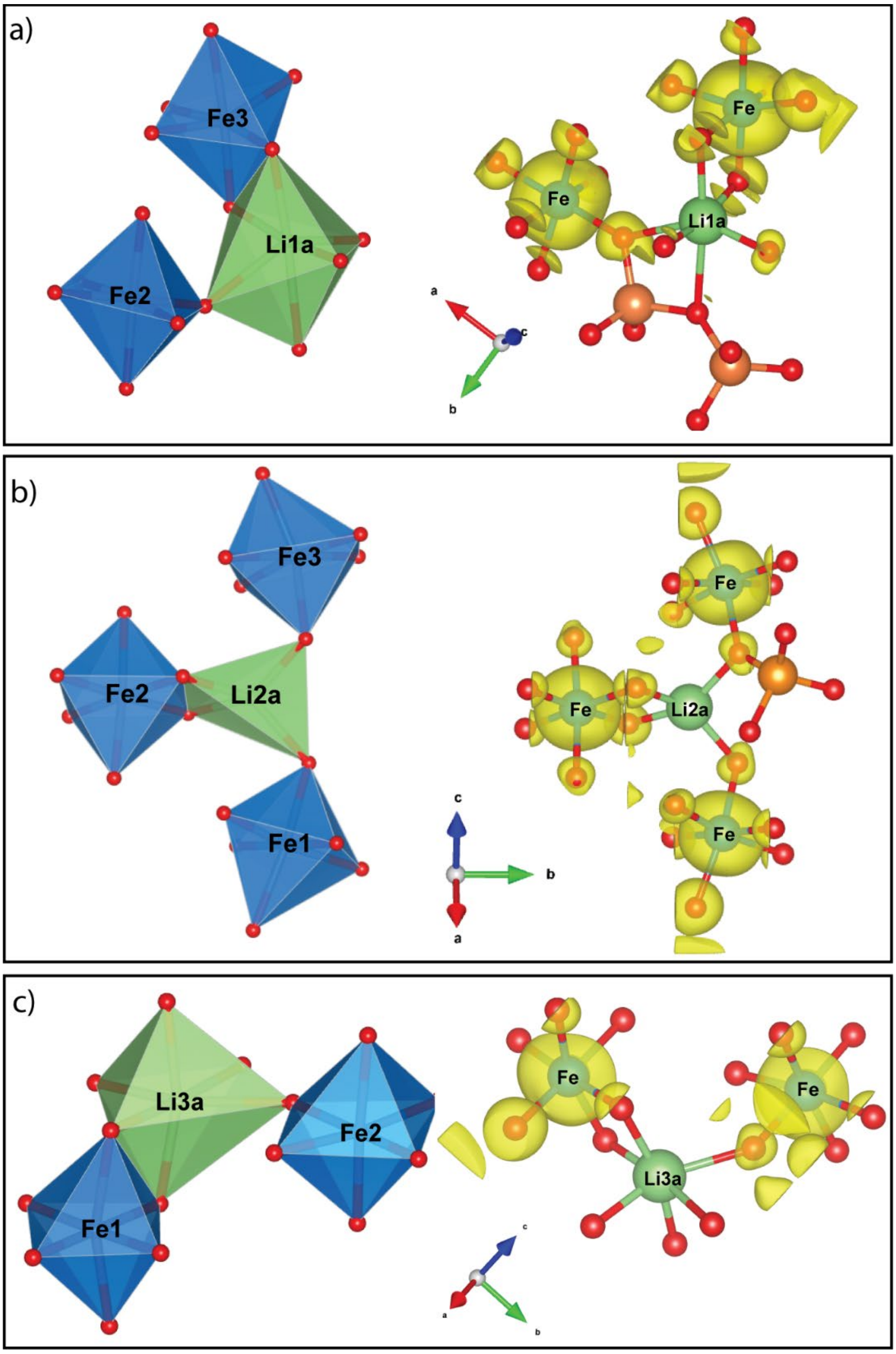

**Figure 4.9.** Environment for the three Li sites of ORG-D showing the local geometry and 3D spin density map calculated with GGA+U ($U_{eff}$= 5.3 eV) with an isosurface value equal to 0.005 spin/Å$^2$. Yellow surfaces indicate positive spin densities. (a) $Li1_a$ (b) $Li2_a$ and (c) $Li3_a$.

For all modeled structures, Li2 was calculated to be the high chemical shift, due to the three $Fe^{3+}$ electron spin density contribution. Conversely, Li1 and Li3, both receive electron spin density transfer from two neighboring $Fe^{3+}$. The distinction in the Fermi contact shifts observed at each lithium site can be attributed to variations in the Fe-Li distance and the Li-O-Fe angle. These geometrical variations directly affect the degree of orbital interaction, consequently adjusting the electron spin transfer magnitude to the lithium sites.

As indicated above, the ORG-D model exhibits the strongest correlation with the experimental $^{7}Li$ NMR spectra. Beyond the number of resonances in the presence of disorder, the experimental shift at 292 ppm closely aligns with the calculated shift for $Li2_a$ at 338.7 ppm. The introduction of disorder, particularly when V2 occupies a disordered position (V2A), brings it nearer to the lithium site ($Li2_a$), and prompts a structural reorganization among surrounding atoms. This adjustment includes a reduction in the Fe2-$Li2_a$ distance from 3.0421 Å in the ORG model to 3.0020 Å in the ORG-D model. Such a decrease enhances the orbital overlap among the Fe $t_{2g}$*, O p, and Li s orbitals, resulting in a pronounced Fermi contact shift. **Tables 4.7, 4.8,** and **4.9** offer information about calculated Li-Fe distances and Li-O-Fe angles for all molded structures.

**Table 4.7.** Calculated Li-Fe distances and Li-O-Fe angle using GGA approach.

| **ORG** | | | **LFVOD** | | |
|---|---|---|---|---|---|
| **Site** | dLi-Fe (Å) | Li-O-Fe angles (°) | Site | dLi-Fe (Å) | Li-O-Fe angles (°) |
| **Li1** | Li1-Fe3 = 3.1199<br>Li1-Fe2 = 4.3147 | Li1-O21-Fe2 = 139.51<br>Li1-O19-Fe3 = 100.72<br>Li1-O03-Fe3 = 92.41 | Li1 | Li1-Fe3 = 3.14778<br>Li1-Fe2 = 3.72287 | Li1-O21-Fe2 = 129.25<br>Li1-O03-Fe3 = 93.80<br>Li1-O19-Fe3 = 101.88 |
| **Li2** | Li2-Fe2 = 3.0527<br>Li2-Fe3 = 3.4602<br>Li2-Fe1 = 3.5226 | Li2-O04-Fe2 = 98.55<br>Li2-O18-Fe2 = 96.47<br>Li2-O20-Fe1 = 118.49<br>Li2-O02-Fe3 = 112.51 | Li2 | Li2-Fe2 = 3.0559<br>Li2-Fe3 = 3.5075<br>Li2-Fe1 = 3.47579 | Li2-O18-Fe2 = 96.88<br>Li2-O4-Fe2 = 98.85<br>Li2-O02-Fe1 = 113.83<br>Li2-O20-Fe3 = 117.45 |
| **Li3** | Li3-Fe1 = 3.18089<br>Li3-Fe2 = 3.73974 | Li3-O15-Fe1 = 102.79<br>Li3-O09-Fe1 = 94.33<br>Li3-O01-Fe2 = 129.53 | Li3 | Li3-Fe1 = 3.15090<br>Li3-Fe2 = 3.14713 | Li3-O09-Fe1 = 99.03<br>Li3-O15-Fe1 = 100.24<br>Li3-O01-Fe2 = 140.21 |

**Table 4.8.** Calculated Li-Fe distances and Li-O-Fe angle using GGA+U (5.3 eV) approach.

| **ORG** | | | **LFVOD** | | |
|---|---|---|---|---|---|
| **Site** | dLi-Fe (Å) | Li-O-Fe angles (°) | Site | dLi-Fe (Å) | Li-O-Fe angles (°) |
| **Li1** | Li1-Fe3 = 3.1389<br>Li1-Fe2 = 4.3273 | Li1-O21-Fe2 = 140.12<br>Li1-O19-Fe3 = 100.70<br>Li1-O03-Fe3 = 100.70 | Li1 | Li1-Fe3 = 3.1716<br>Li1-Fe2 = 3.7070 | Li1-O21-Fe2 = 129.88<br>Li1-O03-Fe3 = 95.75<br>Li1-O19-Fe3 = 101.39 |
| **Li2** | Li2-Fe2 = 3.0421<br>Li2-Fe3 = 3.4569<br>Li2-Fe1 = 3.5458 | Li2-O04-Fe2 = 97.96<br>Li2-O18-Fe2 = 96.80<br>Li2-O20-Fe1 = 118.76<br>Li2-O02-Fe3 = 112.72 | Li2 | Li2-Fe2 = 3.0368<br>Li2-Fe3 = 3.5171<br>Li2-Fe1 = 3.4789 | Li2-O18-Fe2 = 96.97<br>Li2-O04-Fe2 = 98.67<br>Li2-O02-Fe1 = 114.66<br>Li2-O20-Fe3 = 118.13 |
| **Li3** | Li3-Fe1 = 3.1790<br>Li3-Fe2 = 3.7448 | Li3-O15-Fe1 = 102.59<br>Li3-O09-Fe1 = 94.74<br>Li3-O01-Fe2 = 129.57 | Li3 | Li3-Fe1 = 3.1509<br>Li3-Fe2 = 4.2966 | Li3-O09-Fe1 = 98.71<br>Li3-O15-Fe1 = 100.54<br>Li3-O01-Fe2 = 141.77 |

**Table 4.9.** Calculated Li-Fe distances and Li-O-Fe angle for ORG-D using GGA+U (5.3 eV) approach.

| ORG site | ORG-D Site | dLi-Fe (Å) | Li-O-Fe angles (°) |
|---|---|---|---|
| **Li1** | Li1$_{a}$ | Li1$_{a}$-Fe3 = 3.1722<br>Li1$_{a}$-Fe2 = 4.2526 | Li1$_{a}$-O19-Fe3 = 102.71<br>Li1$_{a}$-O21-Fe2 = 138.94<br>Li1$_{a}$-O03-Fe3 = 97.30 |
| **Li1** | Li1$_{b}$ | Li1$_{b}$-Fe3 = 3.2005<br>Li1$_{b}$-Fe2 = 4.2014 | Li1$_{b}$-O03-Fe3 = 99.96<br>Li1$_{b}$-O19-Fe3 = 100.51<br>Li1$_{b}$-O21-Fe2 = 140.56 |
| **Li1** | Li1$_{c}$ | Li1$_{c}$-Fe3 = 3.1379<br>Li1$_{c}$-Fe2 = 4.2804 | Li1$_{c}$-O19-Fe3 = 100.68<br>Li1$_{c}$-O03-Fe3 = 98.64<br>Li1$_{c}$-O21-Fe2 = 141.72 |
| **Li1** | Li1$_{d}$ | Li1$_{d}$-Fe3 = 3.1527<br>Li1$_{d}$-Fe2 = 4.1537 | Li1$_{d}$-O03-Fe3 = 97.25<br>Li1$_{d}$-O19-Fe3 = 101.91<br>Li1$_{d}$-O21-Fe2 = 138.20 |
| **Li2** | Li2$_{a}$ | Li2$_{a}$-Fe2 = 3.0020<br>Li2$_{a}$-Fe3 = 3.4707<br>Li2$_{a}$-Fe1 = 3.4946 | Li2$_{a}$-O02-Fe3 = 114.11<br>Li2$_{a}$-O20-Fe1 = 117.48<br>Li2$_{a}$-O04-Fe2 = 98.04<br>Li2$_{a}$-O18-Fe2 = 96.55 |
| **Li2** | Li2$_{b}$ | Li2$_{b}$-Fe2 = 2.9785<br>Li2$_{b}$-Fe3 = 3.4663<br>Li2$_{b}$-Fe1 = 3.5999 | Li2$_{b}$-O04-Fe2 = 98.04<br>Li2$_{b}$-O18-Fe2 = 96.20<br>Li2$_{b}$-O02-Fe3 = 112.90<br>Li2$_{b}$-O29-Fe1 = 118.13 |
| **Li2** | Li2$_{c}$ | Li2$_{c}$-Fe2 = 3.0699<br>Li2$_{c}$-Fe3 = 3.3429<br>Li2$_{c}$-Fe1 = 3.6970 | Li2$_{c}$-O02-Fe3 = 111.69<br>Li2$_{c}$-O20-Fe1 = 117.57<br>Li2$_{c}$-O18-Fe2 = 97.07<br>Li2$_{c}$-O04-Fe2 = 102.29 |
| **Li2** | Li2$_{d}$ | Li2$_{d}$-Fe2 = 3.0631<br>Li2$_{d}$-Fe3 = 3.5162<br>Li2$_{d}$-Fe1= 3.5750 | Li2$_{d}$-O18-Fe2 = 98.09<br>Li2$_{d}$-O04-Fe2 = 99.01<br>Li2$_{d}$-O02-Fe3 = 112.63<br>Li2$_{d}$-O20-Fe1 = 118.52 |
| **Li3** | Li3$_{a}$ | Li3$_{a}$-Fe1 = 3.1700<br>Li3$_{a}$-Fe2 = 3.8507 | Li3$_{a}$-O01-Fe2 = 132.47<br>Li3$_{a}$-O15-Fe1 = 102.32<br>Li3$_{a}$-O09-Fe1 = 97.81 |
| **Li3** | Li3$_{b}$ | Li3$_{b}$-Fe1 = 3.1103<br>Li3$_{b}$-Fe2 = 3.8206 | Li3$_{b}$-O09-Fe1 = 93.45<br>Li3$_{b}$-O15-Fe1 = 102.26<br>Li3$_{b}$-O01-Fe2 = 131.19 |
| **Li3** | Li3$_{c}$ | Li3$_{c}$-Fe1 = 3.1847<br>Li3$_{c}$-Fe2 = 4.005 | Li3$_{c}$-O15-Fe1 = 101.93<br>Li3$_{c}$-O09-Fe1 = 98.75<br>Li3$_{c}$-O01-Fe2 = 137.60 |
| **Li3** | Li3$_{d}$ | Li3$_{d}$-Fe1 = 3.1649<br>Li3$_{d}$-Fe2 = 3.7304 | Li3$_{d}$-O15-Fe1 = 101.28<br>Li3$_{d}$-O09-Fe1 = 96.69<br>Li3$_{d}$-O01-Fe2 = 129.27 |

## 4.4 Conclusion

In conclusion, the detailed study outlined in this chapter thoroughly explores the complex structural attributes of $LiFeV_2O_7$. $^7$Li ssNMR data reveals a more complex $^7$Li spectrum than expected for the original crystal structure. A new crystal structure for $LiFeV_2O_7$ was determined by single-crystal x-ray diffraction that exhibits the presence of two possible local environments for a fraction of the vanadium centers. It was found that the V2, V6 and O8 sites shift in such a way that the coordination of V2 becomes tetrahedral and V6 trigonal bipyramidal. This disorder provided an explanation for the presence of multiplicity in the $^7$Li NMR. Through DFT calculations, it was possible to elucidate how structural disorders modify lithium environments, leading to significant variations in the electron spin density transfer mechanisms and, consequently, in Fermi contact shifts. The ORG-D model exhibits the closest correlation with experimental NMR spectra, highlighting the relationship between local geometry and electronic interactions. This study shows how ssNMR and DFT calculations are essential tools for gaining detailed insights into the structural intricacies of solid materials. These methodologies are particularly essential for revealing the complexities of local environments and domain structures in oxide materials, such as lithium-ion battery cathodes.

## 4.5 References

(1) Reynaud, M.; Serrano-Sevillano, J.; Casas-Cabanas, M. Imperfect Battery Materials: A Closer Look at the Role of Defects in Electrochemical Performance. *Chem. Mater.* **2023**, *35* (9), 3345–3363. https://doi.org/10.1021/acs.chemmater.2c03481.

(2) Fan, Y.; Zhang, W.; Zhao, Y.; Guo, Z.; Cai, Q. Fundamental Understanding and Practical Challenges of Lithium-Rich Oxide Cathode Materials: Layered and Disordered-Rocksalt Structure. *Energy Storage Mater.* **2021**, *40* (February), 51–71. https://doi.org/10.1016/j.ensm.2021.05.005.

(3) Chen, S. P.; Lv, D.; Chen, J.; Zhang, Y. H.; Shi, F. N. Review on Defects and Modification Methods of LiFePO4Cathode Material for Lithium-Ion Batteries. *Energy and Fuels* **2022**, *36* (3), 1232–1251. https://doi.org/10.1021/acs.energyfuels.1c03757.

(4) Wang, R.; Chen, X.; Huang, Z.; Yang, J.; Liu, F.; Chu, M.; Liu, T.; Wang, C.; Zhu, W.; Li, S. S.; Li, S. S.; Zheng, J.; Chen, J.; He, L.; Jin, L.; Pan, F.; Xiao, Y. Twin Boundary Defect Engineering Improves Lithium-Ion Diffusion for Fast-Charging Spinel Cathode Materials. *Nat. Commun.* **2021**, *12* (1), 1–10. https://doi.org/10.1038/s41467-021-23375-7.

(5) Benabed, Y.; Castro, L.; Penin, N.; Darriet, J.; Dollé, M. Synthesis, Structure, and Electrochemical Properties of LiFeV2O7. *Chem. Mater.* **2017**, *29* (21), 9292–9299. https://doi.org/10.1021/acs.chemmater.7b03271.

(6) Sheldrick, G. M. A Short History of SHELX. *Acta Crystallogr. Sect. A Found. Crystallogr.* **2008**, *64* (1), 112–122. https://doi.org/10.1107/S0108767307043930.

(7) Sheldrick, G. M. Crystal Structure Refinement with SHELXL. *Acta Crystallogr. Sect. C Struct. Chem.* **2015**, *71* (Md), 3–8. https://doi.org/10.1107/S2053229614024218.

(8) Dolomanov, O. V.; Bourhis, L. J.; Gildea, R. J.; Howard, J. A. K.; Puschmann,

H. OLEX2: A Complete Structure Solution, Refinement and Analysis Program. *J. Appl. Crystallogr.* **2009**, *42* (2), 339–341. https://doi.org/10.1107/S0021889808042726.

(9) Kervern, G.; Pintacuda, G.; Emsley, L. Fast Adiabatic Pulses for Solid-State NMR of Paramagnetic Systems. *Chem. Phys. Lett.* **2007**, *435* (1–3), 157–162. https://doi.org/10.1016/j.cplett.2006.12.056.

(10) Pell, A. J.; Pintacuda, G. Broadband Solid-State MAS NMR of Paramagnetic Systems. *Prog. Nucl. Magn. Reson. Spectrosc.* **2015**, *84–85*, 33–72. https://doi.org/10.1016/j.pnmrs.2014.12.002.

(11) Hafner, J. Materials Simulations Using VASP — a Quantum Perspective to Materials Science. **2007**, *177*, 6–13. https://doi.org/10.1016/j.cpc.2007.02.045.

(12) Hafner, R. Ab-Initio Simulations of Materials Using VASP : Density-Functional Theory and Beyond. **2008**. https://doi.org/10.1002/jcc.21057.

(13) Bamine, T.; Boivin, E.; Boucher, F.; Messinger, R. J.; Salager, E.; Deschamps, M.; Masquelier, C.; Croguennec, L.; Ménétrier, M.; Carlier, D. Understanding Local Defects in Li-Ion Battery Electrodes through Combined DFT/NMR Studies: Application to LiVPO4F. *J. Phys. Chem. C* **2017**, *121* (6), 3219–3227. https://doi.org/10.1021/acs.jpcc.6b11747.

(14) Pereira, T. L. E. E.; Sanders, K. J.; Smiley, D. L.; Britten, J. F.; Goward, G. R. Structural Complexity and Evolving Lithium-Ion Dynamics within the Cathode Material LiFeV2O7Revealed by Diffraction and Solid-State NMR. *Chem. Mater.* **2022**, *34* (19), 8551–8560. https://doi.org/10.1021/acs.chemmater.2c01357.

(15) Carlier, D.; Ménétrier, M.; Delmas, C.; Grey, C. P.; Ceder, G. Understanding the NMR Shifts in Paramagnetic Transition Metal Oxides Using Density Functional Theory Calculations. *Phys. Rev. B - Condens. Matter Mater. Phys.* **2003**, *67* (17), 174103. https://doi.org/10.1103/PhysRevB.67.174103.

(16) Riou, D.; Nguyen, N.; Benloucif, R.; Raveau, B. LiFeP2O7 : Structure and Magnetic Properties. *Mater. Res. Bull.* **1990**, *25* (11), 1363–1369.

https://doi.org/10.1016/0025-5408(90)90218-Q.

(17) Momma, K.; Izumi, F. VESTA: A Three-Dimensional Visualization System for Electronic and Structural Analysis. *J. Appl. Crystallogr.* **2008**, *41* (3), 653–658. https://doi.org/10.1107/S0021889808012016.

(18) Smith, S. H.; Wanklyn, B. M. Flux Growth of Rare Earth Vanadates and Phosphates. *J. Cryst. Growth* **1974**, *21* (1), 23–28. https://doi.org/10.1016/0022-0248(74)90145-6.

(19) Anisimov, V. I.; Zaanen, J.; Andersen, O. K. Band Theory and Mott Insulators: Hubbard U Instead of Stoner I. *Phys. Rev. B* **1991**, *44* (3), 943–954. https://doi.org/10.1103/PhysRevB.44.943.

(20) https://next-gen.materialsproject.org/. Materials Project https://next-gen.materialsproject.org/.

(21) Carlier, D.; Ménétrier, M.; Delmas, C. Transferred Hyperfine Interaction between a Tetrahedral Transition Metal and Tetrahedral Lithium: Li6CoO4. *J. Phys. Chem. C* **2010**, *114* (10), 4749–4755. https://doi.org/10.1021/jp911364w.

(22) Castets, A.; Carlier, D.; Zhang, Y.; Boucher, F.; Ménétrier, M. A DFT-Based Analysis of the NMR Fermi Contact Shifts in Tavorite-like LiMPO 4·OH and MPO 4·H 2O (M = Fe, Mn, V). *J. Phys. Chem. C* **2012**, *116* (34), 18002–18014. https://doi.org/10.1021/jp302549s.

(23) Pell, A. J.; Pintacuda, G.; Grey, C. P. Paramagnetic NMR in Solution and the Solid State. *Prog. Nucl. Magn. Reson. Spectrosc.* **2019**, *111*, 1–271. https://doi.org/10.1016/j.pnmrs.2018.05.001.

(24) Kim, J.; Middlemiss, D. S.; Chernova, N. A.; Zhu, B. Y. X. X.; Masquelier, C.; Grey, C. P. Linking Local Environments and Hyperfine Shifts: A Combined Experimental and Theoretical 31P and 7Li Solid-State NMR Study of Paramagnetic Fe(III) Phosphates. *J. Am. Chem. Soc.* **2010**, *132* (47), 16825–16840. https://doi.org/10.1021/ja102678r.

(25) Chazel, C.; Ménétrier, M.; Carlier, D.; Croguennec, L.; Delmas, C. DFT

Modeling of NMR Contact Shift Mechanism in the Ideal LiNi 2O4 Spinel and Application to Thermally Treated Layered Li0.5NiO2. *Chem. Mater.* **2007**, *19* (17), 4166–4173. https://doi.org/10.1021/cm070324n.

# Chapter 5: Quantify Lithium Dynamics and Identify Phase Transformations in $LiFeV_2O_7$ by $^7$Li Solid-State NMR during First Discharge Cycling

## 5.1 Introduction

This chapter presents the application of $^7$Li ssNMR for investigating the phase transitions and ion dynamics within $Li_{1\text{-}x}FeV_2O_7$ electrodes during the first electrochemical cycling. Combining both one-dimensional and two-dimensional ex-situ NMR techniques, this study reveals alterations in local lithium environments and measures lithium ion exchange processes throughout the cycling period. As will be discussed herein, NMR emerges as a very sensitive technique, surpassing other methodologies, for distinguishing between different Li environments within $LiFeV_2O_7$. Ex-situ $^7$Li NMR detects specific modifications in the Li environments triggered by the first discharge cycle. This structural rearrangement is closely associated with a marked enhancement in lithium-ion dynamics. The detailed characterization and quantification of these transformations provide valuable insights into this potential cathode material.

The work presented in this chapter was published in Chemistry of Materials (2022, 34, 8551-8560) with co-authors K.J. Sanders, D.L. Smiley, J.F. Britten, and G.R. Goward. The solid-state synthesis of this material as well as all NMR experiments and subsequent data analysis were carried out at McMaster University under the supervision of Prof. G. Goward.

## 5.2 Experimental Methods

### 5.2.1 Electrochemical Cycling

The cathode material was prepared by grinding the active material in 84:10:6 weight % ratio with Super P carbon black (CB) and polyvinylidene fluoride (PVDF). A solution of 2.0 % PVDF in N-methyl-2-pyrrolidene (NMP) was added to ground active material and CB (to enhance the electronic conduction) and let stir for 2 hours. The resulting slurry was deposited on an aluminum foil current collector using the doctor blade (15 mils) technique. The electrode was dried under a vacuum overnight at 120 °C. After that, the material was punched into discs 1.27 cm in diameter, and assembled in coin cells (CR2025) with $LiPF_6$ (1M $LiPF_6$ in a 1:1 wt% ethylene carbonate: diethyl carbonate solution) as the electrolyte, Celgard 2325 as the separator and Li-metal as the negative electrode in an argon filled glovebox. These cells were cycled on the ARBIN equipment at a rate of C/100 at room temperature. Galvanostatic intermittent titration technique (GITT) measurement of $LiFeV_2O_7$ was conducted between 3.10 and 2.3 V by discharging the half-coin cell at a current of 1.635 $\times10^{-2}$ mA (approximately C/50) for 10 min followed by a relaxation period of 10 min.

### 5.2.2 Solid-State NMR

After cycling the cells, they were disassembled in the glove box and washed with diethyl carbonate (DEC) to remove Li salts at the surface of the electrode and then analyzed by NMR. $^7$Li MAS NMR experiments were acquired using a Bruker Avance III HD spectrometer operating at a Larmor frequency of 116.64 MHz (7.05 T) using a Bruker 1.3 mm HX probe at spinning frequency of 60 kHz. The spectra are referenced to 1M $LiCl_{(aq)}$ at 0 ppm. The temperature was calibrated using $Sm_2Sn_2O_7$ as shift thermometer.[1] One-dimensional $^7$Li MAS spectra were obtained using a double spin echo pulse sequence utilizing short, high-power adiabatic pulses (SHAPs)[2] following a 1.25 μs $\frac{\pi}{2}$ excitation pulse. The SHAPs utilized a tanh/tan shape, a 5 MHz frequency sweep, and were 50 microseconds in length with a maximum RF field strength of 200 kHz. Under these conditions, the SHAPs are expected to be >99% efficient.[3] $T_1$ relaxation times were determined using a standard inversion-recovery sequence. Two-dimensional exchange spectroscopy (EXSY) experiments were acquired using a mixing time of 5 ms. The number of slices in the indirect dimension was 256, number of scans 518 and the hard 90 pulse was 1.25 μs in length with a pulse power of 40 W. Phase-sensitive detection in t1 was achieved through the use of States-TPPI. $^7$Li Selective inversion (SI) experiments were acquired using 180°-$\tau_{mix}$-90° sequence, where the 180° Gaussian shaped pulse was 400 μs in length with a soft pulse power of 0.0178 W at its maximum. The mixing time was varied across a series of 19 experiments from 0.05 μs to 50 ms. A hard, 1.25 μs $\frac{\pi}{2}$ pulse was used to acquire the final signal. Acquisition of the spectra was performed using a recycle delay of 25 ms, acquisition time of 4.9487 ms, and 1024 scans. Non-selective inversion (NSI) experiments were performed using a standard inversion–recovery sequence using the same variable delay time, as was used for mixing time in SI experiments.

### 5.2.3 Data Analysis with CIFIT

The selective inversion data were processed using the CIFIT program developed by A.D Bain at McMaster University as described in Chapter 2.[4,5] For each data set, slices for each mixing time were extracted, the baseline was corrected and each slice was deconvoluted to obtain the integral for each signal involved in the exchange process. These values were normalized to the integration value of the slice with longest mixing time. Deconvolutions of $^7$Li spectra were carried out in ssNake software[6] (version 1.2), which the positions and linewidth of the peaks were fixed while the intensity was free to float according to mixing time for each stage of lithiation. The peaks were fit individually using pure Lorentzian line shape.

## 5.3 Result and Discussion

### 5.3.1 Evaluated structural stability of the lithiated sample

The galvanostatic intermittent titration technique (GITT) was used for the $LiFeV_2O_7$ during the first discharge (from 3.10 V to 2.30 V). A half coin cell was used, with metallic lithium as the counter and reference electrode and $LiFeV_2O_7$ as the working electrode. It was possible to observe that the material is close to a thermodynamic equilibrium voltage. At the beginning of discharge, the voltage recovered a little bit, but we were interested in the second slope of the graphic which the voltage recovered is less than 0.05V as shown in **Figure 5.1**. The results ensure that the composition phase does not undergo any modification when samples were analyzed by ssNMR.

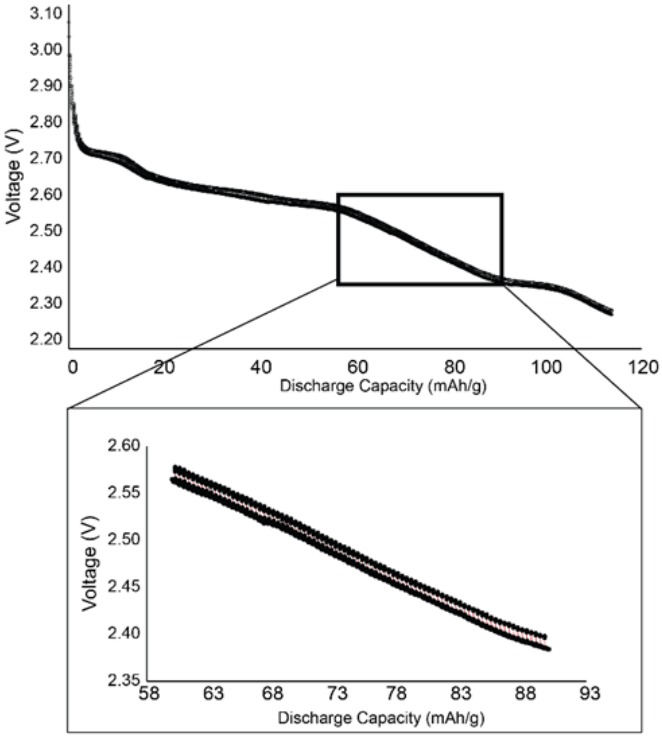

**Figure 5.1.** Galvanostatic intermittent titration technique (GITT) electrochemical curve of $LiFeV_2O_7$ from 3.1 to 2.3 V with a current of 16.35 μA which correspond to C/100

### 5.3.2 $^7$Li 2D EXSY NMR as a Function of Electrochemical Lithiation

Solid state NMR is used to probe the local environment, as shown previously, and to quantify the dynamics in $LiFeV_2O_7$ as a function of lithium content. **Figure 5.2** shows the ex-situ $^7$Li MAS NMR spectra that were collected at various intervals along the discharge curve, according to the lithium content and also the electrochemical data. We note that the electrochemical curve matches extremely well with that published previously [7], in terms of capacity, voltage plateaus, and small voltage hysteresis. These are important indicators that the bulk cathode material used in the electrochemical studies in both our work and the Benabed et al.[7] are structurally identical. The series of $^7$Li spectra reveals dramatic changes in the lithium environment which seem to correlate to significant changes in $Li^+$ ion dynamics. This onset coincides with an inflection point in the electrochemical curve.

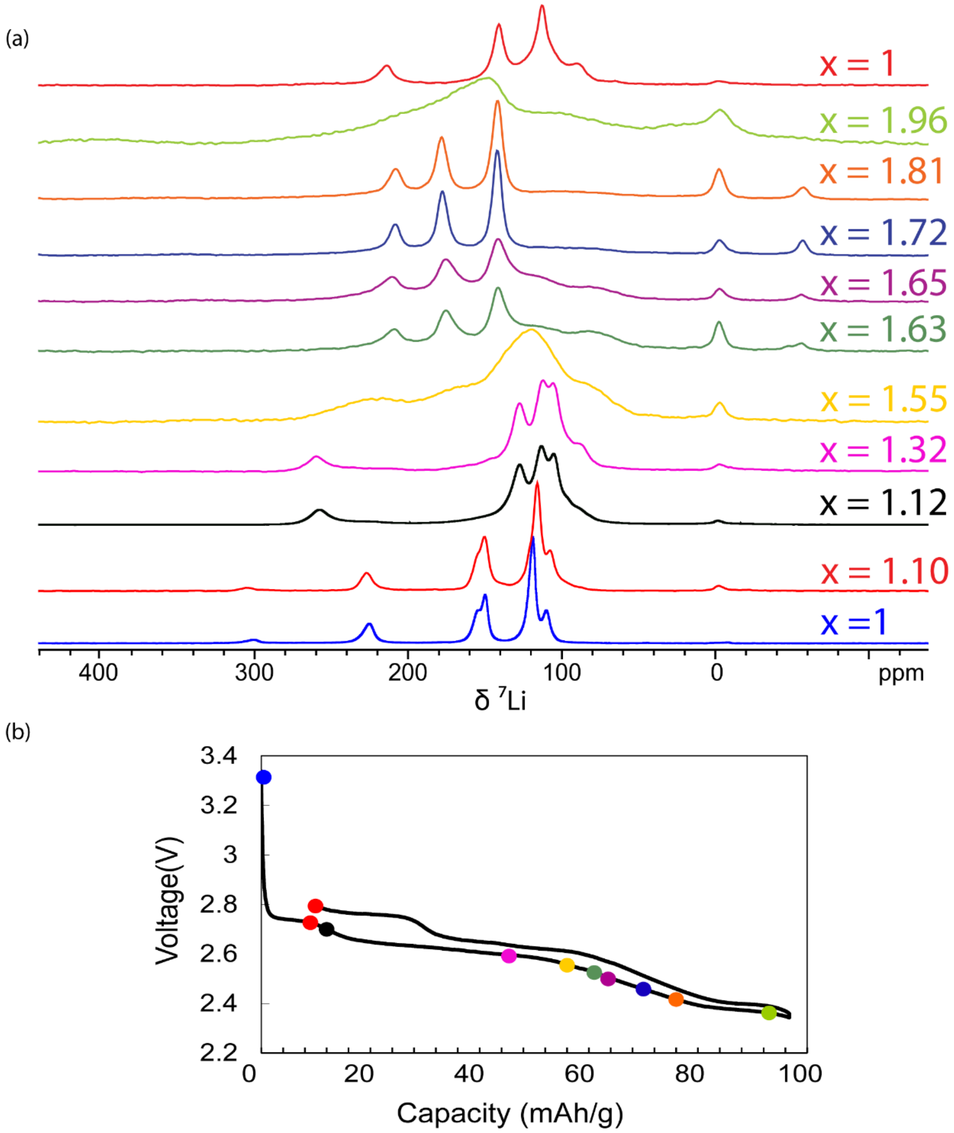

**Figure 5.2.** (a) $^7$Li MAS NMR as a function of stage of lithiation (discharge process) as labeled on the electrochemical curve in (b). Colored spectra are matched to the voltage which $Li_xFeV_2O_7$ was shown in the discharge curve.

In the beginning of lithiation, a significant broadening of the peaks is observed with decreasing cutoff voltage, due to the reduction of $V^{5+}$ to $V^{4+}$, what makes this element paramagnetic, consequently broadening the signal. At 2.51 V, which corresponds to insertion of about 0.60 equivalents of Li, a new line shape is observed with improved spectral resolution. Although broad signals were expected due to the presence of paramagnetic elements, narrow signals were observed in the composition range of $Li_xFeV_2O_7$ ($1.63 \leq x \leq 1.81$) indicating that the effect of rapid dynamics is overcoming the paramagnetic broadening. A new signal is observed at – 55 ppm while the signal at high frequency, 291 ppm, disappears, which is a further indication of the change in local dynamics. The change in the spectra is indicative that a new structural rearrangement was necessary in order to accommodate more Li atoms into the parent structure. This new behavior is observed until discharging to 2.41 V (0.81 Li added) where the signal became broader again. The implications of this structural change and how it affects lithium mobility will be explored in detail in chapter 6.

When the cell is completely charged to a voltage of 2.8 V, the structure is returned back to the initial NMR lineshape, however there are small changes regarding the chemical shift and the peak intensity that can be indicative of a partially irreversible transformation of the structure. The signal present at 0 ppm in all the spectra is assigned to $LiPF_6$ electrolyte salt or other diamagnetic Li salts formed on the surface of the electrode during the discharge process.

NMR has been used to study dynamics in pristine cathode materials[8–10] and as a function of cycling[11–13]. Here, we observe a significant change in the local dynamics within the cathode as a function of lithiation. This is first indicated by changes in the 1D $^7Li$ NMR spectra, where unexpected line narrowing during discharge is attributed to enhanced $Li^+$ mobility. In order to quantify these dynamics, we have employed 2D and SI ex situ NMR experiments to explore ion dynamics in cycled $Li_{1\text{-}x}FeV_2O_7$.

Two dimensional experiments can be used to identify possible exchanges partners through the detection of cross peaks. **Figure 5.3** depicts the 2D EXSY spectra collected for pristine material and three stages of lithiation at room temperature with a mixing time of 5 ms. The absence of cross peaks in the pristine material indicates a lack of dynamics in the initial structure at least on this time scale. Upon cycling, there is minor evidence of an exchange pair (**Figure 5.3b**), at least until the phase transformation that occurs around $Li_{1.60}FeV_2O_7$. At this composition, it was possible to detect exchange between the three crystallographic Li sites corresponding to $Li_A$-$Li_B$, $Li_A$-$Li_C$ and $Li_B$-$Li_C$ exchange pairs, where the signals are labeled A, B and C in order of decreasing resonance frequency. While these three new signals do not represent the full sample composition, it is clear that their appearance marks an intriguing change in the local structure and dynamics. Therefore, we proceed with an analysis of their exchange dynamics. The remaining boarder peaks may also contribute to ion dynamics; however, it is typically observed that $Li^+$ dynamics result in line narrowing, and thus the exchange among the three narrowed peaks is taken as representative of a new dynamics process within the cathode material.

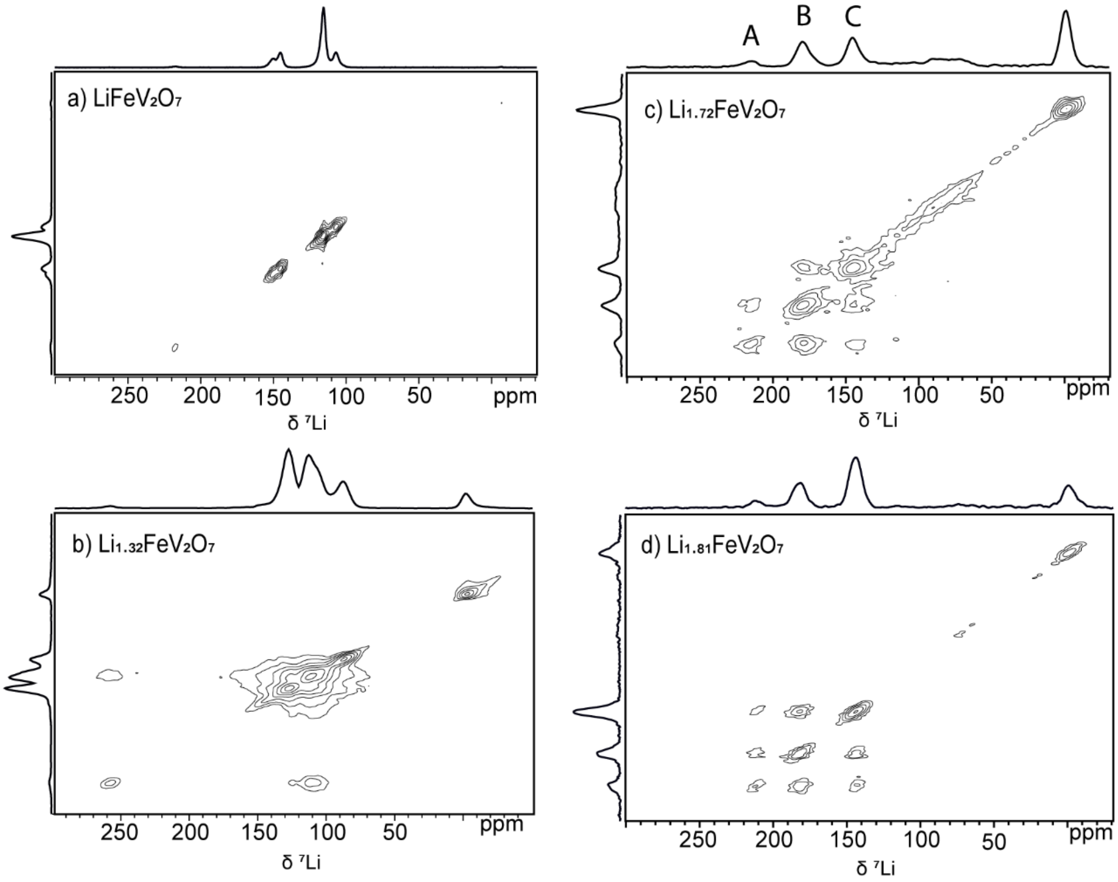

**Figure 5.3.** $^{7}$Li 2D EXSY spectra were collected at room temperature with a mixing time of 5 ms. (a) Pristine material, (b) $Li_{1.32}FeV_2O_7$, (c) $Li_{1.72}FeV_2O_7$, and (d) $Li_{1.81}FeV_2O_7$.

With this evidence, the properties of the cathode material in this range were investigated by assembling a series of extracted cathodes over the lithiation process. Three stages of lithiation, $Li_{1.65}FeV_2O_7$, $Li_{1.72}FeV_2O_7$, and $Li_{1.81}FeV_2O_7$, were used to study Li-Li exchange among the three sites in the new spectral line shape.

### 5.3.2 $^{7}$Li SI NMR as a Tool to Quantify the Li-Li Exchange Rates

EXSY provides excellent visual confirmation of chemical exchange and its practical use as a first method for qualitative identification of exchange pairs. However, data analysis can be a challenge in some cases to obtain quantitative kinetic information for each pair of sites. The one-dimensional (1D) selective inversion (SI) experiment is a more effective method for quantitative determination of exchange rates and requires less experimental time.

The large number of overlapping signals in the $^{7}$Li MAS NMR spectrum is indicative of the complex nature of this material during the electrochemical process. In order to obtain the accurate rate constants for each Li-Li exchange, every spectrum collected using individual mixing time in an SI experiment array was deconvoluted using ssnake software[6] **(Figure 5.4)**. At least eight distinct signals are evident, however for the specific purpose of calculating Li-Li exchange rates, only the three sharp peaks labeled A, B, and C were considered. The consistent peak observed at 0 ppm across all spectra is attributed to the $LiPF_6$ electrolyte salt or other diamagnetic Li salts that accumulate on the electrode surface during discharge. Despite employing a washing process to try to remove these compounds, residual quantities were detected in all NMR spectrum. Details of the parameters from the deconvolution are provided in **Table 5.1**.

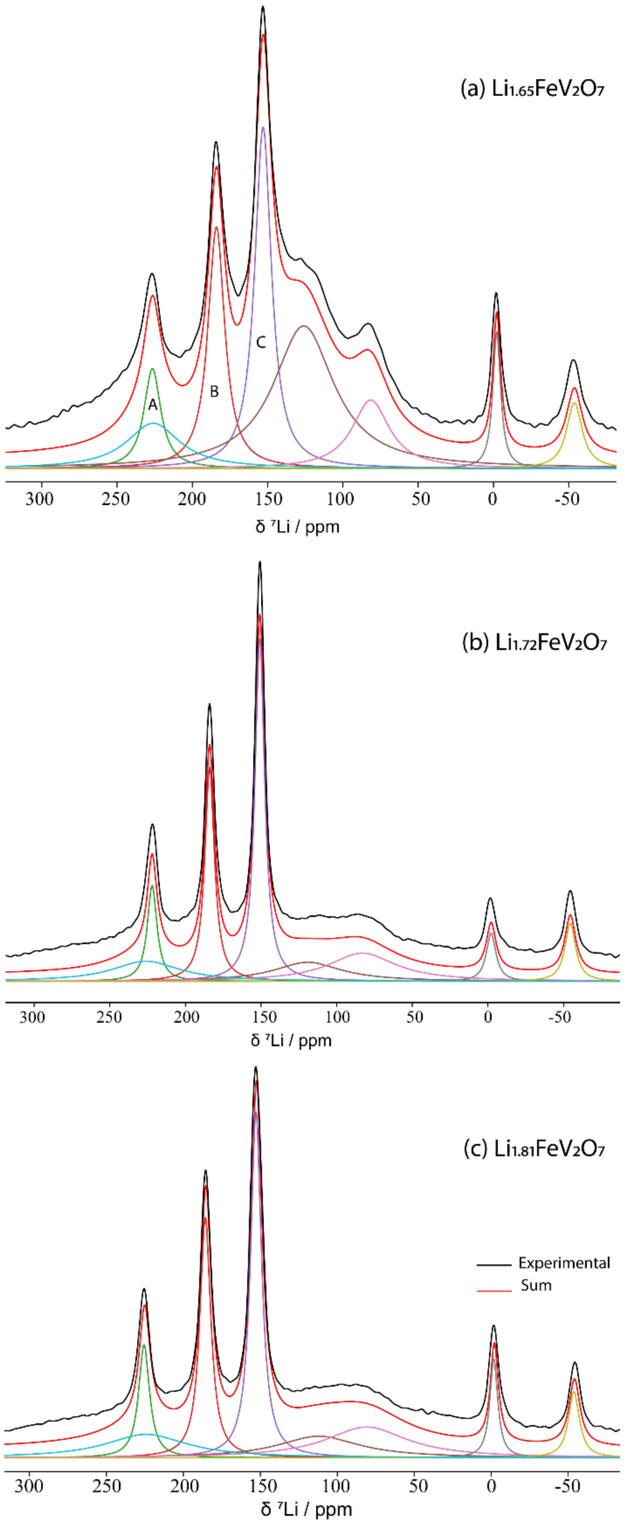

**Figure 5.4.** $^{7}$Li MAS spectrum of $Li_{1.65}FeV_2O_7$, $Li_{1.72}FeV_2O_7$ and $Li_{1.81}FeV_2O_7$ at room temperature and the deconvoluted spectrum indicates at least eight isotropic signals, which the exchange among A, B and C is measured.

**Table 5.1:** Details of deconvolution of the $^7$Li NMR spectrum for $Li_{1.65}FeV_2O_7$, $Li_{1.72}V_2O_7$ and $Li_{1.81}V_2O_7$, carried out in ssNake.

| $Li_{1.65}FeV_2O_7$ | | | $Li_{1.72}V_2O_7$ | | | $Li_{1.81}V_2O_7$ | | |
|---|---|---|---|---|---|---|---|---|
| $\delta_{Isotropic}$ (ppm) | Integral | LB (HZ) | $\delta_{Isotropic}$ (ppm) | Integral | LB (HZ) | $\delta_{Isotropic}$ (ppm) | Integral | LB (HZ) |
| -53.1 | 1.25E+11 | 1200 | -54.5 | 9.20E+10 | 1100 | -53.8 | 9.40E+10 | 1000 |
| -2.2 | 1.53E+11 | 728.8 | -2.2 | 5.20E+10 | 728.8 | -1.7 | 1.02E+11 | 728.8 |
| 81.5 | 3.70E+11 | 3500 | 81.0 | 2.80E+11 | 6300 | 81.0 | 3.00E+11 | 6300 |
| 126.0 | 1.25E+12 | 5700 | 121.0 | 2.00E+11 | 6300 | 112.0 | 2.10E+11 | 6300 |
| *153.0 | 8.20E+11 | 1560 | 152.0 | 4.59E+11 | 900 | 152.8 | 4.88E+11 | 1000 |
| *184.0 | 5.81E+11 | 1560 | 184.8 | 2.98E+11 | 900 | 185.7 | 3.40E+11 | 1000 |
| *226.5 | 2.40E+11 | 1560 | 224.0 | 1.32E+11 | 900 | 225.5 | 1.64E+11 | 1000 |
| 228 | 3.90E+11 | 6300 | 226.0 | 2.00E+11 | 6300 | 226.0 | 2.20E+11 | 6300 |

*Signals involved in chemical exchange.

The experiments were carried out across a range of temperatures (303-318 K) where site A and C were inverted each time and their return to equilibrium was monitored (**Figure 5.5a**). **Figure 5.5b** shows a plot of normalized intensity as a function of mixing time. The build-up curve is related to the inverted signal C, and the transient well curves are measured from the intensity changes at the noninverted sites, peaks A and B, which are the results of their chemical exchange with the inverted site. The same plot for inverted signal A is shown in **Figure 5.5c**. The lines drawn (named A, B, and C) show the best fit to the data from the CIFIT software.

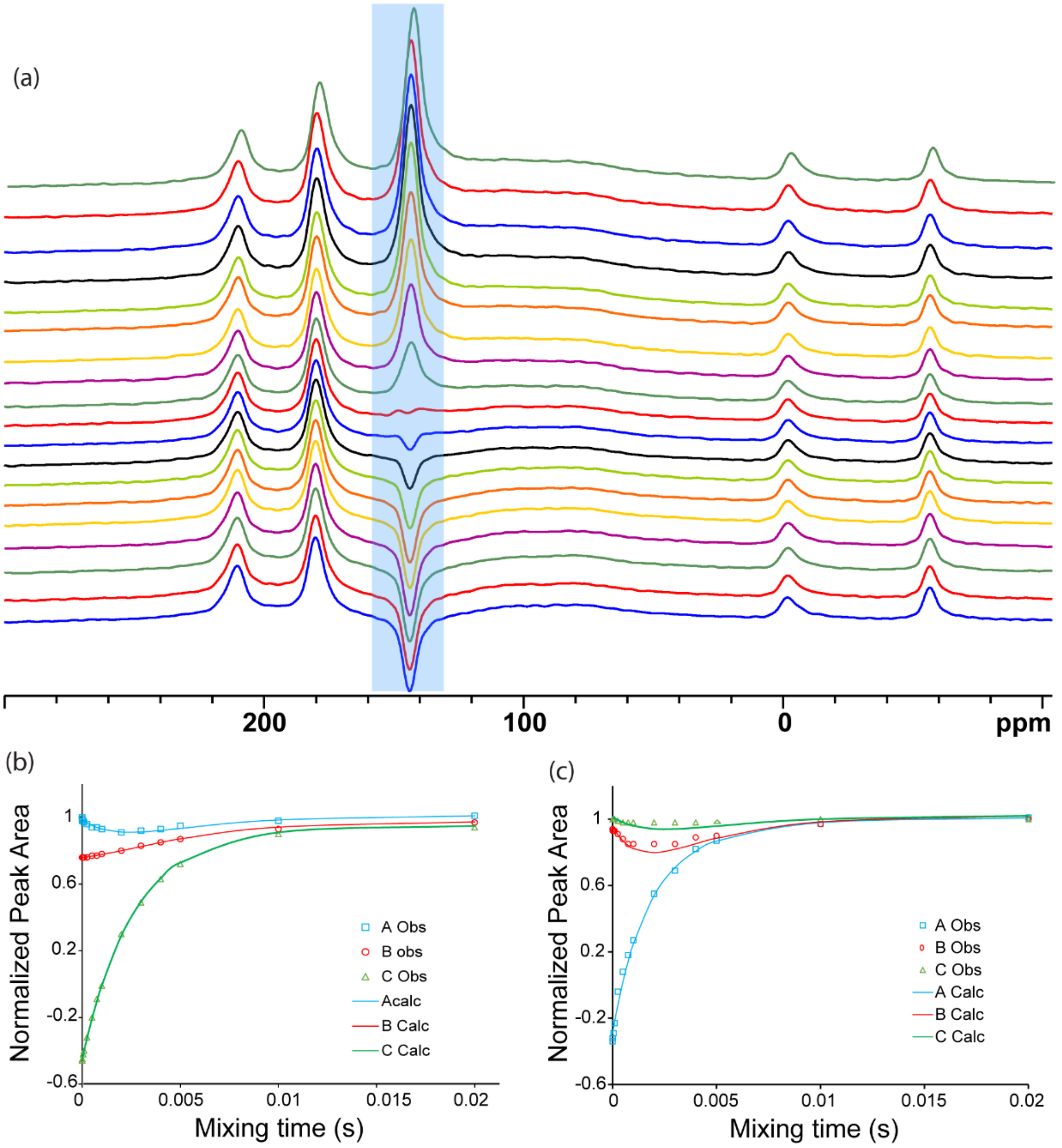

**Figure 5.5.** (a) Stack of 1D MAS spectra of $Li_{1.72}FeV_2O_7$ with increasing mixing time demonstrating the effect of inversion and recovery in an SI experiment. (b) and (c) The normalized integration of each of the deconvoluted peaks in the SI experiment at 318 K, peak A and C being inverted respectively.

In addition, a nonselective inversion experiment was performed using a standard inversion recovery pulse sequence that was implemented to monitor any changes in relaxation properties as a function of temperature. When comparing the NSI and SI build up curve for peak A (**Figure 5.6a** and **5.6b**, respectively), the SI results clearly indicate a difference in the relaxation rate of the magnetization as a function of temperature which is not observed for NSI graph. This exemplifies the difference between the experiments. NSI experiments are governed by the inherent $T_1$ behavior, which is confirmed to be independent of temperature, while SI experiment are affected by chemical exchange which is expected to be temperature dependent.[5,14,15] **Figure 5.6** depicts the experimental data for $Li_{1.79}FeV_2O_7$ sample. It is possible to observe the relationship among the inverted peak A and the noninverted signals B and C with the temperature. The depth of the transient well increases at higher temperature as expected, because the exchange with the inverted peak thermally activated. In the case of $Li_A$-$Li_B$ and $Li_B$-$Li_C$, the fit of the modeled peak intensity matches well with the data collected.

For $Li_{1.65}FeV_2O_7$ composition, the rates of $Li_A$-$Li_B$ extend from 8.9 ± 0.9 x10 $s^{-1}$ at 303 K up to 23 ± 4 x10 $s^{-1}$ at 318 K. Slower kinetics were observed for the $Li_B$-$Li_C$, exchange with time scale ranging from 4.9 ± 0.9 x10 $s^{-1}$ at 303 K up to 12 ± 2 x10 $s^{-1}$ at 318 K. The same behavior is observed in the two other compositions. The exchange rates for each composition can be found in **Table 5.2**. In the case of $Li_A$-$Li_C$ exchange pair, larger errors are observed due to the presence of overlapped peaks. As shown before in **Figure 5.4**, the resonances A and C have broad overlapped signals that may introduce additional error into the measured peak area obtained from the deconvolution of the spectrum, which is subsequently used to determine the exchange rate. Error bars were approximated in the CIFIT program by the variance-covariance matrix of the fit to the data.

**Table 5.2.** Calculated rate constants and error for each of three exchange pairs in three stages of lithiation.

| Sample: $Li_{1.65}$ | | | |
|---|---|---|---|
| T (K) | $k_{AB}(s^{-1})$ x$10^{1}$ | $k_{AC}(s^{-1})$ x$10^{2}$ | $k_{BC}(s^{-1})$ x10 |
| 303 | 8.9 ± 0.9 | 0.6 ±0.1 | 4.9 ± 0.9 |
| 307 | 11 ± 1 | 0.6 ± 0.2 | 6.5 ± 0.9 |
| 311 | 19 ± 4 | 1.0 ± 0.3 | 6.6 ± 0.9 |
| 315 | 22 ± 4 | 1.0 ±0.3 | 12 ± 2 |
| 318 | 23 ± 4 | 1.0 ± 0.3 | 12 ± 2 |

| Sample: $Li_{1.72}$ | | | |
|---|---|---|---|
| T (K) | $k_{AB}(s^{-1})$ x$10^{1}$ | $k_{AC}(s^{-1})$ x$10^{2}$ | $k_{BC}(s^{-1})$ x10 |
| 303 | 4.7 ± 0.6 | 0.2 ± 0.1 | 1.3 ± 0.4 |
| 307 | 5.9 ± 0.7 | 0.3 ± 0.1 | 1.4 ± 0.3 |
| 311 | 8.2 ± 0.8 | 0.4 ± 0.1 | 1.7 ± 0.3 |
| 315 | 13 ±1 | 0.5 ± 0.1 | 2.2 ± 0.3 |
| 318 | 15 ± 1 | 0.5 ± 0.1 | 3.9 ± 0.9 |

| Sample: $Li_{1.81}$ | | | |
|---|---|---|---|
| T (K) | $k_{AB}(s^{-1})$ x$10^{1}$ | $k_{AC}(s^{-1})$ x$10^{2}$ | $k_{BC}(s^{-1})$ x10 |
| 303 | 5.0 ± 0.7 | 0.4 ± 0.1 | 1.5 ± 0.4 |
| 307 | 6.6 ± 0.9 | 0.5 ± 0.1 | 2.0 ± 0.3 |
| 311 | 9.9 ± 0.9 | 0.5 ± 0.1 | 2.5 ± 0.3 |
| 315 | 16 ± 2 | 0.6 ± 0.1 | 4.8 ± 0.3 |
| 318 | 17 ± 2 | 0.8 ± 0.2 | 4.7 ± 0.4 |

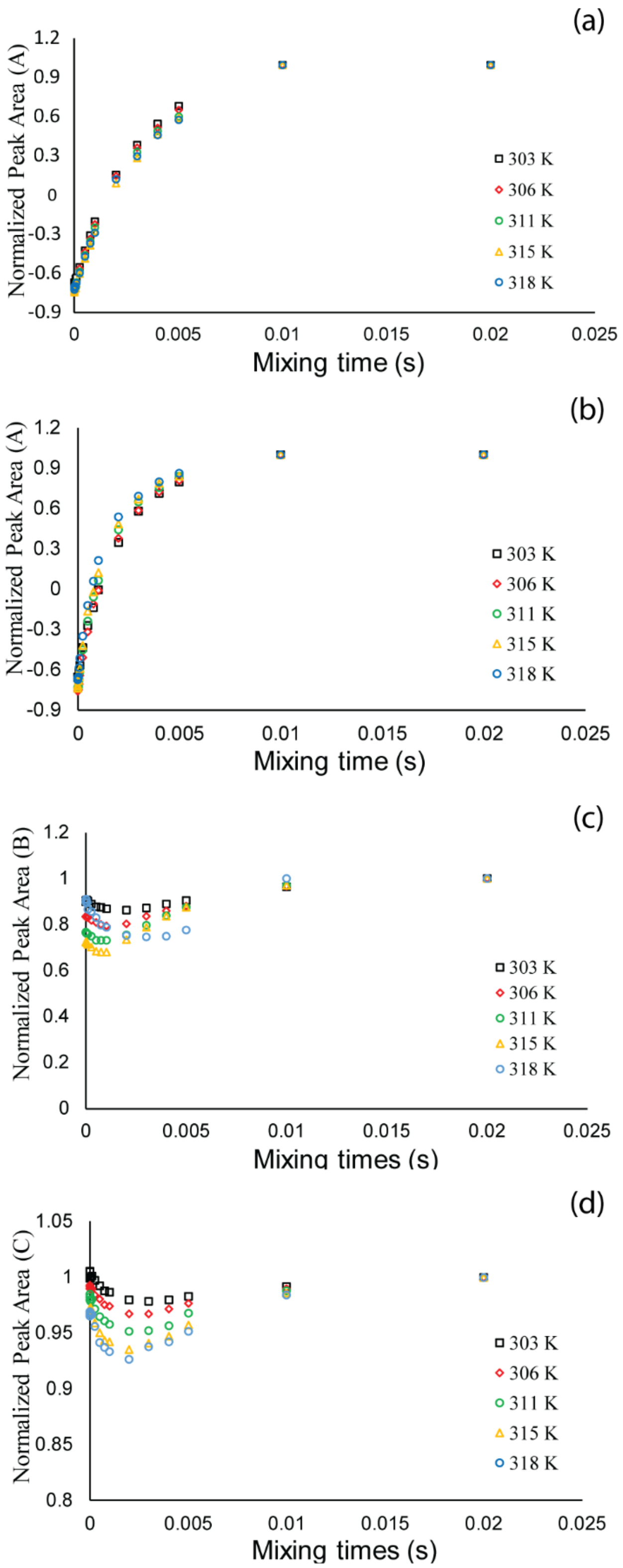

**Figure 5.6.** Plots of peak area dependence on mixing time over five temperatures for $Li_{1.79}FeV_2O_7$ when signal A is inverted. (a) NSI experiment; (b) SI experiment; (c) Transient curve for signal B and (d) Transient curve for signal C.

The higher rate constant associated with the low lithium content and accompanying new structural rearrangement is very intriguing. During the discharge process, it was possible to observe that the material originates in a stage where the dynamics are minimal, which was difficult to quantify by NMR, into the stage where the three sites were easily observed to undergo exchange, and through this composition, to a further region, where the dynamics are again outside the detection limit of this NMR method. Determination of exchange rates for each exchange pair at different temperatures allowed for the calculation of the activation energy (Ea) over the observable composition range of the new phase, listed in **Table 5.3**.

Through Eyring analysis method, which consists of the plot of ln(k/T) vs 1000/T, the activation energy was obtained via the slope of the line (**Figure 5.7**). The error value of the energy barrier was calculated from the standard error of the slope from the regression analysis for AB and BC exchange pairs. However, due to the exchange rate uncertainty, which is large for AC because of the challenge of the selective pulse inverting middle peak B on the adjacent peaks A and C, the activation energy error was calculated based on the maximum and minimum best-fit lines. The values for activation energy are found to range from 0.30-0.67 eV across all the possible exchange pairs for the three measured samples. In general, the activation energy increases as a function of overall lithiation, suggesting that as Li ions are inserted into the structure, it becomes more difficult for them to exchange with each other. This phenomenon may be related to a decreased number of lithium vacancies in the structure with increasing degree of lithiation. In Chapter 6, we will discuss the new structural arrangement and how it affects the lithium-ion dynamics. There, we will compare the three possible Li-Li exchange pairs with their li-li distance and bottleneck.

**Table 5.3**. Activation energies for three Li-Li exchange pairs in three stages of lithiation of $LiFeV_2O_7$ electrode.

| | Activation Energy (eV) | | |
|---|---|---|---|
| Sample | AB | AC | BC |
| $Li_{1.65}$ | 0.59 ± 0.06 | 0.4 ± 0.3 | 0.48 ± 0.07 |
| $Li_{1.72}$ | 0.67 ± 0.04 | 0.5 ± 0.4 | 0.57 ± 0.09 |
| $Li_{1.81}$ | 0.66 ± 0.06 | 0.3 ± 0.3 | 0.57 ± 0.09 |

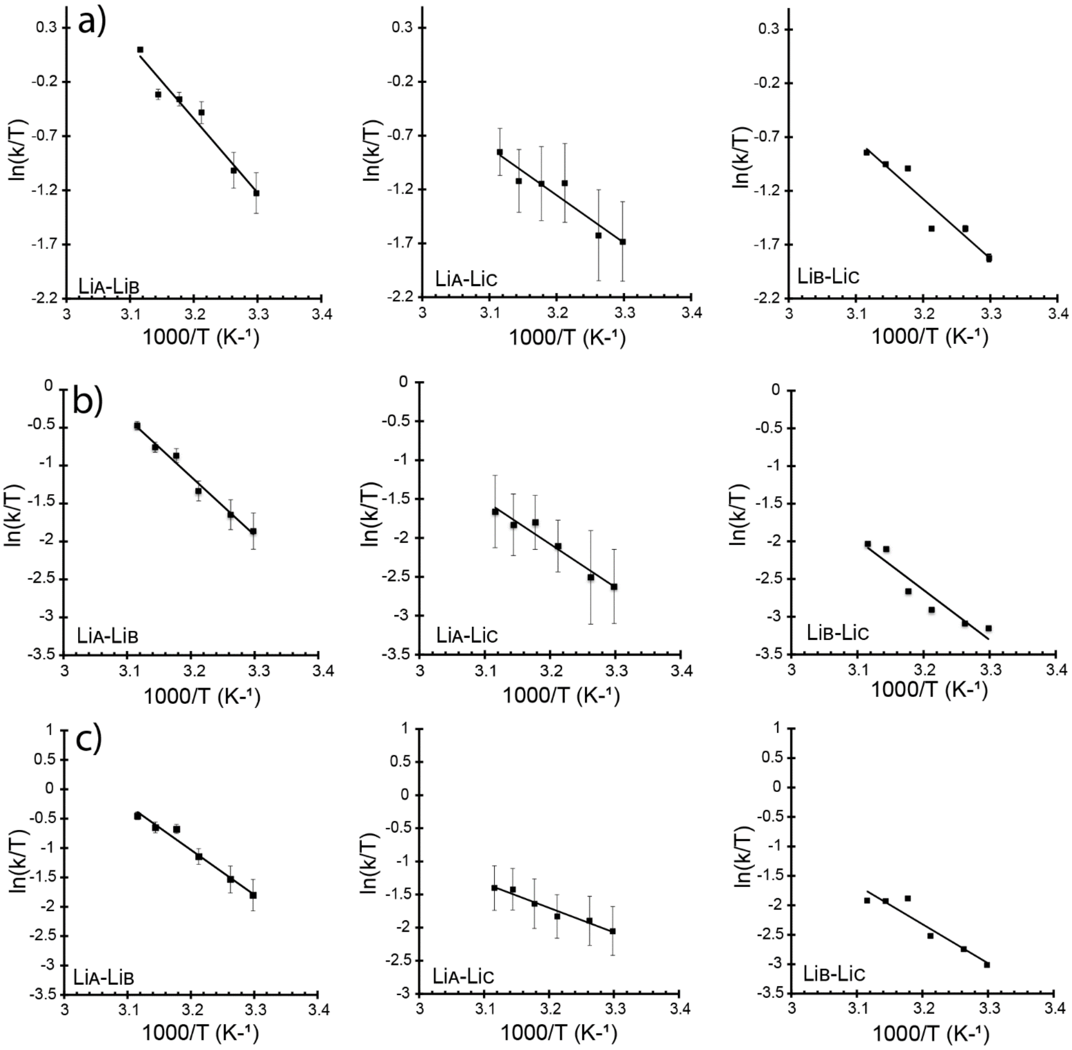

**Figure 5.7.** Eyring plots showing the linear fits to experimental exchange rates to obtain the activation energies for each exchange pair in three lithiation stages. (a) $Li_{1.65}FeV_2O_7$, (b) $Li_{1.72}FeV_2O_7$ and (c) $Li_{1.81}FeV_2O_7$

Comparing activation energies range obtained in this work to others cathode candidates, the exchange among ion pairs in LFVOD is found to be more favorable than $Li_3V_2(PO_4)_3$[16] and, $Li_5V(PO_4)_2F_2$[9] which were shown to have activation energies range from 0.73 - 0.83 and 0.60 – 0.79 eV, respectively. However, the dynamics in LFVOD are less favorable than in the NASICON structure, $Li_3Fe_2(PO_4)_3$[8] for which the energy barrier range is 0.37 – 0.53 eV.

## 5.4 Conclusion

Ex-situ NMR data were collected for cycled $Li_{1.x}FeV_2O_7$ cathode materials, where a new lithium rearrangement was detected around the x=0.60 composition. Using 2D EXSY NMR, it was possible to detect an increase in the dynamics after this change. A quantitative study of Li-Li exchange rates and energy barriers was performed on these cycled materials by selective inversion NMR experiments. Exchange rates among the three main Li sites in the NMR spectra, were calculated in three stages of lithiation: $Li_{1.65}FeV_2O_7$, $Li_{1.72}V_2O_7$ and $Li_{1.81}V_2O_7$. This showed that faster kinetics were observed for the $Li_A$-$Li_B$ exchange pair in all three stages of lithiation. The results showed a trend where, as the overall lithium content increases, the exchange rate decreases, while the energy barrier increases, consistent with the ongoing lithiation process, in which the structure has less vacancies available for Li to diffuse. The selective inversion experiment proved to be very efficient in quantifying the ion hopping, even for this complex structure. This study shows how changes in Li dynamics within electrode materials can be understood by ssNMR and correlated to electrochemical performance of cathode materials.

## 5.5 References

(1) Grey, C. P.; Cheetham, A. K.; Dobson, C. M. Temperature-Dependent Solid-State 119Sn- MAS NMR of Nd2Sn2O7, Sm2Sn2O7, and Y1.8Sm0.2Sn2O7. Three Sensitive Chemical-Shift Thermometers. *Journal of Magnetic Resonance - Series A*. 1993, pp 299–306. https://doi.org/10.1006/jmra.1993.1046.

(2) Kervern, G.; Pintacuda, G.; Emsley, L. Fast Adiabatic Pulses for Solid-State NMR of Paramagnetic Systems. *Chem. Phys. Lett.* **2007**, *435* (1–3), 157–162. https://doi.org/10.1016/j.cplett.2006.12.056.

(3) Pell, A. J.; Pintacuda, G. Broadband Solid-State MAS NMR of Paramagnetic Systems. *Prog. Nucl. Magn. Reson. Spectrosc.* **2015**, *84–85*, 33–72. https://doi.org/10.1016/j.pnmrs.2014.12.002.

(4) Bain, A. D.; Berno, B. Liouvillians in NMR: The Direct Method Revisited. *Prog. Nucl. Magn. Reson. Spectrosc.* **2011**, *59* (3), 223–244. https://doi.org/10.1016/j.pnmrs.2010.12.002.

(5) Bain, A. D. Chemical Exchange in NMR. *Prog. Nucl. Magn. Reson. Spectrosc.* **2003**, *43* (3–4), 63–103. https://doi.org/10.1016/j.pnmrs.2003.08.001.

(6) van Meerten, S. G. J. J.; Franssen, W. M. J. J.; Kentgens, A. P. M. M. SsNake: A Cross-Platform Open-Source NMR Data Processing and Fitting Application. *J. Magn. Reson.* **2019**, *301*, 56–66. https://doi.org/10.1016/j.jmr.2019.02.006.

(7) Benabed, Y.; Castro, L.; Penin, N.; Darriet, J.; Dollé, M. Synthesis, Structure, and Electrochemical Properties of LiFeV2O7. *Chem. Mater.* **2017**, *29* (21), 9292–9299. https://doi.org/10.1021/acs.chemmater.7b03271.

(8) Smiley, D. L.; Davis, L. J. M. M.; Goward, G. R. An Improved Understanding of Li+ Hopping Pathways and Rates in Li3Fe2(PO4)3 Using Selective Inversion 6Li NMR Spectroscopy. *J. Phys. Chem. C* **2013**, *117* (46), 24181–24188. https://doi.org/10.1021/jp407510h.

(9) Davis, L. J. M.; Goward, G. R. Differentiating Lithium Ion Hopping Rates in Vanadium Phosphate versus Vanadium Fluorophosphate Structures Using 1D

6Li Selective Inversion NMR. *J. Phys. Chem. C* **2013**, *117* (16), 7981–7992. https://doi.org/10.1021/jp310790g.

(10) Smiley, D. L.; Tessaro, M. Z.; He, X.; Goward, G. R. Correlation of Electrochemical Performance with Lithium Environments and Cation Dynamics in Li2(Mn1-YFey)P2O7 Using 6Li Solid-State NMR. *J. Phys. Chem. C* **2015**, *119* (29), 16468–16474. https://doi.org/10.1021/acs.jpcc.5b04173.

(11) Li, H.; Hua, W.; Liu-Théato, X.; Fu, Q.; Desmau, M.; Missyul, A.; Knapp, M.; Ehrenberg, H.; Indris, S. New Insights into Lithium Hopping and Ordering in LiNiO2 Cathodes during Li (De)Intercalation. *Chem. Mater.* **2021**, *33* (24), 9546–9559. https://doi.org/10.1021/acs.chemmater.1c02680.

(12) Märker, K.; Reeves, P. J.; Xu, C.; Griffith, K. J.; Grey, C. P. Evolution of Structure and Lithium Dynamics in LiNi0.8Mn0.1Co0.1O2 (NMC811) Cathodes during Electrochemical Cycling. *Chem. Mater.* **2019**, *31* (7), 2545–2554. https://doi.org/10.1021/acs.chemmater.9b00140.

(13) Smiley, D. L.; Goward, G. R. Ex Situ 23Na Solid-State NMR Reveals the Local Na-Ion Distribution in Carbon-Coated Na2FePO4F during Electrochemical Cycling. *Chem. Mater.* **2016**, *28* (21), 7645–7656. https://doi.org/10.1021/acs.chemmater.6b02539.

(14) FORSEN, S. Exchange Rates by Nuclear Magnetic Multiple Resonance. III. Exchange Reactions in Systems with Several Nonequivalent Sites. *J. Chern. Phys.* **1963**, *40* (5), 1189–1196.

(15) Forsén, S.; Huffman, R. A. Study of Moderately Rapid Chemical Exchange Reactions by Means of Nuclear Magnetic Double Resonance. *J. Chem. Phys.* **1963**, *39* (11), 2892–2901. https://doi.org/10.1063/1.1734121.

(16) Cahill, L. S.; Chapman, R. P.; Britten, J. F.; Goward, G. R. 7Li NMR and Two-Dimensional Exchange Study of Lithium Dynamics in Monoclinic Li3v2(PO4)3. *J. Phys. Chem. B* **2006**, *110* (14), 7171–7177. https://doi.org/10.1021/jp057015+.

# Chapter 6: A Combined $^7$Li NMR, Density Functional Theory, and *Operando* Synchrotron X-Ray Powder Diffraction to Investigate a Structural Evolution of $LiFeV_2O_7$

## 6.1 Introduction

A comprehensive understanding of structural changes of cathode materials during the process of charge and discharge is crucial for the development of new materials and the improvement of existing ones. As discussed in Chapter 5, for $LiFeV_2O_7$ an increase in local lithium dynamics was observed after 0.5 mols of lithium was inserted into the structure, through the evolution of the $^7$Li NMR spectra via both 1D $^7$Li MAS data acquired at 60kHz MAS and the combination of chemical exchange methods including $^7$Li 2D EXSY and Selective Inversion spectroscopy. Therefore, the chemical composition, $Li_{1.x}FeV_2O_7$ is an interesting structure that warrants further investigation, to evaluate the unit cell-level changes that facilitate this observed change in lithium dynamics.

In this chapter a detailed study of the lithiated phase combining *operando* synchrotron powder X-ray diffraction (SPXRD), ssNMR, and DFT calculations. The *operando* SPXRD experiment enables the real-time tracking of alterations in the unit cell, linking them to the enhanced lithium dynamics in the bulk material, as discussed in Chapter 5. Additionally, DFT calculations are used to model the lithiated phase and assign the $^7$Li NMR of $Li_{1.71}FeV_2O_7$.

The work presented in this chapter was published as a part of a manuscript: A Combined $^7$Li NMR, Density Functional Theory and *Operando* Synchrotron X-Ray

Powder Diffraction to Investigate a Structural Evolution of $LiFeV_2O_7$ as a Potential Lithium Cathode Material with authors T.L.E. Pereira, J. Serano-Sevillano, B.D. Moreno, J.W. Reid, D. Carlier and G.R. Goward (Faraday Discussion, 2024, DOI: 10.1039/D4FD00077C). The NMR spectroscopy and data analysis was completed at McMaster University under the supervision of Prof. Gillian Goward. The DFT calculations were performed at The Mésocentre de Calcul Intensif Aquitain (MCIA) under the supervision of Prof. Dany Calier. The synchrotron powder X-ray diffraction data were collected at Canadian Light Source under the supervision of Dr. Beatriz D. Moreno.

## 6.2 Methods

### 6.2.1 Synchrotron Powder X-Ray Diffraction

#### 6.2.1.1 Design of *Operando* Cell for SPXRD

The first important step in running an *operando* experiment is to design the *operando* cell. The most common cell container used in research of LIBs is a coin cell design, however, these parts are made of stainless steel which generally decreases the effectiveness of synchrotron sources to deliver quality results. There are many designs of *operando* cells in literature [1], such as modified coin cells and modified pouch cells.

Some aspects were considered during the design of the cell and the experiments:

- The *operando* cell should fit in the synchrotron facilities.
- For SPXRD measurement, the cell needs to have at least a 5 mm hole in all stainless steel parts, (cap case, bottom case, and the spacer).

- The window material shouldn't react with cell components, such as electrolyte and electrode, and be resistant to the redox process (i.e. Kapton, Beryllium or aluminum foil)
- The battery holder needs to be tested due to the different pressures that this can offer.
- Check leak possibilities.

In this thesis, I choose to work with the modified coin cell, as this type of cell is commonly used in the lab, with Kapton tape as window material. **Figure 6.1** shows the modified coin cell parts, the modified coin cell assembled, and the setup experiment at the beam line.

### 6.2.1.2 Battery Preparation

The coin cell was prepared as a routine half-coin cell described in section 5.2.1. The only difference was that for the *operando* Synchrotron Powder X-ray Powder Diffraction (SPXRD) measurement, the coin cells were modified with 5 mm diameter holes at both entry and exit transmission and also in the spacer, as shown in **Figure 6.1a**. The Kapton tape (50.8 ± 2 μm thick) was used on both anode and cathode casings to avoid any air contamination.

In order to prevent any reaction of the cell components with the air, the half-coin cells were stored under argon in a container that was sealed inside the glovebox. The modified half-coin cell was mounted on a modified battery holder (model Adam Tech BH-49C-1-BK) and then fixed to a special holder designed for the powder diffraction beamline at Canadian Light Source (CLS). **Figures 6.1c and 6.1d** provide a better idea of how the experiment and the cell were set up. The cell was discharged on the SRS EC301 Potentiostat from 2.75 V to 2.27 V at a constant current of 5.45 x10$^{-2}$ mA (approximately C/20) at room temperature.

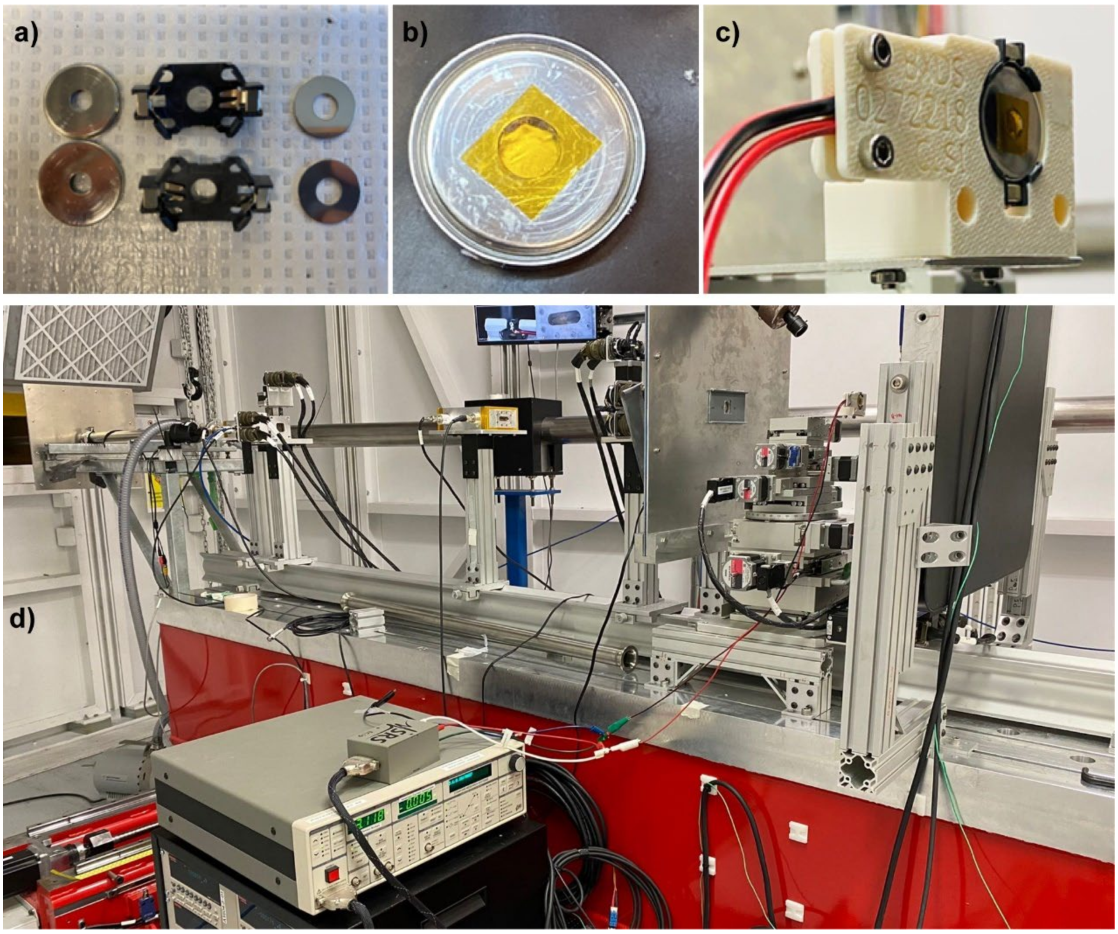

**Figure 6.1:** (a) Modified coin cell parts and battery holder; (b) the modified coin cell assembled; (c-d) the setup experiment at CLS BXDS beam line.

### 6.2.1.3 Synchrotron X-ray measurements

*Operando* powder diffraction measurements were conducted on a half-cell configuration in a modified coin cell on the BXDS higher energy wiggler (HEW) beamline at the Canadian Light Source (CLS). Each pattern was collected using a Perkin Elmer XRD 1621 CN3 EHS 2D detector (pixel size 200 μm x 200 μm) with an exposure time of 0.8 min. The detector distance, position, and tilt were precisely calibrated using a reference standard of Ni powder with GSAS-II, prior to integration of 2D images to point detector patterns from 3° to 25°, 2θ $\lambda = 0.3542$ Å, E= 35 keV. A pattern was collected every 8 min during the first discharge process and data collection was undertaken at room temperature. GSAS-II software was used for sequential Rietveld refinement of $LiFeV_2O_7$ during electrochemical cycling.[2] For the sequential refinement, the unit cell parameters, iron, vanadium, and oxygen coordinates were allowed to vary.

*Ex-situ* PXRD was also conducted on the BXDS lower energy wiggler (LEW) beamline.[3] The detector was a Mythen2 X series 1K strip detector from Dectris mounted on 1.1 m goniometer arm, with a total exposure time of 5.16 min. The wavelength was precisely calibrated using a reference standard of LaB6 powder to be $\lambda = 0.8193$ Å (15 keV).

The description of $^7$Li MAS NMR experiments and VASP calculations can be found in sections 4.2.4 and 4.2.5m respectively.

## 6.3 Results and Discussion

### 6.3.1 Testing Cell Design

Before running the sample at CLS, some tests were made to make sure the data collected there would match what we found in earlier ex-situ experiments. The c-rate, rest time, different coin cell cases, and physical impact were evaluated. The result showed that changing how fast the cell was charged and discharged didn't change how it behaved. After letting a new cell rest for six days, its voltage dropped a bit (OCV from 3.70 to 3.11 V), but it wasn't a big deal since the operating voltage for this cell is from 2.8 to 2.2 V. A commercial coin cell with a Kapton window was also tested, but it didn't work. The seal wasn't properly, causing lithium metal to oxidize. As a last test, the coin cell was kept in a backpack for two days to simulate the journey to CLS and see if this would affect the behavior of the cell. The half-coin cell worked perfectly, showing no effect on the health of the cell.

### 6.3.2 *Operando* Synchrotron PXRD

To understand the evolution of $Li_{1-x}FeV_2O_7$ structure, *operando* SPXRD is carried out on a half-cell configuration (**Figure 6.1**). **Figure 6.2** shows a series of SPXRD patterns that were collected during the electrochemical discharge of $LiFeV_2O_7$ vs Li metal to investigate the structural evolution associated with Li insertion. The cell discharged from 2.75 V to 2.27 V vs. $Li/Li^+$. The different colored lines in the plot represent diffraction patterns acquired at successive states of discharge. From the bottom to the top of the data series, there is a clear change in the observed reflections coincident with the progression of the discharge process. The series of diffractograms suggests a continuous change in the structure. It is evident that there are shifts in the positions of individual reflections as well as variations in intensity, and the coalescence of certain peaks as the electrochemical discharge progresses. These changes are indicative of alterations in the crystal structure, suggesting phase transformations or changes in the lattice parameters due to lithium-ion insertion in the material.

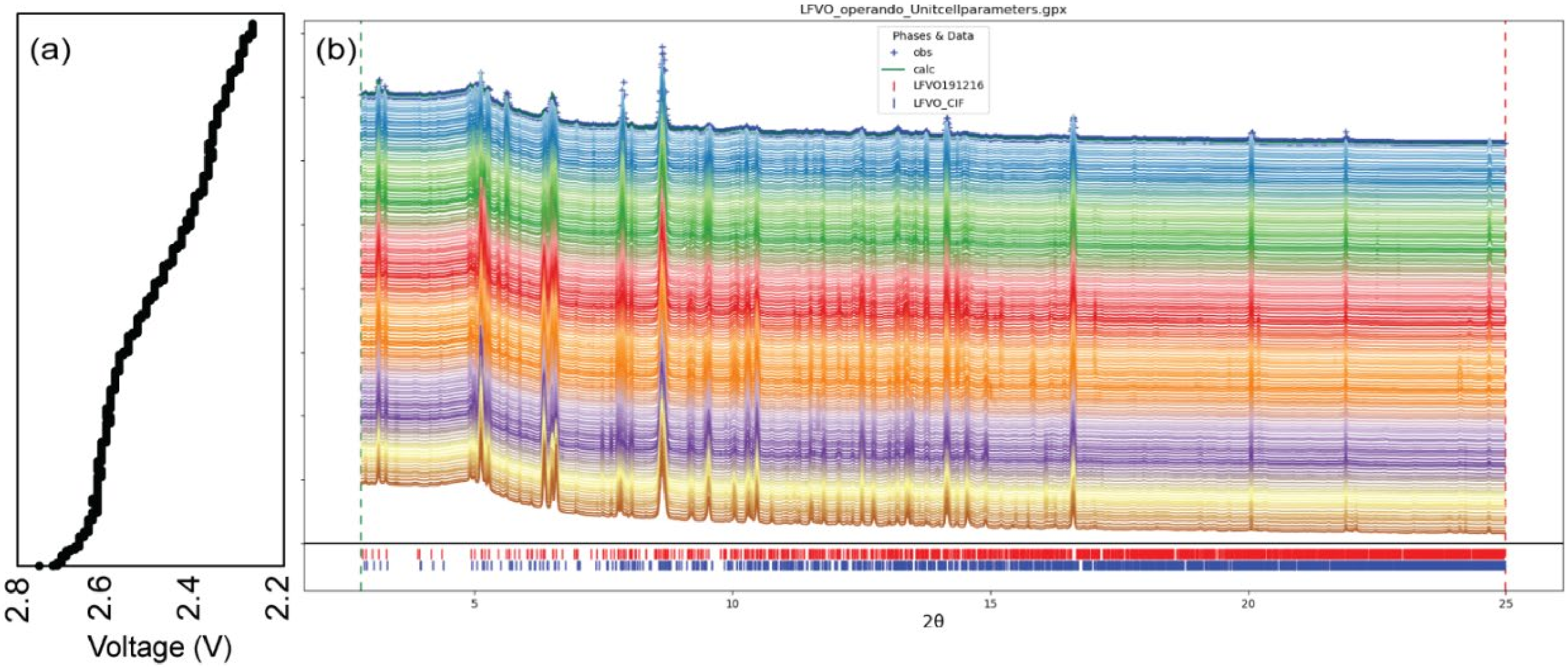

**Figure 6.2.** (a) Voltage profile of first discharge cycle for the *operando* coin cell from 2.75 V to 2.27 V vs. $Li/Li^+$; (b) The evolution of the X-ray diffraction patterns of $Li_{1-x}FeV_2O_7$;

The sequential Rietveld refinement of unit cell parameters over the course of the 139 scans for $LiFeV_2O_7$ is performed using a two-phase model. Even though the second phase is only detected after 0.5 mol of lithium is inserted, we choose to approach the data in this way to monitor the main phase transformation during the lithiated process. $Li_{1.x}FeV_2O_7$ electrode material undergoes a complex $Li^+$ insertion mechanism with sequential biphasic and solid-solution reactions during the first discharge process. The complexity of the data, characterized by a large number of peaks and their overlapping plus complex $Li^+$ insertion mechanism, poses a significant challenge to conducting a detailed analysis. The proximity of many peaks makes it difficult to isolate and analyze individual peak variations with high confidence. Due to these limitations, we focus our analysis on the unit cell parameters evolution during the first discharge cycle for phase 1. This approach provided valuable insights into the structural transformations occurring within the material. Extra information about Phase 2 is found in Appendix B.

**Figure 6.3** shows the evolution of the a, b, and c lattice parameters as well as the unit cell volume for phase 1 during the electrochemical lithiation of $Li_{1.x}FeV_2O_7$. Overall, unit cell volume expands as the experiment progresses, which increases by 0.37 % during the lithiation.  This phenomenon can be attributed to the increment of ionic radii of vanadium and iron produced upon Li insertion due to the reduction process and also the amount of lithium inserted. An increase in the unit cell volume often results in larger interstitial spaces within the crystal structure. These spaces can serve as pathways for lithium ions to move more freely through the electrode material resulting in an increase in the lithium dynamics. This result explains why an increase in lithium dynamics was observed in a lithiated sample by $^7Li$ NMR.

The *operando* SPXRD data provided a comprehensive overview of the transformations occurring within the unit cell. A comparison of the electrochemistry curves from the *operando* XRD cell, which incorporates Kapton windows, with those from the regular coin cell, **Figure 5.2b**, demonstrates similar behavior. This consistency indicates that the presence of Kapton windows does not significantly affect the discharge process. Consequently, there are no concerns regarding the impact of Kapton windows on the electrochemical behavior observed in these experiments. Nonetheless, the evident modification in the diffraction data exhibited a more gradual progression in comparison to the abrupt change in the $^7$Li NMR spectra. To elucidate the impact of lithium insertion on the local structure with greater clarity, further investigation was conducted through ex-situ synchrotron X-ray powder diffraction and ab initio computational studies.

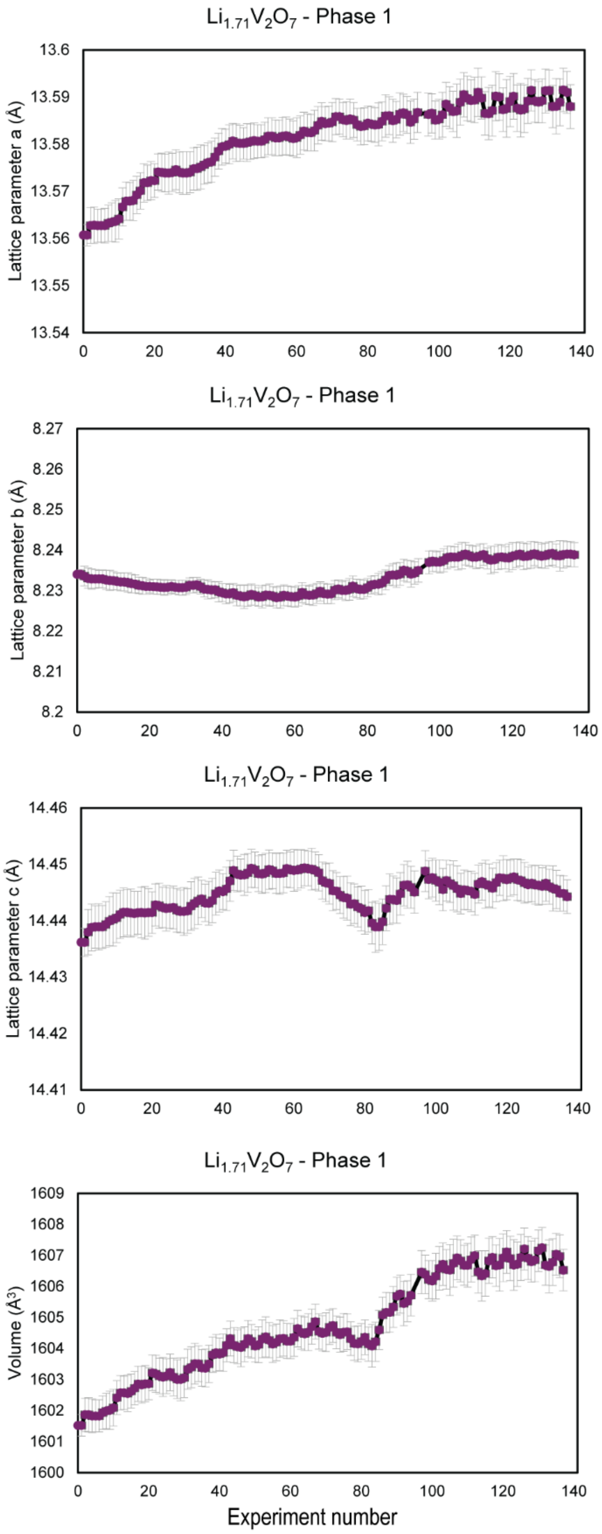

**Figure 6.3.** Lattice parameter and unit cell volume change during the first discharge cycle.

### 6.3.3 Structure Determination of $Li_{1.71}V_2O_7$

#### 6.3.3.1 Ex-situ SPXRD

In order to obtain a more comprehensive understanding of the phases present during the enhancement of lithium-ion dynamics, the ex-situ SPXRD pattern of $Li_{1.71}V_2O_7$ was obtained by discharging the half coin cell to 2.39 V vs $Li/Li^+$. The Rietveld refinement process involves adjusting the scale, background, and lattice parameters of the reference patterns to align with the experimental peaks, resulting in a low Rwp value of 4.69%. $Li_{1.71}FeV_2O_7$ consists of two phases: 65.54% phase 1 and 34.46% phase 2 (**Figure 6.4**). Although these phases share a similar structural framework, they exhibit slight variations in lattice parameters and are presumed to differ in their lithium content. The coexistence of structurally similar crystal phases with subtle differences in elemental composition can be observed not only in cycled battery materials[1,4], but also in the mineralogical system.[5]

Following lithiation, notable modifications in the lattice dimensions and volume were observed compared to the parent structure, while the crystallographic space group, monoclinic Cc, remained unchanged. This indicates that the structural symmetry is preserved even as the framework accommodates extra lithium ions. **Table 6.1** provides the detailed lattice parameters obtained with the Rietveld refinement.

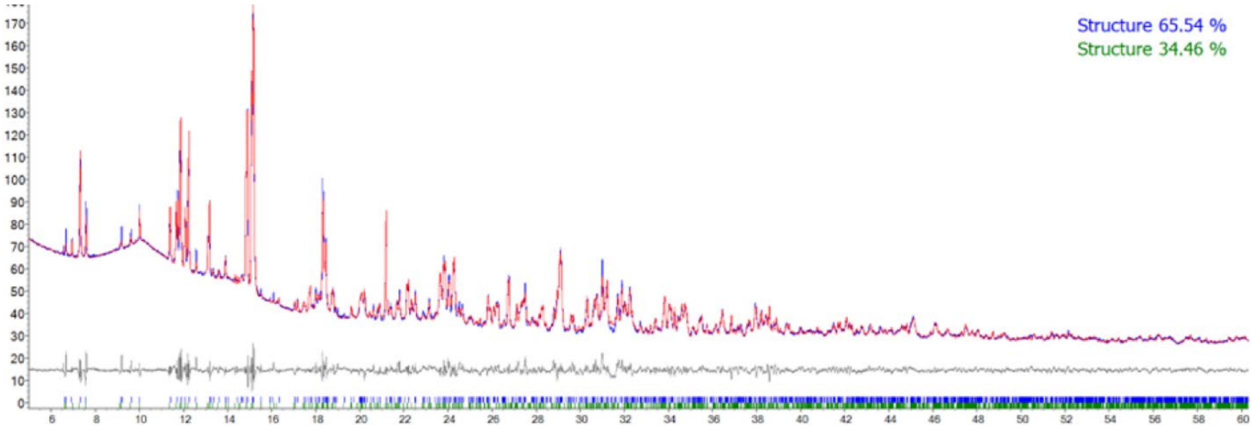

**Figure 6.4.** Rietveld refinement profile obtained for $Li_{1.71}V_2O_7$ from the synchrotron PXRD pattern.

**Table 6.1.** Rietveld refinement unit cell parameters for both phases in the $Li_{1.71}V_2O_7$ compared with the pristine phase.

| **Unit cell parameters** | **Pristine $LiFeV_2O_7$**[6] | **$Li_{1.71}FeV_2O_7$ Phase1** | **$Li_{1.71}FeV_2O_7$ Phase2** |
|---|---|---|---|
| **a (Å)** | 13.469(6) | 13.594(5) | 13.599(9) |
| **b (Å)** | 8.192(4) | 8.250(3) | 8.272(6) |
| **c (Å)** | 14.390(7) | 14.216(6) | 14.308(6) |
| **β (°)** | 96.600(9) | 94.866(5) | 95.309(8) |
| **Volume $(Å)^3$** | 1577.2(1) | 1588.7(7) | 1602.9(2) |

Given the complexity of the material, the investigation is narrowed to the predominant phase, Phase 1. This choice allows for a more in-depth exploration of the phase that plays the most significant role in the interpretation of the $^7Li$ NMR spectra. Ex-situ SPXRD diffractogram pattern does not allow for precise determination of lithium positions. The new lithium sites in $Li_{1.71}V_2O_7$ were deduced from bond valence energy landscape (BVEL) and then the structures were re-examined by DFT calculations.

### 6.3.3.2 Bond Valence Energy Landscape

BVEL calculations have been used to predict possible positions for ions and also to prove ion diffusion pathways in diverse materials.[7–13] With this approach, BVEL were generated, where valence units are transformed into energy units as implemented in the program BondSTR of the Fullprof Suite.[14] Calculations were made using the soft bond valence parameters developed by S. Adams.[15] This approach considers the polarizability of the mobile species, in this case $Li^+$, and the influence of the counterions of the structure up to a distance of 10 Å. This approach allows visualizing conduction pathways in the structure while giving hints to possible conduction mechanisms. In our case, these calculations served as a guide for identifying plausible sites for lithium insertion.

**Figure 6.5** shows the calculated BVEL for $Li^+$ conduction pathways in the $Li_{1.71}FeV_2O_7$ structure phase 1 obtained from the Rietveld refinement with an isosurfaces value of 0.2 valence units. The yellow isosurfaces represent the most likely migration route for Li ions. Utilizing VESTA software, we incorporated eight new lithium sites into a structure refined $Li_{1.71}V_2O_7$ guided by the results obtained by BVEL calculations. After inserting the new lithium ions, the modified structure was submitted to geometry optimization by DFT calculation in VASP to get the stable atomic position of the modified structure. The same approach has been used to predict the lithium position in $LiH_2V_3O_8$ structure which exhibited agreement with the data obtained with neutron diffraction.[7]

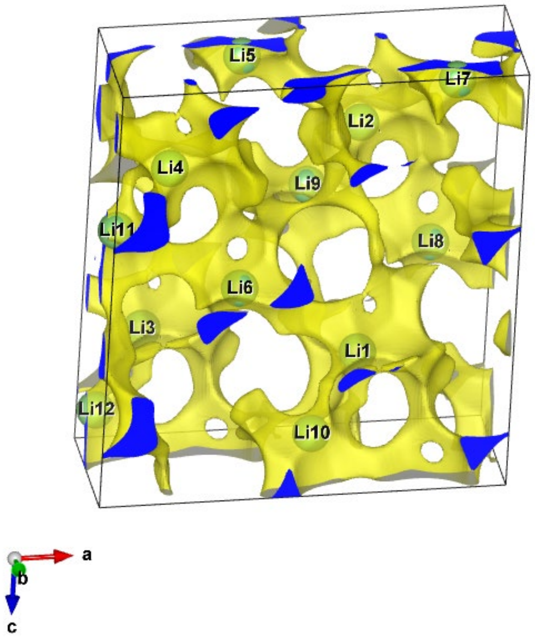

**Figure 6.5**. Bond Valence Energy Landscape (BVEL) calculation for Li-ions in $Li_{1.71}FeV_2O_7$ phase 1 with the isosurfaces of 0.2 plotted in VESTA.

### 6.3.4 DFT Studies of Lithiated Sample

Density functional theory (DFT) calculations were conducted in VASP to investigate the stability of the modeled structure and to elucidate the correlation between experimental $^7$Li NMR shifts and specific sites within the phases formed during the electrochemical lithiation of $LiFeV_2O_7$. For the lithiated phase $Li_{1.71}FeV_2O_7$, geometry optimization focused on Phase 1, which was identified from the Rietveld refinement of $Li_{1.71}FeV_2O_7$ and further analyzed for new lithium sites using BVEL calculations. The original structure $LiFeV_2O_7$ contained 12 Li per unit cell, whereas the modeled Phase 1 of $Li_{1.71}FeV_2O_7$ featured 20 Li. This model served as the basis for structural relaxation, leading to an optimized structure that was subsequently compared with the experimental results in **Table 6.2.** The optimized lattice parameters (a, b, and

c) obtained via the GGA+U method showed a deviation within a 3% error margin when compared with those determined experimentally through the diffraction technique.

**Table 6.2**. Relaxed cell parameters for GGA+U optimized $Li_{1.71}FeV_2O_7$ Phase 1 compared to values obtained from Rietveld refinement.

| **Unit cell parameters** | **$Li_{1.71}FeV_2O_7$* Phase 1** | **$Li_{1.71}FeV_2O_7$ Phase1 – GGAU** |
|---|---|---|
| **a (Å)** | 13.594(5) | 13.875(5) |
| **b (Å)** | 8.2503(3) | 8.3760(2) |
| **c (Å)** | 14.2166(1) | 14.4034(5) |
| **β (°)** | 94.866(5) | 95.874(0) |
| **Volume (Å)$^3$** | 1588.7(7) | 1665.1(7) |

* Data obtained from the Rietveld refinement of $Li_{1.71}FeV_2O_7$ for phase 1.

As mentioned in the *operando* and *ex-situ* SPXRD data, an increase in lattice parameters and unit cell volume suggests more open pathways or larger interstitial sites, providing a reason for the increased lithium mobility observed in the NMR data discussed in Chapter 5. With the structure optimized, we can have a more detailed understanding of the effects of unit cell changes on lithium dynamics. The Li-Li distances and the size of the channels, or bottlenecks, can significantly affect lithium dynamics in cathode materials for lithium-ion batteries.

Summarized in **Table 6.3**, it is possible to compare the lithium dynamics in the pristine and lithiated structure of $Li_{1.x}FeV_2O_7$ using the Li-Li distances and the Li-O bottleneck. Lithium− oxygen (Li−O) bottleneck diffusion area was calculated by the area of the face that the mobile lithium ions share when exchanging with their respective partners. In the pristine structure, the lack of energy barrier data implies that the lithium dynamics were not quantified under the conditions studied. There is a noticeable change in the bottleneck size for the $Li_{1B}$-$Li_{2A}$, and $Li_{1B}$-$Li_{3c}$ pairs, which increases from 4.32 to 4.48 Å$^2$ and 3.84 to 4.06 Å$^2$ respectively. This enlargement of the bottleneck potentially allows for easier lithium-ion movement, contributing to improved lithium dynamics in the lithiated structure.

**Table 6.3.** Summary of activation energy values for the three Li-Li exchange pairs as well as the calculated Li-O bottlenecks of diffusion for Pristine and Lithiated structures**.**

| **Pristine** | **Lithium Pair** | **Energy Barrier** | **Li-Li Distance (A)** | **Li-O Bottleneck ($A^2$)** |
|---|---|---|---|---|
| | $Li1_B$-$Li2_A$ | - | 4.46 | 4.32 |
| | $Li1_B$-$Li3_C$ | - | 3.2 | 3.84 |
| | $Li2_A$-$Li3_C$ | - | 4.68 | 4.86 |
| **Lithiated model**<br>**$Li_{1.71}FeV_2O_7$** | **Lithium Pair** | **Energy Barrier** [6] | **Li-Li Distance (A)** | **Li-O Bottleneck ($A^2$)** |
| | $Li1_B$-$Li2_A$ | 0.59 +/-0.06 | 4.38 | 4.48 |
| | $Li1_B$-$Li3_C$ | 0.48 +/- 0.07 | 3.2 | 4.06 |
| | $Li2_A$-$Li3_C$ | 0.4 +/- 0.3 | 4.64 | 4.95 |

The Li-Li distances do not change significantly upon lithiation, with only slight variations. This suggests that the average spacing between lithium ions does not drastically impact lithium dynamics after lithiation, at least not to the extent that would be indicated by the Li-Li distances alone. However, it is also notable that a short Li-Li distance facilitates easier lithium hopping between these sites, resulting in a lower energy barrier, as observed for $Li_{1B}$-$Li_{3c}$ pair. Both interatomic Li distances and bottleneck sizes are important factors to consider for understanding ionic conductivity in cathode material.

All these changes were evidenced by ssNMR spectroscopy, reflecting altered local environments and enhanced dynamics of lithium ions during the discharge process. The NMR data showed these changes through shifts in signal positions, changes in line widths (indicating changes in lithium mobility), and the appearance of a new signal in negative chemical shift, indicating that a new lithium environment was created.

### 6.3.5 Fermi Contact Shift and Spin Transfer Mechanism of Lithiated Phase

The calculated spin density of state (DOS) for the optimized phase 1 of $Li_{1.71}FeV_2O_7$ is given in **Figure 6.6**. Different from what was observed in the pristine material, the plotted DOS for $Li_{1.71}FeV_2O_7$ shows a change in the relative contributions of the Fe and V in d orbitals suggesting that both are going towards the redox process. The high-spin 3d electron configuration of $Fe^{2+}$ ions is confirmed by the appearance of occupied $e_g$ orbitals and a lift in degeneracy of the $t_{2g}$ down orbitals, one being occupied. For vanadium ions, which previously did not have any d orbital occupied, now a single unpaired electron is located in the $t_{2g}$ orbital. In $LiFeV_2O_7$, there are six vanadium sites situated in two different environments: five of these sites form $VO_4$ tetrahedra, while one adopts a [5]-coordinated $VO_5$ polyhedral geometry. In the presence of new occupied lithium sites, it is noted that vanadium atoms in 5 coordination are reduced in priority relative to the other vanadium atoms during the lithiation process. This is explained based on the charge compensation and the size of polyhedron to better accommodate big cation, $V^{4+}$. This result confirmed the hypothesis raised by Benabed [16]. Initially, the theoretical capacity of $LiFeV_2O_7$ was calculated assuming one $Li^+$ per formula unit, 97 mAh/g. However, the measured discharge capacity at the first cycle reached 100 mAh/g, which was slightly higher than the theoretical capacity, suggesting that vanadium was also partly reduced.

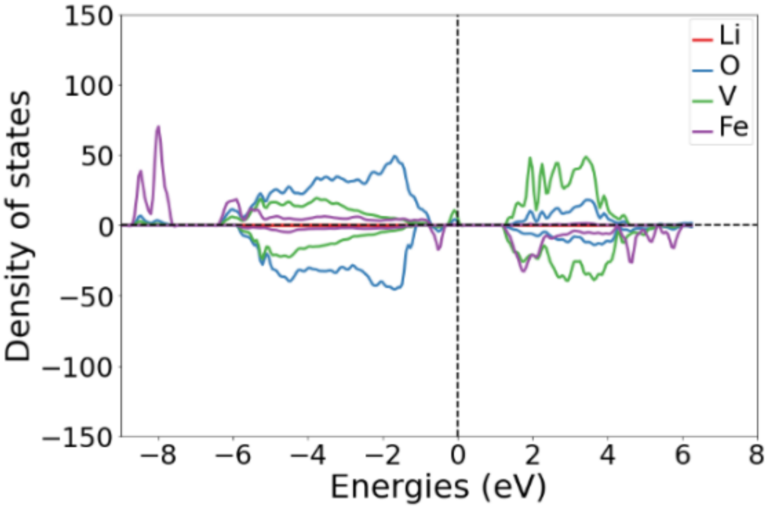

**Figure 6.6.** Calculated total spin DOS for $Li_{1.71}FeV_2O_7$ with GGAU where the color coding of line are elements

DFT calculations confirm that the two transition metals are reduced throughout the discharge process. For paramagnetic samples, the dominant interaction that affects the isotropic shift is the Fermi contact interactions and now in addition to the unpaired electrons from $Fe^{3+}/Fe^{2+}$, we also have unpaired electrons from $V^{4+}$. The $^7Li$ ssNMR Fermi contact shift was computed using the GGA+U method and the results can be found in **Table 6.4**. All computed $^7Li$ Fermi shifts for $Li_{1.71}V_2O_7$ are compared to the experimental spectra in **Figure 6.7**. The experimental data is characterized by multiple signals, including four intense peaks at 211, 178, 144 and -55 ppm. The signal observed around 0 ppm is attributed to electrolyte. The signals are very broad and thus it is possible for multiple signals to overlap.

**Table 6.4**: Calculated shifts for Li sites by GGA+U method for the ORG-D structure.

| **$Li_{1.71}FeV_2O_7$ Phase 1** | | |
|---|---|---|
| **CIF site** | **Site** | **Fermi Shift $^7$Li (ppm)** |
| **Li1** | $Li1_a$ | 59.5 |
| **Li1** | $Li1_b$ | 394.5 |
| **Li1** | $Li1_c$ | -29.7 |
| **Li1** | $Li1_d$ | 387.0 |
| **Li2** | $Li2_a$ | 223.3 |
| **Li2** | $Li2_b$ | 253.0 |
| **Li2** | $Li2_c$ | 156.2 |
| **Li2** | $Li2_d$ | 119.1 |
| **Li3** | $Li3_a$ | 215.8 |
| **Li3** | $Li3_b$ | 133.9 |
| **Li3** | $Li3_c$ | 104.2 |
| **Li3** | $Li3_d$ | 141.4 |
| **New** | Li13 | 59.5 |
| **New** | Li14 | -104.2 |
| **New** | Li15 | 66.98 |
| **New** | Li16 | -96.7 |
| **New** | Li17 | -141.4 |
| **New** | Li18 | 74.4 |
| **New** | Li19 | -89.3 |
| **New** | Li20 | 29.77 |

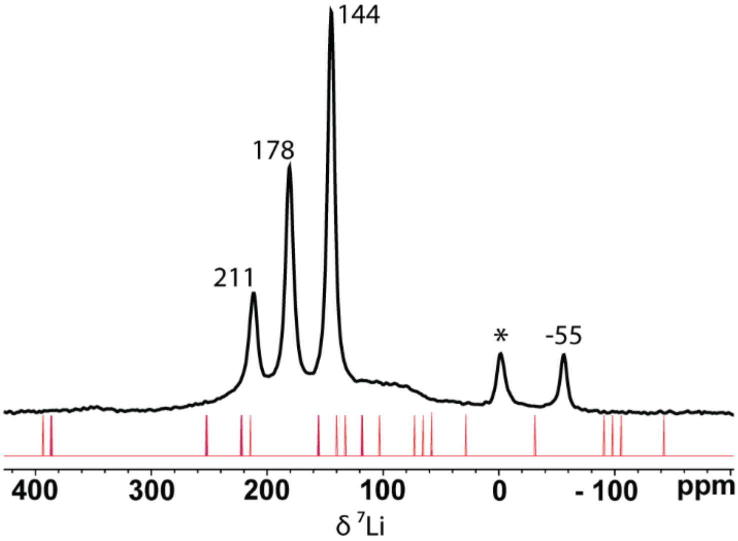

**Figure 6.7.** Comparison between the experimental $^7$Li MAS NMR signal of $Li_{1.71}FeV_2O_7$ and the calculated ones for the modeled supercell. The asterisk indicates the signal from electrolyte residual salt.

In order to understand the electronic spin transfer mechanism from the $V^{4+}$ ions to $Li^+$ in the optimized $Li_{1.71}V_2O_7$ structure, a calculated 3D spin density map was plotted in selected regions of the cell as shown in **Figure 6.8**. The 3D spin density maps of the entire structure can also be found in **Figure 6.9**. The positive and negative electron spins are presented in yellow and blue isosurfaces, respectively. The $V^{4+}$ ion exhibits one unpaired electron localized in the $d_{xz}$ orbital perpendicular to the V-O-Li axis. The z direction used to define the orientation of the orbitals was chosen to run along the V8-O40 interatomic axe as shown in **Figure 6.8**. All of them are independent of the a, b, and c crystallographic directions of the unit cell. As seen in **Figure 6.8**, no orbital overlap involves this $V^{4+}$ $3d_{xz}$ orbital and the spin density does not point toward Li, the V-O-Li angle is equal to 159.76°. However, as can be seen also in **Figure 6.8**, the O 2p orbital is negatively polarized. This is the case where the electron spin density is transferred to the s orbital via polarization mechanism. The unpaired electron of the partially filled $Vt_{2g}$ bands polarizes deeper fully occupied levels resulting from the $Ve_g$ – Op – Lis orbitals hybridization leading to a negative electronic spin on Li and consequently to a negative shift for $^7$Li NMR.[17,18] This behavior has been seen for $V^{4+}$ in other structures, such as $LiVOPO_4$[19] and $Na_3V_2(PO_4)_2FO_2$[20]. These results explain the single resonances observed in -55 ppm in the experimental $^7$Li NMR spectrum and thus confirm the reduction of $V^{5+}$ ions upon discharge.

The reduction of vanadium increases the number of paramagnetic species in the structure. The orientation of the vanadium d orbitals leads to some large shifts compared to the pristine material. However, for the Li1b site, the computed Fermi shift is larger than the experimentally observed shifts. With the addition of new lithium sites, the optimized lithiated structure is reorganized decreasing the Fe2-V4 distance from 3.3342 to 2.9906 Å. This structural change alters the coordination at some vanadium sites from $VO_4$ to $VO_5$. Unlike the scenario with Li1c, for this case the orientation of the vanadium d orbital is such that it aligns towards the Li orbital, facilitating a delocalization mechanism that shifts the chemical shift to higher ppm values. Consequently, the lithium site receives electron spin density from both vanadium and iron. This theoretical outcome, however, does not align with experimental observations, suggesting that additional models should be explored for a more accurate representation.

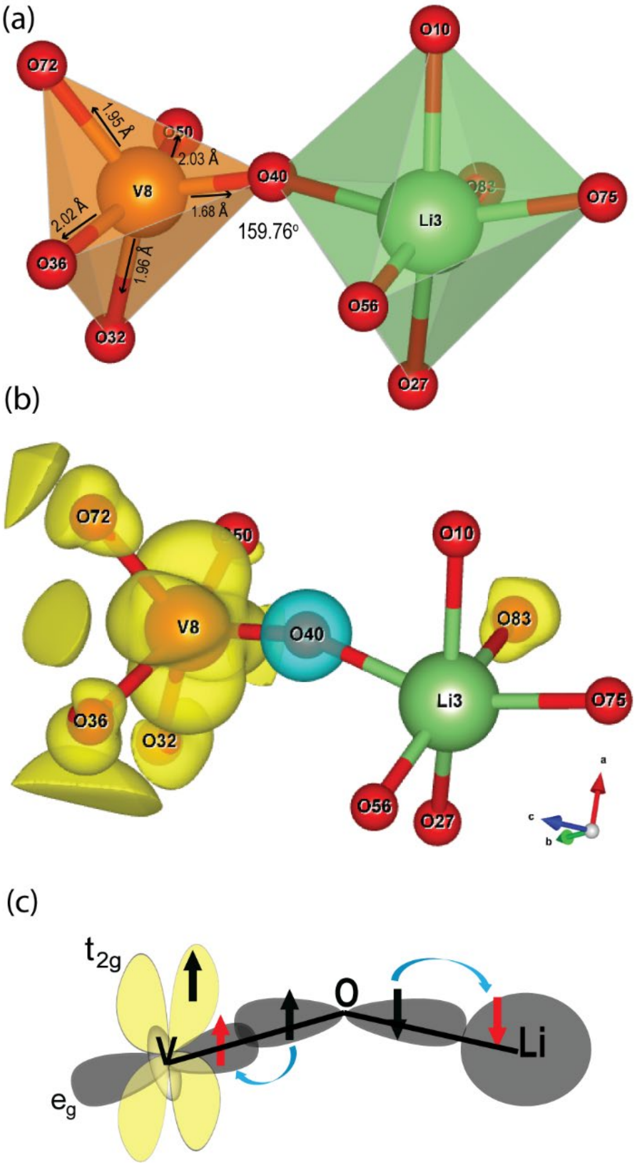

**Figure 6.8.** (a) Local environment of $V^{4+}$ and $Li^{+}$ in $Li_{1.71}FeV_2O_7$ molded structure (b)3D calculated spin density map showing the electron spin density surrounding a $V^{4+}$ ion (0.005 spin/Å$^2$ isosurface value) (c) Schematic representation of orbital overlap that results in a negative electronic spin density being transfer to the 2s orbital via polarization mechanism.

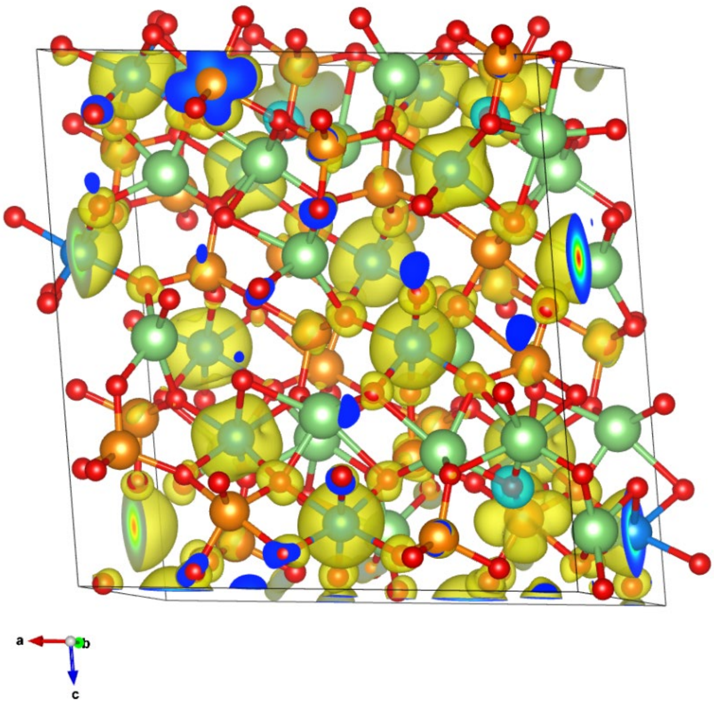

**Figure 6.9.** 3D spin density map calculated for $Li_{1.71}FeV_2O_7$ Phase1with GGA+U and isosurfaces value equal to 0.005 spin/Å$^2$. The positive and negative electron spin densities map are represented in yellow and blue, respectively.

## 6.4 Conclusion

In conclusion, the research presented provides a comprehensive investigation into the structural evolution of $Li_{1.x}FeV_2O_7$ during the lithiation process, correlating it with the dynamics of lithium insertion. The observed volume expansion during the first discharge cycle by *operando* SPXRD contributed to the enhanced lithium dynamics in the bulk material. The lithiated phase $Li_{1.71}FeV_2O_7$ was analyzed using ex-situ SPXRD and molded through BVEL calculations and verified by DFT calculations. Upon comparison between the optimized lithiated structure and its parent framework, an expansion of the bottleneck regions was observed. This structural modification facilitates the movement of lithium ions, significantly enhancing the lithium dynamics within the lithiated structure. These findings established the involvement of vanadium in the redox processes giving rise to a negative Fermi contact shift through the polarization mechanism.

## 6.5 References

(1) Bak, S. M.; Shadike, Z.; Lin, R.; Yu, X.; Yang, X. Q. In Situ/Operando Synchrotron-Based X-Ray Techniques for Lithium-Ion Battery Research. *NPG Asia Mater.* **2018**, *10* (7), 563–580. https://doi.org/10.1038/s41427-018-0056-z.

(2) Toby, B. H.; Von Dreele, R. B. GSAS-II: The Genesis of a Modern Open-Source All Purpose Crystallography Software Package. *J. Appl. Crystallogr.* **2013**, *46* (2), 544–549. https://doi.org/10.1107/S0021889813003531.

(3) Leontowich, A. F. G.; Gomez, A.; Moreno, B. D.; Muir, D.; Spasyuk, D.; King, G.; Reid, J. W.; Kim, C. Y.; Kycia, S. The Lower Energy Diffraction and Scattering Side-Bounce Beamline for Materials Science at the Canadian Light Source Leontowich Adam F. G. *J. Synchrotron Radiat.* **2021**, *28*, 961–969. https://doi.org/10.1107/S1600577521002496.

(4) Tahmasebi, M. H.; Obrovac, M. N. Quantitative Measurement of Compositional Inhomogeneity in NMC Cathodes by X-Ray Diffraction. *J. Electrochem. Soc.* **2023**, *170* (8), 080519. https://doi.org/10.1149/1945-7111/acefff.

(5) Antao, S. M. The Mystery of Birefringent Garnet: Is the Symmetry Lower than Cubic? *Powder Diffr.* **2013**, *28* (4), 265–272. https://doi.org/10.1017/S0885715613000523.

(6) Pereira, T. L. E. E.; Sanders, K. J.; Smiley, D. L.; Britten, J. F.; Goward, G. R. Structural Complexity and Evolving Lithium-Ion Dynamics within the Cathode Material LiFeV2O7Revealed by Diffraction and Solid-State NMR. *Chem.*

*Mater.* **2022**, *34* (19), 8551–8560. https://doi.org/10.1021/acs.chemmater.2c01357.

(7) Kuhn, A.; Pérez-Flores, J. C.; Prado-Gonjal, J.; Morán, E.; Hoelzel, M.; Díez-Gómez, V.; Sobrados, I.; Sanz, J.; García-Alvarado, F. Lithium Intercalation Mechanism and Critical Role of Structural Water in Layered H2V3O8High-Capacity Cathode Material for Lithium-Ion Batteries. *Chem. Mater.* **2022**, *34* (2), 694–705. https://doi.org/10.1021/acs.chemmater.1c03283.

(8) Lander, L.; Rousse, G.; Abakumov, A. M.; Sougrati, M.; Van Tendeloo, G.; Tarascon, J. M. Structural, Electrochemical and Magnetic Properties of a Novel KFeSO4F Polymorph. *J. Mater. Chem. A* **2015**, *3* (39), 19754–19764. https://doi.org/10.1039/c5ta05548b.

(9) Lander, L.; Reynaud, M.; Carrasco, J.; Katcho, N. A.; Bellin, C.; Polian, A.; Baptiste, B.; Rousse, G.; Tarascon, J. M. Unveiling the Electrochemical Mechanisms of Li2Fe(SO4)2 Polymorphs by Neutron Diffraction and Density Functional Theory Calculations. *Phys. Chem. Chem. Phys.* **2016**, *18* (21), 14509–14519. https://doi.org/10.1039/c6cp02175a.

(10) Zou, Z.; Ma, N.; Wang, A.; Ran, Y.; Song, T.; He, B.; Ye, A.; Mi, P.; Zhang, L.; Zhou, H.; Jiao, Y.; Liu, J.; Wang, D.; Li, Y.; Avdeev, M.; Shi, S. Identifying Migration Channels and Bottlenecks in Monoclinic NASICON-Type Solid Electrolytes with Hierarchical Ion-Transport Algorithms. *Adv. Funct. Mater.* **2021**, *31* (49), 1–12. https://doi.org/10.1002/adfm.202107747.

(11) Auckett, J. E.; Lopez-Odriozola, L.; Clark, S. J.; Evans, I. R. Exploring the Nature of the Fergusonite-Scheelite Phase Transition and Ionic Conductivity

Enhancement by Mo6+doping in LaNbO4. *J. Mater. Chem. A* **2021**, *9* (7), 4091–4102. https://doi.org/10.1039/d0ta07453e.

(12) Zhang, Z.; Avdeev, M.; Chen, H.; Yin, W.; Kan, W. H.; He, G. Lithiated Prussian Blue Analogues as Positive Electrode Active Materials for Stable Non-Aqueous Lithium-Ion Batteries. *Nat. Commun.* **2022**, *13* (1). https://doi.org/10.1038/s41467-022-35376-1.

(13) Xiao, R.; Li, H.; Chen, L. High-Throughput Design and Optimization of Fast Lithium Ion Conductors by the Combination of Bond-Valence Method and Density Functional Theory. *Sci. Rep.* **2015**, *5* (June), 1–11. https://doi.org/10.1038/srep14227.

(14) Rodrı´guez-Carvajal, J. *FullProfSuite*.

(15) Adams, S. From Bond Valence Maps to Energy Landscapes for Mobile Ions in Ion-Conducting Solids. *Solid State Ionics* **2006**, *177* (19-25 SPEC. ISS.), 1625–1630. https://doi.org/10.1016/j.ssi.2006.03.054.

(16) Benabed, Y.; Castro, L.; Penin, N.; Darriet, J.; Dollé, M. Synthesis, Structure, and Electrochemical Properties of LiFeV2O7. *Chem. Mater.* **2017**, *29* (21), 9292–9299. https://doi.org/10.1021/acs.chemmater.7b03271.

(17) Pell, A. J.; Pintacuda, G.; Grey, C. P. Paramagnetic NMR in Solution and the Solid State. *Prog. Nucl. Magn. Reson. Spectrosc.* **2019**, *111*, 1–271. https://doi.org/10.1016/j.pnmrs.2018.05.001.

(18) Grey, C. P.; Dupré, N. NMR Studies of Cathode Materials for Lithium-Ion Rechargeable Batteries. *Chem. Rev.* **2004**, *104* (10), 4493–4512.

https://doi.org/10.1021/cr020734p.

(19) Britto, S.; Seymour, I. D.; Halat, D. M.; Hidalgo, M. F. V.; Siu, C.; Reeves, P. J.; Zhou, H.; Chernova, N. A.; Whittingham, M. S.; Grey, C. P. Evolution of Lithium Ordering with (de)-Lithiation in β-LiVOPO4: Insights through Solid-State NMR and First Principles DFT Calculations. *J. Mater. Chem. A* **2020**, *8* (11), 5546–5557. https://doi.org/10.1039/d0ta00121j.

(20) Nguyen, L. H. B. B.; Camacho, P. S.; Broux, T.; Olchowka, J.; Masquelier, C.; Croguennec, L.; Carlier, D.; Sanz Camacho, P.; Broux, T.; Olchowka, J.; Masquelier, C.; Croguennec, L.; Carlier, D. Density Functional Theory-Assisted 31P and 23Na Magic-Angle Spinning Nuclear Magnetic Resonance Study of the Na3V2(PO4)2F3-Na3V2(PO4)2FO2 Solid Solution: Unraveling Its Local and Electronic Structures. *Chem. Mater.* **2019**, *31* (23), 9759–9768. https://doi.org/10.1021/acs.chemmater.9b03546.

# Chapter 7: Outlook and Future

In this thesis, a potential cathode for lithium-ion batteries was deeply investigated for its physical and electrochemical properties. Below, a detailed summary of each chapter and its contribution to this research is provided.

## 7.1 Summary and Conclusion

The motivation for the research presented in this thesis was to explore $LiFeV_2O_7$ as a potential cathode material. The combination of these two elements, iron, and vanadium, has been explored based on the ternary phase diagram $Li_2O$, $Fe_2O_3$, and $V_2O_5$. [1] Iron is a particularly desirable cathode active material due to its low cost and natural abundance, as well as low toxicity. Furthermore, vanadium can move among four oxidation states, thus being able to exhibit a wide range of capacities as a cathode material. Notably, certain vanadium-doped $LiFePO_4$ structures, such as $LiFe_{1-3/2y}V_yPO_4$ has demonstrated promising properties for application in batteries.[2]

In Chapter 4, the research focused on the structural characteristics of $LiFeV_2O_7$, employing $^7Li$ ssNMR, single-crystal XRD, and DFT calculations. The unexpected complexity observed in the $^7Li$ MAS spectra prompted a detailed investigation into the crystal structure using single-crystal XRD. This analysis revealed local disorder at the V2, V6, and O8 positions alters the vanadium coordination environments around these sites, shifting to tetrahedral and trigonal bipyramidal geometries. These structural changes impact the electron spin density transfer mechanisms, leading to noticeable variations in Fermi contact shifts detected by solid-state NMR. The DFT calculations supported these experimental findings, highlighting the susceptibility of Li environments to these local structural alterations.

In Chapter 5, the lithium-ion dynamics were quantified in different stages of lithiation, $Li_{1-x}FeV_2O_7$. Ex situ $^7$Li MAS ssNMR experiments were used to track structural changes of the $LiFeV_2O_7$ electrode during electrochemical cycling. A new lithium arrangement was observed during the lithium insertion process, which occurs at a similar point of the electrochemical process as a notable increase of the lithium-ion dynamics as observed by 2D EXSY experiments. $^7$Li NMR selective inversion (SI) experiments were measured over a temperature range of 303−318 K to quantify the exchange rates and energy barriers of ion mobility for each exchange pair present in the structure. In general, the activation energy increases as a function of the lithiation, suggesting that the lithium vacancies play a significant role in the current dynamics after the new lithium arrangement.

In Chapter 6, a detailed study of the lithiated phase was conducted combining *operando* synchrotron powder X-ray diffraction (SPXRD) and DFT calculations. A noticeable volume expansion was observed through the first discharge cycle which contributes to the enhanced lithium dynamics in the bulk material, as supported by ssNMR data shown in Chapter 5. DFT calculations are used to model the lithiated phase and demonstrate that both iron and vanadium participate in the redox process. The electronic structure of the $V^{4+}$ exhibits a single electron on the $3d_{xy}$ orbital perpendicular to the V-O-Li bond being a source of a negative Fermi contact shift observed in the $^7$Li NMR of the lithiated phase.

Observed as a whole, the work presented in this thesis demonstrates that both experimental and theoretical methodologies are complementary to each other. Solid-state NMR is shown to be highly sensitive to local structures that sometimes are not detected in powder X-ray diffraction and very effective in quantifying the lithium dynamics. DFT calculations are demonstrated to be an essential tool to better interpret complex systems. The series of experiments, data analysis, and testing hypotheses that make up this thesis contribute to this broader area of scientific discovery, primarily from a physical chemistry perspective, in an effort to better understand both the materials of interest as well as the methods that can be used to characterize materials in the future.

## 7.2 Future Work

To explore new material compositions, further investigation of the ternary phase diagram comprising $Li_2O$, $Fe_2O_3$, and $V_2O_5$ is recommended. This work has demonstrated that high concentrations of lithium can optimize lithium dynamics, suggesting the potential for discovering novel compositions and improving performance. Despite its promise, this phase diagram remains underexplored and warrants more extensive research. Together density functional theory (DFT) and Machine learning (ML) can significantly enhance the exploration of this phase diagram.[3–6] Advanced algorithms can analyze complex datasets to identify patterns and predict the stability and properties of new cathode materials. For instance, ML models can predict the stability and electrochemical properties of novel cathode materials[7,8] Guo et al.[9] mapped the lithium thiophosphate (LPS) phase diagram by combining DFT, ML, and artificial intelligence (AI) methods. Based on the discovered trends in the LPS phase diagram, Guo et al. propose a candidate solid-state electrolyte composition, $(Li_2S)_x(P_2S_5)_{1-x}$($x$~0.725), that exhibits high ionic conductivity of >$10^{-2}$ $Scm^{-1}$, demonstrating a design strategy for amorphous or glassy/ceramic solid electrolytes.[10]

With regard to further enhancing the understanding of the new arrangement observed in the $^7$Li NMR spectra of the lithiated phase ($Li_{1.71}FeV_2O_7$), two approaches can be considered. The first approach is to analyze the sample using neutron diffraction. Neutron diffraction is particularly well-suited for determining the positions of light atoms in materials[11,12], as it interacts directly with atomic nuclei, unlike X-ray diffraction, which primarily interacts with the electron cloud surrounding atoms and is more effective for heavier atoms. If access to neutron diffraction is still not possible, an alternative approach is to use molecular dynamics calculations to refine the lithiated model presented in this thesis. Molecular dynamics can provide detailed insights into atomic interactions and lithium positions within the structure. It is worth mentioning that this type of calculation is computationally expensive.

The comprehensive work presented in this thesis employs diverse techniques, emphasizing the ability of solid-state NMR and DFT calculations to investigate cathode materials for lithium-ion batteries. This research focuses on the structural and dynamic characterization of the novel cathode material $LiFeV_2O_7$, with the dual objectives of enhancing existing battery technologies and deepening the chemical understanding of energy storage mechanisms. Motivated by the urgent global need for sustainable and clean energy solutions, this study contributes to the ongoing advancements in battery development. Through a combination of experimental techniques and theoretical calculations, this thesis provides valuable insights into the local structures and dynamics of cathode materials, helping to improve energy storage technology.

## 7.3 References

(1) Padhi, A.k.; Nanjundaswamy, K.S.; Goodenough, J. B. Phospho-olivines as Positive-Electrode Materials for Rechargeable Lithium Batteries. *Soc. Electrochem.* **1997**, *144* (4), 1188–1194.

(2) Yang, M. R.; Ke, W. hsin; Wu, S. huang. Improving Electrochemical Properties of Lithium Iron Phosphate by Addition of Vanadium. *J. Power Sources* **2007**, *165* (2), 646–650. https://doi.org/10.1016/j.jpowsour.2006.10.054.

(3) Deffrennes, G.; Terayama, K.; Abe, T.; Tamura, R. A Machine Learning–Based Classification Approach for Phase Diagram Prediction. *Mater. Des.* **2022**, *215*, 110497. https://doi.org/10.1016/j.matdes.2022.110497.

(4) Lund, J.; Wang, H.; Braatz, R. D.; García, R. E. Machine Learning of Phase Diagrams. *Mater. Adv.* **2022**, *3* (23), 8485–8497. https://doi.org/10.1039/d2ma00524g.

(5) Ransom, B.; Zhao, N.; Sendek, A. D.; Cubuk, E. D.; Chueh, W.; Reed, E. J. Two Low-Expansion Li-Ion Cathode Materials with Promising Multi-Property Performance. *MRS Bull.* **2021**, *46* (12), 1116–1129. https://doi.org/10.1557/s43577-021-00154-9.

(6) Kam, R. L.; Jun, K. J.; Barroso-Luque, L.; Yang, J. H.; Xie, F.; Ceder, G. Crystal Structures and Phase Stability of the Li2S-P2S5 System from First Principles. *Chem. Mater.* **2023**, *35* (21), 9111–9126. https://doi.org/10.1021/acs.chemmater.3c01793.

(7) Lv, C.; Zhou, X.; Zhong, L.; Yan, C.; Srinivasan, M.; Seh, Z. W.; Liu, C.; Pan, H.; Li, S.; Wen, Y.; Yan, Q. Machine Learning: An Advanced Platform for Materials Development and State Prediction in Lithium-Ion Batteries. *Adv. Mater.* **2022**, *34* (25), 1–17. https://doi.org/10.1002/adma.202101474.

(8) Ng, M. F.; Sun, Y.; Seh, Z. W. Machine Learning-Inspired Battery Material Innovation. *Energy Adv.* **2023**, *2* (4), 449–464. https://doi.org/10.1039/d3ya00040k.

(9) Guo, H.; Wang, Q.; Urban, A.; Artrith, N. Artificial Intelligence-Aided Mapping of the Structure-Composition-Conductivity Relationships of Glass-Ceramic Lithium Thiophosphate Electrolytes. *Chem. Mater.* **2022**, *34* (15), 6702–6712. https://doi.org/10.1021/acs.chemmater.2c00267.

(10) Hu, S. Machine-Learning Approaches for the Discovery of Electrolyte Materials for Solid-State Lithium Batteries. **2023**, 1–12.

(11) Pecher, O.; Carretero-Gonzalez, J.; Griffith, K. J.; Grey, C. P. Materials' Methods: NMR in Battery Research. *Chem. Mater.* **2017**, *29* (1), 213–242. https://doi.org/10.1021/acs.chemmater.6b03183.

(12) Alonso, J. A.; Martínez-Lope, M. J.; Aguadero, A.; Daza, L. Neutron Powder Diffraction as a Characterization Tool of Solid Oxide Fuel Cell Materials. *Prog. Solid State Chem.* **2008**, *36* (1–2), 134–150. https://doi.org/10.1016/j.progsolidstchem.2007.03.004.

# Appendix A: Single Crystal - Structure Refinement

## lfvo191216

**Table A1 Crystal data and structure refinement for lfvo191216.**

| | |
|---|---|
| Identification code | lfo191216 |
| Empirical formula | $FeLiO_7V_2$ |
| Formula weight | 276.67 |
| Temperature/K | 296.15 |
| Crystal system | monoclinic |
| Space group | Cc |
| a/Å | 13.469(6) |
| b/Å | 8.192(4) |
| c/Å | 14.390(7) |
| α/° | 90 |
| β/° | 96.600(9) |
| γ/° | 90 |
| Volume/Å$^3$ | 1577.2(13) |
| Z | 12 |
| $\rho_{calc}$g/cm$^3$ | 3.495 |
| μ/mm$^{-1}$ | 6.178 |
| F(000) | 1572.0 |
| Crystal size/mm$^3$ | 0.3 × 0.2 × 0.2 |
| Radiation | MoKα (λ = 0.71073) |
| 2Θ range for data collection/° | 5.7 to 61.258 |
| Index ranges | $-19 \le h \le 19$, $-11 \le k \le 11$, $-20 \le l \le 20$ |
| Reflections collected | 24292 |
| Independent reflections | 4827 [$R_{int} = 0.0724$, $R_{sigma} = 0.0720$] |
| Data/restraints/parameters | 4827/410/309 |
| Goodness-of-fit on F$^2$ | 1.046 |
| Final R indexes [I>=2σ (I)] | $R_1 = 0.0387$, $wR_2 = 0.0839$ |
| Final R indexes [all data] | $R_1 = 0.0551$, $wR_2 = 0.0896$ |
| Largest diff. peak/hole / e Å$^{-3}$ | 0.69/-0.61 |
| Flack parameter | 0.43(5) |

**Table A2 Fractional Atomic Coordinates ($\times10^4$) and Equivalent Isotropic Displacement Parameters ($Å^2\times10^3$) for lfvo191216. $U_{eq}$ is defined as 1/3 of of the trace of the orthogonalised $U_{IJ}$ tensor.**

| Atom | *x* | *y* | *z* | U(eq) |
|---|---|---|---|---|
| Fe1 | 4985.1(9) | 8014.5(18) | 3679.4(9) | 6.0(3) |
| Fe2 | 8506.0(13) | 8254.4(11) | 5408.6(13) | 6.46(19) |
| Fe3 | 6989.5(9) | 3054.6(18) | 7118.4(9) | 5.5(3) |
| V1 | 4235.9(11) | 10266(3) | 1760.3(11) | 6.0(4) |
| V2 | 7046.7(13) | 9636(3) | 3577.1(12) | 5.4(3) |
| V3 | 5736.7(11) | 4570(3) | 5146.1(11) | 6.0(4) |
| V4 | 6260.6(10) | 9544(3) | 5669.4(10) | 5.9(4) |
| V5 | 2736.7(11) | 9740(3) | 4043.6(11) | 6.0(4) |
| V6 | 4060.5(13) | 4592(3) | 2411.5(13) | 5.5(3) |
| O1 | 4790(5) | 3226(9) | 4847(5) | 8.1(15) |
| O2 | 3218(5) | 11482(10) | 1463(5) | 6.8(16) |
| O3 | 2383(5) | 9915(9) | 2868(5) | 6.8(15) |
| O4 | 3962(5) | 4868(8) | 1207(5) | 8.2(15) |
| O5 | 4184(6) | 6424(10) | 2941(5) | 12.4(16) |
| O6 | 2919(6) | 11616(10) | 4495(6) | 9.8(17) |
| O7 | 5258(6) | 8819(8) | 6246(5) | 6.8(13) |
| O8 | 6199(6) | 7907(10) | 3034(6) | 7.6(11) |
| O9 | 5914(5) | 9685(9) | 4428(4) | 7.4(13) |
| O10 | 6774(5) | 11375(10) | 3071(5) | 8.3(15) |
| O11 | 6604(6) | 11381(10) | 6096(6) | 11.0(17) |
| O12 | 6718(6) | 3788(8) | 4579(6) | 10.3(13) |
| O13 | 2903(5) | 3662(9) | 2799(5) | 10.0(15) |
| O14 | 5061(6) | 3463(10) | 2756(6) | 11.3(16) |
| O15 | 4557(5) | 10040(8) | 2930(5) | 9.4(16) |
| O16 | 5412(5) | 6427(10) | 4730(6) | 8.2(15) |
| O17 | 4046(5) | 8425(9) | 1301(5) | 7.8(16) |
| O18 | 7908(5) | 10046(8) | 4540(5) | 11.1(16) |
| O19 | 6129(5) | 4636(10) | 6331(5) | 10.0(15) |
| O20 | 3757(5) | 8537(9) | 4355(5) | 8.5(16) |
| O21 | 7190(5) | 8184(9) | 5980(5) | 10.1(16) |
| Li1 | 6386(14) | 6740(20) | 7101(14) | 21(4) |
| Li2 | 3420(20) | 6927(16) | 5371(19) | 22(3) |

| Atom | *x* | *y* | *z* | U(eq) |
|---|---|---|---|---|
| Li3 | 5255(14) | 11850(20) | 3771(13) | 20(4) |
| V2A | 7852(8) | 10412(17) | 3358(7) | 5.4(3) |
| V6A | 4880(7) | 5398(17) | 2213(7) | 5.5(3) |
| O8A | 5760(30) | 7150(60) | 2800(30) | 7.6(11) |

**Table A3 Anisotropic Displacement Parameters ($Å^2×10^3$) for lfvo191216. The Anisotropic displacement factor exponent takes the form: $-2\pi^2[h^2a^{*2}U_{11}+2hka^*b^*U_{12}+…]$.**

| Atom | $U_{11}$ | $U_{22}$ | $U_{33}$ | $U_{23}$ | $U_{13}$ | $U_{12}$ |
|---|---|---|---|---|---|---|
| Fe1 | 6.2(7) | 5.5(7) | 6.1(7) | 0.4(6) | -0.2(5) | 0.0(6) |
| Fe2 | 6.1(4) | 6.3(4) | 7.0(4) | 0.2(8) | 1.3(3) | -0.3(8) |
| Fe3 | 5.1(6) | 6.2(7) | 5.3(7) | 0.4(6) | 1.4(5) | 0.0(6) |
| V1 | 6.9(7) | 6.3(9) | 4.8(8) | 0.4(8) | 0.7(6) | -0.1(7) |
| V2 | 6.2(8) | 5.5(8) | 4.7(7) | 0.4(5) | 1.1(6) | 0.5(6) |
| V3 | 7.1(8) | 5.3(8) | 6.0(8) | -0.5(8) | 1.7(6) | -0.6(7) |
| V4 | 5.8(7) | 6.5(8) | 5.4(8) | 0.1(8) | -0.4(6) | -0.6(7) |
| V5 | 5.3(7) | 6.6(8) | 6.0(8) | 0.1(8) | -0.4(6) | 0.4(7) |
| V6 | 5.1(7) | 5.8(8) | 5.5(7) | -0.2(6) | 0.3(6) | 0.3(6) |
| O1 | 10(3) | 7(4) | 7(3) | 2(3) | -1(3) | -2(3) |
| O2 | 8(2) | 7(3) | 5(2) | 1(2) | -1(2) | -1(2) |
| O3 | 8(3) | 8(4) | 4(3) | -1(2) | 2(3) | -1(3) |
| O4 | 11(3) | 6(4) | 7(3) | 1(2) | -1(2) | 6(2) |
| O5 | 17(3) | 10(3) | 11(4) | 0(3) | 3(3) | 3(3) |
| O6 | 15(4) | 6(4) | 8(4) | -4(3) | 0(3) | -1(3) |
| O7 | 7(2) | 8(2) | 6(2) | -1(2) | 3.2(18) | 2(2) |
| O8 | 4(3) | 10(3) | 8(3) | -1(2) | 0(2) | -1(2) |
| O9 | 10(3) | 6(3) | 6(3) | 0(3) | -3(2) | 0(3) |
| O10 | 6(3) | 12(3) | 7(3) | 1(3) | 2(2) | 6(3) |
| O11 | 13(4) | 6(4) | 13(4) | 0(3) | 0(3) | -1(3) |
| O12 | 9(3) | 10(3) | 12(3) | 2(3) | 3(2) | 3(3) |
| O13 | 14(3) | 6(3) | 8(4) | -3(2) | -5(3) | 0(3) |
| O14 | 14(3) | 9(3) | 12(3) | 0(3) | 3(3) | 1(3) |
| O15 | 10(3) | 9(4) | 10(3) | 2(3) | 1(3) | 0(3) |
| O16 | 9(3) | 10(4) | 6(3) | 1(3) | 2(3) | 0(3) |
| O17 | 6(3) | 8(4) | 9(4) | 3(3) | -1(3) | 0(3) |
| O18 | 17(3) | 10(4) | 7(3) | 1(2) | 4(3) | 2(3) |
| O19 | 12(3) | 11(3) | 7(3) | 0(3) | 0(2) | 1(3) |
| O20 | 5(3) | 10(3) | 11(3) | 0(3) | 2(2) | 2(2) |
| O21 | 5(3) | 11(4) | 15(4) | 1(3) | 3(3) | 3(3) |
| Li1 | 27(10) | 10(7) | 25(9) | -1(6) | 0(7) | 2(7) |
| Li2 | 36(10) | 9(6) | 20(6) | 2(8) | 3(6) | 6(9) |

| **Atom** | **$U_{11}$** | **$U_{22}$** | **$U_{33}$** | **$U_{23}$** | **$U_{13}$** | **$U_{12}$** |
|---|---|---|---|---|---|---|
| Li3 | 30(9) | 6(6) | 23(9) | -1(5) | -6(7) | 5(6) |
| V2A | 6.2(8) | 5.5(8) | 4.7(7) | 0.4(5) | 1.1(6) | 0.5(6) |
| V6A | 5.1(7) | 5.8(8) | 5.5(7) | -0.2(6) | 0.3(6) | 0.3(6) |
| O8A | 4(3) | 10(3) | 8(3) | -1(2) | 0(2) | -1(2) |

**Table A4 Bond Lengths for lfvo191216.**

| Atom | Atom | Length/Å |
|---|---|---|
| Fe1 | O5 | 1.931(8) |
| Fe1 | O8 | 1.972(8) |
| Fe1 | O9 | 2.071(7) |
| Fe1 | O15 | 2.026(7) |
| Fe1 | O16 | 2.026(8) |
| Fe1 | O20 | 2.058(7) |
| Fe1 | Li3 | 3.161(17) |
| Fe1 | V6A | 3.000(12) |
| Fe1 | O8A | 1.88(5) |
| Fe2 | O1$^{1}$ | 1.991(8) |
| Fe2 | O4$^{2}$ | 1.975(7) |
| Fe2 | O6$^{3}$ | 1.979(8) |
| Fe2 | O17$^{2}$ | 1.964(8) |
| Fe2 | O18 | 2.033(7) |
| Fe2 | O21 | 2.038(8) |
| Fe2 | Li2$^{1}$ | 3.011(13) |
| Fe3 | V2$^{4}$ | 3.039(3) |
| Fe3 | O2$^{2}$ | 2.032(8) |
| Fe3 | O3$^{2}$ | 2.020(7) |
| Fe3 | O8$^{4}$ | 1.953(8) |
| Fe3 | O11$^{5}$ | 2.034(8) |
| Fe3 | O13$^{6}$ | 2.043(7) |
| Fe3 | O19 | 2.000(7) |
| Fe3 | Li1 | 3.128(19) |
| Fe3 | O8A$^{4}$ | 2.02(5) |
| V1 | O2 | 1.709(8) |
| V1 | O7$^{7}$ | 1.800(8) |
| V1 | O15 | 1.700(8) |
| V1 | O17 | 1.654(8) |
| V1 | Li2$^{7}$ | 3.16(2) |
| V1 | Li3 | 3.320(18) |
| V4 | O9 | 1.797(6) |
| V4 | O11 | 1.670(8) |
| V4 | O21 | 1.697(7) |
| V4 | Li1 | 3.07(2) |
| V5 | O3 | 1.710(7) |
| V5 | O6 | 1.676(8) |
| V5 | O12$^{8}$ | 1.824(8) |
| V5 | O20 | 1.708(7) |
| V5 | Li2 | 3.066(19) |
| V6 | O4 | 1.738(7) |
| V6 | O5 | 1.682(8) |
| V6 | O13 | 1.877(8) |
| V6 | O14 | 1.662(8) |
| V6 | Li2$^{9}$ | 3.21(2) |
| V6 | Li3$^{5}$ | 3.279(18) |
| O1 | Li3$^{5}$ | 2.07(2) |
| O2 | Li2$^{7}$ | 2.08(2) |
| O3 | Li1$^{10}$ | 2.13(2) |
| O4 | Li2$^{9}$ | 1.99(2) |
| O4 | V6A | 1.844(12) |
| O5 | V2A$^{11}$ | 2.125(14) |
| O5 | V6A | 1.705(14) |
| O7 | Li1 | 2.51(2) |
| O9 | Li3 | 2.150(18) |
| O10 | Li1$^{7}$ | 2.11(2) |
| O10 | Li3 | 2.41(2) |
| O10 | V2A | 1.661(13) |
| O13 | V2A$^{11}$ | 1.649(14) |
| O14 | Li1$^{9}$ | 2.12(2) |
| O14 | Li3$^{5}$ | 1.97(2) |
| O14 | V6A | 1.772(14) |

| Atom | Atom | Length/Å |
|---|---|---|
| V2 | O8 | 1.928(9) |
| V2 | O9 | 2.064(7) |
| V2 | O10 | 1.622(8) |
| V2 | O13$^{1}$ | 1.875(8) |
| V2 | O18 | 1.734(7) |
| V2 | Li3 | 3.055(18) |
| V3 | O1 | 1.702(8) |
| V3 | O12 | 1.753(8) |
| V3 | O16 | 1.675(8) |
| V3 | O19 | 1.727(7) |
| V3 | Li3$^{5}$ | 3.003(17) |
| V4 | O7 | 1.766(8) |
| O15 | Li3 | 2.068(19) |
| O18 | Li2$^{1}$ | 2.02(2) |
| O18 | V2A | 1.721(12) |
| O19 | Li1 | 2.06(2) |
| O19 | V6A$^{4}$ | 2.220(13) |
| O20 | Li2 | 2.06(3) |
| O21 | Li1 | 2.36(2) |
| Li1 | Li3$^{12}$ | 3.21(3) |
| Li1 | V6A$^{4}$ | 2.70(2) |
| Li2 | V2A$^{11}$ | 3.16(3) |
| V6A | O8A | 1.99(5) |

$^{1}$1/2+X,1/2+Y,+Z; $^{2}$1/2+X,3/2-Y,1/2+Z; $^{3}$1/2+X,-1/2+Y,+Z; $^{4}$+X,1-Y,1/2+Z; $^{5}$+X,-1+Y,+Z; $^{6}$1/2+X,1/2-Y,1/2+Z; $^{7}$+X,2-Y,-1/2+Z; $^{8}$-1/2+X,1/2+Y,+Z; $^{9}$+X,1-Y,-1/2+Z; $^{10}$-1/2+X,3/2-Y,-1/2+Z; $^{11}$-1/2+X,-1/2+Y,+Z; $^{12}$+X,2-Y,1/2+Z

**Table A5 Bond Angles for lfvo191216.**

| Atom | Atom | Atom | Angle/° |
|---|---|---|---|
| O5 | Fe1 | O8 | 98.7(3) |
| O5 | Fe1 | O9 | 176.7(3) |
| O5 | Fe1 | O15 | 98.8(3) |
| O5 | Fe1 | O16 | 94.0(3) |
| O5 | Fe1 | O20 | 88.4(3) |
| O5 | Fe1 | Li3 | 138.4(4) |
| O5 | Fe1 | V6A | 32.1(3) |
| O8 | Fe1 | O9 | 77.9(3) |
| O8 | Fe1 | O15 | 89.2(3) |
| O8 | Fe1 | O16 | 98.2(3) |
| O8 | Fe1 | O20 | 170.5(3) |
| O8 | Fe1 | Li3 | 88.1(5) |
| O9 | Fe1 | Li3 | 42.5(4) |
| O9 | Fe1 | V6A | 144.6(3) |
| O15 | Fe1 | O9 | 81.6(3) |
| O15 | Fe1 | O16 | 164.0(3) |
| O15 | Fe1 | O20 | 83.5(3) |
| O15 | Fe1 | Li3 | 39.9(4) |
| O15 | Fe1 | V6A | 102.9(3) |
| O16 | Fe1 | O9 | 86.2(3) |
| O16 | Fe1 | O20 | 87.4(3) |
| O16 | Fe1 | Li3 | 125.8(4) |
| O16 | Fe1 | V6A | 93.0(3) |
| O20 | Fe1 | O9 | 95.0(3) |
| O20 | Fe1 | Li3 | 82.4(4) |
| O20 | Fe1 | V6A | 120.4(3) |
| V6A | Fe1 | Li3 | 137.3(4) |
| O8A | Fe1 | O5 | 72.2(15) |
| O8A | Fe1 | O9 | 104.5(15) |
| O8A | Fe1 | O15 | 95.5(13) |
| O8A | Fe1 | O16 | 97.5(13) |
| O8A | Fe1 | O20 | 160.1(14) |
| V2 | O10 | Li3 | 96.4(6) |
| Li1$^{7}$ | O10 | Li3 | 90.1(7) |
| V2A | O10 | Li3 | 136.9(7) |
| V4 | O11 | Fe3$^{13}$ | 155.5(5) |
| V3 | O12 | V5$^{3}$ | 133.2(4) |
| V2$^{10}$ | O13 | Fe3$^{14}$ | 101.6(4) |
| V2$^{10}$ | O13 | V6 | 126.4(4) |
| V6 | O13 | Fe3$^{14}$ | 127.7(4) |
| V6 | O14 | Li1$^{8}$ | 127.4(7) |
| V6 | O14 | Li3$^{5}$ | 129.1(7) |
| Li3$^{5}$ | O14 | Li1$^{8}$ | 103.3(8) |
| Fe1 | O15 | Li3 | 101.1(6) |
| V1 | O15 | Fe1 | 129.8(4) |
| V1 | O15 | Li3 | 123.3(7) |
| V3 | O16 | Fe1 | 152.9(5) |
| V1 | O17 | Fe2$^{11}$ | 158.2(4) |
| V2 | O18 | Fe2 | 122.2(4) |
| V2 | O18 | Li2$^{1}$ | 140.4(7) |
| Li2$^{1}$ | O18 | Fe2 | 95.9(6) |
| V2A | O18 | Fe2 | 134.7(6) |
| Fe3 | O19 | Li1 | 100.8(6) |
| Fe3 | O19 | V6A$^{4}$ | 95.5(4) |
| V3 | O19 | Fe3 | 129.1(4) |
| V3 | O19 | Li1 | 124.8(7) |
| V3 | O19 | V6A$^{4}$ | 113.4(4) |
| Li1 | O19 | V6A$^{4}$ | 78.2(7) |
| Fe1 | O20 | Li2 | 117.3(7) |
| V5 | O20 | Fe1 | 131.5(4) |
| V5 | O20 | Li2 | 108.6(8) |
| Fe2 | O21 | Li1 | 141.1(6) |
| V4 | O21 | Fe2 | 121.7(4) |
| V4 | O21 | Li1 | 97.2(6) |

| Atom | Atom | Atom | Angle/° |
|---|---|---|---|
| O8A | Fe1 | Li3 | 109.4(15) |
| O8A | Fe1 | V6A | 40.5(15) |
| O1$^{1}$ | Fe2 | O18 | 93.4(3) |
| O1$^{1}$ | Fe2 | O21 | 177.71(19) |
| O1$^{1}$ | Fe2 | Li2$^{1}$ | 92.2(6) |
| O4$^{2}$ | Fe2 | O1$^{1}$ | 91.1(3) |
| O4$^{2}$ | Fe2 | O6$^{3}$ | 171.3(3) |
| O4$^{2}$ | Fe2 | O18 | 82.5(2) |
| O4$^{2}$ | Fe2 | O21 | 90.8(3) |
| O4$^{2}$ | Fe2 | Li2$^{1}$ | 40.6(5) |
| O6$^{3}$ | Fe2 | O1$^{1}$ | 91.3(3) |
| O6$^{3}$ | Fe2 | O18 | 88.9(3) |
| O6$^{3}$ | Fe2 | O21 | 87.1(3) |
| O6$^{3}$ | Fe2 | Li2$^{1}$ | 130.8(5) |
| O17$^{2}$ | Fe2 | O1$^{1}$ | 89.1(3) |
| O17$^{2}$ | Fe2 | O4$^{2}$ | 95.6(3) |
| O17$^{2}$ | Fe2 | O6$^{3}$ | 92.82(19) |
| O17$^{2}$ | Fe2 | O18 | 176.9(3) |
| O17$^{2}$ | Fe2 | O21 | 89.4(3) |
| O17$^{2}$ | Fe2 | Li2$^{1}$ | 136.3(5) |
| O18 | Fe2 | O21 | 88.1(3) |
| O18 | Fe2 | Li2$^{1}$ | 41.9(5) |
| O21 | Fe2 | Li2$^{1}$ | 90.1(6) |
| V2$^{4}$ | Fe3 | Li1 | 133.8(4) |
| O2$^{2}$ | Fe3 | V2$^{4}$ | 119.9(2) |
| O2$^{2}$ | Fe3 | O11$^{5}$ | 86.8(3) |
| O2$^{2}$ | Fe3 | O13$^{6}$ | 82.7(3) |
| O2$^{2}$ | Fe3 | Li1 | 92.3(4) |
| O3$^{2}$ | Fe3 | V2$^{4}$ | 104.1(2) |
| O3$^{2}$ | Fe3 | O2$^{2}$ | 85.2(3) |

| Atom | Atom | Atom | Angle/° |
|---|---|---|---|
| Fe3 | Li1 | Li3$^{12}$ | 119.2(6) |
| V4 | Li1 | Fe3 | 136.1(7) |
| V4 | Li1 | Li3$^{12}$ | 103.8(6) |
| O3$^{2}$ | Li1 | Fe3 | 39.8(4) |
| O3$^{2}$ | Li1 | V4 | 143.8(9) |
| O3$^{2}$ | Li1 | O7 | 176.9(10) |
| O3$^{2}$ | Li1 | O21 | 111.3(9) |
| O3$^{2}$ | Li1 | Li3$^{12}$ | 99.6(7) |
| O3$^{2}$ | Li1 | V6A$^{4}$ | 89.3(7) |
| O7 | Li1 | Fe3 | 143.3(8) |
| O7 | Li1 | V4 | 35.1(3) |
| O7 | Li1 | Li3$^{12}$ | 79.0(6) |
| O7 | Li1 | V6A$^{4}$ | 93.0(7) |
| O10$^{12}$ | Li1 | Fe3 | 131.1(8) |
| O10$^{12}$ | Li1 | V4 | 83.6(7) |
| O10$^{12}$ | Li1 | O3$^{2}$ | 91.7(8) |
| O10$^{12}$ | Li1 | O7 | 85.3(7) |
| O10$^{12}$ | Li1 | O14$^{4}$ | 85.5(8) |
| O10$^{12}$ | Li1 | O21 | 89.4(8) |
| O10$^{12}$ | Li1 | Li3$^{12}$ | 48.8(5) |
| O10$^{12}$ | Li1 | V6A$^{4}$ | 124.5(9) |
| O14$^{4}$ | Li1 | Fe3 | 98.7(7) |
| O14$^{4}$ | Li1 | V4 | 111.9(8) |
| O14$^{4}$ | Li1 | O3$^{2}$ | 103.4(9) |
| O14$^{4}$ | Li1 | O7 | 77.2(6) |
| O14$^{4}$ | Li1 | O21 | 145.1(10) |
| O14$^{4}$ | Li1 | Li3$^{12}$ | 36.7(6) |
| O14$^{4}$ | Li1 | V6A$^{4}$ | 40.9(5) |
| O19 | Li1 | Fe3 | 38.9(4) |
| O19 | Li1 | V4 | 105.8(8) |

| Atom | Atom | Atom | Angle/° | Atom | Atom | Atom | Angle/° |
|---|---|---|---|---|---|---|---|
| O3$^{2}$ | Fe3 | O11$^{5}$ | 166.1(3) | O19 | Li1 | O3$^{2}$ | 78.5(7) |
| O3$^{2}$ | Fe3 | O13$^{6}$ | 101.8(3) | O19 | Li1 | O7 | 104.5(8) |
| O3$^{2}$ | Fe3 | Li1 | 42.4(4) | O19 | Li1 | O10$^{12}$ | 169.9(11) |
| O8$^{4}$ | Fe3 | V2$^{4}$ | 38.2(3) | O19 | Li1 | O14$^{4}$ | 94.2(8) |
| O8$^{4}$ | Fe3 | O2$^{2}$ | 157.6(3) | O19 | Li1 | O21 | 96.5(9) |
| O8$^{4}$ | Fe3 | O3$^{2}$ | 95.8(3) | O19 | Li1 | Li3$^{12}$ | 129.8(10) |
| O8$^{4}$ | Fe3 | O11$^{5}$ | 95.9(3) | O19 | Li1 | V6A$^{4}$ | 53.6(6) |
| O8$^{4}$ | Fe3 | O13$^{6}$ | 75.2(3) | O21 | Li1 | Fe3 | 110.5(7) |
| O8$^{4}$ | Fe3 | O19 | 108.5(3) | O21 | Li1 | V4 | 33.2(3) |
| O8$^{4}$ | Fe3 | Li1 | 103.5(5) | O21 | Li1 | O7 | 68.0(6) |
| O8$^{4}$ | Fe3 | O8A$^{4}$ | 25.9(12) | O21 | Li1 | Li3$^{12}$ | 128.9(7) |
| O11$^{5}$ | Fe3 | V2$^{4}$ | 89.7(2) | O21 | Li1 | V6A$^{4}$ | 140.6(9) |
| O11$^{5}$ | Fe3 | O13$^{6}$ | 88.4(3) | V6A$^{4}$ | Li1 | Fe3 | 64.4(5) |
| O11$^{5}$ | Fe3 | Li1 | 126.9(4) | V6A$^{4}$ | Li1 | V4 | 122.7(7) |
| O13$^{6}$ | Fe3 | V2$^{4}$ | 37.2(2) | Fe2$^{10}$ | Li2 | V1$^{12}$ | 134.9(8) |
| O13$^{6}$ | Fe3 | Li1 | 144.1(4) | Fe2$^{10}$ | Li2 | V5 | 140.4(9) |
| O19 | Fe3 | V2$^{4}$ | 145.9(2) | Fe2$^{10}$ | Li2 | V6$^{4}$ | 65.9(4) |
| O19 | Fe3 | O2$^{2}$ | 93.8(3) | Fe2$^{10}$ | Li2 | V2A$^{10}$ | 68.2(5) |
| O19 | Fe3 | O3$^{2}$ | 82.5(3) | V1$^{12}$ | Li2 | V6$^{4}$ | 70.5(5) |
| O19 | Fe3 | O11$^{5}$ | 86.8(3) | V1$^{12}$ | Li2 | V2A$^{10}$ | 153.4(8) |
| O19 | Fe3 | O13$^{6}$ | 174.2(3) | V5 | Li2 | V1$^{12}$ | 84.5(3) |
| O19 | Fe3 | Li1 | 40.3(4) | V5 | Li2 | V6$^{4}$ | 152.9(7) |
| O19 | Fe3 | O8A$^{4}$ | 82.8(14) | V5 | Li2 | V2A$^{10}$ | 72.6(6) |
| O8A$^{4}$ | Fe3 | Li1 | 81.9(14) | O2$^{12}$ | Li2 | Fe2$^{10}$ | 128.3(11) |
| O2 | V1 | O7$^{7}$ | 106.5(4) | O2$^{12}$ | Li2 | V1$^{12}$ | 30.0(4) |
| O2 | V1 | Li2$^{7}$ | 37.5(6) | O2$^{12}$ | Li2 | V5 | 86.8(5) |
| O2 | V1 | Li3 | 103.3(4) | O2$^{12}$ | Li2 | V6$^{4}$ | 66.3(7) |
| O7$^{7}$ | V1 | Li2$^{7}$ | 70.4(6) | O2$^{12}$ | Li2 | V2A$^{10}$ | 153.9(10) |
| O7$^{7}$ | V1 | Li3 | 86.4(4) | O4$^{4}$ | Li2 | Fe2$^{10}$ | 40.4(3) |
| O15 | V1 | O2 | 114.6(4) | O4$^{4}$ | Li2 | V1$^{12}$ | 94.5(9) |

| Atom | Atom | Atom | Angle/° |
|---|---|---|---|
| O15 | V1 | O7$^{7}$ | 109.5(3) |
| O15 | V1 | Li2$^{7}$ | 137.4(5) |
| O15 | V1 | Li3 | 31.4(4) |
| O17 | V1 | O2 | 110.4(4) |
| O17 | V1 | O7$^{7}$ | 107.8(4) |
| O17 | V1 | O15 | 107.8(4) |
| O17 | V1 | Li2$^{7}$ | 112.6(5) |
| O17 | V1 | Li3 | 137.2(4) |
| Li2$^{7}$ | V1 | Li3 | 110.3(5) |
| Fe3$^{8}$ | V2 | Li3 | 122.4(3) |
| O8 | V2 | Fe3$^{8}$ | 38.8(2) |
| O8 | V2 | O9 | 79.1(3) |
| O8 | V2 | Li3 | 92.0(4) |
| O9 | V2 | Fe3$^{8}$ | 117.5(2) |
| O9 | V2 | Li3 | 44.7(4) |
| O10 | V2 | Fe3$^{8}$ | 109.9(3) |
| O10 | V2 | O8 | 111.7(4) |
| O10 | V2 | O9 | 96.0(4) |
| O10 | V2 | O13$^{1}$ | 103.2(4) |
| O10 | V2 | O18 | 106.6(4) |
| O10 | V2 | Li3 | 51.7(5) |
| O13$^{1}$ | V2 | Fe3$^{8}$ | 41.2(2) |
| O13$^{1}$ | V2 | O8 | 79.7(3) |
| O13$^{1}$ | V2 | O9 | 155.5(3) |
| O13$^{1}$ | V2 | Li3 | 148.5(4) |
| O18 | V2 | Fe3$^{8}$ | 130.8(2) |
| O18 | V2 | O8 | 140.9(3) |
| O18 | V2 | O9 | 89.7(3) |
| O18 | V2 | O13$^{1}$ | 99.1(3) |
| O18 | V2 | Li3 | 106.0(4) |
| O4$^{4}$ | Li2 | V5 | 175.7(13) |
| O4$^{4}$ | Li2 | V6$^{4}$ | 28.2(5) |
| O4$^{4}$ | Li2 | O2$^{12}$ | 94.5(11) |
| O4$^{4}$ | Li2 | O18$^{10}$ | 82.6(5) |
| O4$^{4}$ | Li2 | O20 | 143.9(15) |
| O4$^{4}$ | Li2 | V2A$^{10}$ | 107.3(7) |
| O18$^{10}$ | Li2 | Fe2$^{10}$ | 42.2(3) |
| O18$^{10}$ | Li2 | V1$^{12}$ | 177.0(10) |
| O18$^{10}$ | Li2 | V5 | 98.4(9) |
| O18$^{10}$ | Li2 | V6$^{4}$ | 106.4(7) |
| O18$^{10}$ | Li2 | O2$^{12}$ | 149.1(15) |
| O18$^{10}$ | Li2 | O20 | 99.0(12) |
| O18$^{10}$ | Li2 | V2A$^{10}$ | 29.5(5) |
| O20 | Li2 | Fe2$^{10}$ | 129.9(11) |
| O20 | Li2 | V1$^{12}$ | 83.9(6) |
| O20 | Li2 | V5 | 31.9(4) |
| O20 | Li2 | V6$^{4}$ | 147.0(11) |
| O20 | Li2 | O2$^{12}$ | 101.2(6) |
| O20 | Li2 | V2A$^{10}$ | 69.5(8) |
| Fe1 | Li3 | V1 | 62.8(3) |
| Fe1 | Li3 | V6$^{13}$ | 127.6(6) |
| Fe1 | Li3 | Li1$^{7}$ | 112.9(6) |
| V2 | Li3 | Fe1 | 59.7(3) |
| V2 | Li3 | V1 | 86.6(4) |
| V2 | Li3 | V6$^{13}$ | 133.7(7) |
| V2 | Li3 | Li1$^{7}$ | 72.3(6) |
| V3$^{13}$ | Li3 | Fe1 | 141.3(7) |
| V3$^{13}$ | Li3 | V1 | 154.2(6) |
| V3$^{13}$ | Li3 | V2 | 112.8(6) |
| V3$^{13}$ | Li3 | V6$^{13}$ | 86.4(4) |

| Atom | Atom | Atom | Angle/° | Atom | Atom | Atom | Angle/° |
|---|---|---|---|---|---|---|---|
| O1 | V3 | O12 | 103.3(4) | V3$^{13}$ | Li3 | Li1$^{7}$ | 98.1(6) |
| O1 | V3 | O19 | 113.9(4) | V6$^{13}$ | Li3 | V1 | 67.8(4) |
| O1 | V3 | Li3$^{5}$ | 41.8(5) | O1$^{13}$ | Li3 | Fe1 | 122.0(8) |
| O12 | V3 | Li3$^{5}$ | 62.5(5) | O1$^{13}$ | Li3 | V1 | 137.2(8) |
| O16 | V3 | O1 | 109.9(4) | O1$^{13}$ | Li3 | V2 | 134.6(8) |
| O16 | V3 | O12 | 110.2(4) | O1$^{13}$ | Li3 | V3$^{13}$ | 33.2(3) |
| O16 | V3 | O19 | 111.3(4) | O1$^{13}$ | Li3 | V6$^{13}$ | 84.4(6) |
| O16 | V3 | Li3$^{5}$ | 114.3(4) | O1$^{13}$ | Li3 | O9 | 105.4(9) |
| O19 | V3 | O12 | 108.0(4) | O1$^{13}$ | Li3 | O10 | 138.0(9) |
| O19 | V3 | Li3$^{5}$ | 133.8(4) | O1$^{13}$ | Li3 | Li1$^{7}$ | 125.1(7) |
| O7 | V4 | O9 | 111.3(3) | O9 | Li3 | Fe1 | 40.6(3) |
| O7 | V4 | Li1 | 54.6(4) | O9 | Li3 | V1 | 99.8(6) |
| O9 | V4 | Li1 | 134.6(4) | O9 | Li3 | V2 | 42.4(4) |
| O11 | V4 | O7 | 108.9(4) | O9 | Li3 | V3$^{13}$ | 106.0(7) |
| O11 | V4 | O9 | 109.7(4) | O9 | Li3 | V6$^{13}$ | 167.6(8) |
| O11 | V4 | O21 | 109.3(4) | O9 | Li3 | O10 | 74.0(6) |
| O11 | V4 | Li1 | 115.7(5) | O9 | Li3 | Li1$^{7}$ | 114.8(9) |
| O21 | V4 | O7 | 103.7(3) | O10 | Li3 | Fe1 | 85.6(5) |
| O21 | V4 | O9 | 113.8(3) | O10 | Li3 | V1 | 81.9(5) |
| O21 | V4 | Li1 | 49.6(5) | O10 | Li3 | V2 | 31.8(3) |
| O3 | V5 | O12$^{9}$ | 108.4(4) | O10 | Li3 | V3$^{13}$ | 105.4(7) |
| O3 | V5 | Li2 | 135.2(5) | O10 | Li3 | V6$^{13}$ | 104.0(7) |
| O6 | V5 | O3 | 108.5(4) | O10 | Li3 | Li1$^{7}$ | 41.0(6) |
| O6 | V5 | O12$^{9}$ | 108.2(4) | O14$^{13}$ | Li3 | Fe1 | 129.2(8) |
| O6 | V5 | O20 | 110.5(4) | O14$^{13}$ | Li3 | V1 | 67.0(6) |
| O6 | V5 | Li2 | 115.3(5) | O14$^{13}$ | Li3 | V2 | 111.7(9) |
| O12$^{9}$ | V5 | Li2 | 66.5(6) | O14$^{13}$ | Li3 | V3$^{13}$ | 89.4(6) |
| O20 | V5 | O3 | 115.6(4) | O14$^{13}$ | Li3 | V6$^{13}$ | 23.2(3) |
| O20 | V5 | O12$^{9}$ | 105.3(4) | O14$^{13}$ | Li3 | O1$^{13}$ | 99.3(8) |
| O20 | V5 | Li2 | 39.5(6) | O14$^{13}$ | Li3 | O9 | 153.4(11) |
| O4 | V6 | O13 | 112.2(3) | O14$^{13}$ | Li3 | O10 | 81.1(8) |

| Atom | Atom | Atom | Angle/° |
|---|---|---|---|
| O4 | V6 | Li2$^{8}$ | 32.6(4) |
| O4 | V6 | Li3$^{5}$ | 131.3(4) |
| O5 | V6 | O4 | 109.1(4) |
| O5 | V6 | O13 | 105.6(4) |
| O5 | V6 | Li2$^{8}$ | 139.6(4) |
| O5 | V6 | Li3$^{5}$ | 109.0(4) |
| O13 | V6 | Li2$^{8}$ | 88.2(5) |
| O13 | V6 | Li3$^{5}$ | 84.9(4) |
| O14 | V6 | O4 | 109.6(4) |
| O14 | V6 | O5 | 109.1(4) |
| O14 | V6 | O13 | 111.0(3) |
| O14 | V6 | Li2$^{8}$ | 100.4(5) |
| O14 | V6 | Li3$^{5}$ | 27.8(4) |
| Li2$^{8}$ | V6 | Li3$^{5}$ | 110.0(4) |
| Fe2$^{10}$ | O1 | Li3$^{5}$ | 131.4(7) |
| V3 | O1 | Fe2$^{10}$ | 123.4(4) |
| V3 | O1 | Li3$^{5}$ | 105.0(7) |
| Fe3$^{11}$ | O2 | Li2$^{7}$ | 114.6(8) |
| V1 | O2 | Fe3$^{11}$ | 131.7(4) |
| V1 | O2 | Li2$^{7}$ | 112.5(8) |
| Fe3$^{11}$ | O3 | Li1$^{11}$ | 97.9(6) |
| V5 | O3 | Fe3$^{11}$ | 128.6(4) |
| V5 | O3 | Li1$^{11}$ | 123.2(7) |
| Fe2$^{11}$ | O4 | Li2$^{8}$ | 99.0(7) |
| V6 | O4 | Fe2$^{11}$ | 131.6(4) |
| V6 | O4 | Li2$^{8}$ | 119.2(8) |
| Fe1 | O5 | V2A$^{10}$ | 123.0(5) |
| V6 | O5 | Fe1 | 150.6(5) |
| V6 | O5 | V2A$^{10}$ | 74.8(4) |
| V6A | O5 | Fe1 | 111.0(5) |
| V5 | O6 | Fe2$^{9}$ | 155.4(5) |
| O14$^{13}$ | Li3 | O15 | 92.0(8) |
| O14$^{13}$ | Li3 | Li1$^{7}$ | 40.1(5) |
| O15 | Li3 | Fe1 | 39.0(4) |
| O15 | Li3 | V1 | 25.4(3) |
| O15 | Li3 | V2 | 80.4(6) |
| O15 | Li3 | V3$^{13}$ | 165.1(9) |
| O15 | Li3 | V6$^{13}$ | 89.0(6) |
| O15 | Li3 | O1$^{13}$ | 132.2(11) |
| O15 | Li3 | O9 | 78.7(6) |
| O15 | Li3 | O10 | 89.5(7) |
| O15 | Li3 | Li1$^{7}$ | 92.4(7) |
| Li1$^{7}$ | Li3 | V1 | 70.8(5) |
| Li1$^{7}$ | Li3 | V6$^{13}$ | 63.2(4) |
| O5$^{1}$ | V2A | Li2$^{1}$ | 89.0(6) |
| O10 | V2A | O5$^{1}$ | 119.1(7) |
| O10 | V2A | O18 | 105.5(7) |
| O10 | V2A | Li2$^{1}$ | 98.8(7) |
| O13$^{1}$ | V2A | O5$^{1}$ | 96.7(6) |
| O13$^{1}$ | V2A | O10 | 112.1(7) |
| O13$^{1}$ | V2A | O18 | 109.3(8) |
| O13$^{1}$ | V2A | Li2$^{1}$ | 140.2(7) |
| O18 | V2A | O5$^{1}$ | 113.9(6) |
| O18 | V2A | Li2$^{1}$ | 35.3(5) |
| O4 | V6A | Fe1 | 133.9(6) |
| O4 | V6A | O19$^{8}$ | 91.8(5) |
| O4 | V6A | Li1$^{8}$ | 103.9(7) |
| O4 | V6A | O8A | 144.7(14) |
| O5 | V6A | Fe1 | 36.9(4) |
| O5 | V6A | O4 | 103.4(6) |
| O5 | V6A | O14 | 103.1(7) |
| O5 | V6A | O19$^{8}$ | 149.7(8) |

| Atom | Atom | Atom | Angle/° |
|---|---|---|---|
| V1[12] | O7 | Li1 | 122.0(6) |
| V4 | O7 | V1[12] | 135.7(4) |
| V4 | O7 | Li1 | 90.3(6) |
| Fe3[8] | O8 | Fe1 | 151.8(5) |
| V2 | O8 | Fe1 | 105.1(4) |
| V2 | O8 | Fe3[8] | 103.1(4) |
| Fe1 | O9 | Li3 | 97.0(5) |
| V2 | O9 | Fe1 | 97.0(3) |
| V2 | O9 | Li3 | 92.9(6) |
| V4 | O9 | Fe1 | 123.2(4) |
| V4 | O9 | V2 | 117.6(3) |
| V4 | O9 | Li3 | 122.5(6) |
| V2 | O10 | Li1[7] | 165.2(7) |
| O5 | V6A | Li1[8] | 145.7(7) |
| O5 | V6A | O8A | 74.3(14) |
| O14 | V6A | Fe1 | 109.6(5) |
| O14 | V6A | O4 | 100.4(7) |
| O14 | V6A | O19[8] | 99.6(6) |
| O14 | V6A | Li1[8] | 51.6(6) |
| O14 | V6A | O8A | 114.5(13) |
| O19[8] | V6A | Fe1 | 115.7(5) |
| O19[8] | V6A | Li1[8] | 48.2(5) |
| Li1[8] | V6A | Fe1 | 122.1(5) |
| O8A | V6A | Fe1 | 37.8(14) |
| Fe1 | O8A | Fe3[8] | 156(3) |
| Fe1 | O8A | V6A | 102(2) |

[1] 1/2+X,1/2+Y,+Z; [2] 1/2+X,3/2-Y,1/2+Z; [3] 1/2+X,-1/2+Y,+Z; [4] +X,1-Y,1/2+Z; [5] +X,-1+Y,+Z; [6] 1/2+X,1/2-Y,1/2+Z; [7] +X,2-Y,-1/2+Z; [8] +X,1-Y,-1/2+Z; [9] -1/2+X,1/2+Y,+Z; [10] -1/2+X,-1/2+Y,+Z; [11] -1/2+X,3/2-Y,-1/2+Z; [12] +X,2-Y,1/2+Z; [13] +X,1+Y,+Z; [14] -1/2+X,1/2-Y,-1/2+Z

**Table A6 Torsion Angles for lfvo191216.**

| A | B | C | D | Angle/° | A | B | C | D | Angle/° |
|---|---|---|---|---|---|---|---|---|---|
| Fe1 | O5 | V6A | O4 | -150.4(5) | O15 | V1 | O2 | Fe3$^{2}$ | -29.8(7) |
| Fe1 | O5 | V6A | O14 | 105.3(6) | O15 | V1 | O2 | Li2$^{4}$ | 137.1(7) |
| Fe1 | O5 | V6A | O19$^{1}$ | -32.1(14) | O15 | V1 | O17 | Fe2$^{2}$ | 154.9(13) |
| Fe1 | O5 | V6A | Li1$^{1}$ | 67.5(15) | O16 | Fe1 | O8A | Fe3$^{1}$ | -91(6) |
| Fe1 | O5 | V6A | O8A | -6.9(13) | O16 | Fe1 | O8A | V6A | 85.8(16) |
| Fe2$^{2}$ | O4 | V6A | Fe1 | 47.5(9) | O16 | V3 | O1 | Fe2$^{9}$ | -71.0(6) |
| Fe2$^{2}$ | O4 | V6A | O5 | 71.8(7) | O16 | V3 | O1 | Li3$^{10}$ | 104.6(6) |
| Fe2$^{2}$ | O4 | V6A | O14 | 178.1(5) | O16 | V3 | O12 | V5$^{5}$ | 29.1(8) |
| Fe2$^{2}$ | O4 | V6A | O19$^{1}$ | -81.8(6) | O16 | V3 | O19 | Fe3 | -158.4(5) |
| Fe2$^{2}$ | O4 | V6A | Li1$^{1}$ | -129.1(6) | O16 | V3 | O19 | Li1 | -9.2(9) |
| Fe2$^{2}$ | O4 | V6A | O8A | -10(3) | O16 | V3 | O19 | V6A$^{6}$ | 82.4(6) |
| Fe2 | O18 | V2A | O5$^{3}$ | -79.6(10) | O17 | V1 | O2 | Fe3$^{2}$ | 92.2(6) |
| Fe2 | O18 | V2A | O10 | 148.0(7) | O17 | V1 | O2 | Li2$^{4}$ | -100.9(8) |
| Fe2 | O18 | V2A | O13$^{3}$ | 27.3(11) | O17 | V1 | O15 | Fe1 | 14.1(6) |
| Fe2 | O18 | V2A | Li2$^{3}$ | -128.6(12) | O17 | V1 | O15 | Li3 | 162.0(7) |
| Fe3$^{1}$ | V2 | O10 | Li1$^{4}$ | 0(3) | O18 | V2 | O10 | Li1$^{4}$ | 147(3) |
| Fe3$^{1}$ | V2 | O10 | Li3 | 116.1(5) | O18 | V2 | O10 | Li3 | -97.5(5) |
| Fe3$^{1}$ | V2 | O18 | Fe2 | -42.7(6) | O19 | V3 | O1 | Fe2$^{9}$ | 54.6(5) |
| Fe3$^{1}$ | V2 | O18 | Li2$^{3}$ | 155.2(13) | O19 | V3 | O1 | Li3$^{10}$ | -129.8(6) |
| O1 | V3 | O12 | V5$^{5}$ | 146.4(6) | O19 | V3 | O12 | V5$^{5}$ | -92.7(7) |
| O1 | V3 | O16 | Fe1 | -59.8(11) | O19 | V3 | O16 | Fe1 | 173.1(9) |
| O1 | V3 | O19 | Fe3 | 76.8(6) | O20 | Fe1 | O8A | Fe3$^{1}$ | 165(2) |
| O1 | V3 | O19 | Li1 | -134.1(8) | O20 | Fe1 | O8A | V6A | -18(5) |
| O1 | V3 | O19 | V6A$^{6}$ | -42.4(6) | O20 | V5 | O3 | Fe3$^{2}$ | -135.1(5) |
| O2 | V1 | O15 | Fe1 | 137.5(5) | O20 | V5 | O3 | Li1$^{2}$ | 87.9(8) |
| O2 | V1 | O15 | Li3 | -74.6(8) | O20 | V5 | O6 | Fe2$^{7}$ | -26.5(15) |
| O2 | V1 | O17 | Fe2$^{2}$ | 29.0(15) | O21 | V4 | O7 | V1$^{12}$ | 147.4(6) |
| O3 | V5 | O6 | Fe2$^{7}$ | -154.2(12) | O21 | V4 | O7 | Li1 | 7.6(6) |
| O3 | V5 | O20 | Fe1 | 29.4(7) | O21 | V4 | O9 | Fe1 | 79.9(5) |
| O3 | V5 | O20 | Li2 | -130.9(7) | O21 | V4 | O9 | V2 | -40.5(5) |

| A | B | C | D | Angle/° |
|---|---|---|---|---|
| O4 | V6 | O5 | Fe1 | -108.8(10) |
| O4 | V6 | O13 | Fe3$^{8}$ | 35.9(6) |
| O4 | V6 | O13 | V2$^{9}$ | -116.6(4) |
| O4 | V6 | O14 | Li1$^{1}$ | 27.2(9) |
| O4 | V6 | O14 | Li3$^{10}$ | -145.8(8) |
| O5 | Fe1 | O8A | Fe3$^{1}$ | 177(6) |
| O5 | Fe1 | O8A | V6A | -6.0(12) |
| O5 | V6 | O4 | Fe2$^{2}$ | -24.8(6) |
| O5 | V6 | O4 | Li2$^{1}$ | -162.2(9) |
| O5 | V6 | O13 | Fe3$^{8}$ | 154.8(3) |
| O5 | V6 | O13 | V2$^{9}$ | 2.2(6) |
| O5 | V6 | O14 | Li1$^{1}$ | -92.3(9) |
| O5 | V6 | O14 | Li3$^{10}$ | 94.7(9) |
| O6 | V5 | O3 | Fe3$^{2}$ | -10.4(6) |
| O6 | V5 | O3 | Li1$^{2}$ | -147.4(8) |
| O6 | V5 | O20 | Fe1 | -94.3(6) |
| O6 | V5 | O20 | Li2 | 105.4(8) |
| O7$^{4}$ | V1 | O2 | Fe3$^{2}$ | -151.0(5) |
| O7$^{4}$ | V1 | O2 | Li2$^{4}$ | 15.9(8) |
| O7$^{4}$ | V1 | O15 | Fe1 | -103.0(5) |
| O7$^{4}$ | V1 | O15 | Li3 | 45.0(8) |
| O7$^{4}$ | V1 | O17 | Fe2$^{2}$ | -87.0(14) |
| O7 | V4 | O9 | Fe1 | -36.8(5) |
| O7 | V4 | O9 | V2 | -157.2(4) |
| O7 | V4 | O9 | Li3 | 89.2(8) |
| O7 | V4 | O11 | Fe3$^{11}$ | 47.9(12) |
| O7 | V4 | O21 | Fe2 | 173.4(4) |
| O7 | V4 | O21 | Li1 | -8.2(6) |
| O8 | V2 | O10 | Li1$^{4}$ | -41(3) |
| O8 | V2 | O10 | Li3 | 74.6(6) |
| O21 | V4 | O9 | Li3 | -154.1(7) |
| O21 | V4 | O11 | Fe3$^{11}$ | -64.8(12) |
| Li1 | V4 | O7 | V1$^{12}$ | 139.8(9) |
| Li1 | V4 | O9 | Fe1 | 23.9(7) |
| Li1 | V4 | O9 | V2 | -96.4(6) |
| Li1 | V4 | O9 | Li3 | 150.0(8) |
| Li1 | V4 | O11 | Fe3$^{11}$ | -11.2(13) |
| Li1 | V4 | O21 | Fe2 | -178.4(8) |
| Li1$^{4}$ | O10 | V2A | O5$^{3}$ | 14.5(14) |
| Li1$^{4}$ | O10 | V2A | O13$^{3}$ | -97.2(11) |
| Li1$^{4}$ | O10 | V2A | O18 | 143.9(10) |
| Li1$^{4}$ | O10 | V2A | Li2$^{3}$ | 108.4(10) |
| Li1$^{1}$ | O14 | V6A | Fe1 | -115.9(6) |
| Li1$^{1}$ | O14 | V6A | O4 | 99.6(7) |
| Li1$^{1}$ | O14 | V6A | O5 | -153.9(7) |
| Li1$^{1}$ | O14 | V6A | O19$^{1}$ | 5.9(7) |
| Li1$^{1}$ | O14 | V6A | O8A | -75.3(17) |
| Li2$^{4}$ | V1 | O2 | Fe3$^{2}$ | -166.9(10) |
| Li2$^{4}$ | V1 | O15 | Fe1 | 175.2(7) |
| Li2$^{4}$ | V1 | O15 | Li3 | -36.9(11) |
| Li2$^{4}$ | V1 | O17 | Fe2$^{2}$ | -11.3(16) |
| Li2 | V5 | O3 | Fe3$^{2}$ | -178.2(7) |
| Li2 | V5 | O3 | Li1$^{2}$ | 44.9(12) |
| Li2 | V5 | O6 | Fe2$^{7}$ | 16.3(15) |
| Li2 | V5 | O20 | Fe1 | 160.3(10) |
| Li2$^{1}$ | V6 | O4 | Fe2$^{2}$ | 137.4(11) |
| Li2$^{1}$ | V6 | O5 | Fe1 | -123.5(12) |
| Li2$^{1}$ | V6 | O13 | Fe3$^{8}$ | 13.3(5) |
| Li2$^{1}$ | V6 | O13 | V2$^{9}$ | -139.3(5) |
| Li2$^{1}$ | V6 | O14 | Li1$^{1}$ | 59.7(9) |

| A | B | C | D | Angle/° |
|---|---|---|---|---|
| O8 | V2 | O18 | Fe2 | 12.4(8) |
| O8 | V2 | O18 | Li2$^{3}$ | -149.7(14) |
| O9 | Fe1 | O8A | Fe3$^{1}$ | -3(6) |
| O9 | Fe1 | O8A | V6A | 173.8(12) |
| O9 | V2 | O10 | Li1$^{4}$ | -122(3) |
| O9 | V2 | O10 | Li3 | -6.1(5) |
| O9 | V2 | O18 | Fe2 | 84.6(4) |
| O9 | V2 | O18 | Li2$^{3}$ | -77.5(14) |
| O9 | V4 | O7 | V1$^{12}$ | -89.9(6) |
| O9 | V4 | O7 | Li1 | 130.3(5) |
| O9 | V4 | O11 | Fe3$^{11}$ | 169.9(10) |
| O9 | V4 | O21 | Fe2 | 52.4(5) |
| O9 | V4 | O21 | Li1 | -129.2(6) |
| O10 | V2 | O18 | Fe2 | -179.2(4) |
| O10 | V2 | O18 | Li2$^{3}$ | 18.7(14) |
| O11 | V4 | O7 | V1$^{12}$ | 31.2(7) |
| O11 | V4 | O7 | Li1 | -108.6(6) |
| O11 | V4 | O9 | Fe1 | -157.4(4) |
| O11 | V4 | O9 | V2 | 82.2(5) |
| O11 | V4 | O9 | Li3 | -31.4(8) |
| O11 | V4 | O21 | Fe2 | -70.5(6) |
| O11 | V4 | O21 | Li1 | 107.9(6) |
| O12 | V3 | O1 | Fe2$^{9}$ | 171.5(4) |
| O12 | V3 | O1 | Li3$^{10}$ | -12.9(7) |
| O12 | V3 | O16 | Fe1 | 53.3(10) |
| O12 | V3 | O19 | Fe3 | -37.3(6) |
| O12 | V3 | O19 | Li1 | 111.9(8) |
| O12 | V3 | O19 | V6A$^{6}$ | -156.5(5) |
| O12$^{7}$ | V5 | O3 | Fe3$^{2}$ | 107.0(5) |
| O12$^{7}$ | V5 | O3 | Li1$^{2}$ | -30.0(8) |

| A | B | C | D | Angle/° |
|---|---|---|---|---|
| Li2$^{1}$ | V6 | O14 | Li3$^{10}$ | -113.4(9) |
| Li2$^{1}$ | O4 | V6A | Fe1 | -153.8(16) |
| Li2$^{1}$ | O4 | V6A | O5 | -129.5(17) |
| Li2$^{1}$ | O4 | V6A | O14 | -23.1(18) |
| Li2$^{1}$ | O4 | V6A | O19$^{1}$ | 76.9(16) |
| Li2$^{1}$ | O4 | V6A | Li1$^{1}$ | 29.6(18) |
| Li2$^{1}$ | O4 | V6A | O8A | 149(3) |
| Li2$^{3}$ | O18 | V2A | O5$^{3}$ | 49.0(11) |
| Li2$^{3}$ | O18 | V2A | O10 | -83.4(11) |
| Li2$^{3}$ | O18 | V2A | O13$^{3}$ | 155.9(9) |
| Li3 | Fe1 | O8A | Fe3$^{1}$ | 41(6) |
| Li3 | Fe1 | O8A | V6A | -142.0(13) |
| Li3 | V1 | O2 | Fe3$^{2}$ | -60.9(7) |
| Li3 | V1 | O2 | Li2$^{4}$ | 106.1(8) |
| Li3 | V1 | O15 | Fe1 | -147.9(10) |
| Li3 | V1 | O17 | Fe2$^{2}$ | 168.6(12) |
| Li3 | V2 | O10 | Li1$^{4}$ | -116(3) |
| Li3 | V2 | O18 | Fe2 | 126.7(5) |
| Li3 | V2 | O18 | Li2$^{3}$ | -35.4(14) |
| Li3$^{10}$ | V3 | O1 | Fe2$^{9}$ | -175.6(8) |
| Li3$^{10}$ | V3 | O12 | V5$^{5}$ | 136.7(8) |
| Li3$^{10}$ | V3 | O16 | Fe1 | -14.8(12) |
| Li3$^{10}$ | V3 | O19 | Fe3 | 31.6(9) |
| Li3$^{10}$ | V3 | O19 | Li1 | -179.2(8) |
| Li3$^{10}$ | V3 | O19 | V6A$^{6}$ | -87.5(8) |
| Li3$^{10}$ | V6 | O4 | Fe2$^{2}$ | -164.6(5) |
| Li3$^{10}$ | V6 | O4 | Li2$^{1}$ | 58.0(11) |
| Li3$^{10}$ | V6 | O5 | Fe1 | 40.4(12) |
| Li3$^{10}$ | V6 | O13 | Fe3$^{8}$ | -96.9(5) |
| Li3$^{10}$ | V6 | O13 | V2$^{9}$ | 110.5(5) |

| A | B | C | D | Angle/° |
|---|---|---|---|---|
| O12$^{7}$ | V5 | O6 | Fe2$^{7}$ | 88.3(13) |
| O12$^{7}$ | V5 | O20 | Fe1 | 149.1(5) |
| O12$^{7}$ | V5 | O20 | Li2 | -11.2(8) |
| O13$^{3}$ | V2 | O10 | Li1$^{4}$ | 43(3) |
| O13$^{3}$ | V2 | O10 | Li3 | 158.6(5) |
| O13$^{3}$ | V2 | O18 | Fe2 | -72.5(5) |
| O13$^{3}$ | V2 | O18 | Li2$^{3}$ | 125.4(14) |
| O13 | V6 | O4 | Fe2$^{2}$ | 92.0(6) |
| O13 | V6 | O4 | Li2$^{1}$ | -45.5(10) |
| O13 | V6 | O5 | Fe1 | 130.4(9) |
| O13 | V6 | O14 | Li1$^{1}$ | 151.7(8) |
| O13 | V6 | O14 | Li3$^{10}$ | -21.3(9) |
| O14 | V6 | O4 | Fe2$^{2}$ | -144.2(5) |
| O14 | V6 | O4 | Li2$^{1}$ | 78.4(10) |
| O14 | V6 | O5 | Fe1 | 11.0(12) |
| O14 | V6 | O13 | Fe3$^{8}$ | -87.1(5) |
| O14 | V6 | O13 | V2$^{9}$ | 120.3(4) |
| O15 | Fe1 | O8A | Fe3$^{1}$ | 79(6) |
| O15 | Fe1 | O8A | V6A | -103.5(15) |

| A | B | C | D | Angle/° |
|---|---|---|---|---|
| Li3$^{10}$ | V6 | O14 | Li1$^{1}$ | 173.1(15) |
| Li3 | O10 | V2A | O5$^{3}$ | -144.2(9) |
| Li3 | O10 | V2A | O13$^{3}$ | 104.0(11) |
| Li3 | O10 | V2A | O18 | -14.8(14) |
| Li3 | O10 | V2A | Li2$^{3}$ | -50.4(12) |
| Li3$^{10}$ | O14 | V6A | Fe1 | 5(2) |
| Li3$^{10}$ | O14 | V6A | O4 | -140(2) |
| Li3$^{10}$ | O14 | V6A | O5 | -33(2) |
| Li3$^{10}$ | O14 | V6A | O19$^{1}$ | 127(2) |
| Li3$^{10}$ | O14 | V6A | Li1$^{1}$ | 121(2) |
| Li3$^{10}$ | O14 | V6A | O8A | 45(3) |
| V2A$^{9}$ | O5 | V6A | Fe1 | -157.0(8) |
| V2A$^{9}$ | O5 | V6A | O4 | 52.6(9) |
| V2A$^{9}$ | O5 | V6A | O14 | -51.7(8) |
| V2A$^{9}$ | O5 | V6A | O19$^{1}$ | 170.9(10) |
| V2A$^{9}$ | O5 | V6A | Li1$^{1}$ | -89.5(14) |
| V2A$^{9}$ | O5 | V6A | O8A | -163.8(14) |
| V6A | Fe1 | O8A | Fe3$^{1}$ | -177(7) |

$^{1}$+X,1-Y,-1/2+Z; $^{2}$-1/2+X,3/2-Y,-1/2+Z; $^{3}$1/2+X,1/2+Y,+Z; $^{4}$+X,2-Y,-1/2+Z; $^{5}$1/2+X,-1/2+Y,+Z; $^{6}$+X,1-Y,1/2+Z; $^{7}$-1/2+X,1/2+Y,+Z; $^{8}$-1/2+X,1/2-Y,-1/2+Z; $^{9}$-1/2+X,-1/2+Y,+Z; $^{10}$+X,-1+Y,+Z; $^{11}$+X,1+Y,+Z; $^{12}$+X,2-Y,1/2+Z

## Table A7 Atomic Occupancy for lfvo191216.

| Atom | *Occupancy* | Atom | *Occupancy* | Atom | *Occupancy* |
|---|---|---|---|---|---|
| V2 | 0.846(3) | V6 | 0.846(3) | O8 | 0.846(3) |
| V2A | 0.154(3) | V6A | 0.154(3) | O8A | 0.154(3) |

### Experimental

A single crystal of $FeLiO_7V_2$ **[lfvo191216]** was selected and mounted on a **Bruker Apex2 CCD** diffractometer. The crystal was kept at 296.15 K during data collection. The structure was determined by XT [1] and refined using XL [2} package within OLEX2 [3] software,

1. Sheldrick, G. M. A Short History of SHELX. Acta Crystallogr. Sect. A Found. Crystallogr. 2008, 64 (1), 112–122.
2. Sheldrick, G. M. Crystal Structure Refinement with SHELXL. Acta Crystallogr. Sect. C Struct. Chem. 2015, 71 (Md), 3–8.
3. Dolomanov, O.V., Bourhis, L.J., Gildea, R.J, Howard, J.A.K. & Puschmann, H. (2009), J. Appl. Cryst. 42, 339-341.

### Crystal structure determination of [lfvo191216]

**Crystal Data** for $FeLiO_7V_2$ ($M$ =276.67 g/mol): monoclinic, space group Cc (no. 9), $a$ = 13.469(6) Å, $b$ = 8.192(4) Å, $c$ = 14.390(7) Å, $\beta$ = 96.600(9)°, $V$ = 1577.2(13) Å$^3$, $Z$ = 12, $T$ = 296.15 K, $\mu$(MoK$\alpha$) = 6.178 mm$^{-1}$, $Dcalc$ = 3.495 g/cm$^3$, 24292 reflections measured ($5.7° \leq 2\Theta \leq 61.258°$), 4827 unique ($R_{\mathrm{int}}$ = 0.0724, $R_{\mathrm{sigma}}$ = 0.0720) which were used in all calculations. The final $R_1$ was 0.0387 ($I > 2\sigma(I)$) and $wR_2$ was 0.0896 (all data).

### Refinement model description

Number of restraints - 410, number of constraints - unknown.

Details:

```
1. Twinned data refinement
 Scales: 0.57(5)
 0.43(5)
2. Uiso/Uaniso restraints and constraints
Uanis(O20) ≈ Ueq: with sigma of 0.02 and sigma for terminal atoms of 0.04
Uanis(O7) ≈ Ueq, Uanis(O2) ≈ Ueq: with sigma of 0.002 and sigma for
terminal atoms of 0.004
Uanis(V2) = Uanis(V2A)
Uanis(V6A) = Uanis(V6)
Uanis(O8) = Uanis(O8A)
3. Rigid body (RIGU) restrains
 All non-hydrogen atoms
 with sigma for 1-2 distances of 0.004 and sigma for 1-3 distances of 0.004
4. Others
 Sof(V2A)=Sof(V6A)=Sof(O8A)=1-FVAR(1)
 Sof(V2)=Sof(V6)=Sof(O8)=FVAR(1)
```

# Appendix B - Lattice Parameters For Phase 2

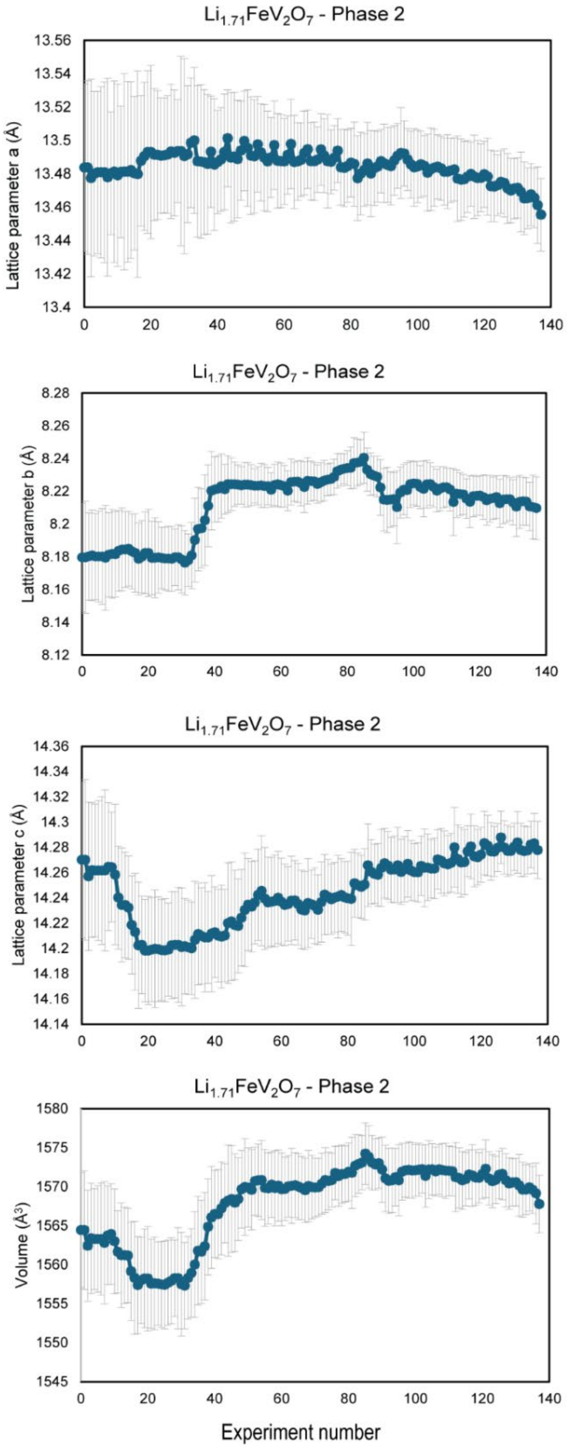

**Figure B1.** Lattice parameters and unit cell volume change for phase 2 during the first discharge cycle.